D56341 85

Silicon Molecular Beam Epitaxy

by

Weng Yee Leong

A thesis submitted to the
Council for National Academic Awards
in partial fulfilment of
the requirements for the degree
of
Doctor of Philosophy

Department of Physics,
City of London Polytechnic,
31, Jewry Street,
London EC3 2EY.

March, 1985

Abstract

This thesis reports on the techniques used in the growth and doping of Si-MBE layers prepared in a commercial molecular beam growth system and in the evaluation of their electrical and crystallographic properties. A number of technological problems associated with flux monitoring, the flaking of excess Si deposits and the use of closed-cycle He cryopumps during system bakeout were addressed.

The electrical and crystallographic qualities of the undoped and doped Si-MBE materials were assessed using preferential defect etching, four-point probe and Hall measurements, electrochemical CV profiling, Auger electron surface analysis, transmission electron microscopy (TEM), secondary ion mass spectroscopy (SIMS) analysis, spreading resistance measurement, and photoluminescence. The basic material grown was found to be of high quality and comparable to the Si-MBE material grown in other laboratories. Two electrically active contaminants, boron and phosphorus, were identified in our materials. The boron contamination was observed to occur at the substrate/epitaxial interface where the presence of an oxide layer prior to growth was apparently critical for its accumulation.

Two new techniques in co-evaporative doping in Si-MBE are reported. The use of co-evaporated boron doping was investigated enabling the growth of Si-MBE material with bulk-like mobilities and carrier concentrations up to $^{-}1x10^{20}$ cm^{-3} and giving excellent dopant profile control over a range of growth temperatures. The second technique called Potential Enhanced Doping (PED) involves applying a substrate potential during layer growth which enhances Sb dopant incorporation coefficient by up to a factor of 1000. Doping transitions were obtained by stepping the substrate potential. Using the PED technique, a maximum Sb dopant conentration of $2-3x10^{19}$ cm^{-3} at $850^{\circ}C$ and dopant transitions as abrupt as $<200\text{Å/decade}$ were acheived. Possible mechanisms for the observed PED effect are presented.

LIST OF CONTENTS

Chapter 1: Introduction

1.1 Si-MBE: historic account

Silicon Molecular Beam Epitaxy (Si-MBE) is the epitaxial growth of Si on a heated Si substrate by evaporation of Si in an ultra-high vacuum environment(UHV). This method of growth was established in the early 1960's through the work of Unvala[1] and Abbink et al[2]. Widmer[3] studied the influence of vacuum ambients in the growth of Si films. Joyce and his co-workers[4,5,6] investigated the roles played by residual gas reactions and surface contaminants on the substrate surface in disrupting the two dimensional epitaxial growth of Si. In 1968, Thomas and Francombe[7] reported the formation of a p-n junction by sublimation of Si in UHV. Few details of the electrical properties of the grown layers were given.

Throughout the early part of 1970's, very few reports of Si-MBE were published. It is considered that the overwelming success of CVD as a commercial epitaxial growth technique and the rapid emergence of III-V MBE had relegated Si-MBE to the reign of academic and scientific interest. In the mid 1970's, however, there was a re-emergence of Si-MBE work. This re-newed interest in Si-MBE came as a result of the growing uncertainty over CVD in meeting the requirement of VLSI technology and recognition of the potential of Si-MBE as a epitaxial growth technique with unmatched versatility in the dopant profile and thickness control.

The present-day Si-MBE owes much to its rapid development to the progress made in III-V MBE which stimulated the development in UHV/MBE system technologies. A number of excellent reviews of the development of MBE have been published[8]. Progress reviews of Si-MBE and related areas are given in a number of recent publications[9-11]. A comprehensive bibliography of

Si-MBE work between 1962-1982 has been compiled by Bean and McAfee[12].

Success in Si-MBE has recently stimulated research work in related areas such as Si on sapphire (SOS)[13], metal silicide growth[14,15], Si on amorphous substrates[16], solid phase epitaxy (SPE)[17], and differential epitaxy[9]. Growth of novel semiconductor materials such as SiGe superlattices has also been attempted[18,19,20].

1.2 General Growth requirements in Si-MBE

Investigations of the Si growth mechanism by Joyce et al[4,5,6] and Thomas and Francombe[21] have identified some of the growth requirements to achieve high quality epitaxial material by MBE, namely, low hydrocarbon backgrounds in the growth environment, generation of atomically clean Si surface prior to growth and generation of Si fluxes of high purity.

As in III-V MBE, it is generally conidered that the residual vapour pressures of O_2, H_2O and hydrocarbons in the growth chamber should be maintained below 10^{-10} torr levels during growth. In Si-MBE, it is known that the epitaxial growth improves drastically as the base pressure in the growth chamber reduces[10]. While residual CH_4 is reported to be detrimental to the Si-MBE growth[22], it is apparently unaffected by H_2. It has even been claimed that low level H_2 ambients can actually improve the MBE growth of GaAs by their etching reaction on carboneous species[23]. The choice of UHV pumping is a important consideration in Si-MBE system. Vacuum quality is affected by the pumps used because of the species-dependent pumping characteristics of different pumps. Many types of pumps have been employed in Si-MBE systems. Though ion pumps with auxillary Ti sublimation pumps are a common choice, the less well-established cryopumps[24] and

turbomolecular pumps[25] have also been used. A typical MBE system consists of a growth chamber and a preparation chamber. Analytical instruments such as residual gas analyzer(RGA) and RHEED are commonly installed in the system to monitor the vacuum cleanliness and epitaxial growth. A significant development in MBE system is the incorporation of a sample load lock to the growth/preparation chamber such that substrates can be loaded and unloaded without breaking the UHV environment. Use of the sample load lock has been observed to improve the vacuum cleanliness by avoidance of re-contamination and reduced degassing of the source materials and system components[26]. The improvement is reflected in the sequential improvement in the material quality of layers grown. The throughput of the system is also substantially increased through the use of the sample load lock.

Early attempts at Si-MBE growth using Si vapour generated from a graphite crucible[9] were unsuccessful due to severe contamination of the Si molecular beam. In the present-day Si-MBE system, the generation of Si flux is achieved by e-beam evaporation where an energetic electron beam is used to melt the central portion of a solid Si charge such that the molten Si is confined within the outer solid Si charge and thus prevented from contamination by the wall of the copper hearth of the evaporator in contact with the Si charge. The co-evaporation dopant sources in Si-MBE are similar in design to the effusion sources used in III-V MBE. Another type of dopant source involving the generation of ionized dopant species has also been used in Si-MBE. The ionized dopant species are accelerated towards the substrate during layer deposition where they are implanted and buried a few atomic layers below the surface. Use of such doping technique overcomes the problem associated with the low sticking coefficient and exponential temperature dependence encountered in

3

co-evaporative doping. It is however a very complex and costly technique.

1.3 Surface cleaning

Atomically clean surfaces are essential in order to achieve good epitaxial growth of Si layers. Direct correlation between interfacial C and defect content in the layer has been reported[27,28]. Si epitaxial growth occurs by nucleation at the atomic steps on the substrate[29]. The atomic steps may be formed at the crystallographic planes of the substrate or nucleated at the site of surface contaminants. The two common contaminants on as-received Si substrate are its native oxide and C. While the native oxide can be removed by heating the substrate above $900^{\circ}C$, the C absorbate reacts with Si to form SiC which is much less volatile. Certain hydrocarbon species such as ethylene admitted into the growth enviraonment has been known to react with the Si surface also to form SiC[30]. Smith et al[27] showed that stacking faults would inevitably nucleate at the sites of SiC perturbance during the epitaxial growth. On heating to $^{\sim}1100^{\circ}C$, the surface C diffuses into the substrate leaving behind a atomically clean Si surface[31].

Suguira and Yamaguchi[32] have examined the effect of prolonged preheat treatment of the substrate surface above $1000^{\circ}C$ on the defect content in the epitaxial layers subsequently grown. For a preheat treatment at $<1080^{\circ}C$ for 20 minutes, very high densities of stacking faults were obtained (Fig.1.1(a)). As the preheat temperature was increased to $1160^{\circ}C$, the SF density dropped to $<10^4 cm^{-2}$. At $1250^{\circ}C$, they occasionally observed a wavy texture on the film indicating thermal faceting of the substrate during the preheat treatment. Similar behaviour in the dislocation content with preheat temperature was also observed (Fig.1.1(b)), but prolonged
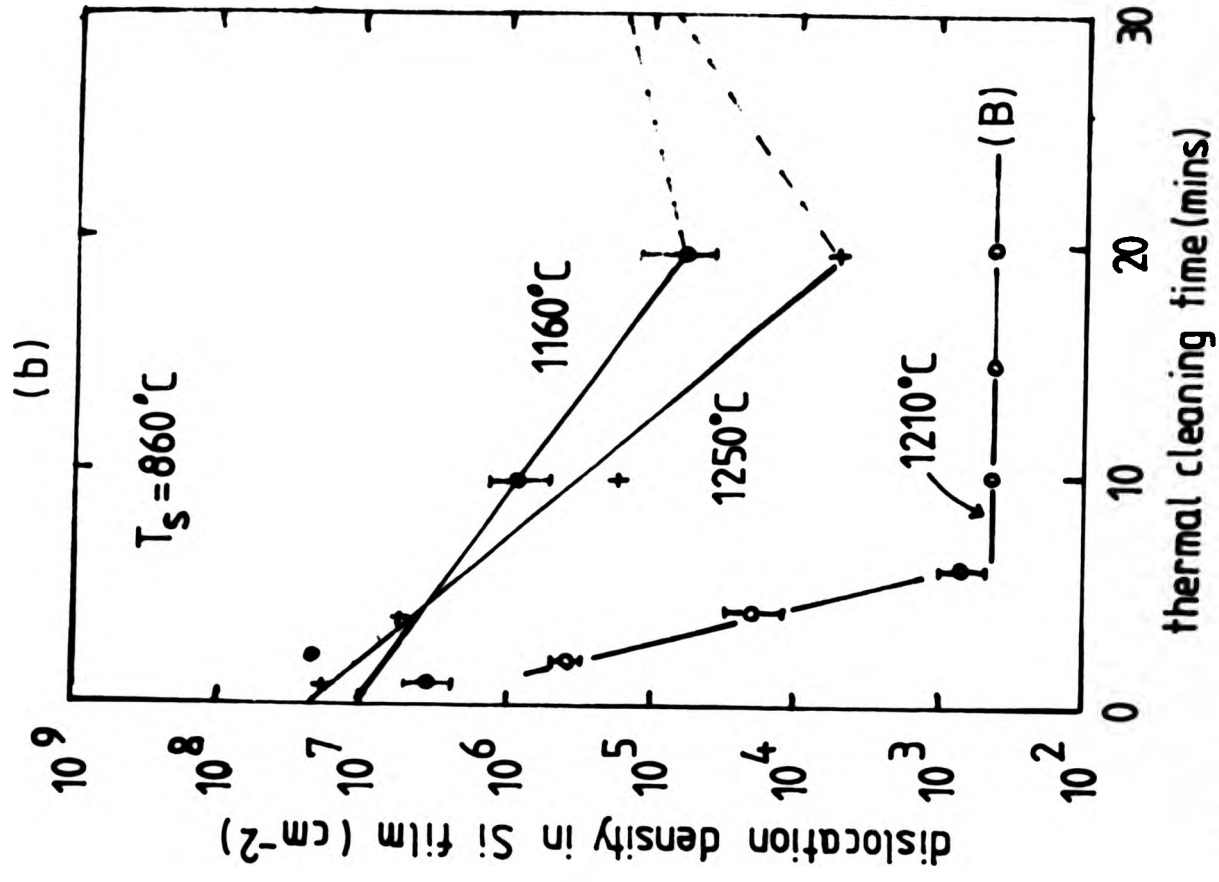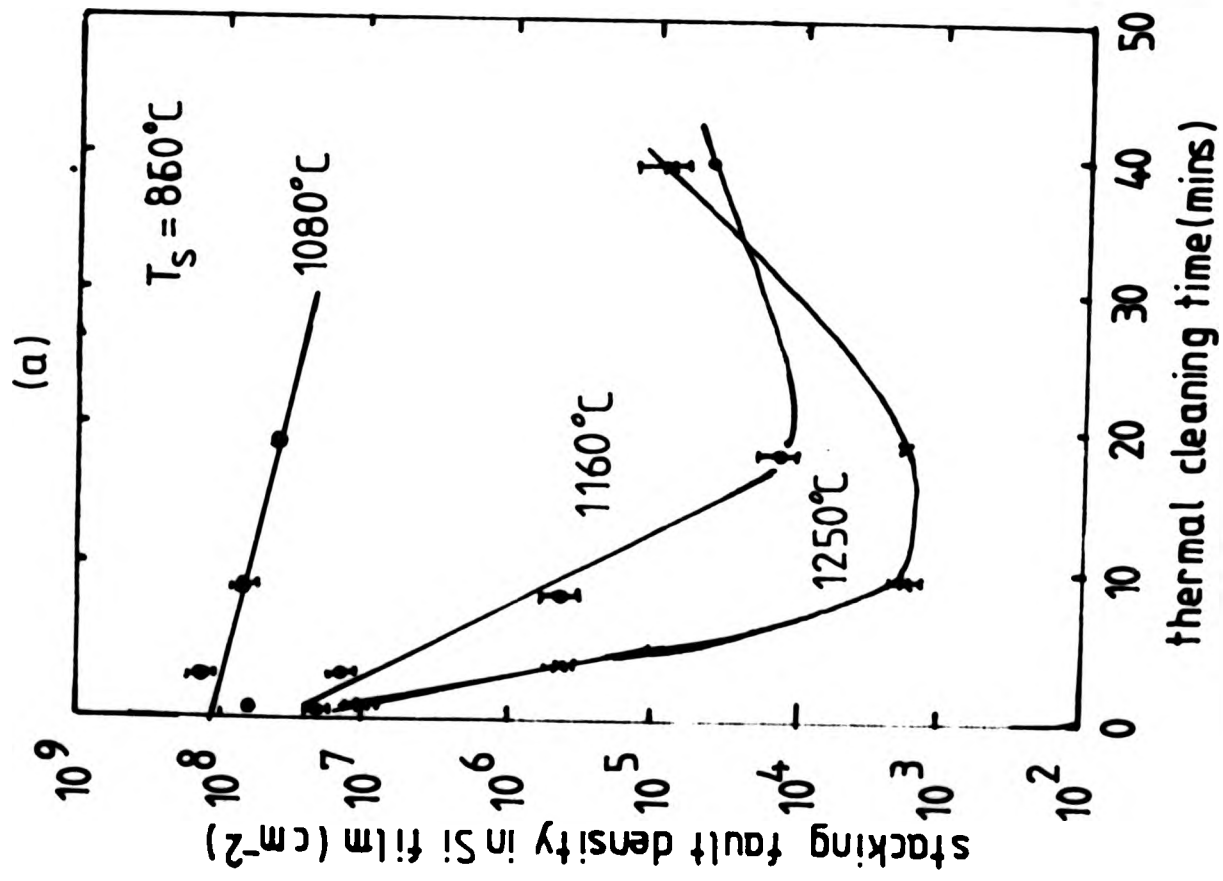
Fig.1.1(a)&(b)   The effect of thermal cleaning of substrates at 1080 -1250°C for different lengths of time on the defects observed in the Si-MBE layers. When the substrate was allowed to slide freely during the preheat treatment (B), a significant reduction in the dislocation density in the layer was observed.

5

heat treatment generated additional dislocations in the films at thermal slip lines in the substrate induced by thermal stress. By modifying the substrate holder/heater design such that the substrate was heated more uniformly and allowed to slide freely during the preheat treatment, they showed that thermal slip could be avoided during the preheat treatment[33].

Though heating to high temperatures seems highly effective and reproducible, this method of surface preparation has a number of potential difficulties when employed on large area substrates. Firstly, very high power input will be required to heat the substrate to these high temperatures, and secondly, the problem with thermal slip will be immense. Furthermore, a high temperature process will forsake the very benefit of the low temperature epitaxial growth possible in Si-MBE. For these reasons, alternative low temperature surface treatments, compatible with round substrate format used in the conventional integrated circuit technologies, have been investigated.

In a typical low temperature treatment, the substrate surface is subjected to either a chemical treatment or a physical sputter cleaning followed by an in-situ low temperature preheat treatment (<900°C) prior to epitaxial growth. A number of methods have been attempted in Si-MBE with varying degree of success. Some of these methods are described in the following sections.

(a) Ex-situ chemical treatment

Numerous chemical cleaning solutions have been developed over the years for removing contaminants from the substrate surfaces after various stages of device processing. Of these, the commonly known RCA cleaning[34] consisting of alkaline/acidic peroxide boils has been modified and adopted in Si-MBE. Most Si-MBE

workers include some form of chemical treatment of their substrates prior to growth. Unfortunately few have examined closely the effectiveness of their surface treatment.

Henderson[35] has examined the effectiveness of peroxide cleaning of Si substrates using AES. He found that the final oxide formed by the peroxide solution was crucial in preventing carbon contamination, coming from the laboratory ambient, of the Si surface and should never be removed before loading into the UHV system.

Ishizaka et al[36] reported an improvement to the Henderson cleaning method in which an HNO_3 boil was included prior to the peroxide treatment. Typical Auger spectra of their chemically treated Si surface before and. after a low temperature heat treatment in UHV are given in Fig.1.2. They showed that the treatment produced a carbon-free surface after heating in UHV at temperatures as low as $710^{\circ}C$. They considered that the chemical treatment left a very thin oxide layer, estimated to be ~5Å thick, on the surface which could be desorbed more easily compared to the native oxide.

(b) Ion sputter cleaning

Ion sputter cleaning[37] is a method in which low energy noble gas ions are employed to physically remove the top few monolayers of the surface material of the substrate. The ion bombardment induces some ion damage at the surface region which requires subsequent thermal annealing to re-order and to expel at least some of the bombarding species which are retained in the substrate.

Bean et al[38] have examined the dependence of residual damage on temperature during Ar^+ sputter cleaning of Si. The sputtered samples were annealed at $800^{\circ}C$ for 10 minutes to re-order the surface. The residual damage was then examined using TEM and RBS. They found an increase in disorder and retained Ar in the sample with increasing sputtering temperature. It was concluded
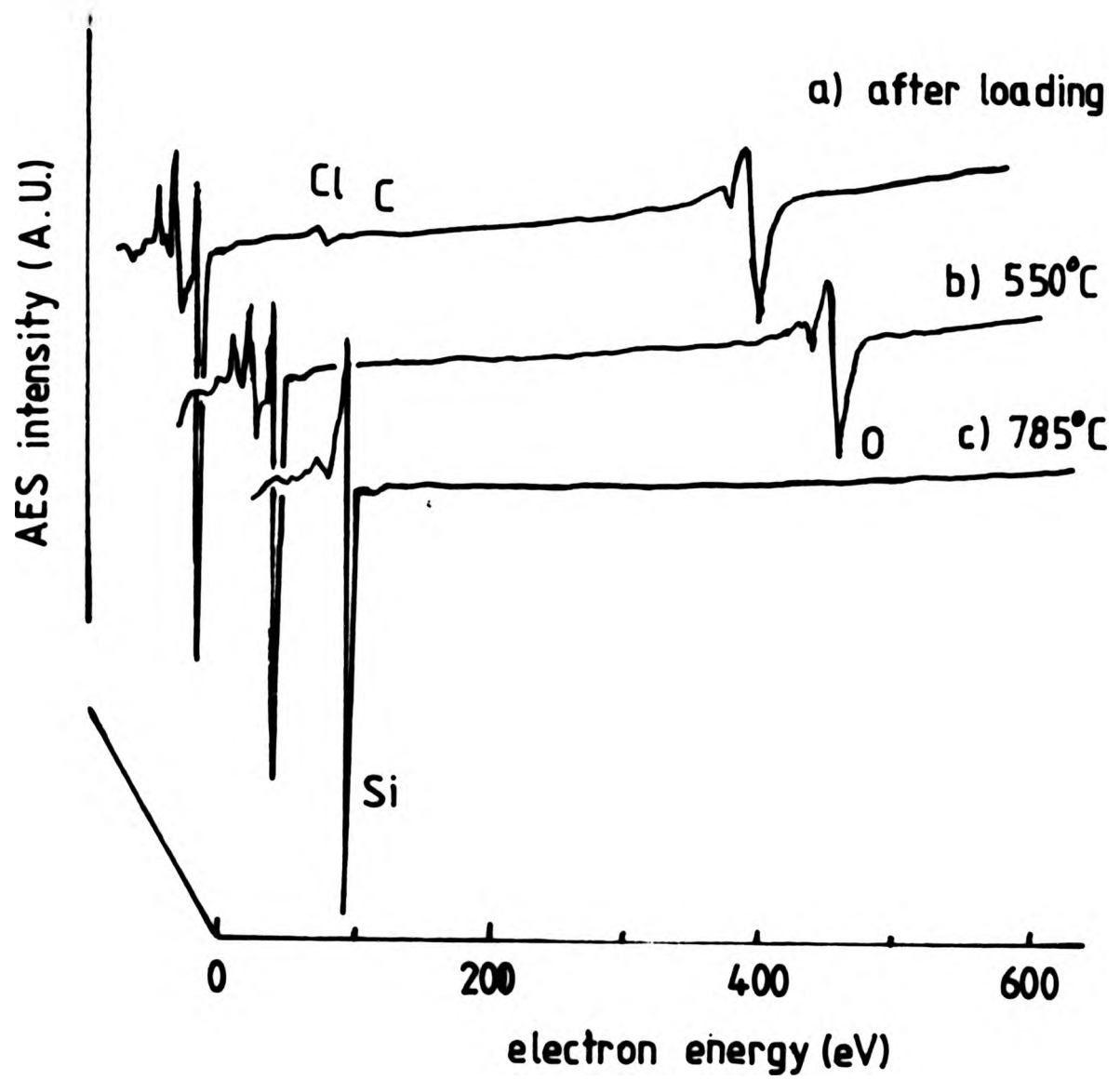
Fig.1.2   Auger   spectra   of   Shiraki-chemical   treated   Si
surface before and after heat treatment in UHV.

8

Fig.1.2 Auger spectra of Shiraki-chemical treated Si surface before and after heat treatment in UHV.

8
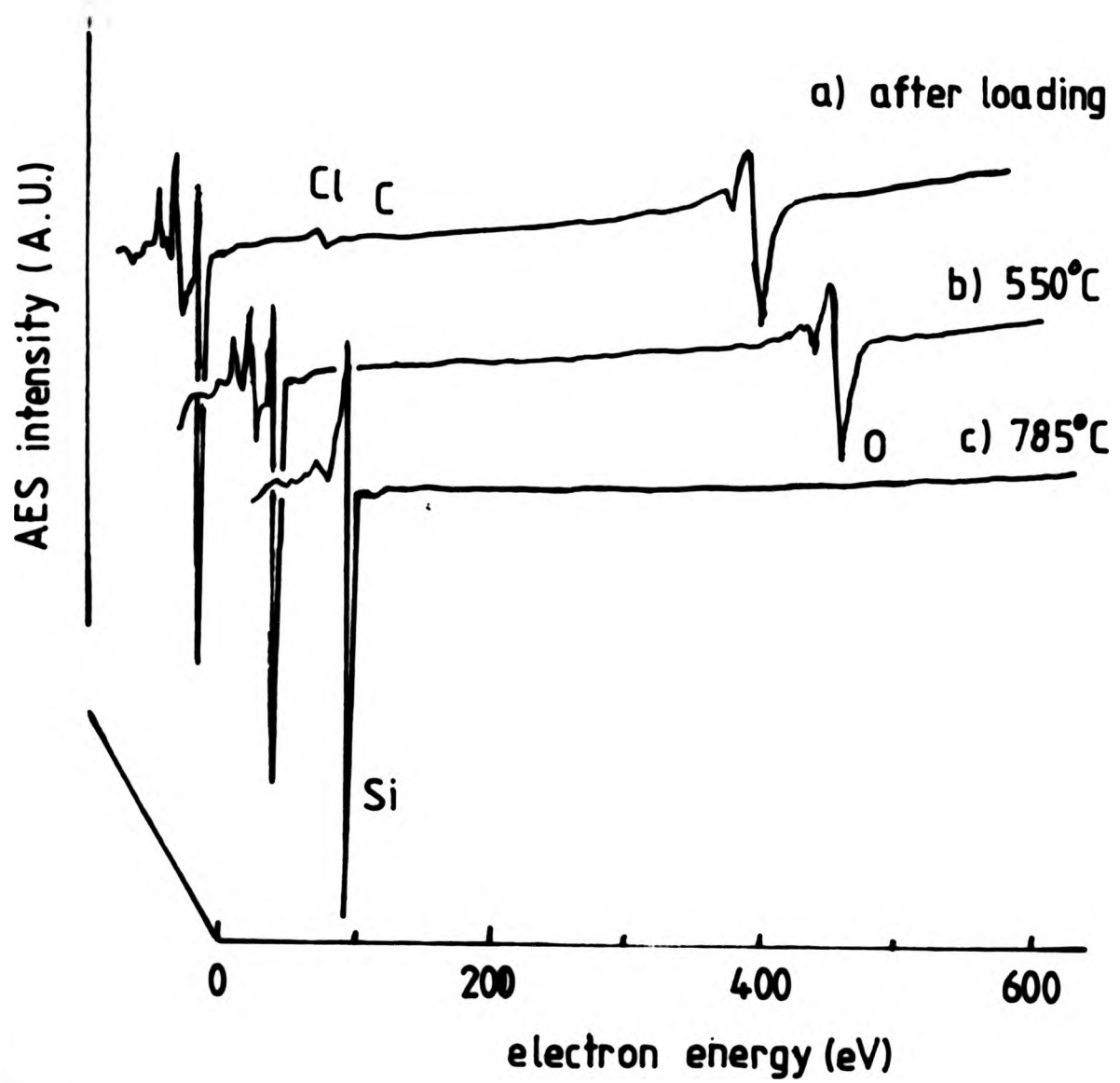
that Ar$^+$ sputter cleaning should be performed at room temperature in order to minimize residual surface damage after annealing.

Yamada et al[39] have studied the residual damage to clean Si surfaces after low energy ion bombardment with Ar, Kr and Ne followed by a thermal annealing at 720°C for 15 mins in UHV. The clean Si surface was initially prepared by direct current heating of the substrate at 1250°C for 2 mins. Prior to ion sputtering, the Si surface was exposed to 200 Langmuirs of O_2 at room temperature. Ion energies ranging between 1-4 keV were used in the study. The surface disorder in the sample was evaluated by surface minority carrier lifetime and RBS measurements. They found that in Ne and Kr bomarded surfaces the damage could be almost fully recovered after the annealing. In the case of Ar, the surface damage was comparatively more difficult to remove and the residual damage after annealing increased with increasing bombarding energy. They concluded that in order to obtain clean and well-ordered Si surfaces by ion sputtering followed by thermal annealing, Ar should not be used.

Robinzohn et al[40] compared the effectiveness of cleaning of Si and GaAs surfaces by ion bombardment by Ar, Ne and Kr in the 50-1500eV range at room temperature. They observed that Si surfaces could be cleaned by ion bombardment at energies down to 70eV as monitored using AES. In contrast to Yamada's results, they observed that low energy Ne$^+$ ions (< 1 keV) induced more disorder than heavier ions. Heating the sample during the ion bombardment caused the incorporated bombarding species to penerate deeper into the sample and become more difficult to remove subsequently.

(c) Reactive etching under Ga

Wright and Kromer[41] demonstrated that the oxide on Si surfaces could be removed by heating in a Ga

9

molecular beam at 800°C. It was considered that the following chemical reactions take place:

$$SiO_2 + 4Ga \rightarrow Si + 2Ga_2O$$
$$SiO_2 + 2Ga \rightarrow SiO + Ga_2O$$
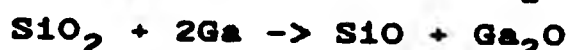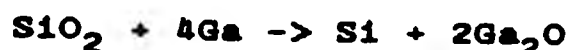
Since the vapour pressures of SiO and Ga_2O are higher than SiO_2 at 800°C, the oxide layer is removed much more effectively than by conventional thermal reduction. No residual Ga could be detected by AES on the surface of the substrate at 800°C even after one hour of continuous exposure to Ga. This method of "galliation" has been employed in the preparation of substrates for Si-MBE[42]. It is particularly convenient in systems where Ga is also used as a p-type dopant material.

(d) SiO_2 etching under Si

Joyce et al[43] observed an induction period during which no Si growth occurred on a heated Si substrate in a molecular beam of SiH_4. They suggested that a reaction between incoming Si atoms and the oxide occurs at the surface leading to its final removal before epitaxy can take place. Tabe[44] later confirmed their work by demonstrating clearly the etching reaction of thick SiO_2 films under an impinging Si beam. He found that at a given Si impinging rate, this etching reaction occurred only when the substrate was heated above a critical temperature. For example, at an impinging rate of $1 \times 10^{15} cm^{-2}s^{-1}$ corresponding to a deposition rate of $2A\ s^{-1}$, the critical temperature was observed to be ⁻930°C. This critical temperature decreased with a decrease in the Si impinging rate. Below the critical temperature, poly-Si or amorphous Si was deposited on the substrate under the impinging Si.

Though this etching reaction allows the removal of oxide from the substrate surface, it is not known whether similar reaction occurs with the surface C. Its potential use as a surface preparation method may therefore be

limited.

(e) UV ozone treatment

McClintok et al[45] showed that exposure of GaAs substrate to ozone produced by UV radiation in air was effective in removing carbon contamination on the surface. They examined the cleanliness of UV ozone-treated surface as compared to the as-received surface of GaAs substrate using AES. No discernible C peak was detected on the UV ozone-treated surface even prior to heating. They indicated that UV ozone-treated substrates have been successfully used for growing high mobility GaAs MBE layers.

Tabe[46] has investigated the effect of UV ozone exposure on Si substrates. Prior to growth of Si-MBE layers, the substrates were first removed of native oxide by HF dip and treated to UV radiation in a clean air environment. He found that a UV ozone exposure of the substrates for 5 minutes with a preheat treatment at $900^{\circ}C$ was sufficient to reduce the defect densities in the layers from 10^6-$10^7 cm^{-2}$ to 10^3-$10^4 cm^{-2}$. The reduction in the amount of C contaminants on the treated surfaces were confirmed by XPS. However the defect density in both treated and untreated samples was dependent on the preheat treatment prior to epitaxy. At low preheat temperature, the treated samples showed a higher defect density indicating an incomplete removal of the thick oxide formed during ozone exposure. The optimum exposure time was chosen such that effective carbon removal by ozone occurred whilst surface oxide formation was minimized.

This preliminary work of Tabe suggests UV ozone treatment to a simple and yet effective way of removing surface C on Si substrates. However further work is required to assess the effectiveness of the treatment on as-received and processed substrates generally used in Si-MBE.

(f) Laser cleaning

Zehner et al[47] have reported that pulsed laser irradiation can be used to reduce the levels of C and O surface contaminants on Si substrates to within the detecton limits of AES. This process is inherently clean and rapid, and can be performed in-situ. There are, at present, few studies[48] indicating that high quality epitaxy can be readily achieved on the laser-treated surfaces. Though scanned laser beam has been used for annealing implanted structures[49], the suitability of laser processing in large area substrate and VLSI device applications has yet to be proven[50].

No one preferred method of substrate surface preparation has been agreed amongst the Si-MBE workers. This is not unexpected since, as frequently encountered in the current device fabrication technologies, the optimum surface treatment can only be selected after careful consideration of the various influencing factors in the entire fabrication process. Typically the substrate may require to undergo a number of process steps such as oxidation, dopant diffusion, metallization and ion implantation steps prior to epitaxy by Si-MBE. Kasper and Worner[51] reported that surface steps and oxide patterns left on the substrate could adversely affected the efficiency of their substrate cleaning method used on as-received substrates. It was considered that the nature of surface contamination was different from that found in as-received substrates generally used in Si-MBE research work.

Workers at Bell Laboratories[52] currently favour a low energy Ar^+ sputter cleaning followed by a low temperature annealing in their surface preparation of substrate prior to epitaxial growth, whilst workers at Hitachi[36] and AEG-Telefunken[51] adopt the approach

of wet chemical cleaning followed by a low temperature preheat treatment. The future trend in substrate surface cleaning is unclear, but it is most likely to follow the approach adopted by workers at Hitachi and AEG-Telefunken where, in addition, a reactive molecular beam etching (e.g. "galliation") may be used to further lower the temperature required for substrate cleaning.

1.4 Doping in Si-MBE

A major attribute of Si-MBE is its flexibility and ease with the introduction of arbitrary and accurate dopant profiles into the epitaxial layer. In principle, doping profile in Si-MBE is achieved by controlling the dopant flux arriving at the epitaxial surface during growth.

The dopant flux can be generated in two distinct ways. Firstly, a molecular beam of dopant species can be thermally generated from a effusion cell in which the dopant species arrive at the growing Si surface as neutral species with thermal energies. This method of doping is known as co-evaporative doping (or molecular doping). In the other method, the dopant species are ionized and accelerated towards the growing Si surface. The ionized dopant species may be generated either through the ionization of the dopant vapour or in a plasma discharge of a dopant-containing gas (e.g. BF_3). This method of doping is called ion doping.

1.4.1 Co-evaporative Doping

Though a number of dopants have been used in Si[53], the choice of dopants suitable in Si-MBE is somewhat restricted from a consideration of their vapour pressure characteristics. Due to the high vapour characteristics of P and As, they are difficult to control in a UHV system and likely to produce high residual

doping in the layer, they are therefore generally considered not suitable as co-evaporated dopants in Si-MBE. Despite its comparative large molecular size and lower solid solubility limit in Si, Sb has been exclusively used as the co-evaporated n-type dopant in Si-MBE[54]. In contrast, the very low vapour characteristic of B has discouraged its use as a p-type co-evaporated dopant in Si-MBE, only Ga, Al and In have so far been considered suitable candidates [55].

In co-evaporative doping, the dopant flux is usually generated in a effusion cell whose temperature is accurately controlled in order to achieve a constant doping flux. An accurate temperature control is very critical due to the exponential dependence of vapour pressure of dopant on the temperature[54,55]. Changes in the doping level are obtained by changing the cell temperature to the pre-determined values. The abruptness of doping transition is determined by the temperature response of the source cell, growth rate and incoporation behaviour of dopant. Improved source cell design and a lowering in the growth rate has been found to enhance the abruptness of doping transition in Si doping in MBE GaAs[56].

It has been shown that high quality Si-MBE layers doped with co-evaporated Sb, Ga , In and Al can be grown for growth temperatures between 600 - 900°C (54,55,57,58). However, there are two problems related to co-evaporative doping in Si-MBE, namely surface segregation effect and low sticking coefficients of dopant at typical growth conditions. Surface segregation effect[59] has previously been observed in Sn doping in GaAs which hampered the arbitrary control of the dopant profile. The phenomenon of Sn surface segregation in GaAs has been investigated by a number of authors[59-61]. In Si-MBE, as the growth temperature is increased, segregation effects are reduced. The severity of smearing in the dopant profile is also observed to be strongly dependent on

14

dopant species. For example, good profile control of Sb and Ga doping can be achieved when the growth temperature is above 850°C and 600°C respectively[54,55], whilst profile control of Al doping remains poor even at 900°C[55].

Though segregation effects can be minimized by increasing the growth temperature, this is not in line with the general trend of lowering the growth temperatures to reduce dopant diffusion and autodoping. Since the sticking coefficient of co-evaporated Si-MBE dopants decreases exponentially with the growth temperature, excessively high dopant fluxes are required to achieve high doping levels in the layers[62].

The smearing of the dopant profiles produced by surface segregation effects can be avoided by the technique known as "building up and flashing off" the surface adlayer of the dopant to the pre-determined level whilst arresting the growth temporarily[63]. Iyer et al[64] have demonstrated that this technique can be used in co-evaporated Sb and Ga doping in Si-MBE where doping transitions as abrupt as 100Å/decade have been reported. However the potential detrimental effect of repeated interruption to growth during the period of "building-up and flashing-off" the surface dopant adlayer on the quality of the layers has yet to be investigated in detail.

At sufficiently low temperature (e.g. room temperature) unity sticking coefficient for the dopant species can be expected. In principle, by simultaneously depositing Si and dopant at room temperature and then epitaxially re-growing the deposited layer at an elevated temperature, excellent dopant profile control in the layer should be possible[17]. This forms the basis of solid phase epitaxy (SPE). Though doping levels of Ga exceeding the solid solubility limits has been reported, the crystallographic and electrical properties of the regrown layer may well be proven to be inferior.

15

1.4.2 Ion Doping

In ion doping, low energy dopant ions with energies below 1keV are implanted into the the layer during growth. It is considered that the dopant atoms are buried a few monolayers below the growing epitaxial surface. This reduces the likelihood of re-evaporation of the dopant atoms from the surface and hence leads to a near-unity sticking coefficient. Due to the ease of controlling and monitoring the dopant ion beam and near-unity sticking coefficient, excellent control of dopant profile can be attained. Ion doping offers further advantages in minimizing excess dopant introduction into the growth environment compared to co-evaporative doping, and in achieving doping levels exceeding the expected solid solubility limit at the growth temperature used.

Ota[65] modified a Coultron G-2 ion gun[66] with a de-accelerator and a beam scanner in his study of As$^+$ doping in Si-MBE. Fig.1.3 shows the layout of the ion source in his Si-MBE system. Ion energies between 400 and 800 eV were used. He showed that high quality As$^+$ doped layers with accurately controlled dopant profile and low dislocation densities could be grown. He reported a degradation in their electrical properties as the energy of the the ions was increased and the growth temperature decreased indicating some ion irradiation damage in the layers.

Swartz et al[67] described a development to ion doping technique in which B and As ion doping could be rapidly alternated from a single source. In this technique, BF$_3$ gas and As vapour were admitted simultaneously into to the ionization /plasma chamber of the ion source. The separation and selection of the required ion species were achieved using a ExB filter. Rapid switching of the dopant type was obtained by altering
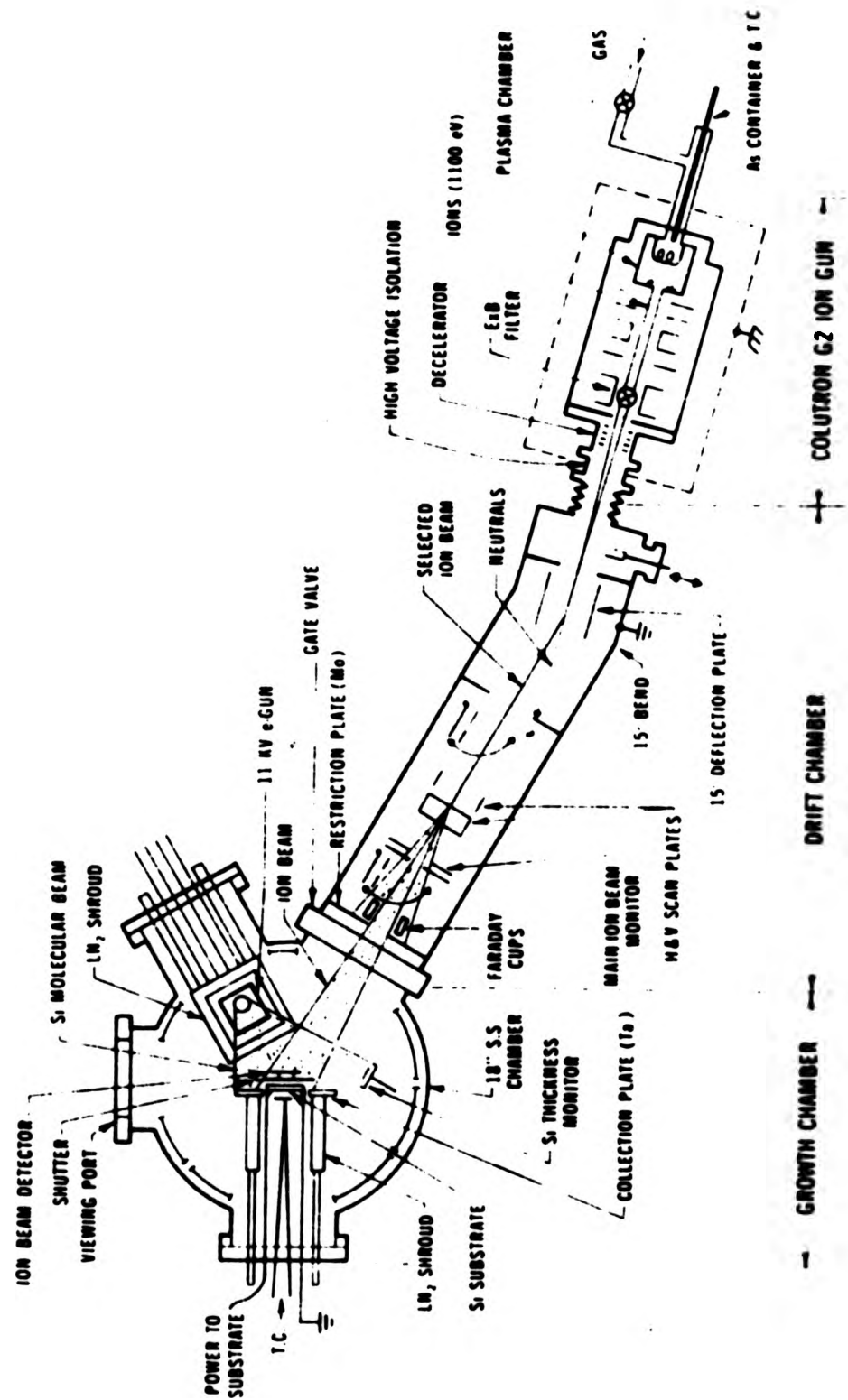
Fig.1.3 Plasma ion implantation system used in Si-MBE.

17

the B field while maintaining a constant E field.

Suguira[68] has investigated Sb ion doping in
Si-MBE. His dopant ion source[69] was simple in
contruction and could be operated in growth chamber unlike
the plasma ion sources where differential pumping is
required to remove the associated gas load. Fig.1.4
is a shematic diagram of the construction of the Sb ion
source. A reported doping efficiency of ˜100% was claimed
over the range of 10^{16}-10^{20}cm^{-3}. Good agreement
between the Sb concentration levels determined
independently by neutron activation analysis and carrier
concentration measurement indicated that all the dopant
atoms were electrically active. The absence of a surface
Sb peak in the RBS spectra taken from the layers showed a
neligible segregation of Sb on the surface during ion
doping in marked contrast to co-evaporative doping[70].

Komuro et al[71] have reported a liquid Ga ion
dopant source for Si-MBE. A shematic diagram of their ion
dopant source is given in Fig.1.5. Ga was heated in a Ta
coil to form a liquid reservior in which a W needle was
embedded serving as the ion emitter for the source. The
ions were accelerated to an energy of between 500-1000eV.
They reported a maximum carrier concentration of
1×10^{19}cm^{-3} at growth temperatures of 700-800°C which
is several times higher than the expected solid solubility
limit of Ga in Si[53]. At higher growth temperatures,
they observed a rapid decrease in the incoporation
efficiency of Ga which they attributed to the
re-evaporation of the implanted Ga atoms.

It is clear that ion doping offers substantial
benefits over co-evaporative doping in terms of its dopant
profile control and reproducibility, and probably the
maximum achievable dopant concentrations. However a
widespread use of ion doping in Si-MBE may be restricted by
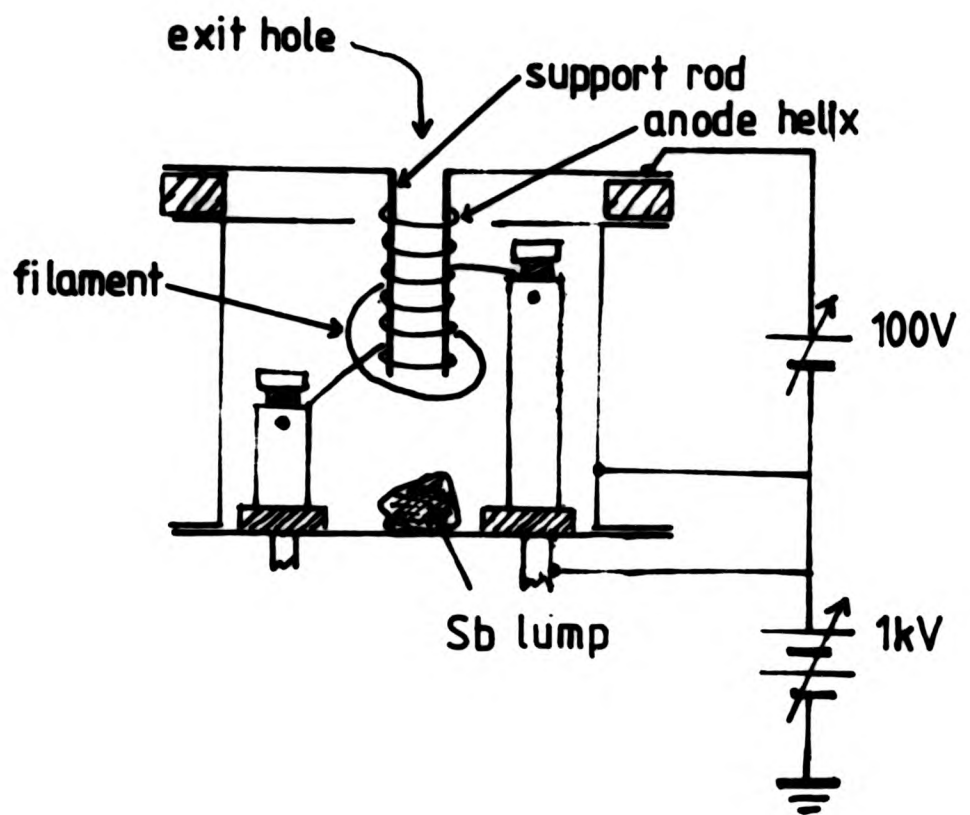a number of factors. Firstly, a degradation in material

18

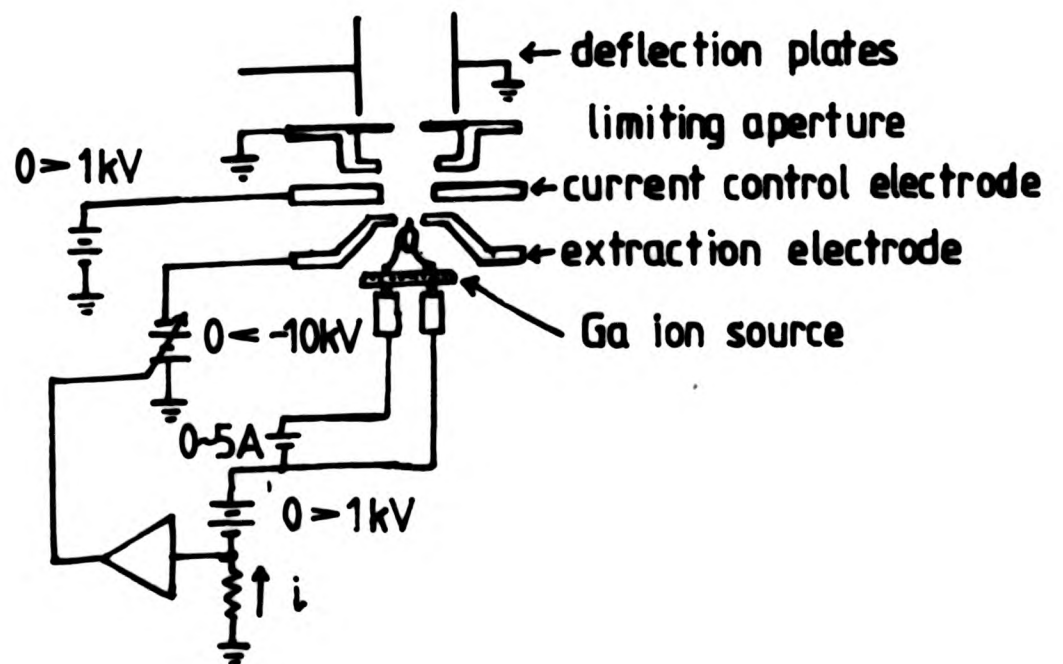Fig.1.4 Schematic diagram of an Sb ion source.

Fig.1.5 Schematic diagram of a liquid Ga ion source.

19

quality of ion doped layers[72] as monitored by minority carrier lifetime measurements has been observed at doping levels > $1 \times 10^{18} cm^{-3}$. And secondly, the high complexity and cost of the ion dopant source compared to the evaporation source, may possibly make it economically unviable.

1.5 Device Applications of Si-MBE

A number of discrete device structures have been fabricated using epitaxial layers grown by Si-MBE. These include the microwave hyperabrupt diodes[73], MOSFET's[74], bipolar junction transistors[75] and Schottky mixer diodes[76]. Significant improvements in their performance have been acheived compared to similar device structures fabricated by the conventional technologies. These improvements can generally be attributed to the accurate dopant profile and thickness control available in Si-MBE.

Reports of the application of Si-MBE in integrated circuit fabrication have not been extensive so far. Recently Swartz et al[77] reported the fabrication of simple NMOS digital test circuits and devices in epitaxial layers grown by Si-MBE. The circuit and device characteristics were found to be comparable to those of identical circuits and devices processed conventionally. In addition, Si-MBE devices were observed to show exceptionally high low-field mobolities.

Kasper and Worner[51] reported their attempt at directly substituting the vapour phase epitaxy (VPE) step with Si-MBE in the fabrication of a commercial frequency divider used in television tuners. Prior to epitaxy, diffusion and implantation were used to fabricate the necessary As^+ buried region and B-channel stopper. After the epitaxy, further thermal processes such as diffusion of the collector contact, isolation oxide formation and

20

annealing of implanted base and emitter regions were used. They concluded that technically, Si-MBE could replace Si-VPE in the fabrication of high speed IC without altering other process steps or layout rules. However the yield was considerably reduced when Si-MBE was used because the usual surface cleaning methods used in Si-MBE were found to be less effective on processed wafers.

Though routine hitherto small-scale fabrication of microwave IMPATT Si-MBE devices[51] for commercial uses is underway, the scarcity of reported attempts at complex device fabrication in Si-MBE makes an informed judgment on the prospects of Si-MBE in VLSI technology difficult. Undoubtedly, intensive research and development in this area are in progress and, for commercial reasons, the details of the work are proprietary in nature. Nevertheless, evidence of wider interest in Si-MBE as a potential commercially viable technology is apparent from the increasing number of industry-based research laboratories entering the field and the development of high throughput Si-MBE systems by a number of UHV systems manufacturers.

1.7 Aim of Thesis

Broadly speaking, the aim of the Si-MBE work at CLP is to establish a background "know-how" in this area such that an informed assessment on the prospects of Si-MBE for industrial applications can be made.

This thesis covers the following areas of the work:

(a) practical problems associated with operating and maintaining the Si-MBE UHV system

(b) evaluation of thin Si-MBE layers

(c) study of the parameters affecting the electrical and crystallographic quality of undoped Si-MBE layers

(d) study of co-evaporative p- and n-type doping and dopant profile control in Si-MBE

Chapter 2: Layer growth and assessment techniques

2.1 Description of V80 Si-MBE system

The V80 Si-MBE system was similar in design to that of the V80H III-V MBE system which consists of a growth chamber, a preparation/analysis chamber and a load lock. The system is schematically represented in Figs.2.1(a) and (b). Both the growth and preparation chambers were each pumped separately by a closed-cycle He cryopump (CTI Torr80) and an auxillary Ti sublimation pump. The load lock which was connected to the preparation chamber was pumped by the cryopump to the same chamber. The growth and preparation chambers were interconnected through a manually operated gate-valve thus allowing independent operation of the two chambers. The roughing of the system was achieved in two steps; an oil-free vane pump (Edwards ECB1) was first used to evacuate the system to less than 100 torr before the system was valved to the sorption pumps. We found that the liquid nitrogen consumption of the sorption pumps was reduced significantly by the use of the vane pump. The cryopumps were first evacuated to less than 10^{-3}torr by the sorption pumps before they were switched on. It took about two hours for the cold heads of the cryopumps to reach their normal operating temperature of 15K. At this point, the isolation valves of the cryopumps were opened and the chambers were pumped by the cryopumps alone. Typically, the pressure in the chambers dropped to 5×10^{-7}torr after one hour. The system was protected against cryopump failures by pneumatically operated isolation gate-valves adjacent to the cryopumps which closed automatically in the event of power and water supply failures, and/or any abnormal rise in the system pressure.

In the growth chamber, two 40cc e-gun evaporators (Airco Temescal CV14) were installed. In this work, both guns were used for evaporating Si, but it was envisaged

GROWTH   PREPARATION/ANALYSIS
CHAMBER   CHAMBER

substrate

load lock

AES+MEED

LN₂ cryopanels
viewports

substrate
heater

ion-
sputter
gun

high
temperature
stage

quartz
crystal
monitor+
RHEED+
RGA
facilities

e-gun evaporators
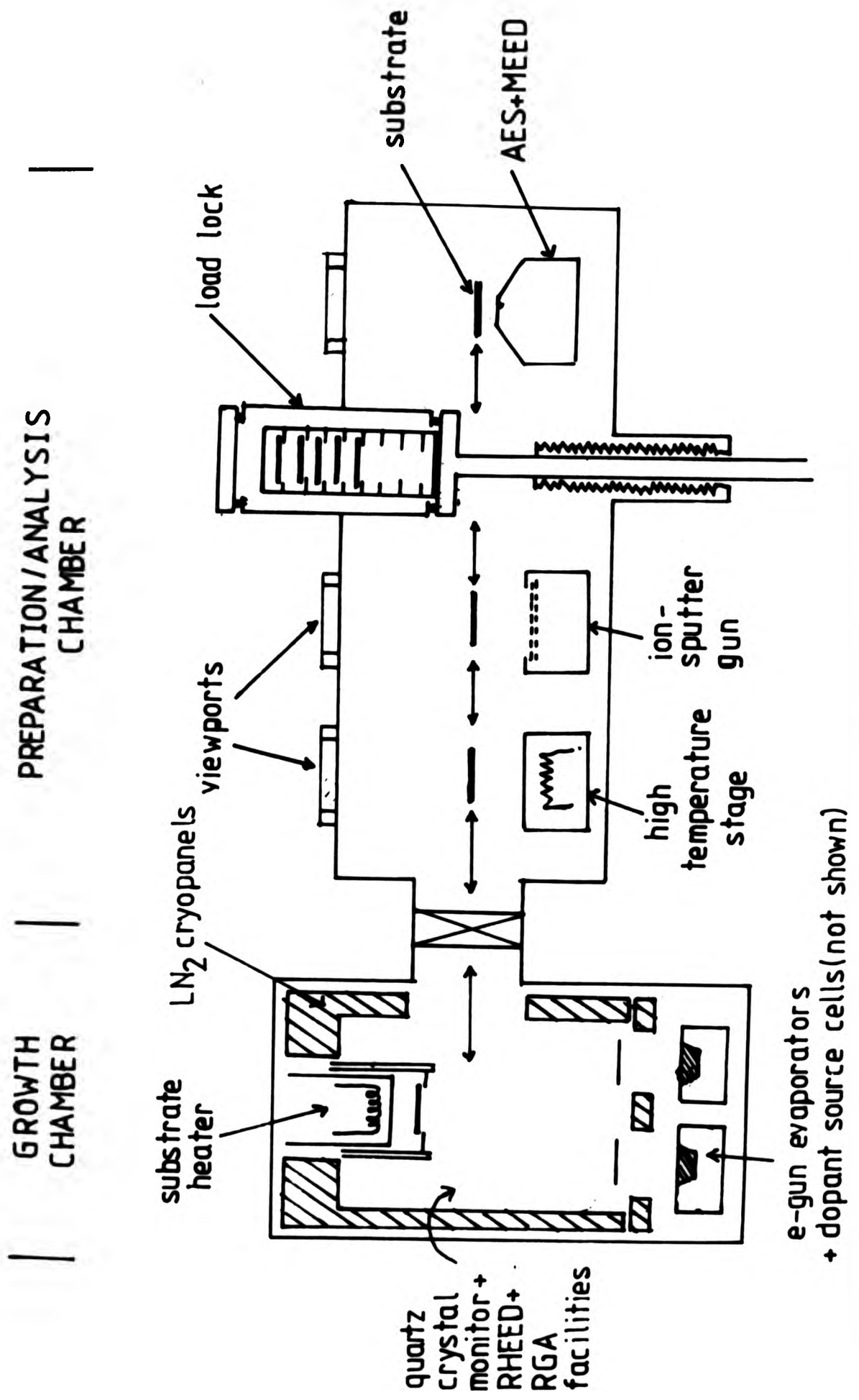+ dopant source cells(not shown)

Fig.2.1(a)   The   V80   Si-MBE   system: General   layout   of   the   chambers   and
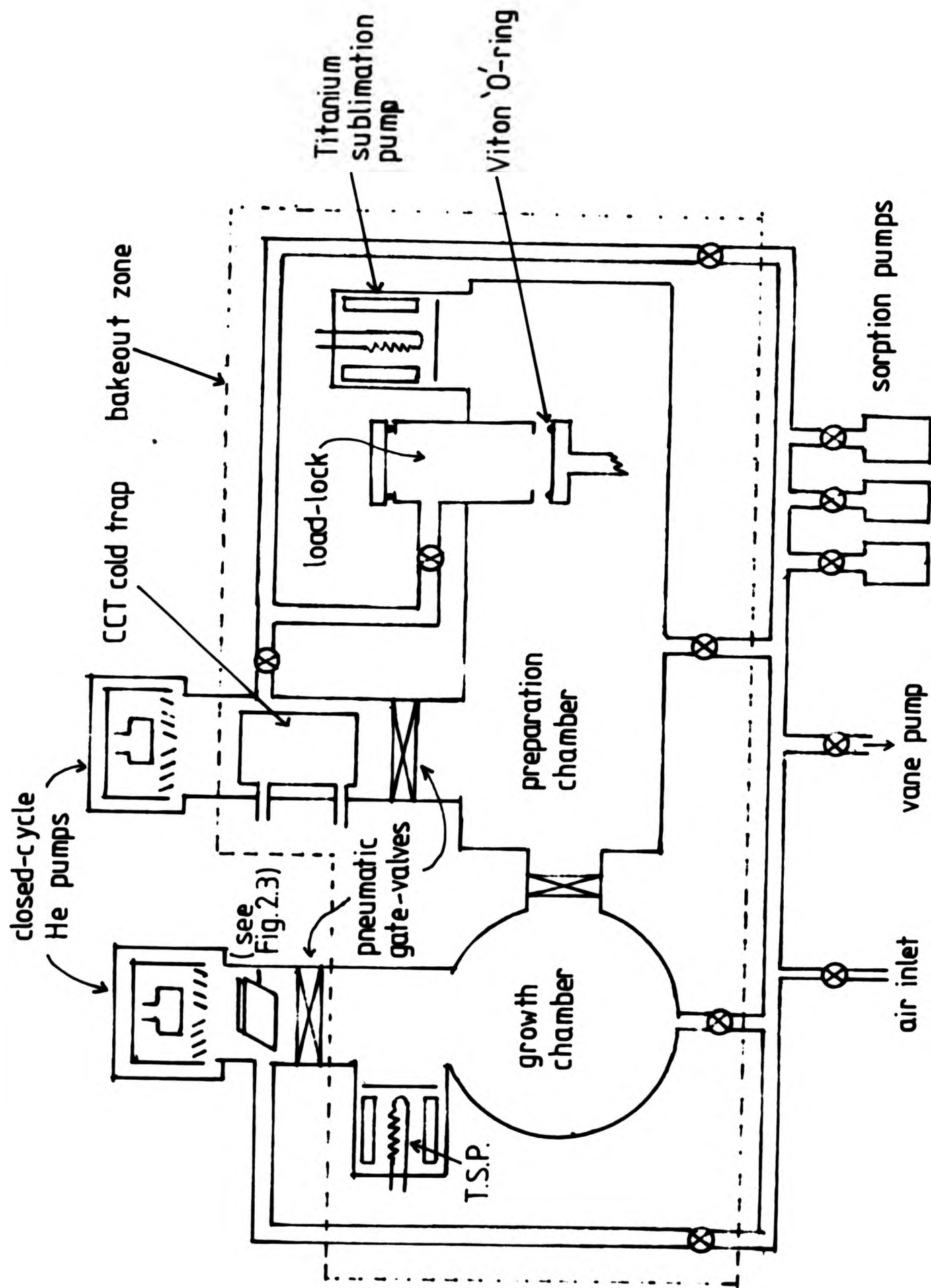facilities.

23

Fig.2.1(b) The V80 S1-MBE system: Pumping and bakeout arrangement in the system.

24

that one of the guns could be used for metal evaporation for silicide growth in the later part of our project. The doping facilities as supplied consisted of two 40cc Knudsen source cells. Two spare ports were also available for additional dopant sources including ion dopant sources. The maximium evaporation temperature attainable in the Knudsen cells was specified at $1400^{o}C$. The substrate heater was designed to accomodate wafers of up to 3" diameter. Continuous 360 degree substrate rotation at speeds up to 120 rpm was available during growth. The substrate heating element consisted of a parallel layout of strips of tantalum foil connected in series. The maximum substrate temperature attainable with the heater was about $950^{o}C$. Reflective high energy electron diffraction (RHEED) and residual gas analysis (RGA) facilities were available in the growth chamber for monitoring the epitaxial growth and UHV environment respectively. Layer thickness and growth rate control was achieved by means of quartz crystal monitors (Airco Temescal FDC8000). The quartz crystal sensor heads were positioned such that the flux from each e-gun evaporator was sampled independently.

The preparation chamber was equipped with a high temperature stage capable of reaching temperatures above $1500^{o}C$ and an ion sputter gun (FAB94, Ion Tech Ltd., UK) for substrate preparation. A combined facility of Auger electron spectrocopy (AES) and medium energy electron diffraction (MEED) was available in the chamber for monitoring the surface cleanliness before and after the substrate preparation. A maximium of 10 substrates could be loaded into the system via the load-lock. Each substrate was originally held loosely in a graphite ring cassette supported on a molydenum holder (Fig.2.2). Due to difficulties experienced with outgassing the graphite ring after air exposure, it was later replaced with Ta. The substrate in the molydenum holder was transferred between the chambers within the system by means of a trolley-on-rail system.
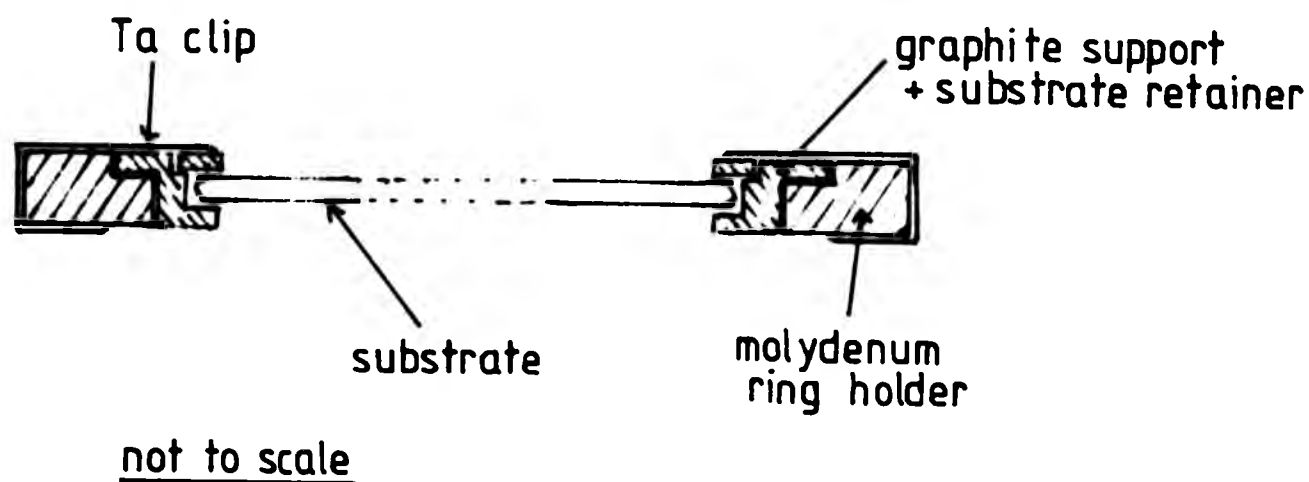
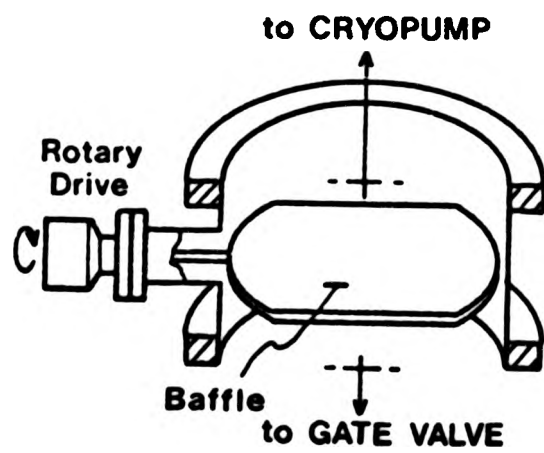Fig.2.2 A schematic diagram of the substrate holder.

Fig.2.3 Construction of a rotatable radiation baffle for facilitating high temperature bakeout of a close-cycled He cryopumped MBE system.

2.1.1 Choice of UHV Pumping for Si-MBE System

Oil-diffusion, ion and turbo-molecular pumps have all been employed for MBE systems. Recently, closed cycle He cryopumps with suitable modification have also been used[24]. The choice of primary pumping for MBE systems is based largely on the requirement of achieving hydrocarbon-free environment, reliability and cost, personal experience and materials to be grown in the system. In some cases, the choice of pumping is restricted by the species to be pumped where they are harmful to and/or not pumped efficiently by certain types of pumps. For example, diffusion pumping is found to be most suitable for a MBE system where P source is to be used[78].

In a Si-MBE system, there are few restrictions on the choice of pumping due to the source materials used in the typical growth process. The critical requirement of the pumping is the generation of low partial pressures of O_2, H_2O and hydrocarbons in the growth environment[79]. At the time when the choice of pumping for our system was considered, all the above mentioned pumps have all been employed in Si-MBE application. There was, however, no general consenses to indicate that certain type of pumping was superior and it appeared that the choice of pumps was very much a matter of personal experience which, in many cases, could not be supported by well-founded studies. In a recent report, Davies et al[80] showed that high quality GaAs can be grown in oil diffusion pumped system despite a number of claims that the oil backstreaming can degrade the layer quality.

Though the ion pumps can withstand bakeout temperatures and offer clean and maintenance-free UHV pumping, they were not chosen as the primary pumps due to their lower pumping speeds and higher cost. The final choice of closed cycle He cryopumps as the primary pumps in our system was based on their potential of achieving a low

hydrocarbon background in the system and their superior pumping speeds.

The main difficulty with using cryopumps in a UHV system occurs during the bakeout of the system. The cryopumps cannnot withstand direct bake and must be located outside the bakeout zone. Furthermore, the cold head and condensing arrays (chevrons) of the cryopump cannot cope with the heat load (typically 1-40W) before they desorb their condensed species back into the system. The usual way around this problem was to use a right-angled interconnection for the cryopump or introducing a cooled baffle in front of the cryopump such that the amount of direct radiation from the baked system is reduced[81]. These methods however reduce the effective pumping speed at the chamber.

We investigated this problem in some detail[82] and came up with an alternative solution which allowed us to bake the system at temperatures up to $200^{o}C$ without compromising the high pumping speed of the cryopump during normal system operation. In our investigation, we found that during the bakeout, difficulties arised *arose* due to the thermal radiation from the baked zone reaching the cold head and chevrons directly. We were unable to bake the system above $120^{o}C$ as the thermal radiation load exceeded the the cooling capacity of the cryogenerator and the previously condensed gaseous species started to desorb back into the chamber. To overcome these difficulties, we introduced a rotateable radiation baffle midway along a 6" long spacer as illustrated in Fig.2.3. The baffle consisted of two parallel stainless steel plates, one with its surface roughened and the other polished. In practice, the surface finish was found to be not critical in terms of the effectiveness of thermal baffling. During the bakeout, the baffle was rotated to reduce the cross-sectional area of the spacer tube by about 75% and thus reducing the amount of thermal load on the cryopump. Though the pumping speed at the chamber was significantly reduced, we experienced no

28

difficulty in achieving satisfactory pumping during the bakeout even at 210°C. At the end of the bakeout, the baffle was rotated to restore the pumping speed of the cryopump. We estimated that the reduction in pumping speed due to the spacer and baffle in the "open" position was about 10-20%. This compared favourably with the other methods mentioned above where a reduction by a factor of 2 to 3 can be expected. A base pressure of 1×10^{-10} mbar was readily attained in the chamber without secondary pumping by the titanium sublimation pump or cooling of the cryo-shrouds of the chamber with liquid nitrogen. With the secondary pumping, the pressure in the chamber dropped to mid 10^{-11} mbar.

An example of the residual gas analysis of the unbaked system is given by the RGA spectrum as shown in Fig.2.4(a). In the unbaked system, the H_2O peak at 18 amu was the major peak as expected after air exposure of the system. The presence of hydrocarbons in the system was evident from the RGA. The peak height at 43 amu can be considered as an estimate of the amount of hydrocarbons in the system[83]. Most of the hydrocarbons consisted of solvents such as acetone (43 amu) and propan-2ol (45 amu) which were regularly used for cleaning the UHV components. Other hydrocarbons gave rise to groups of peaks at 12-16 and 26-30 amu. The presence of F was indicated by the peak at 19 amu presumably as a result of use of PTFE and HF. Two peaks at 55 and 57 amu generally associated with rotary pump oils were present even though we had never used a rotary pump in the system at CLP. We later understood that as part of their high temperature (250°C) system bakeout procedure the manufacturer pumped the system into a liquid nitrogen trapped rotary pump. The large O_2 peak at 32 amu indicated the presence of leaks in the system. After detecting and curing the leaks, it was reduced to a low level.

After a system bakeout at 180°C for 24 hours, the system pressure dropped to about 1×10^{-10} mBar and the RGA
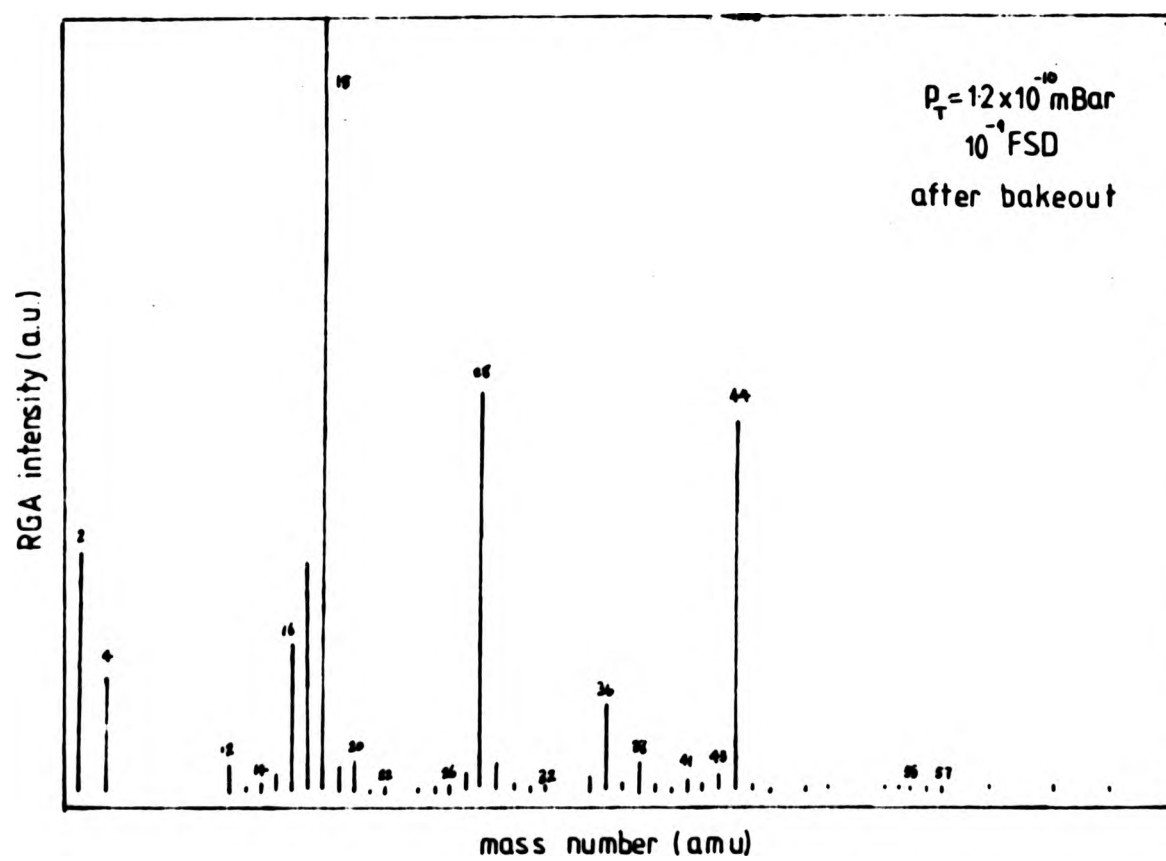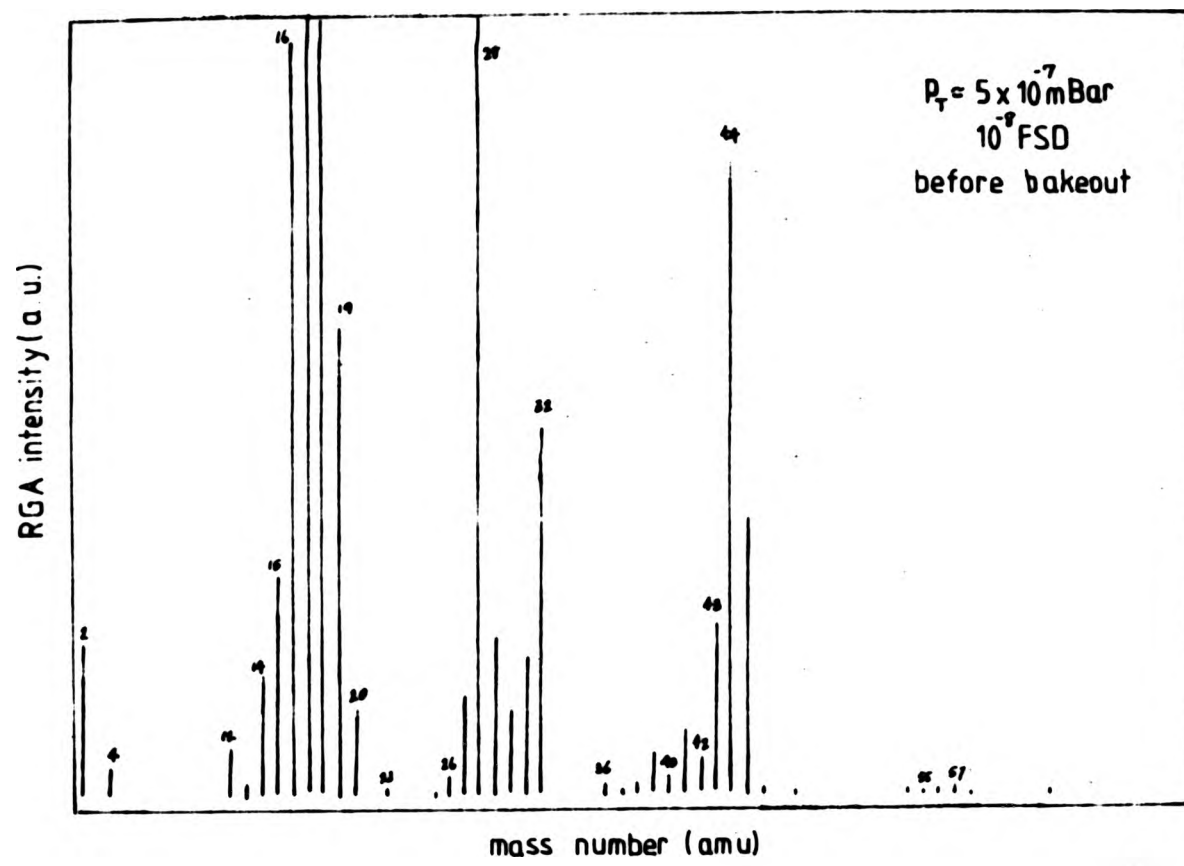
Fig.2.4 Residual gas analysis of the growth chamber; (a) before bakeout and (b) after baking at 170°C for 24 hours.

spectrum of the system is given in Fig.2.4(b). The three major peaks in the spectrum were at 16, 18, 28 and 44 amu corresponding to CH_4^+, H_2O^+, N_2^+ / CO^+ / $C_2H_4^+$, and CO_2^+ respectively. The peak at 43 amu was considerably smaller indicating a reduction of the hydrocarbon level in the system after the bakeout. Peaks at 55 and 57 amu were still detected, but at reduced levels.

Fig.2.5 is a RGA spectrum of a new ion-pumped V80 III-V MBE system after a bakeout. Comparable amount of hydrocarbons was also present in the system as indicated by the peak at 43 amu. Peaks were also visible at 55 and 57 amu suggesting possible contamination of rotary pump oils. With the limited data available and lack of careful calibration of the mass spectrometers, it is difficult to give a reliable comparison of the UHV systems based on their respective RGA spectra. To the best of our knowledge, there was no evidence to indicate that cryopumps compared less favourably to other types of pumps in achieving clean UHV.

2.1.2 Substrate Temperature Monitoring

Accurate temperature monitoring of the substrate was particularly difficult to achieve as the substrate was rotated during growth and where it was not possible to have a close-contact thermocouple on the substrate surface. Instead, the thermocouple was placed in contact to the radiation shields surrounding the substrate heater where it was about 1cm above the edge of the substrate. The thermocouple reading was found to vary between growth runs with the same current input to the substrate heater.

An alternative approach which involved monitoring the radiation from the substrate with an infra-red pyrometer was used. The pyrometer (Mikron M65H) used had a spectral reponse range of 0.78 - 1.06 μm and a focus distance at 60 cm. It was specified to work over the temperature range of 600 -1000°C. Infra-red radiation

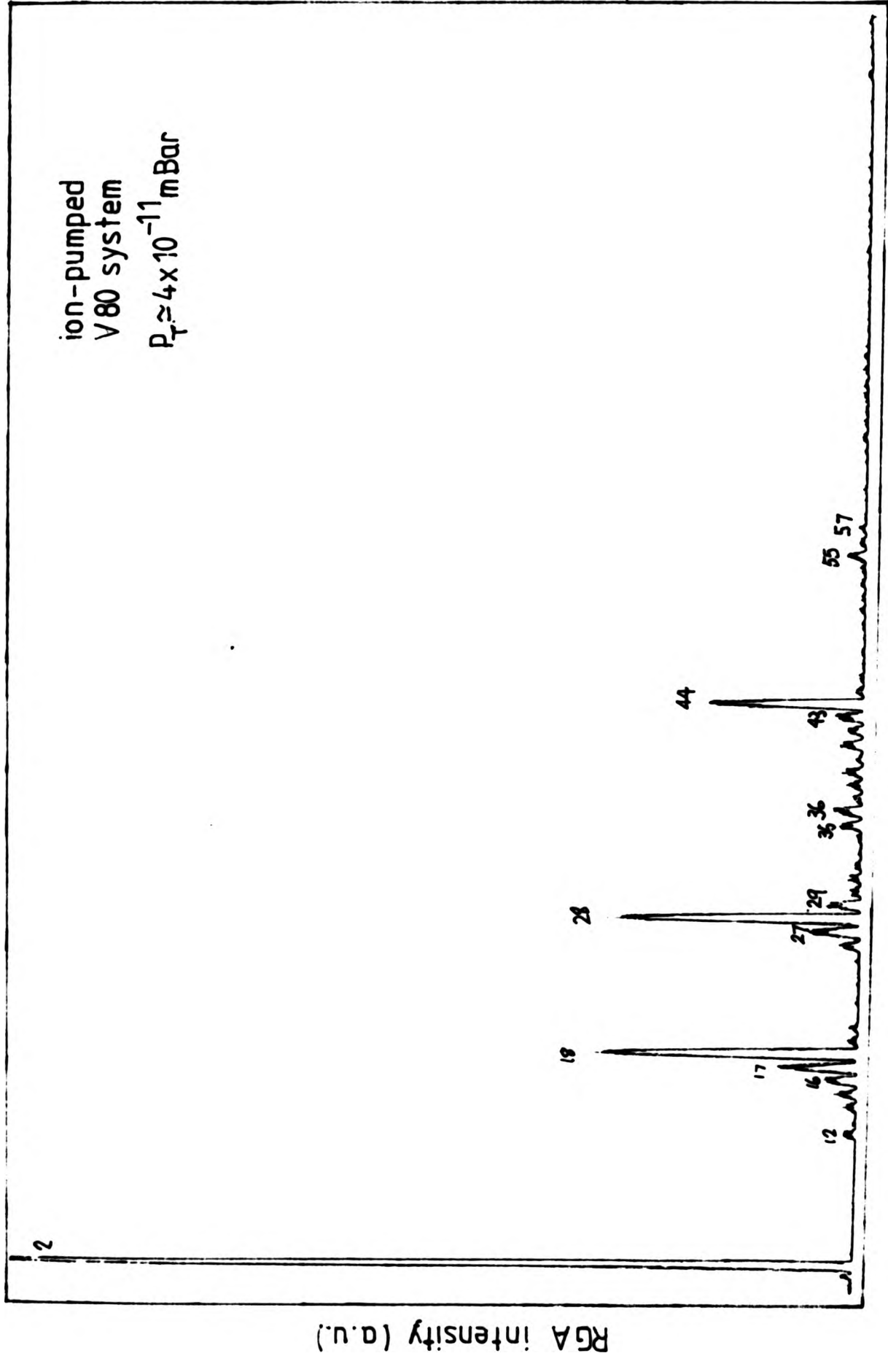Fig.2.5 Residual gas analysis of a baked ion-pumped V80 UHV system.

from an area of 1" diameter was sampled by the pyrometer. The pyrometer was initially calibrated against a 2" diameter p^{++} substrate heated in a furnace under a nitrogen environment. An Cromel-Alumel thermocouple was placed in contact to the back surface of the substrate. To account for the effect of the absorption of radiation due to the glass window of the viewport, it was held in front of the pyrometer during the calibration. A set of calibration curves of the thermocouple against the pyrometer readings at different emissivity settings were obtained. These curves were used in the setting and determining of the substrate temperature during growth.

Though the pyrometer was satisfactory in operation, as the viewport window became progressively coated with re-evaporated dopant material, the reading of the pyrometer became less reliable. This problem was particularly severe in the case of our heavy doping work where a high dopant flux was used. Due to the large sampling area of the pyrometer, we were not able to use it to map the radial temperature variation of the substrate. The accuracy of the pyrometer at the lower temperature range ($< 700^{\circ}$C) was also doubtful even though the pyrometer was specified to work down to 600°C. The problem with coating of the viewport window with dopant material remains a major difficulty in achieving long-term reliability in substrate temperature monitoring.

In most of the growth runs, we found that the temperature reading on the pyrometer reproduced fairly well to the constant current input to the substrate heater. In view of the difficulties encountered with using the pyrometer during our heavy doping work, we routinely set our substrate temperature on the basis of the current input to the substrate heater.

2.1.3 Si Flux Generation and Control

Because Si has a low vapour pressure, it is

33

considerably more difficult to generate Si fluxes sufficed for layer growth using the conventional Knudsen sources. The alternative method involving heating by high energy electron irradiation is used. In this method, the e-gun evaporator generates an intense electron beam from a hot tungsten filament which is accelerated through a potential between 5 and 10kV. The e-beam is then focussed magnetically(or electrostatically in certain type of evaporator) at the central top region of a Si source charge (Fig.2.6). The Si charge was shaped to fit closely in the copper hearth of the evaporator. Before use, the charge was degreased and etched in CP4A (5 HNO_3:3 HF:3 Acetic acid) for ¯5mins to remove machine surface damages and contamination. During the deposition, the copper hearth was water cooled such that the charge was cooled by surface conduction. Only the central region of the Si charge was made molten by the e-beam, and the remaining unmolten charge forms a protective crucible for the molten pool so that potential contamination of the Si source from the copper hearth was prevented.

The e-beam can be either tightly focussed to a small spot at high power density or diffused to increase the surface area of molten pool. The e-gun evaporator has the facilities of rapid x-y scanning of the e-beam by means of two sets of electromagnets. Increasing the area of the molten pool has the added advantage of increasing the amount of evaporant available from each charge. The evaporant distribution from the evaporator is dependent on the operating parameters[84]. To the first order, this distribution can be approximated by the well-known cosine distribution of a Knudsen source[85]. In order to achieve thickness uniformity, methods such as offsetting and increasing the distance r between the source and substrate have been used. This has the disadvantage of reducing the deposition rate by $1 / r^2$. Alternatively, substrate rotation during deposition can be employed such that the directional properties of the sources are "averaged"
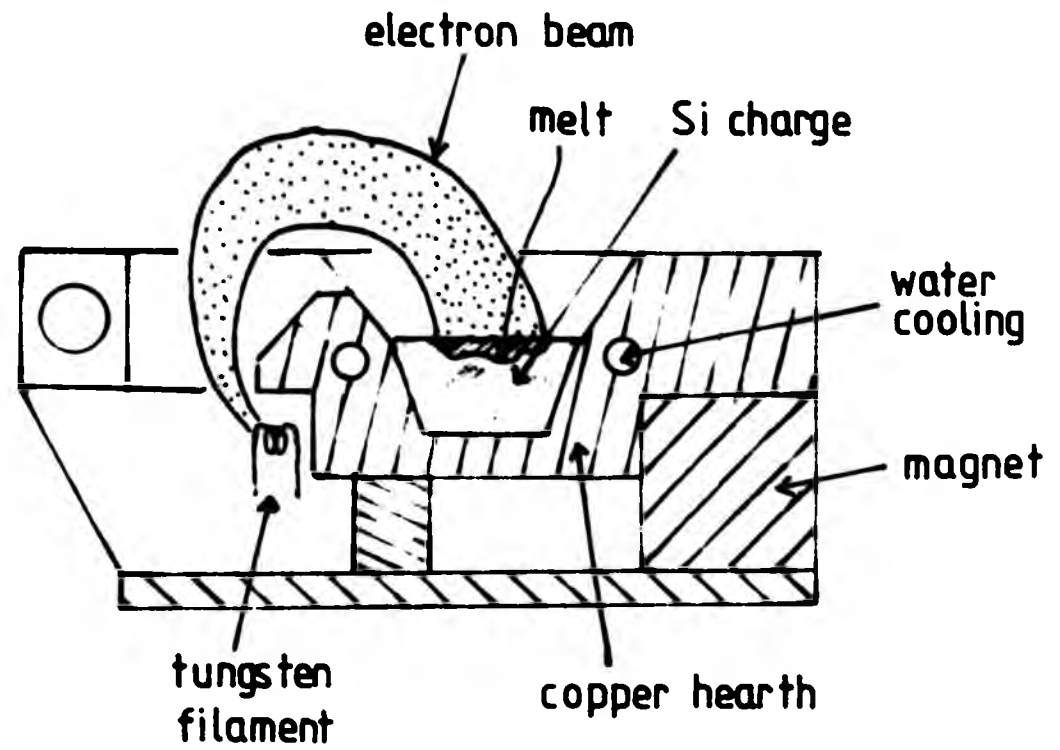
34

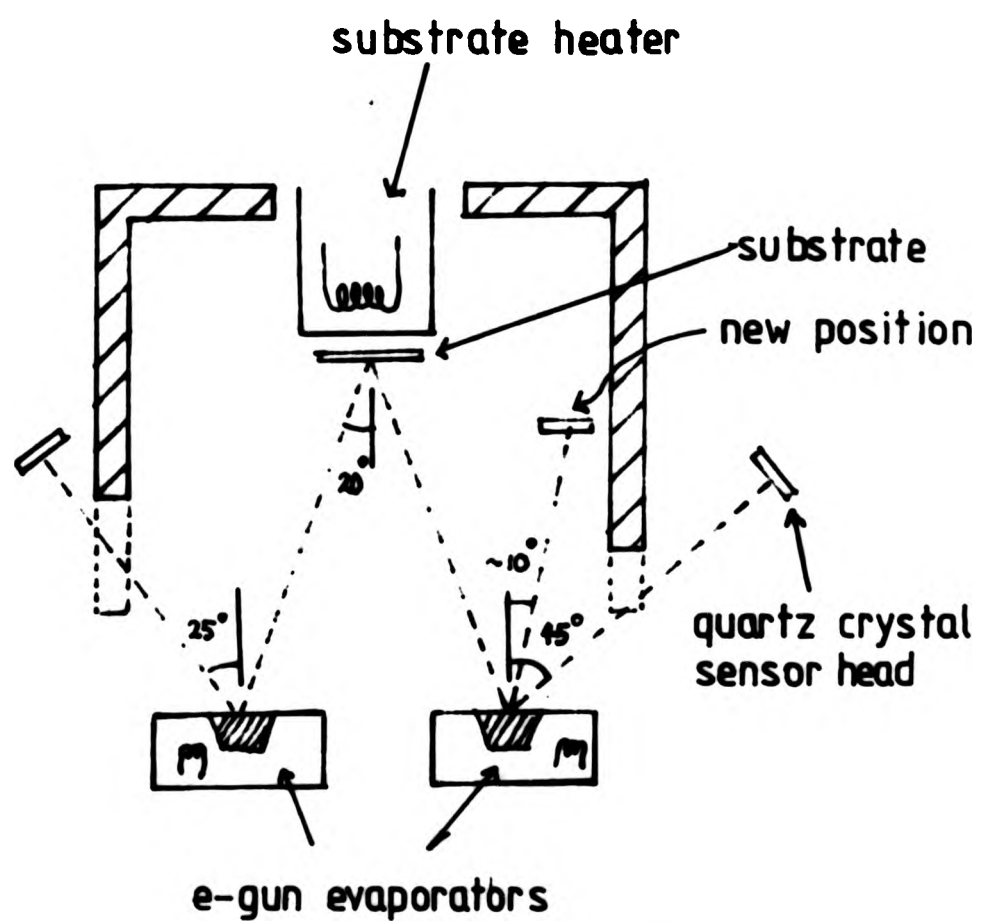Fig.2.6 A schematic diagram of the e-gun evaporator.

Fig.2.7 Illustration of the relative positioning of the
substrate, quartz crystal sensors, and e-gun evaporators.

out.

The positions of the substrate and the e-gun evaporators in our system are shown schematically in Fig.2.7. Two sets of quartz crystal sensor heads were positioned such that one was at 45° and the other at 25° to the vertical at their respective source charges. The effect of the use of substrate rotation on the resultant deposition from the evaporator is depicted in Fig.2.8. In layers group (a), no rotation was used and a thickness variation between the central and near edge regions was estimated to be about 20%. In layers group (b), the substrate was rotated at ~20 rpm, no difference in the thickness of the deposited layer around the edge of the substrate was measured at the three sites as illustrated in Fig.2.8 using a Talystep equipment[86]. We estimated from our electrochemical CV profiling measurement that in the later case the thickness variation from centre to edge was probably less than 5%.

Layer thickness was controlled by a quartz crystal monitor. The monitor measures the amount of shift in the resonance frequency of the quartz crystal due to the mass of the deposit on the quartz crystal over a given time to give the deopsition rate and the time integral of the rate gives the total thickness deposited. Though this method of thickness and rate monitoring operated satisfactory initially and on the short terms, we experienced a number of problems associated to their long-term use. Firstly, each quartz crystal has a rather limited life corresponding to about 10 μm of Si deposition on the substrate. Although we had two separate sensor heads for each evaporator, continuous monitoring of deposition was in practice still very restricted. We overcame this problem by implementing a load lock to the sensor head such that the crystal could be replaced without breaking the UHV in the growth chamber. This solution has the disadvantage of introduction of some contamination after each air exposure of the sensor head.

36
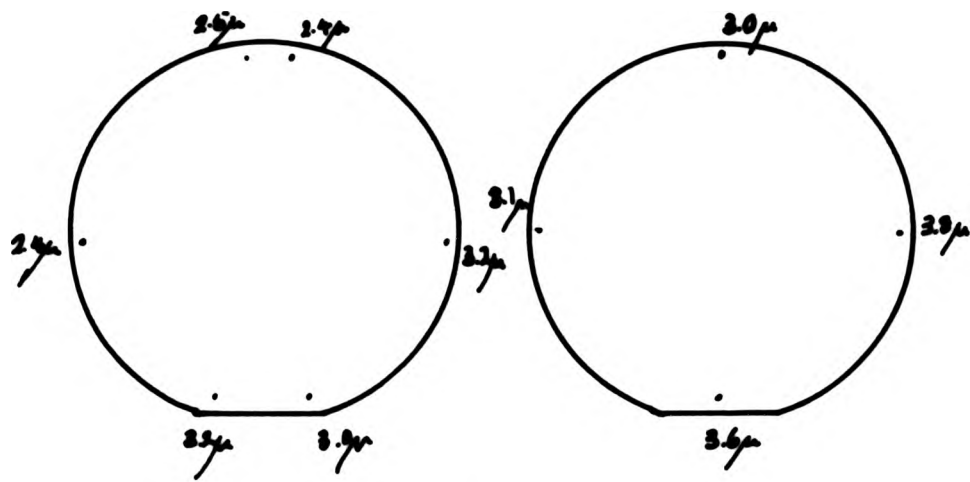
(a) without substrate rotation
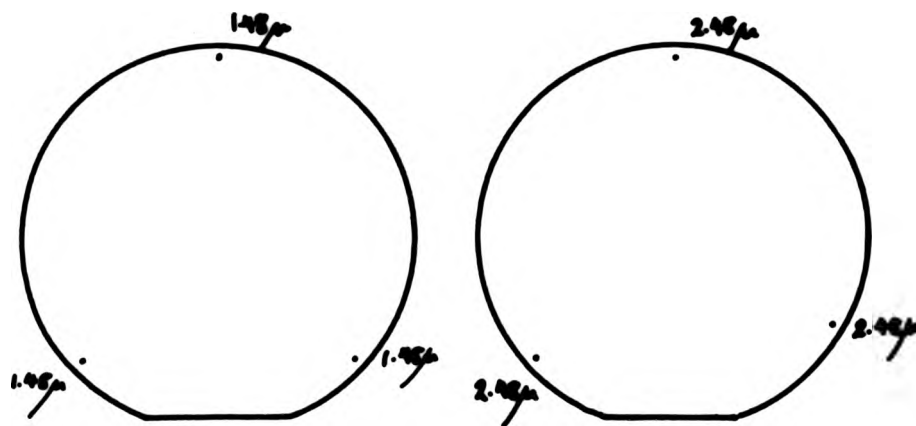
(b) with substrate rotation

Fig.2.8 Effect of use of substrate rotation on the uniformity in deposition of Si films.

Secondly, the flux at the sensor head was strongly affected by the operating conditions of the e-gun evaporator and the crater formed in the Si source charge during layer deposition. This led to a very poor reproducibility in the growth rate between runs. It was considered that the acute angled positioning of the sensor head relative to the evaporator was reponsible for the poor control.

When the sensor head was re-located as illustrated in Fig.2.7, the Si flux from the e-gun evaporator was found to be much more stable than previously observed with the monitor. Reproducibility of the growth rate with operating conditions of the e-gun evaporator was significantly improved. However the closer proximicity of the sensor head to the e-gun evaporator meant that the useful life of each quartz crystal was correspondingly reduced.

2.1.4 Uniformity of Dopant Concentration Distribution

The lateral dopant distribution in the layer is determined by two factors. Firstly, any lateral non-uniformity in the substrate temperature will perturb the dopant uniformity according to the temperature dependence in the sticking coefficient of dopant. Secondly the dopant flux distribution of the source cells at the substrate can also affect the lateral doping uniformity.

The commonly used Si-MBE dopants such as Sb, Ga, Al and In[54,55,57,58] are all known to exhibit a exponential temperature dependence of their sticking coefficient over the growth temperature range of 650 - 1000°C. It is clear that any lateral variation in substrate temperature will reflect a corresponding variation in the resultant dopant concentration distribution. To separate the effect due to the flux distribution of the dopant source, we examined first the dopant concentration distribution in intentionally undoped layers. The distribution was obtained by moving the four

38

point probes radially across the wafer in steps of 5 mm. The probes were lowered such that they were parallel to the radius of the wafer. The measured resistivity was then converted to the dopant concentration using the Irwin's curve. Fig.2.9 is the radial dopant distribution in an undoped layer grown at ~850°C. It can be seen that the carrier concentration increased from the central region towards the edge region indicative of a drop in the substrate temperature at the edge. Typically an increase of about 80 - 100% was observed at ~5mm from the edge. For a substrate temperature of ~850°C, we estimated that this variation corresponded to a drop in the substrate temperature of about 50 C^o near the edge using the sticking coefficient data of Sb published by Bean[54].

The dopant concentration distributions in layers doped with Sb Knudsen sources are illustrated in Fig.2.10. In all the layers shown, there was a slight dip at the central and near-edge regions. The over all variation was about 20%. This distribution is clearly more uniform that one would expect from a consideration of the substrate temperature variation described above. This apparent improvement is a consequence of off-setting the plane of the substrate from the point of intersection of the axes of the substrate rotation and dopant source. The dopant flux distribution partially compensated the effect of substrate temperature on the sticking coefficient of the dopant and led to the observed improvement.

Fig.2.11 shows the dopant concentration distribution in two boron doped layers using two different furnace designs. Since our doping studies showed that boron exhibits unity sticking coefficient in Si over the growth temperatures of 650 - 900°C in contrast to all other Si-MBE dopants, the variation observed in the boron doped layers was therefore due to the dopant flux distribution of the boron source. The uniformity in both layers were relatively poor. However by appropriately positioning of the boron furnace, the uniformity of the dopant
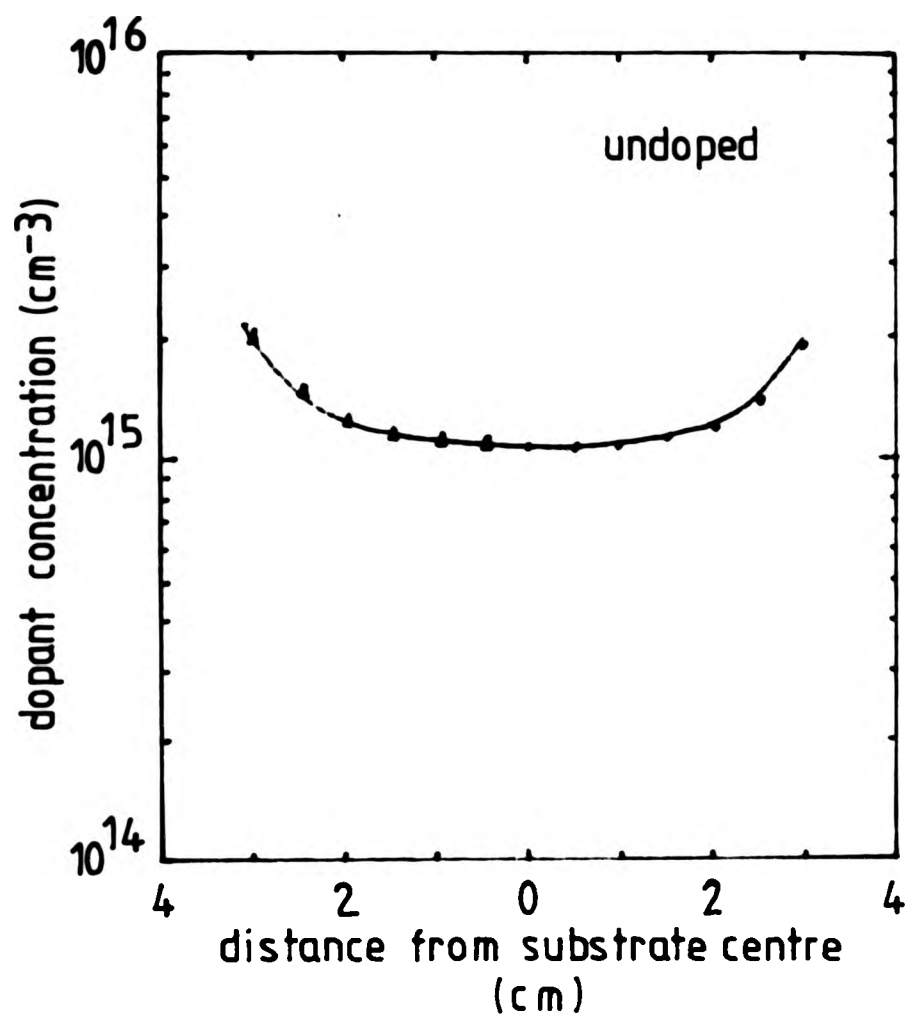
39

Fig.2.9 A typical radial distribution of the carrier concentration measured in undoped Si-MBE layers.
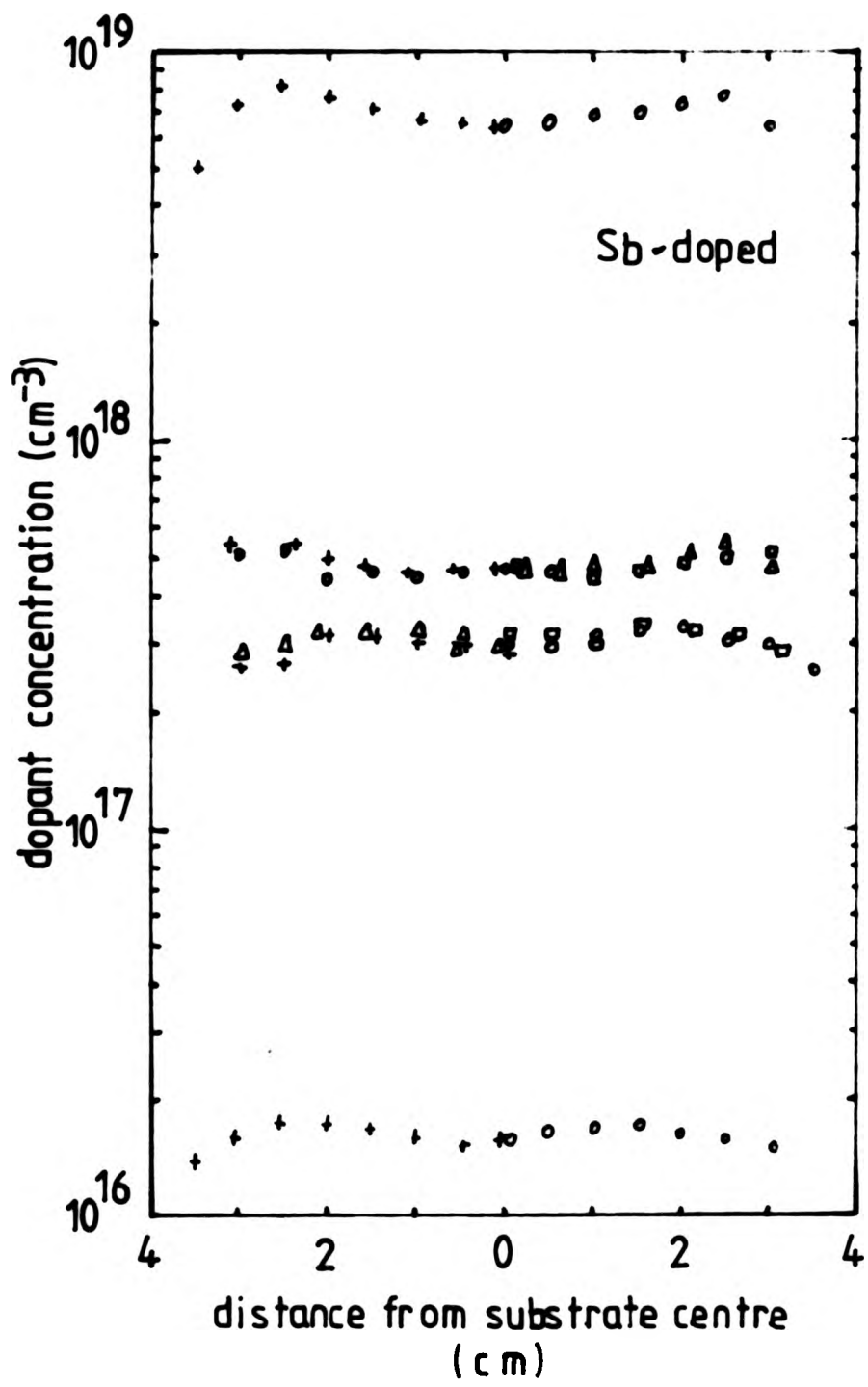
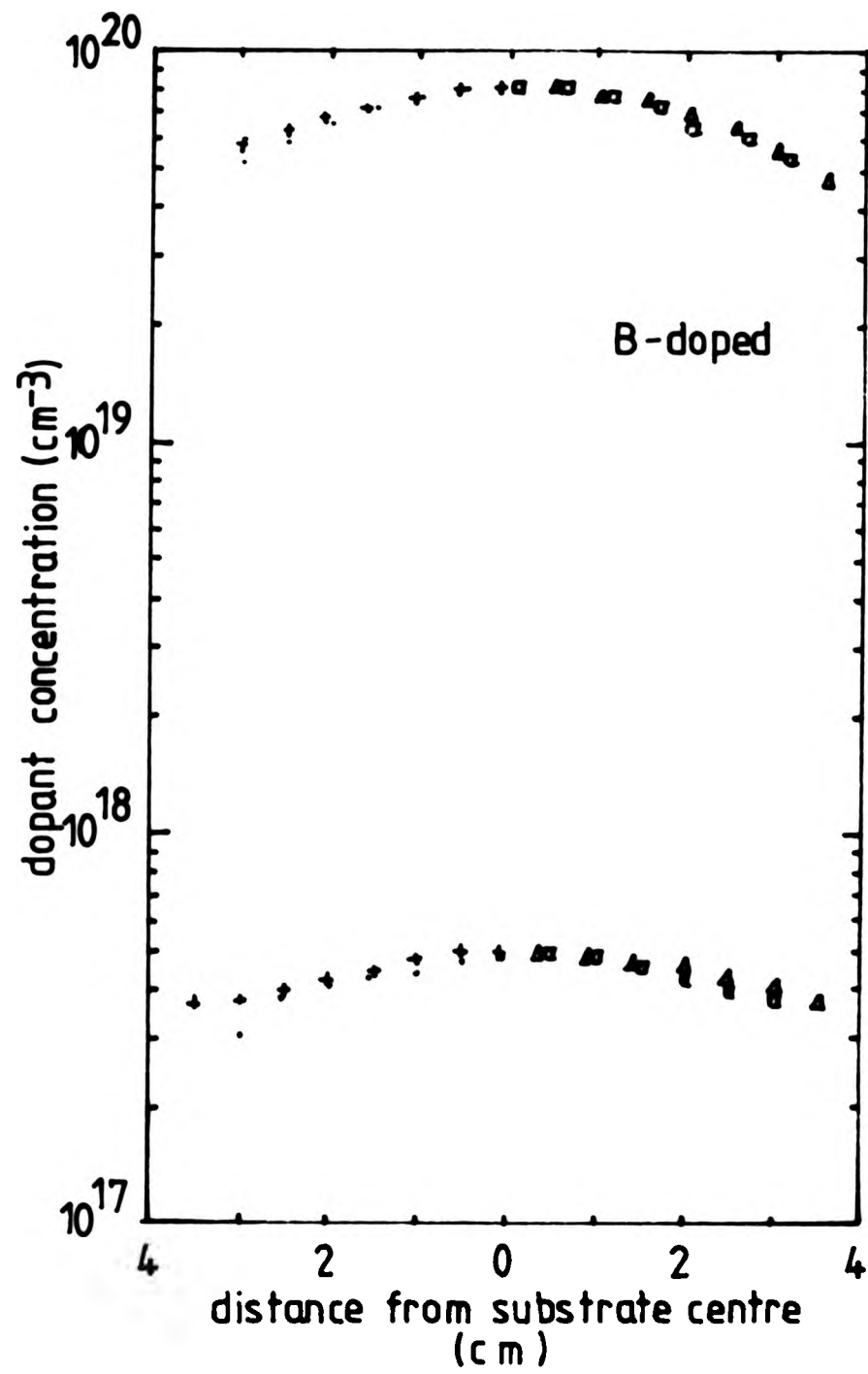Fig.2.10 Radial distributions of dopant concentration measured in Sb-doped layers.

41

Fig.2.11 Radial distributions of dopant concentration
measured in boron-doped layers.

42

concentration should be significantly improved.

2.1.5 Si Shielding of E-gun Evaporators and Chamber Walls

Ota[9,87] found that Si shielding of the e-gun evaporator and chamber walls were crucial in achieving low residual doping and defect levels in Si-MBE. It was considered that electron bombardment of the copper hearth of the e-gun evaporator and stainless steel chamber walls would introduce metallic contaminants in the epitaxial layers.

To examine the effectiveness of Si shielding, we covered one of the e-gun evaporators in our system with machined high purity Si pieces as described by Ota[65] and intentionally left the other evaporator exposed. We also covered the surrounding chamber walls with high resistivity Si substrates. A number of layers were then grown using either e-gun evaporator. Preliminary examinations of these layers using preferential defect etching, Hall and CV measurements showed no significant differences in their electrical properties and defect content. SIMS and DLTS analysis of the layers indicated very low levels of metallic contamination and deep energy states ($<1 \times 10^{13} cm^{-3}$) respectively.

We observed that after a few deposition runs, a substantial part of the copper hearth and surrounding chamber walls were rapidly coated with Si. It is considered that this deposited Si layer would act effectively as the Si shielding of any surface of the system exposed to the Si flux. Nevertheless, we believe that Si shielding of surfaces exposed to potential electron bombardment should be used as a matter of precaution.

2.2 Assessment and Characterization of Si-MBE Layers

2.2.1 Hall Measurements by Van der Pauw Method

In the Van der Pauw method[88], four small contacts located at the circumference around an arbitrary shaped sample are required (Fig.2.12(a)). A magnetic field B is applied perpendicular to the sample. During the measurement, a constant current is passed between two of the contacts and the voltage between the other two contacts is measured. The theory shows that the resistivity ρ of the sample with thickness d is given by:

$$\rho = \frac{\pi d}{\ln 2} \frac{\left(R_{ab,cd} + R_{bc,da} \right)}{2} f \quad \text{--------(2.1)}$$

where $R_{ab,cd}$ is defined as $(V_d - V_c)/I$ with the current flowing from a to b, and f is a correction factor for the non-symmetrical sample shape. The Hall mobility μ_H is given by:

$$\mu_H = \frac{d}{B} \frac{\Delta R_{bd,ac}}{\rho} \quad \text{---------(2.2)}$$

where $\Delta R_{bd,ac}$ is the change of $R_{bd,ac}$ due to the magnetic field B. The carrier concentration n of the sample can be calculated using

$$n = r / \rho \mu_H \quad \text{---------(2.3)}$$

where r =scattering factor. The magnetic field, B, used in our Hall measurement was 0.52T. The scattering factor, r, was taken to be unity in calculating n. However, it has been shown that r =1 only in the case when a high magnetic field is used[89]. In practice, r is found to be about 0.8 and 1.12 in low doped p- and n-type Si (< $1 \times 10^{16} cm^{-3}$) respectively. The sample contacts are generally large and not located at the circumference of the sample due to practical difficulties. Van der Pauw[88] showed that the large contacts could introduce errors in the measurement, but their influence could be eliminated by using a cloverleaf-shaped sample.

When assessing thin epitaxial layers,

44
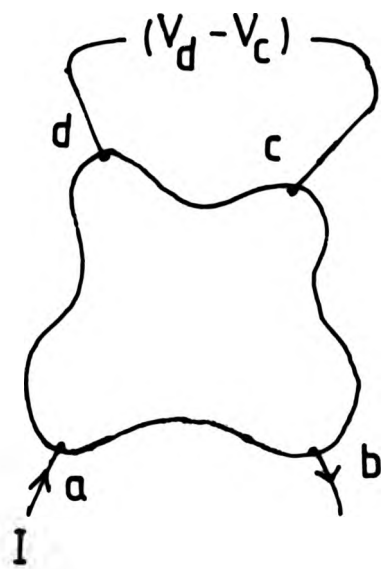
$$R_{ab,cd} = \frac{(V_d - V_c)}{I}$$

(a)
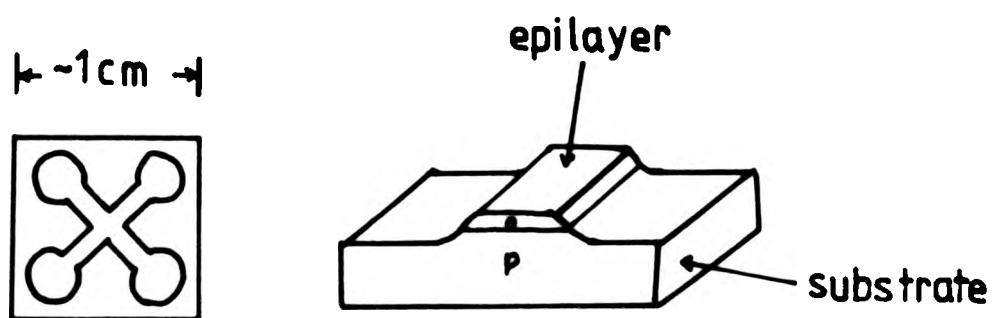
(b)

Fig.2.12 (a) Hall measurement by the Van der Pauw method.
(b) A typical Van der Pauw sample used in our Hall
measurements showing the electrical isolation of the
epitaxial layer from the substrate by means of the reverse
biased p-n junction.

complications in the interpretation of the Hall measurement can occur due the formation of the space charge layers at the substrate interface and at the epitaxial surface of the layer. They affect the effective thickness of the layer in the measurement. In this work, the layers were generally grown on substrates of the opposite conduction type. The resultant p-n junction formed at the interface, when under reverse biased, maintains the necessary electrical isolation of the epitaxial layer from the substrate during the measurement. The effective thickness of the layer is however reduced due to the depletion of carriers adjacent to the p-n junction. The width of this depleted region, which is dependent on the dopant concentrations of the substrate and layer and the dopant transition at the junction, can be calculated. For the case of a abrupt junction, the depleted width w into the layer under zero bias is given by[53]:

$$ w = \sqrt{ \left\{ \frac{2\epsilon kT}{q^2} \left(\frac{1}{N_L} + \frac{1}{N_S} \right) \left[\ln 2 \frac{N_L N_S}{n_i} - 2 \right] \right\} } \quad ---- \quad (2.4) $$

where N_1 = layer dopant concentration

N_s = substrate dopant concentration

N_i = intrinsic carrier density

q = electronic charge

k = Boltzmann's constant

ϵ = permittivity of sample

T = sample temperature

A plot of the depletion width w in a layer doped at N_L on a substrate doped with N_S is shown in Fig.2.13. For example, at N_1 = $1 \times 10^{14} cm^{-3}$ and N_s = $1 \times 10^{15} cm^{-3}$, the depleted width w is calculated to be 2.3 μm. This shows that, in very low doped layers, a substantial part of the layer can be depleted. It can also be seen that this depletion in the layer is reduced by using high resistivity substrates ($<1 \times 10^{13} cm^{-3}$). Unfortunately, high resistivity Si substrates are not readily available.
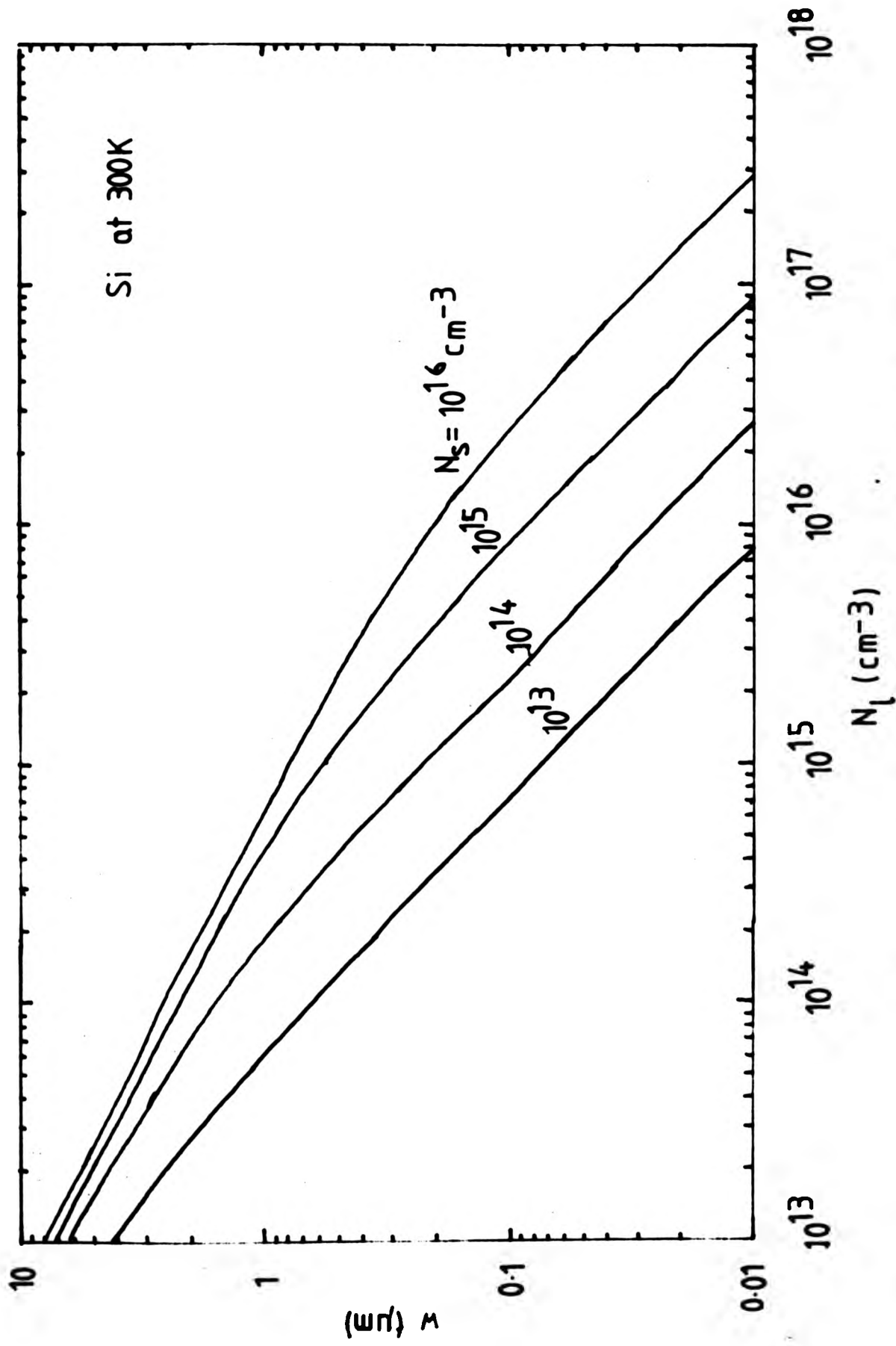
Fig.2.13 The depletion region w_D in an epitaxial layer of dopant concentration N_l grown on a substrate of the opposite type dopant concentration N_s.

We also encountered further complication due to the boron contamination in our layers which produced an uncertain p-n junction at the substrate epitaxial interface (see Section 3.4.1). Use of this correction procedure for the depletion width at the junction is therefore limited.

Van der Pauw mesa samples suitable for Hall measurement were prepared by first scribing out convenient square shapes (typically 7x7 mm) from the layers with a diamond cutter. The epitaxial surface of the sample was then degreased in propano-2ol and blown dry and dust-free. The required Van der Pauw shape was masked onto the sample surface with black wax. One simple way of masking was to dissolve the black wax in a small amount of of xylene to form an inky mixture which was then be applied onto the surface with a brush. With a little practice, complex shapes can be made. A typical sample shape used in our measurement is shown in Fig.2.12(b). Numerical analysis of this structure by David and Baller[90] showed that the error introduced by the contact area to the sheet resistance measurement was less than 0.1%. The sample was left in a dust free environment until the wax was fully solidified. The masked sample was etched in CP4A solution (5 HNO_3:3 HF:3 Acetic acid) for a period of 20-30s to remove the unprotected epitaxial layer completely and some of the underlying substrate material. The rate of Si removal was estimated to be about 7 μm per 10s. The etched sample was rinsed with and left in a large volume of distilled water for about 30 minutes. The masking wax was then dissolved away from the sample using fresh xylene. The sample was then washed immediately in propan-2ol and distilled water to remove the last traces of wax on the epitaxial surface.

Contacts to the sample were made by using either an In amalgam[91] or In-Ga eutectic. The In amalgam was formed by simply wetting a piece of In wire in Hg, whereas the In-Ga eutectic was obtained by heating a mixture of 3Ga:1In in a container. Both of them were liquid at room

48

temperature. Just before applying the contact, the contact area was first removed of surface oxide with dilute HF. Special care was taken to ensure that the "active" region of the sample was not attacked by the acid. A piece of Au was placed on top of the In amalgam to form a solid contact pad. The ohmicity of the contacts was checked using a curve tracer before Hall measurement. This simple ohmic contact was found satisfactory at room temperature for p and n-type samples with dopant concentration down to as low as $5 \times 10^{14} \text{cm}^{-3}$. Preliminary tests also showed ohmicity remained generally satisfactory down to 77K. For highly doped samples ($>10^{18} \text{cm}^{-3}$), the contacts remained satisfactory even at ~20K. The p-n junction isolation of the etched sample was excellent provided, of course, that a good p-n interface was originally formed at the epitaxial-substrate interface.

The sample preparation technique described above has a number of advantages. Firstly, surface treatment to the as-grown layer is minimized thus avoiding unstable surface effects which are difficult to control and account for. Secondly, no heat treatment of the sample is necessary in making the ohmic contacts. Thirdly, Hall samples can be prepared and measured very quickly.

2.2.2 Four-point Probe Measurement

Four-point probe measurement is the most commonly used method for determining the resistivity of Si material due to its simplicity and ease of use. The equipment consists simply of four collinear probes which form ohmic contacts on the surface of the sample. The measurement involves passing a constant current through the outer two probes and measuring the voltage between the inner two probes. For a thin layer with thickness much smaller than the diameter and the probe spacing, the resisitivity of the layer ρ is given by:

$$\rho = \left(\frac{\pi}{\ln 2}\right) \frac{V}{I} t \qquad \text{------- (2.5)}$$

Since our four-point probe equipment (supplied by Universal Probe, Jandel Engineering Ltd., UK) has a probe spacing of ¯ 1mm, layers with thickness less than 100 μm can be measured without having to introduce correction factor to Eq.(2.5). For thicker layers such as Si slices, it is necessary to include a correction factor. Tabulated correction factors relating the thickness and diameter of slices to the probe spacing are published in the ASTM 1983 Handbook[92].

In our work, four-point probe measurements were made on layers grown on substrates of the opposite conductivity type. The isolation of the layer is maintained by the p-n junction at the epitaxial substrate interface. Use of the junction isolation may present some problems in obtaining accurate measurement of the resistivity of the layer. The effect of leakage current of the p-n junction on sheet resistance measurement has been investigated by Patrick[93]. He found that, at high measurement currents, the p-n junction isolation could affect the measurement of sheet resistance in two ways. Firstly, as the current was increased, the depletion width of the p-n junction increased due to a corresponding increase in the reverse bias potential of the junction. The effective thickness of the epitaxial layer was hence reduced and a higher sheet resistance was measured. Secondly, at very high currents, the junction might break down and significant conduction occurred in the substrate. In this case, the measured sheet resistance dropped sharply. This effect could be minimized by keeping the measurement current low enough so that the p-n junction was near zero-bias condition. In practice, four-point probe measurements were made at different current levels and accepted when the measurements did not vary by more than 2%.

The resistivity measurement is affected by the depletion of carriers within the epitaxial layer due to the

presence of the p-n junction. In principle, the depleted layer can be calculated if the dopant concentration of the substrate is known and the p-n junction is assumed to be abrupt or graded. The effective thickness of the layer is then given by the difference of the metallurgic thickness and the calculated depletion width (see Section 2.2.1). However, further complications occur in the case of our Si-MBE layers which often suffered from boron contamination at the epitaxial substrate interface (see Section 3.4.1). In the case of n-type layers, a narrow p-type region appeared at the interface which made a calculation of the depletion width virtually impossible. For low p-type doped layers, the narrow p-type region could dominate the conduction in the layer and lead to an underestimate of the resistivity of the layer.

The surface conditions of the epitaxial surface can also affect the measurement. The effects of various chemical treatment and air exposure of the epitaxial surface on resistivity measurement have been discussed by Kramer and Ruyven[94]. At present, there is no simple method of calculating the correction for the effect due to the difficulty in determining the surface conditions. It is generally believed that freshly grown layers apparently show negligible surface effects though this is very much dependent on the growth process used. Our experience with Si-MBE layers showed that as long as the layers were not subjected to further chemical treatment after growth, reproducible measurements were possible and good agreement with CV measurements was readily obtained.

The accuracy of our four-point probe measurement was likely to be affected by the uncertainties involved with the boron contamination which prevented accurate correction to the effective thickness. In the case of the n-type layers, a highly compensated region was formed immediately adjacent to the n-type layer, the depleted region in the n-type layer thus became negligible. But it is not possible to determine the thickness of the n-type layer without

51

resorting to some profiling techniques such as CV and SR measurements.

2.2.3 Spreading Resistance Profiling Technique

Spreading resistance is the resistance measured between two ohmic contacts on a semiconductor surface[95]. In practice, two metal probes pressure contacted to the surface are used, a constant voltage is applied between the probes and the current flow is measured to give the spreading resistance. Theoretical modelling shows that carriers immediately under the probe and within a volume of a few probe radii are "sampled" in the measurement and the spreading resistance, Rs, due to each probe can be related to the resistivity ρ of the bulk material by:

$$R_s = \rho / 4a \quad \text{---------------- (2.6)}$$

where a is the "contact" area of the probe with the material. To obtain the resistivity directly using Eq.(2.6), it is necesssary to measure "a" which is difficult. Alternatively, one can use a comparative method in which a sample with known resistivity is measured with the same probes and the contact area "a" is calculated using Eq.(2.6). This method assumes that the contact area remains the same in both measurements.

Spreading resistance profiling technique[96] is a further development of the measurement in which the profile of the spreading resistance of the probes down a bevelled surface of the sample is obtained by lowering and raising the probes with a carefully controlled rate of decent and contact pressure. This is important to achieve reproducibility of the probe contact and ensure consistent layer penetration at each measurement in order to obtain a reliable profile. Using the same probes, a calibration curve of Rs vs resistivity is also obtained on a set of

bulk samples of known resistivity with the same type conduction and crystal orientation.

The raw Rs profile data and the calibration curve are used to calculate the corresponding dopant concentration profile on a digital computer. Sophisticated algorithms involving corrections for the effects of probe contact and sampling volume are used to obtain the dopant concentration profile. It is important to note that in the calculation bulk properties are necessarily assumed in the sample which of course may not be valid. In the case where the carrier mobility is reduced in the sample, the calculation will over-estimate the dopant concentration. The reliability of the measurement is highly dependent on the skill of the operator in preparing the sample and probes and using the equipment. Nevertheless, this profiling technique is particularly valuable for assessing samples of multilayer structure with both carrier type conductions.

2.2.4 Electrochemical CV profiling

It has been shown[53] that a Schottky barrier under a reverse bias exhibits a capacitance/ voltage characteristics given by:

$$d(1/C^2)/dV = 2/ qenA^2 \quad \text{--------------(2.7)}$$

where C = capacitance of barrier junction
A = area of barrier junction
n = dopant concentration of substrate
q = electronic charge
e = permittivity of material

The depletion width w_D is given by:

$$w_D = eA/C \quad \text{-------------(2.8)}$$

53

Since n represents the dopant concentration at the measured depletion width, a profile of n can be obtained by increasing the reverse bias potential of the barrier junction. In fact, Eqs.(2.7) and (2.8) form the basis of all CV dopant profiling method.

The required Schottky barrier can be formed by evaporating Au on n-Si or Al on p-Si at room temperature. A number of methods have been used to implement the above expressions for obtaining the dopant concentration profile. The straight forward method is to measure C vs V and process the data to give the profile on a digital computer[97]. Methods involving analoge signal processing include the Miller feedback[98] and modulation methods[99]. Both methods use a phase sensitive detection technique in which the depletion width of the diode is modulated to obtain the carrier concentration profile.

The conventional CV profiling technique suffers a limitation on the maximium profile depth obtainable because of avalanche breakdown of the Schottky barrier as the reverse bias is increased. This breakdown occurs in Si[53] when a surface charge density in the depleted region exceeds a value of about $2x10^{12}cm^{-2}$. Fig.2.14 shows the depletion width w_{max} at breakdown for a given dopant concentration of the substrate. Whilst this limitation is generally acceptable for low doped materials, the maximium profile depth in materials doped above 10^{17} cm^{-3} is less than 0.3 μm. In order to extend the profile depth beyond the breakdown limit, a step layer stripping technique followed by a CV measurement may be used. This method is however very tedious and time-consuming.

Studies of the electrochemical behaviour of the interface between n-GaAs and KOH electrolyte[101,102] showed that ideal Schottky barrier characteristics can be obtained whilst anodic dissolution of the material can occur at certain bias conditions. Ambridge and Facktor[103] have employed these electrochemical characteristics in an automatic profiling technique in
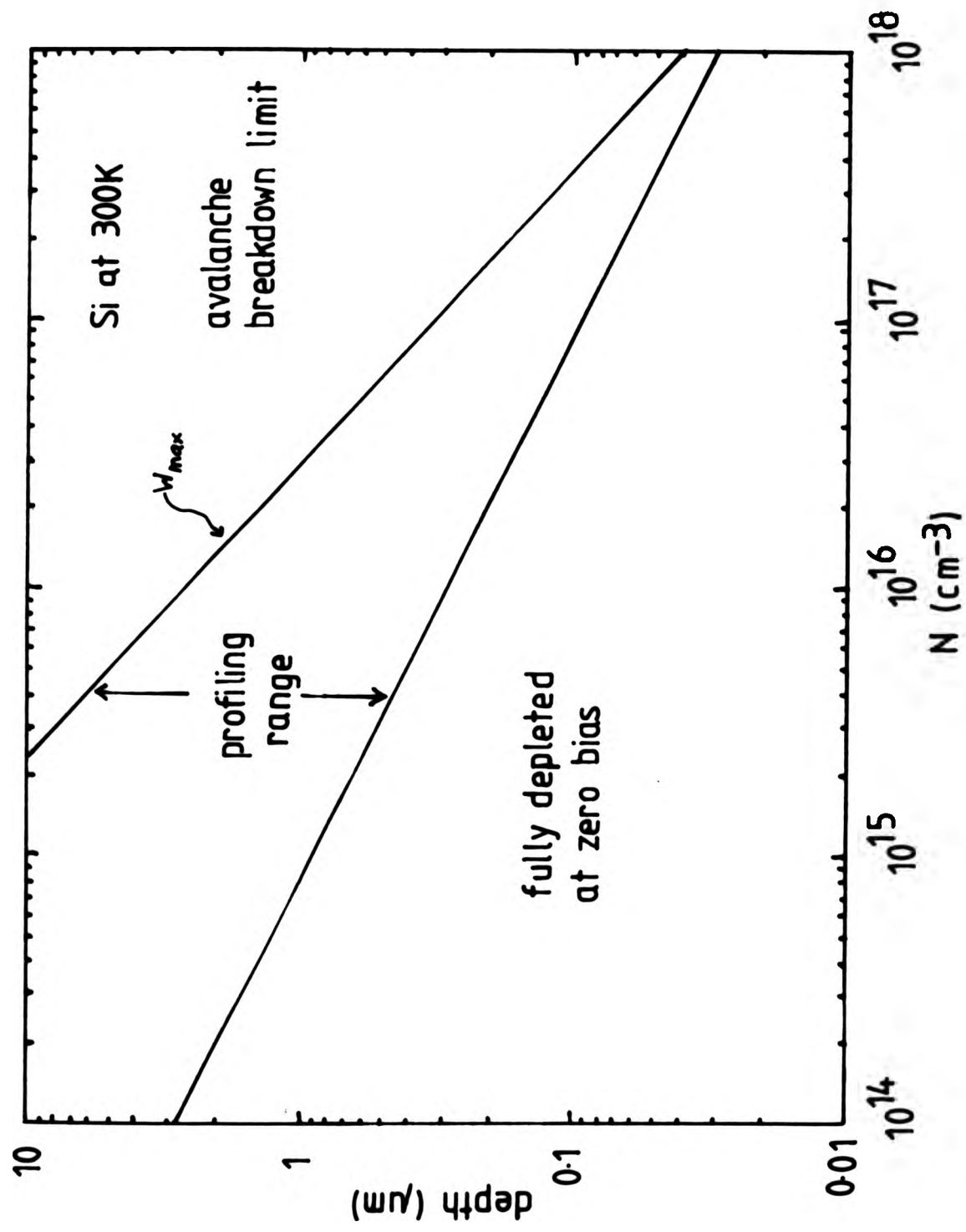
54

Fig.2.14 The limitation on the profileable depth in Si material by the conventional CV measurement due to junction breakdown of the Schottky diode.

55

which a repeated cycle of anodic dissolution and CV measurement of n-GaAs in a suitable electrolyte such as KOH or Tiron is performed to obtain a continuous carrier concentration profile over any required depth. This electrochemical CV profiling technique has been demonstrated in a number of semiconductors, namely, GaAs[104], InP[105] and Si[106]. Fully automated profilers based on this technique are commercially available[107].

A detailed description of the automatic profile plotter has been given in an excellent article by Ambridge and Faktor[103]. The block diagram of the system is reproduced in Fig.2.15. Features of the system, particularly relevant to profiling of Si material, will be described here. Interested readers should refer to the original article mentioned above for the details of the operation of the system.

The two major components of the system are the electrochemical cell and system control/measurement unit. Fig.2.16 shows the basic contruction of the electrochemical cell. Two cathodes are used in the cell; a carbon fibre DC cathode for anodic dissolution and a Pt wire AC cathode for capacitance measurement. The bias potential on the sample is applied via a saturated calomel electrode (SCE). A notable feature in the electrochemical cell is the jet mechanism which directs fresh electrolyte at the sample surface during dissolution at regular intervals. This is important in profiling Si materials as the hydrogen bubbles formed during the anodic dissolution can affect the uniformity of material removal and the capacitance measurement.

The most critical part of the electrochemical cell is the PVC seal ring which defines the area of the sample in contact with the electrolyte. Uncontrolled seepage under the seal surface can lead to difficulties in determining the contact area. In the anodic dissolution of p-type material, the area of the region of material removal A_0
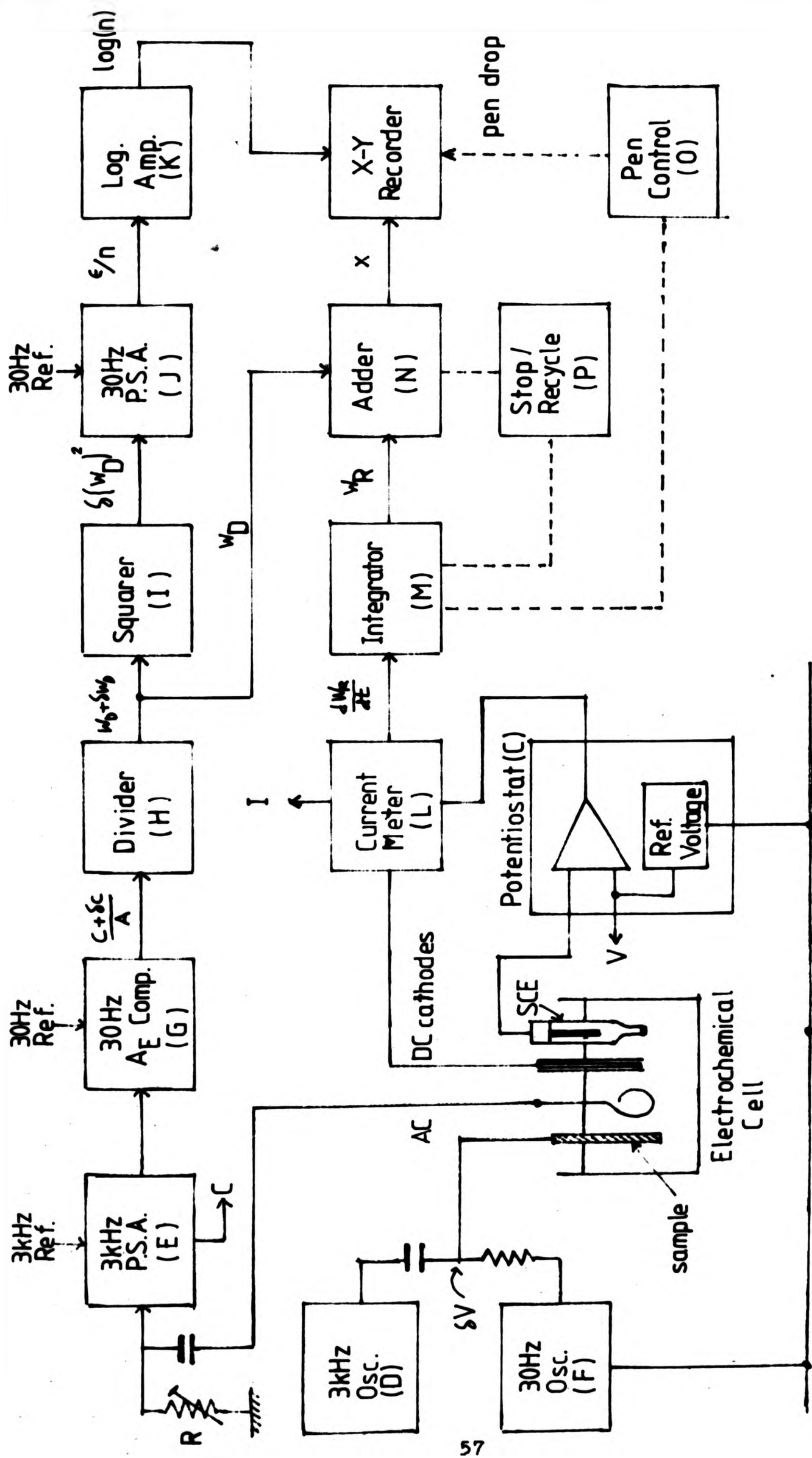
Fig.2.15 Functional block diagram of the automatic electrochemical CV profile plotter.

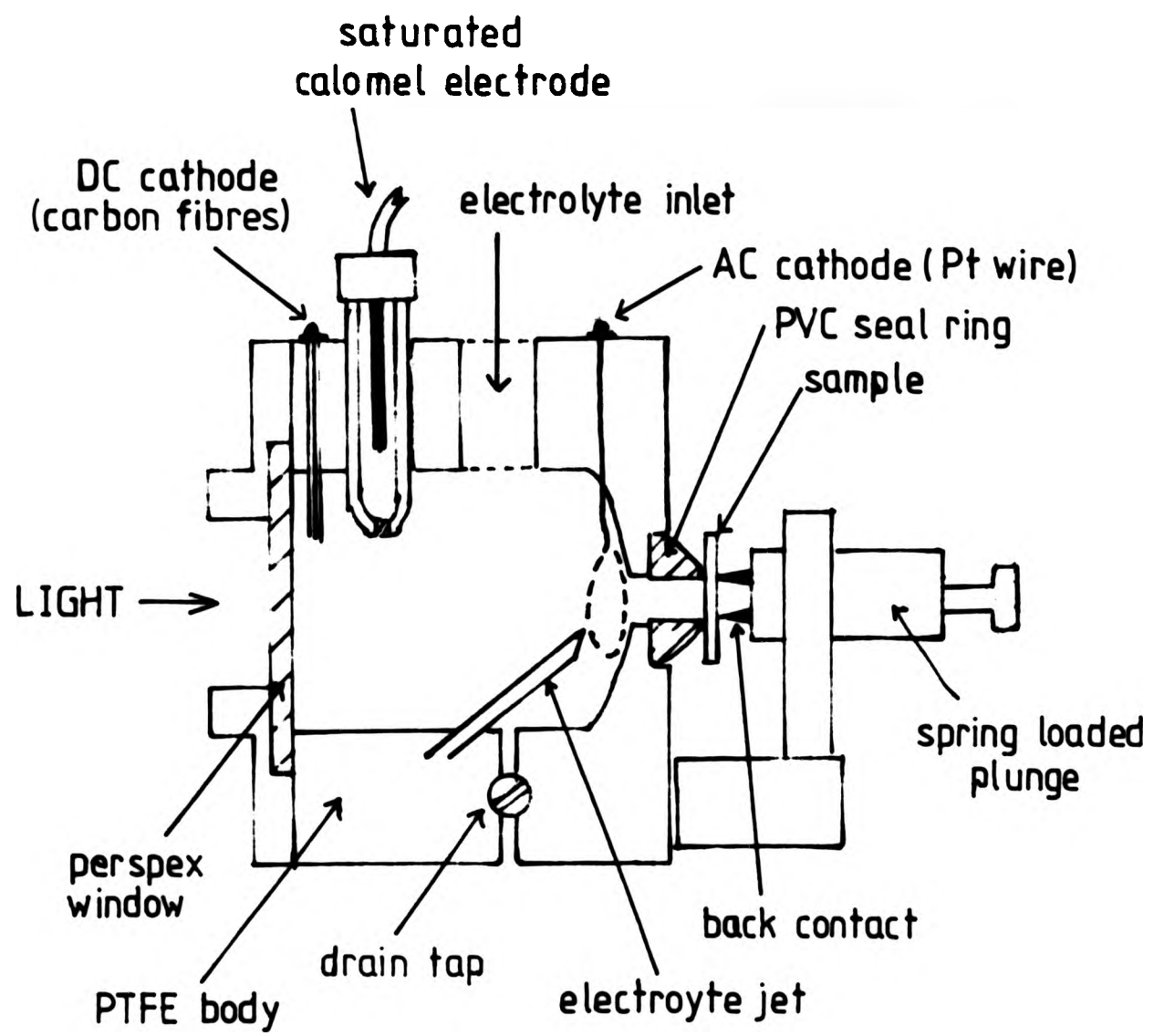**Fig.2.16 Diagram of the electrochemical cell.**

saturated calomel electrode

DC cathode (carbon fibres)

electrolyte inlet

AC cathode (Pt wire)

PVC seal ring

sample

LIGHT →

spring loaded plunge

perspex window

drain tap

back contact

PTFE body

electroyte jet

is defined by the seal ring, i.e. the area in contact with the electrolyte. In the n-type material however holes required for dissolution are generated by illumination of the sample surface through the perspex window. The region of material removal in this case is defined by the illuminated area A_I. Since the measurement of C is related to area in contact with the electrolyte in both p- and n-type materials, the excess are $A_E = (A_O - A_I)$ has to be taken in account in the determination to the depletion width and carrier concentration.

Measurements of A_O and A_I were made using an oxidized n-type Si sample. The required oxide layer was grown anodically in an electrolyte of $0.05M$ KNO_3 in ethylene gycol under ambient illumination. The anodic potential applied to the n^{++} substrate was increased gradually until a bluish film became visible. The blue oxide layer on the sample in contact with the electrolyte was gradually dissolved away whilst the illuminated region was anodically removed. The diameters of the two circular regions were then examined and measured under a travelling microscope. In practice, with the improved seal ring developed at British Telecom Reasearch Centre, the problem with electrolyte seepage is minimal, and the excess area is generally below 2% of A_O. Since the travelling microscope we used has a measurement error of 1%, the correction setting for the excess area in the measurement unit was not used.

The depth x below the original semiconductor surface corresponding to the measured value of n is given by the depletion layer width w_D added to the thickness of material w_R removed by anodic dissolution, i.e. $x = (w_D + w_R)$. w_D is obtained from simply measuring C and using Eq.(2.8). w_R is obtained from the time integral of the dissolution current I:

$$w_R = \frac{M}{NFDA} \int I \, dt \qquad \text{----------(2.9)}$$

59

where M = molecular weight of semiconductor

N = valence number

A = area of sample

D = density of semiconductor

F = Faraday number

Eqs.(2.7) and (2.8) can be combined and expressed in a form relevant to the measurement approach adopted in the profiler:

$$n = \frac{2F}{q} \frac{\delta V}{\delta(W_D^2)} \quad \text{---------}(2.10)$$

Measurements of the depletion layer width and carrier concentration are based on a modulation technique in which a small modulation of the bias potential is added to produce a correspondind modulation of the depletion width and hence of the measured capacitance. Two oscillators (D and F) at 3kHz and 30Hz are used for modulation of the depletion width. The imaginary component of the current passing through resistor R is determined using a 3kHz phase sensitive amplifier (E) to give a measure of C corresponding to the depletion layer width W_D. Modulation of the depletion layer width is achieved by means of the 30Hz oscillator whose output is maintained at 100mV rms. This results in a 30Hz component in the dc output of the 3kHz phase sensitive amplifier, corresponding to δC. Both signals of C and δC include a constant contribution due to the excess area A_E, so that a fraction of the signals has to be offset using the compensator unit (G). The compensated signals are then fed into a number of processing units and amplifiers (J,K) to give the required outputs of x and log n which can be displayed on a x-y chart recorder.

Preliminary work of Sharpe et al[100,106] has shown some promising successes at profiling CVD and implanted Si materials using an electrolyte of 1M NaF/0.05M

H_2SO_4. They indicated that careful choice of the profiling conditions were essential in order to obtain accurate measurement. They observed some variability in the effective dissolution valence number N with the illumination level and electrolyte strength.

We have examined the electrochemical behaviour of Si in the same electrolyte under different conditions of illumination level, anodic potential and electrolyte strength; and arrived at a set of optimum conditions for achieving accurate measurement of very abrupt dopant structures grown by Si-MBE.

Another alternative electrolyte consisting of 0.07M $NH_4F.HF$ [108] was also used in our early work. Due to the hydrophilic and unstable nature of the $NH_4F.HF$ compound, the same strength of electrolyte was difficult to be maintained routinely. As our study with the 1M NaF/0.05M H_2SO_4 electrolyte showed a strong dependence of the electrolyte strength in the effective dissolution valence number, use of $NH_4F.HF$ was abandoned. A type PN4100 Post Officer Plotter was used in our study. Some of the experimental details decribed in the following paragraphs are instrument specific.

The anodic dissolution behaviour of n-type Si in the NaF/H_2SO_4 electrolyte is complex and dependent on a number of factors such as the dilution factor x of the electrolyte with H_2O, illumination level IL, and anodic potential V_{master}. The dependence of the effective valence number N (the number of electronic charge required to remove one Si atom) on these factors is shown in Fig.2.17. At IL=8, N varies linearly with x over the range studied, whereas at IL=4, N drops well below 3.5 at low x and increases sharply at about x=1.3. It was observed that when N is much less than 3.5 the etch surface finish becomes badly pitted and covered with with brown deposit. Studies of the dissolution behaviour of Si in a HF-containing solution by Uhlir[109] and Turner[110] showed similar results in which reducing the anodic
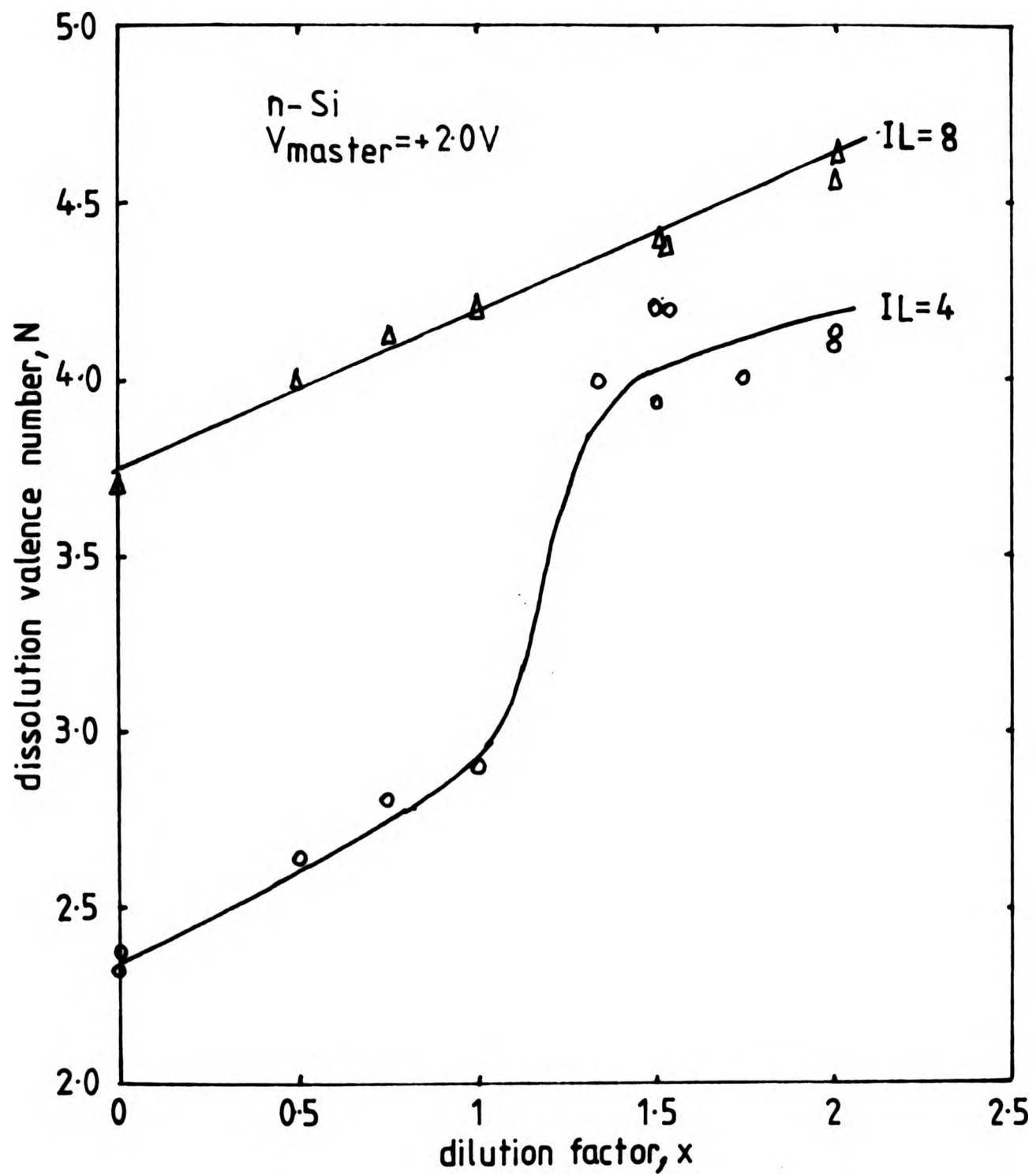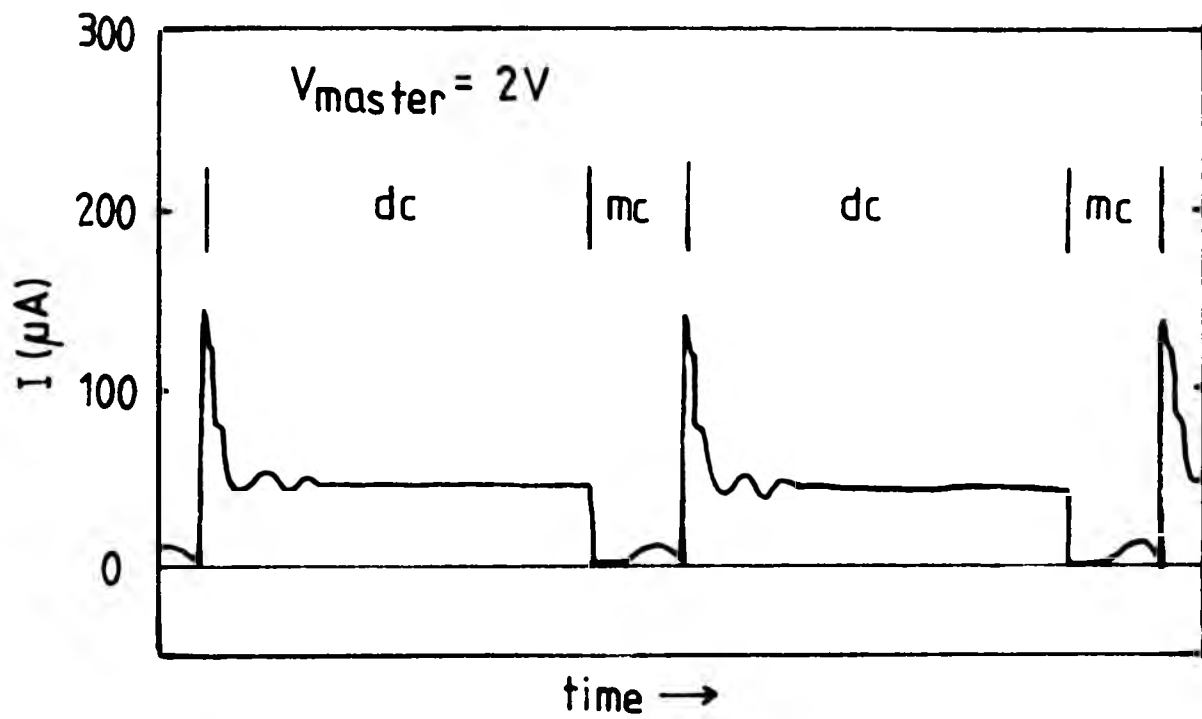
61

Fig.2.17 The dependence of the dissolution valence number N of n-Si in 1M NaF/ 0.05M H_2SO_4 electrolyte on the dilution factor x and illumination level IL under a dissolution voltage V_{master} of +2.0V.

mc = measure cycle
dc = dissolution cycle

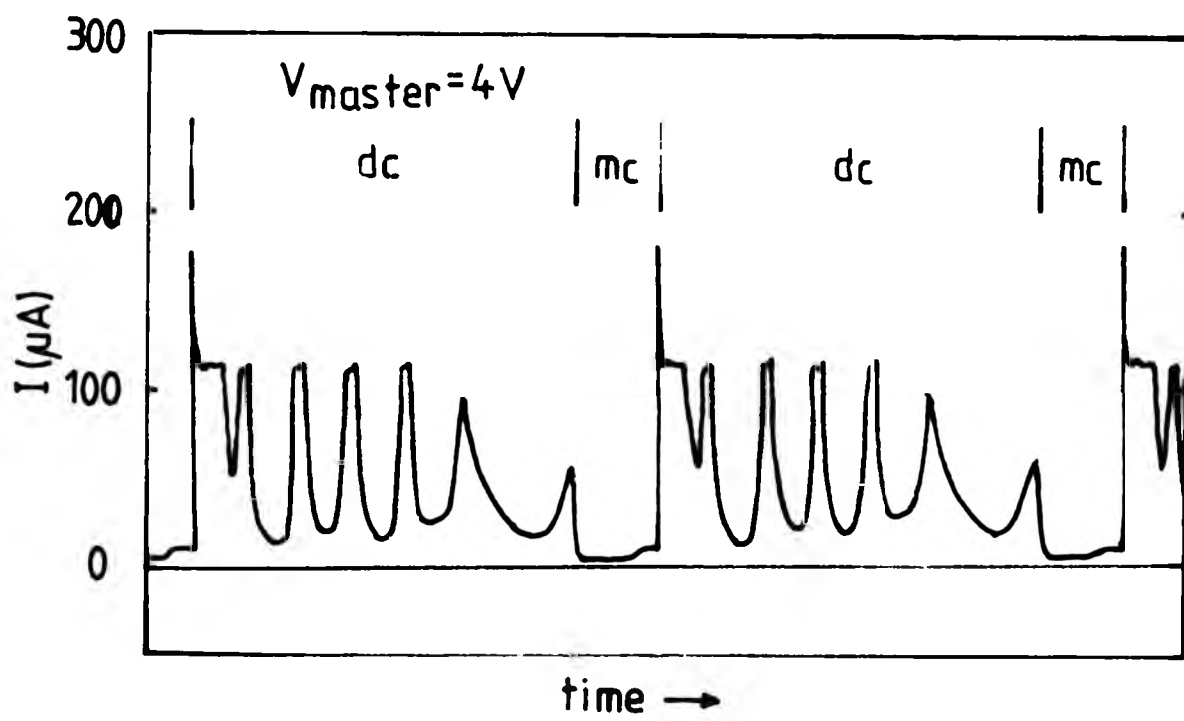Fig.2.18 The dissolution current I characteristic observed
in n-Si at V_{master} = 2.0 and 4.0V, and with the
illumination level setting at IL=8. Note the pronounced
oscillation in I when V_{master} is increased to 4.0V.

potential would reduce the effective value of N and was more likely to produce poorer etch surface finish. Increasing the anodic potential from 2V to 4V however produced no corresponding increase in N. There was a distinct oscillatory behaviour in the dissolution current when V_{master}=4V was used (see Fig.2.18). This could be a consequence of the rapid rate of oxide formation which exceeds the rate of oxide dissolution in the elctrolyte and prevents further oxidation temporarily. This effect did not appear to affect the etch surface finish but did affect the measurement of n severely. The surface uniformity generally improved with the increase in the dilution factor x. The accompanying profiling rate with the dilution factor x is as shown in Fig.2.19. Similar dissolution behaviour was also observed in p-type Si except that use of illumination during the dissolution did not affect the behaviour significantly.

During the anodic dissolution, hydrogen bubbles are evolved at the Si electrode which interfere with the desired uniform dissolution of material. It is essential that the bubbles are removed from the surface. A small pump which directs a pulse of electrolyte at regular intervals is implemented in the profile plotter for this purpose as described earlier. Experience showed that the positioning of the direction of the electrolyte jet had a marked effect on the resultant uniformity of the bottom of the etch pit and the proper removal of bubble from the surface. A slight undercutting around the edge of the etch pit as illustrated in Fig.2.20 was often observed with an accompanying degradation in depth resolution. This undercutting was possibly a consequence of the restricted flow of the electrolyte pulse at the dissolving surface due to the wall of the seal ring. When the pressure of the electrolyte jet was increased, the undercutting was considerably deepened and the central region was occasionally found to be stained. By means of a "not-too-elegant" trial-and-error method, the pressure and
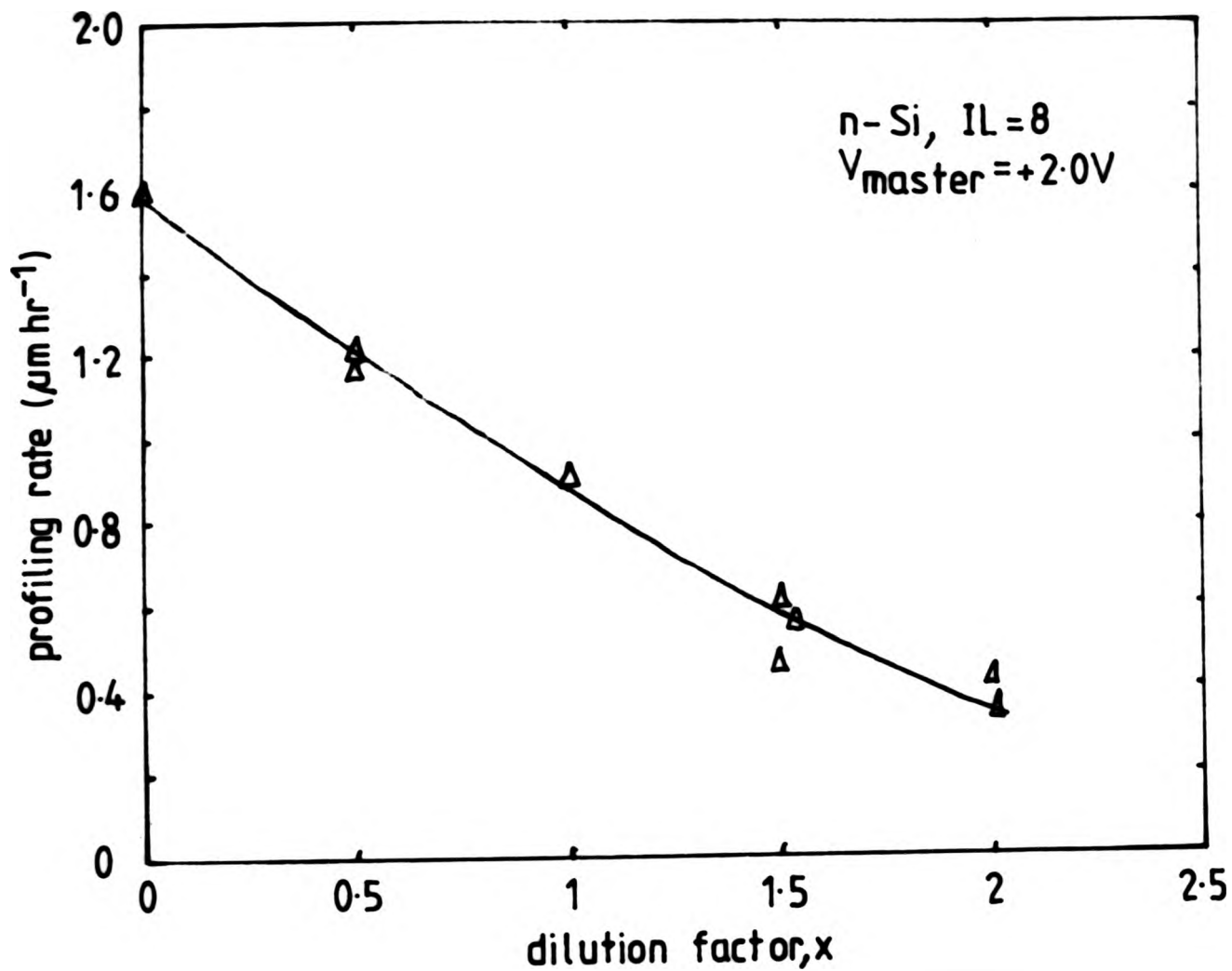
64

Fig.2.19 The variation in the profiling rate of n-Si obtained in 1M NaF/ 0.05M H_2SO_4 electrolyte with the dilution factor x using the normal dissolution conditions of IL=8 and V_{master}=+2.0V.
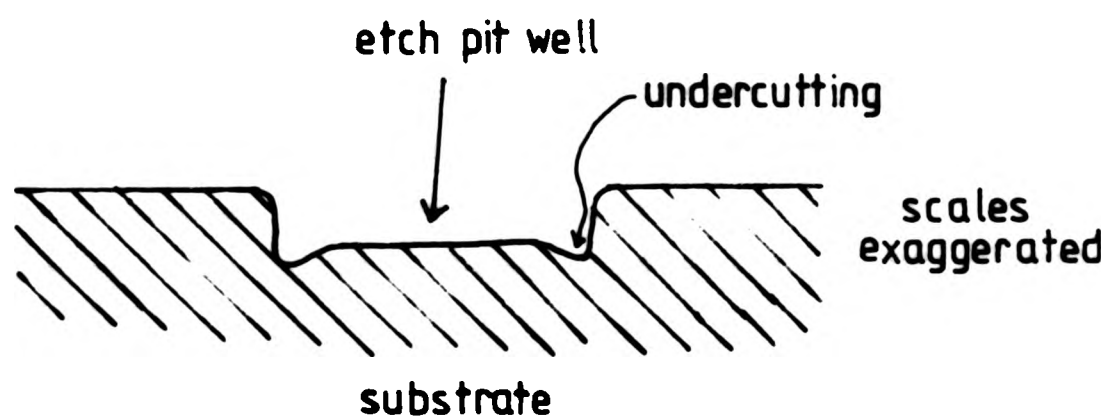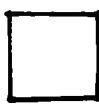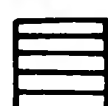

Fig.2.20 Undercutting at the edge of the etch pit as a result of improper positioning of the electrolyte jet and/or choice of jet pressure.

positioning of the electrolyte jet were adjusted until no bubble interference and stain formation was apparent on the etch pit.

Fig.2.21 is a chart showing the etch surface finish under different dissolution conditions of IL, V_{master} and electrolyte strength. For the range of dissolution conditions studied, the optimum surface finish was obtained under the dissolution conditions of IL=8 and V_{master}=2V. A high dilution factor was preferred for better uniformity in the etch well. We have obtained satisfactory results using the electrolyte with a dilution factor between 0 to 1. Most of our electrochemical CV profiles were obtained using the dissolution conditions of x=0.75, V_{master}=2V and IL=8 (IL=0 for p-type material) which gave a profiling rate of about 1 μm hr^{-1}.

It was found that there was some variability in N as previously reported by Sharpe et al[106]. This introduces a potential error in the measurement of W_R (and x) of about 5%. The factors influencing the observed variability in N were not certain. There was some indication that changes in the temperature of the electrolyte might be important. This variability can, to some extent, be overcome by collecting the data of n and x on a microcomputer for re-processing. The correction factor, obtained from measuring the depth of the etch pit with a Talystep and the calibration depth, is used to calculate the corrected depth. The final profile is then re-plotted using the corrected depth. Fig.2.22 is a block diagram of a microcomputer/interface system we used to accomplish this correction procedure in our profile plotter. Similar correction procedure to the depth measurement has also been described by Sharpe and Achar[111].

The accuracy of the carrier concentration and depletion width measurement depends on the Schottky barrier characteristic of the semiconductor and electrolyte interface. Typical examples of the CV, IV and GV
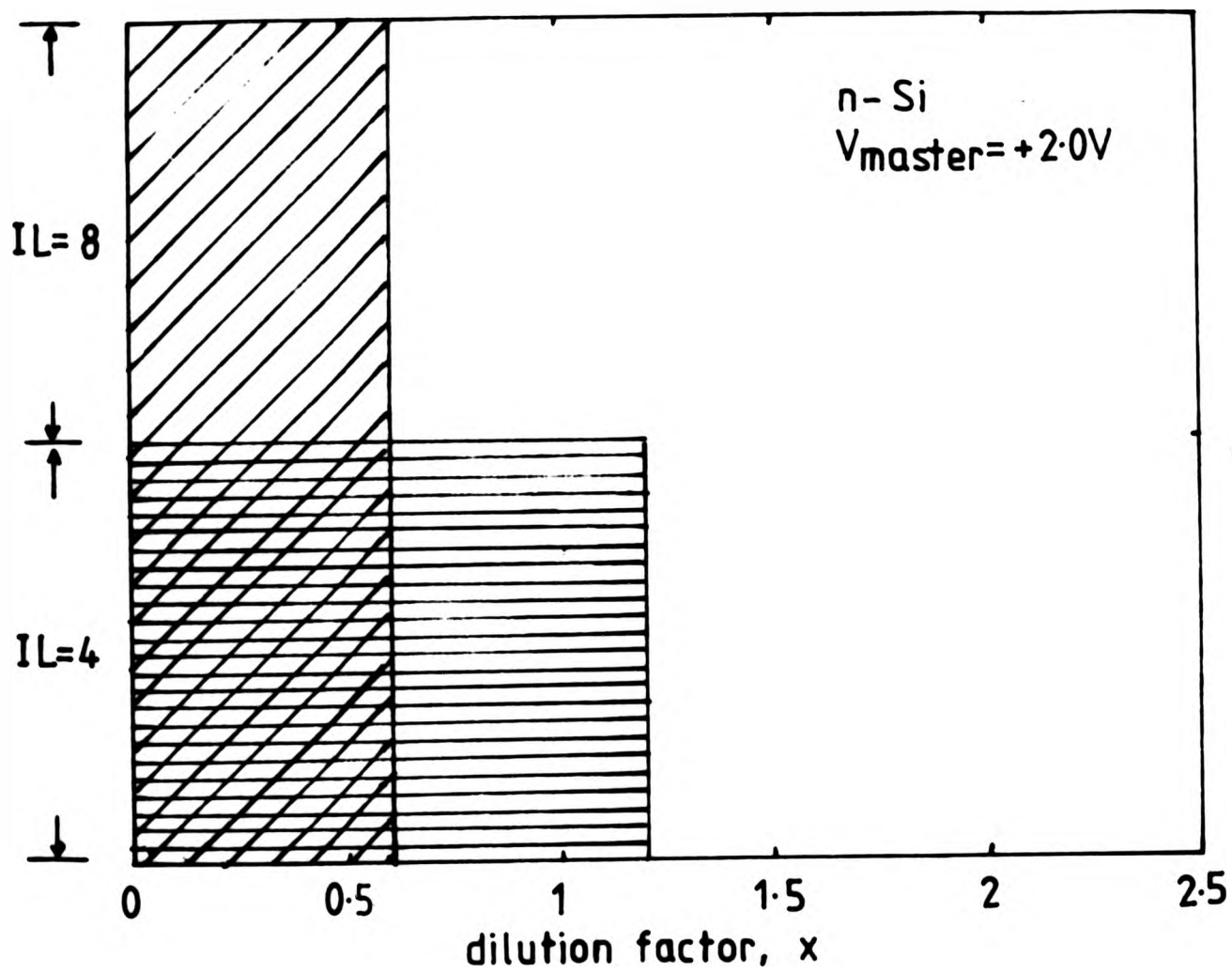
66

Fig.2.21 Description of the etch pit surface finish obtained under different dissoluting conditions.
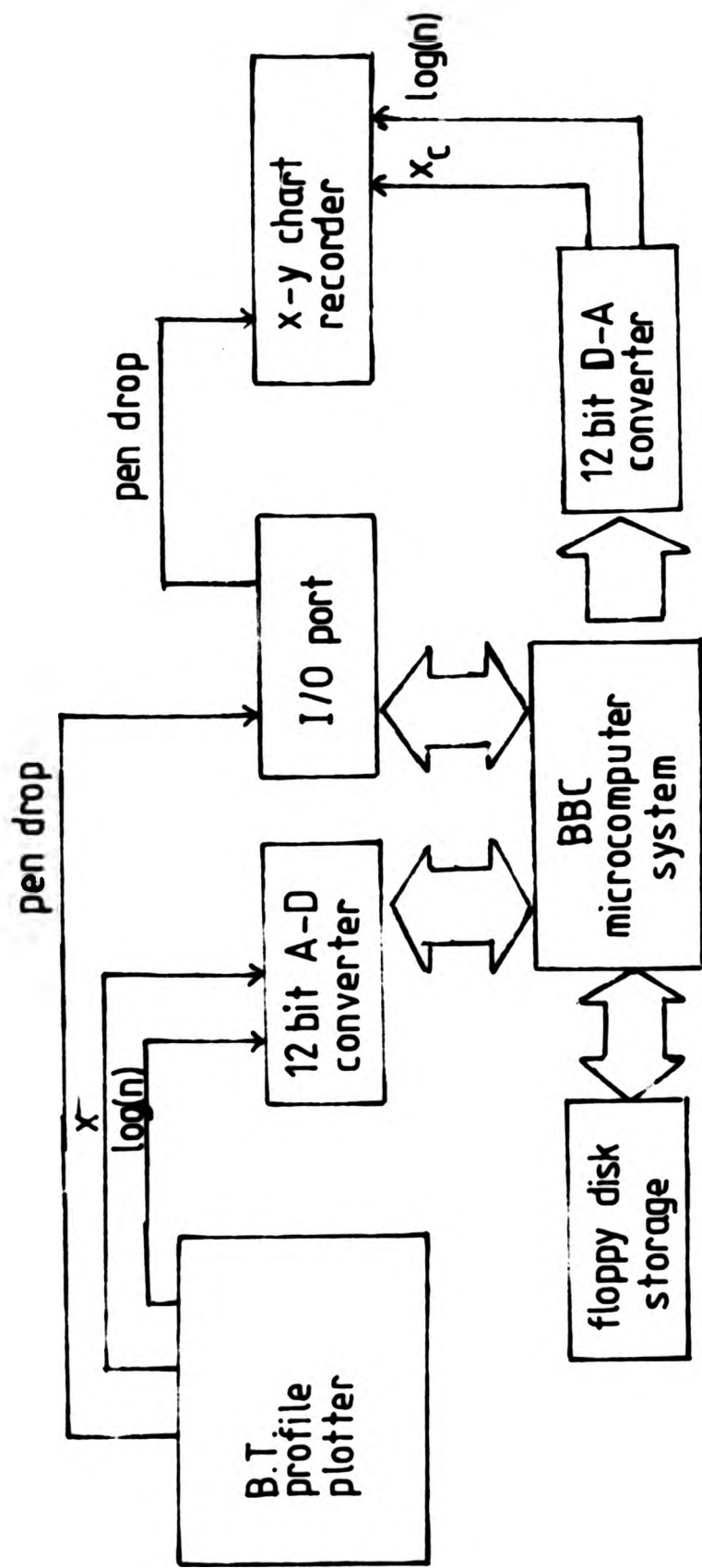
Fig.2.22 Block diagram of a microcomputer system used with the profile plotter for correcting the depth measurement.

characteristics of n-type Si (2.4 ohm cm, $n=2 \times 10^{15}$ cm^{-3}) in 1 M NaF/0.05M H_2SO_4 are shown in Fig.2.23(a). The plot of n vs $V_{measure}$ in Fig.2.23(b) shows that good agreement with the four point probe measurement of the same sample is obtained over the range of bias potential between 0 and 2V. Below 0V, a drop in the measurement of n is observed which also corresponds to a non-steady state in the GV curve. In order to obtain a reliable measurement of n, it is paramount that the bias potential lies in a region such that (a) the leakage current is low, (b) a low and steady G value occurs and (c) no anomaly in the CV characteristic. For low doped n-Si (n < $1 \times 10^{17} cm^{-3}$), a reverse bias potential between 0 and 1V has been found to give a reliable and consistent carrier concentration measurement. Generally speaking, using samples with no doped region above $5 \times 10^{17} cm^{-3}$ and a setting of $V_{measure}$ between 0 and 1V, attention required to monitor the profile measurement is minimal. When the dopant concentration exceeds $5 \times 10^{17} cm^{-3}$, however, the dark leakage current increases rapidly. High leakage current has been known to introduce erroreous measurement of n[112]. One example of this problem is depicted in the electrochemical CV profile of a "hi-lo-hi-lo" Sb-doped multilayer structure shown in Fig.2.24. At depth A, the dark leakage current increased suddenly as the dopant concentration approached 1×10^{18} cm^{-3} giving a measured carrier concentration lower than expected. At depth B, the bias potential was reduced and reliable measurement of n was retrieved. The electrochemical profile was found to be not affected by the dilution of the electrolyte. Fig.2.25 shows two electrochemical CV profiles of the same layer using the 1M NaF/0.05M H_2SO_4 electrolyte diluted at x=0.5 and 1 respectively. The two profiles are practically identical.

We have studied the doping profiles of our layers obtained by the spreading resistance and electrochemical CV measurements. Fig.2.26 is the Sb doping profile of a
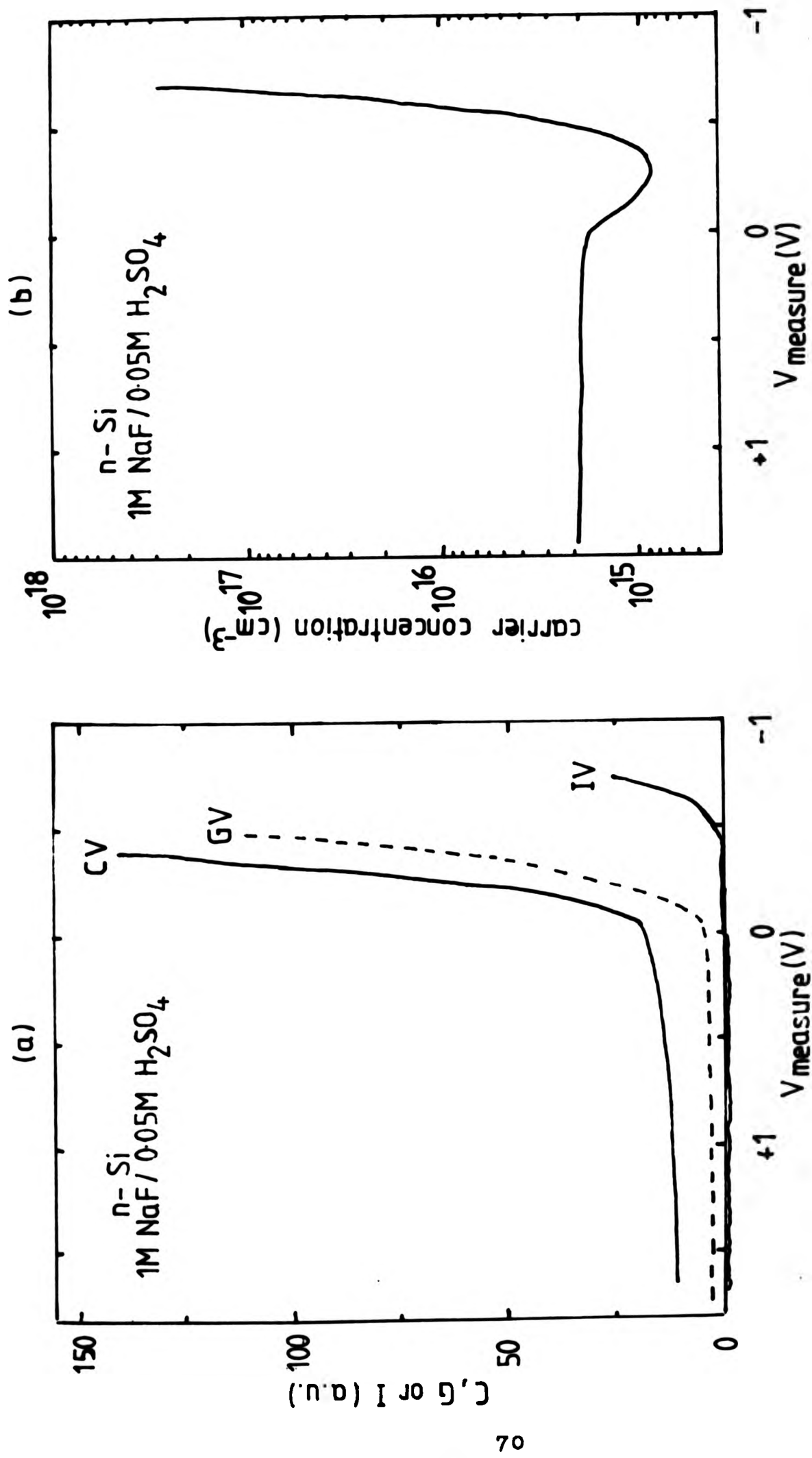
Fig.2.23 (a) The CV, GV and IV characteristic of the barrier interface of n-Si (2.4ohm cm) in an electrolyte of 1M NaF/ 0.05M H$_2$SO$_4$. and (b) its corresponding carrier concentration measurement.

70
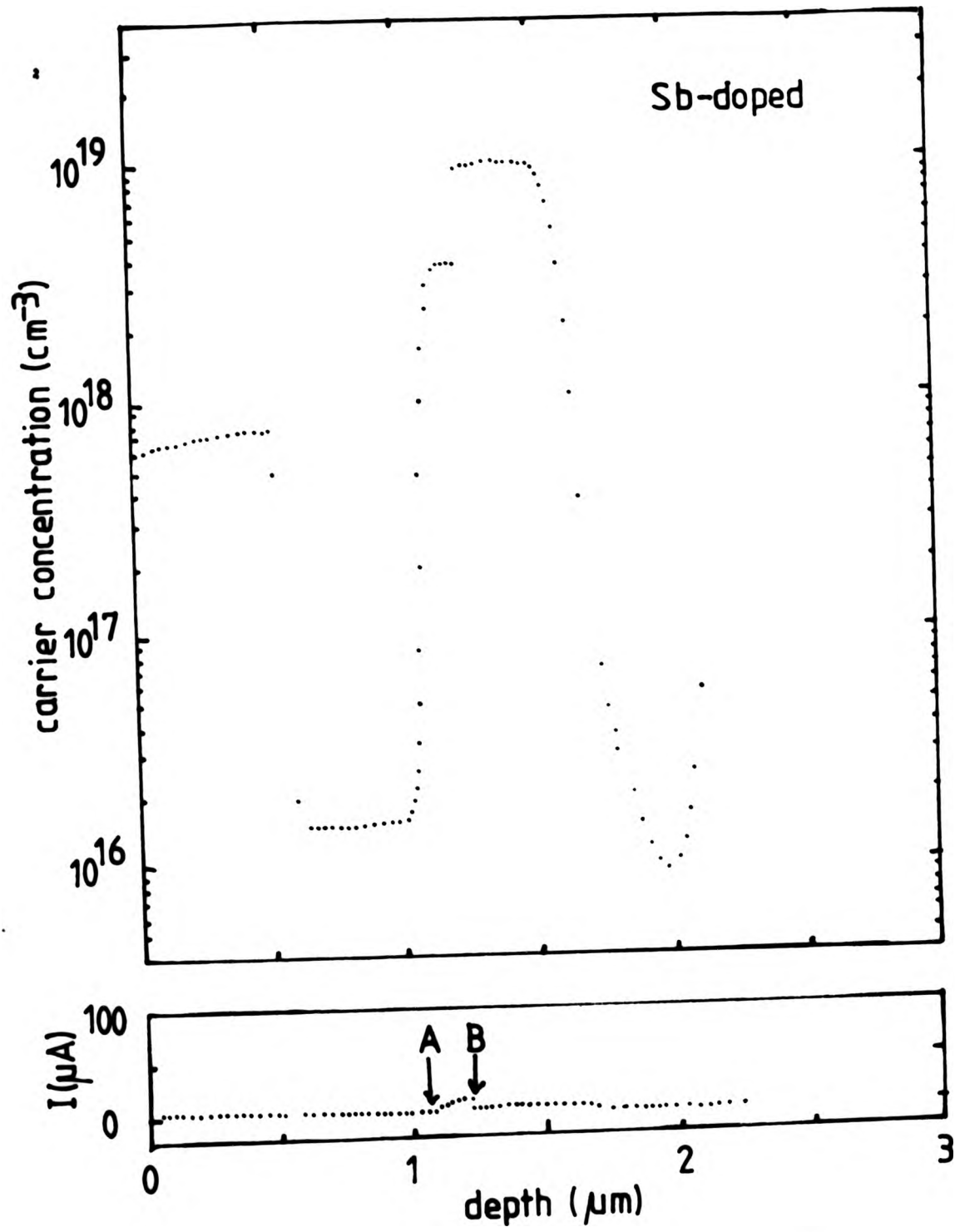
Fig.2.24 Effect of high dark leakage current on electrochemical CV measurement of highly doped Si-MBE materials.

71
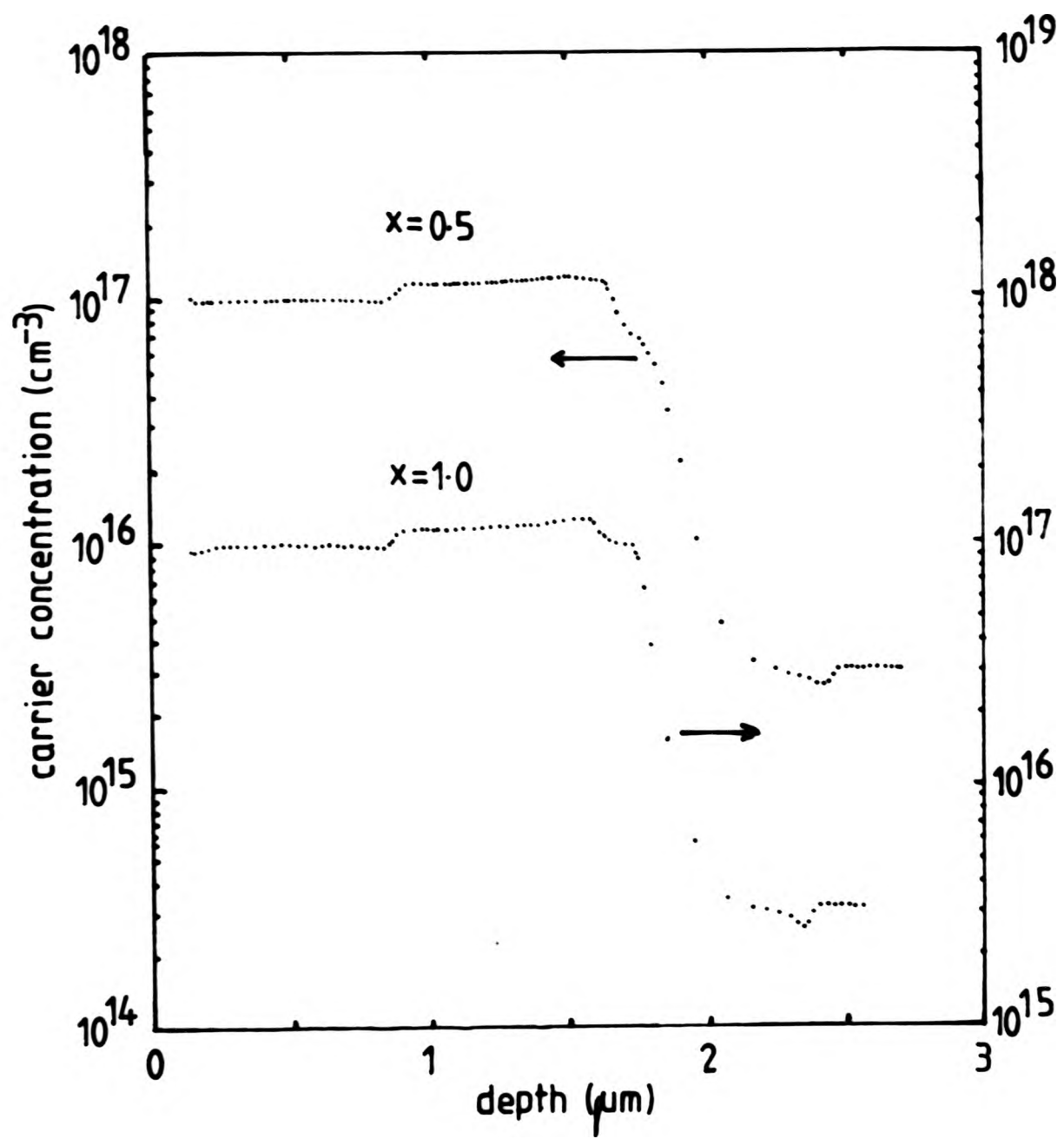
Fig.2.25 Electrochemical CV profiles of a Ga-doped layer obtained using the 1M NaF/0.05M H_2SO_4 electrolyte at two different dilution factors x.

typical layer used in the study. Both measurements indicated close agreement over the range of the dopant concentration levels in the layer. Fig.2.27 is a summary of the measurements on a number of similar samples. The data shows that the agreement of the two measurements was about 35% over the carrier concentration range of 10^{15}-5x 10^{18}cm^{-3}. For carrier concentrations above 5x 10^{18}cm^{-3}, the electrochemical CV measurement of n becomes less consistent. Similar results were also obtained with our boron-doped layers.

The capability of both techniques to measure very abrupt profiles is demonstrated in the measurement of a n-layer grown on a n^{++} substrate (Fig.2.28). The dopant concentration transition at the epitaxial substrate interface was estimated to be < 250 $\overset{\circ}{A}$/decade. Further examples of electrochemical CV profiles with equally abrupt transitions are included in Chapter 4.

Our studies show that, despite the problems associated with profiling Si, reliable and abrupt profiles can be obtained using the electrochemical CV technique. It offers a relatively inexpensive and rapid profiling tehcnique for Si with submicron structures.

2.2.5 Defect Assessment by Preferential Chemical Etch

We routinely used wet chemical preferential defect etch to reveal the crystallographic defects in our layers. This chemical etching method is simple and can provide useful information on the quality of the layers. It works on the principle that the chemical etch attacks the strained bonds of the defective regions of the crystal leaving behind etch features characteristic of the type of defects in the layer.

Over the past 30 years, a number of defect etches have been formulated. Table 2.1 is a list of defect etches commonly used for assessing Si materials. Most of the defect etches were originally developed for use with Si
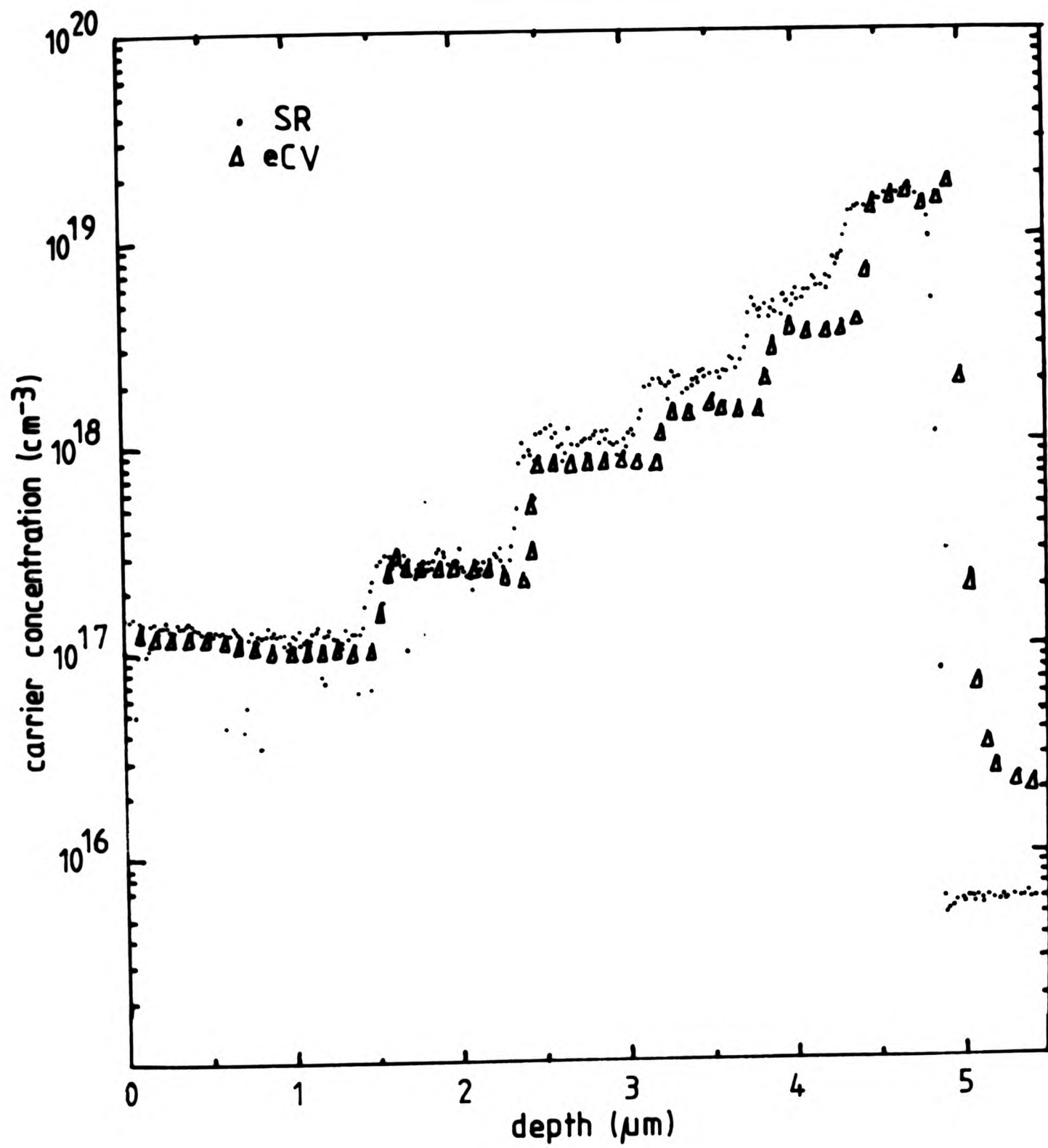
73

Fig.2.26 The spreading resistance (·) and electrochemical
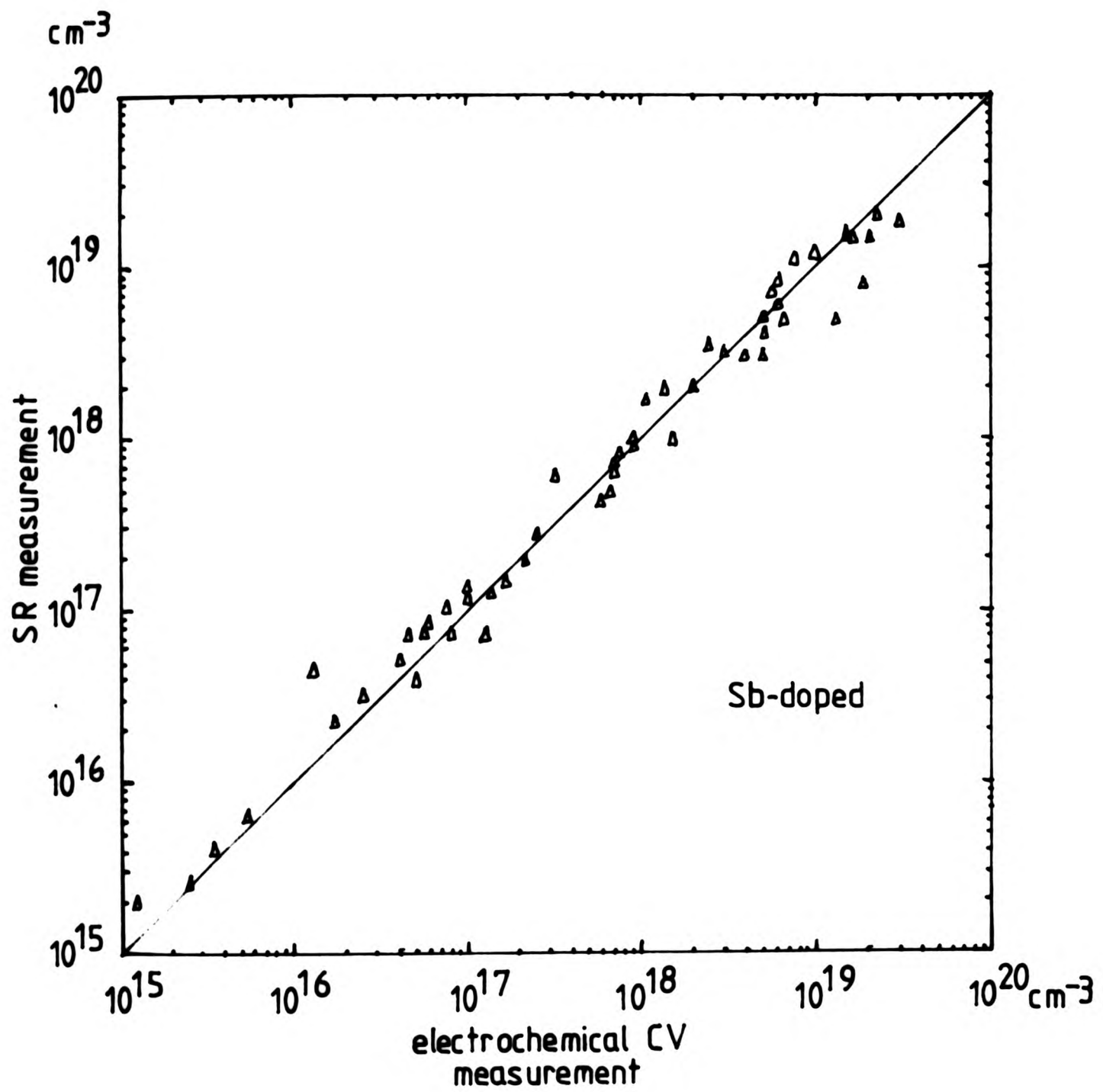CV (Δ) profiles of a stepped Sb-doped Si-MBE layer.

Fig.2.27 Comparison of the carrier concentration measurement of Sb-doped Si-MBE layers by the SR and electrochemical CV techniques.
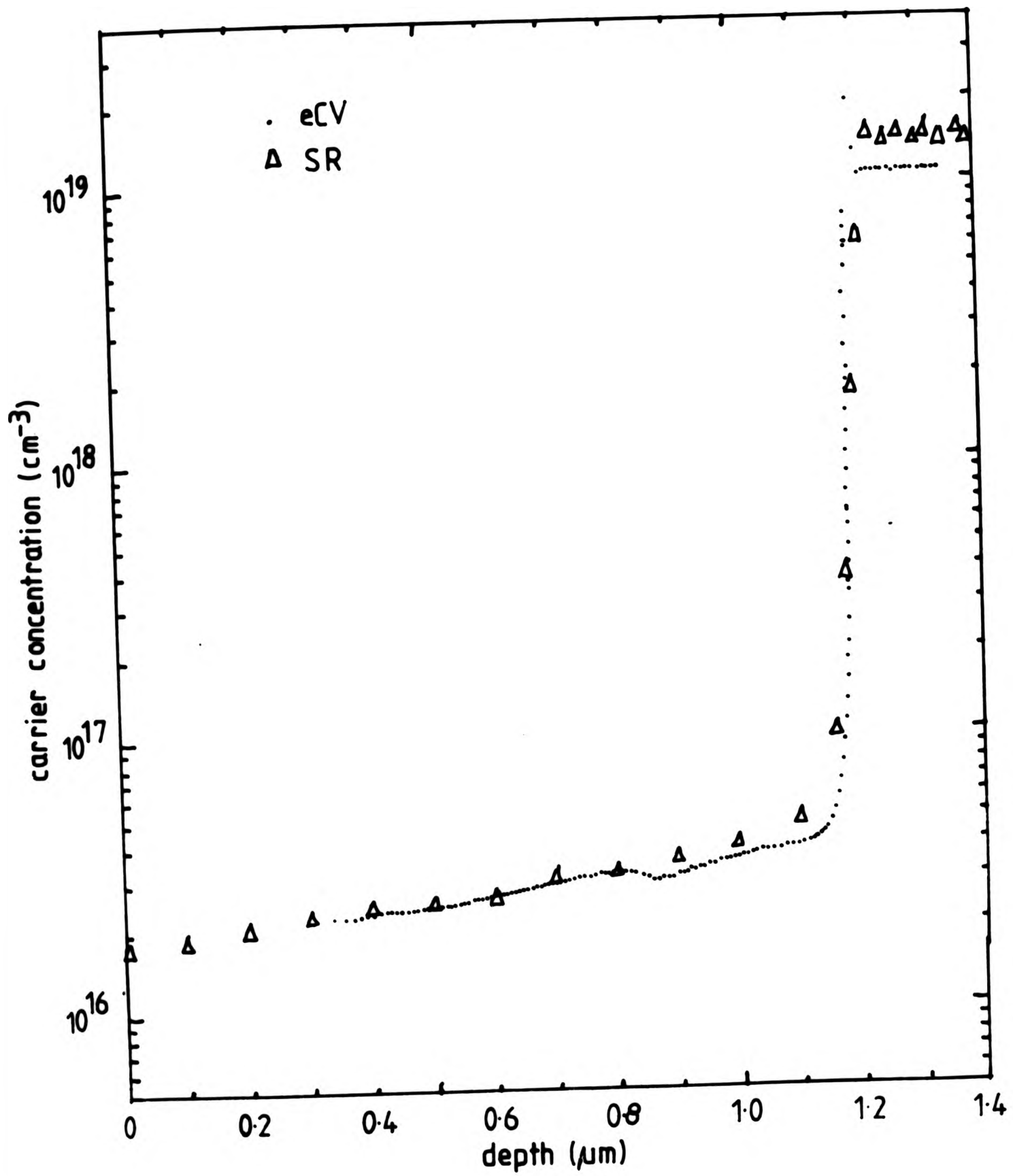
Fig.2.28 Comparison of the electrochemical 'CV and SR profiles of a Sb-doped Si-MBE layer grwon on a n[++] substrate (As-doped).

ingots where the period of etching and the amount of
material removed are not critical. Typically, when
assessing ingot materials, extended periods of etching (>>
5 minutes) are used such that large pits are developed for
accurate identification under a microscope. However, in
Si-MBE, where the layer thickness routinely grown is
between 0.5 μm and 3μm, extended periods of etching cannot
be used. Shorter etching times (< 2 mins) are generally
required to avoid complete removal of the epitaxial
material. The etch features are generally less
well-defined. This can lead to some difficulties in
identifying the defects. Studies by Ota[87] showed that
a number of precautions are necessary in order to obtain a
reliable assessment of defect content in thin epitaxial
layers. He found that the etching characteristic can be
influenced by the existence of a p-n junction in the sample
and by heavy doping (> $1x10^{17}cm^{-3}$).

The first four defect etches listed in Table 2.1
were used for defect assessment. Secco and Wright etches
were most frequently used as most of our layers were grown
on (100) substrates. In the case of heavily boron-doped
layers (> $4x10^{17}cm^{-3}$), dilute Schimmel etch was found
necessary to avoid the stain formation which interfered
with the defect assessment.

The etching procedure we found satisfactory is as
follows. The sample was first degreased in hot propan-2ol
and rinsed in DI H_2O. If the sample had been badly
contaminated, additional cleaning would be recommended.
This involved first scrubbing the sample surface with a
suitable detergent (e.g. Decon 90 and Triton), prior to the
degreasing step in propan-2ol. The sample was blown dry
with filtered N_2 and chemically cleaned in a self-heating
mixture of H_2SO_4 : H_2O_2 for 10 minutes. The sample
was rinsed thoroughly in DI H_2O after the chemical
treatment. The sample was then blown dry with filtered N_2
and placed in a Teflon beaker with the epitaxial surface
facing upwards. The defect etchant was poured in until the

Fig.2.29 Typical dislocation etch pits seen on a (100) Si-MBE layer after 2 min Secco etch.

(a)

Fig.2.30   A series of micrographs showing the etch features revealed in a 2.4μm (100) Si-MBE layer after (a) 30s, (b) 1min, and (c) 2 mins of Wright etch.

Fig.2.29 Typical dislocation etch pits seen on a (100) Si-MBE layer after 2 min Secco etch.

(a)

Fig.2.30 A series of micrographs showing the etch features revealed in a 2.4μm (100) Si-MBE layer after (a) 30s, (b) 1min, and (c) 2 mins of Wright etch.

(b)

(c)

Fig.2.30   A series of micrographs showing the etch features revealed in   a   2.4μm (100) Si-MBE layer after (a) 30s, (b) 1min, and (c) 2 mins of Wright etch.
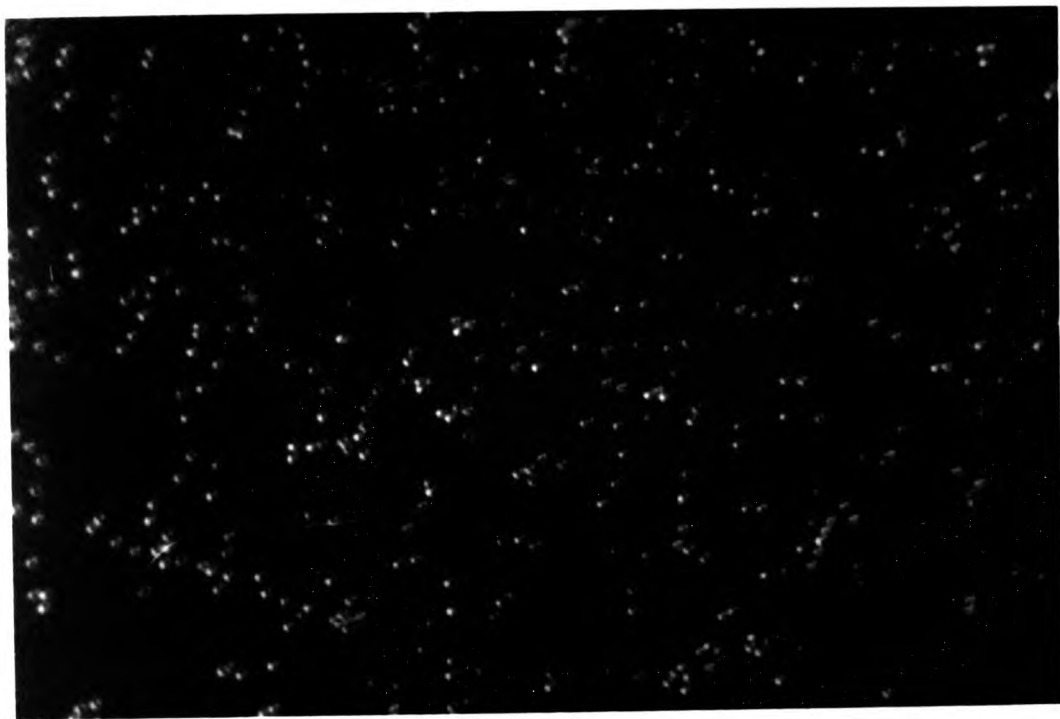
(b)

(c)

Fig.2.30 A series of micrographs showing the etch features
revealed in a 2.4μm (100) Si-MBE layer after (a) 30s, (b)
1min, and (c) 2 mins of Wright etch.
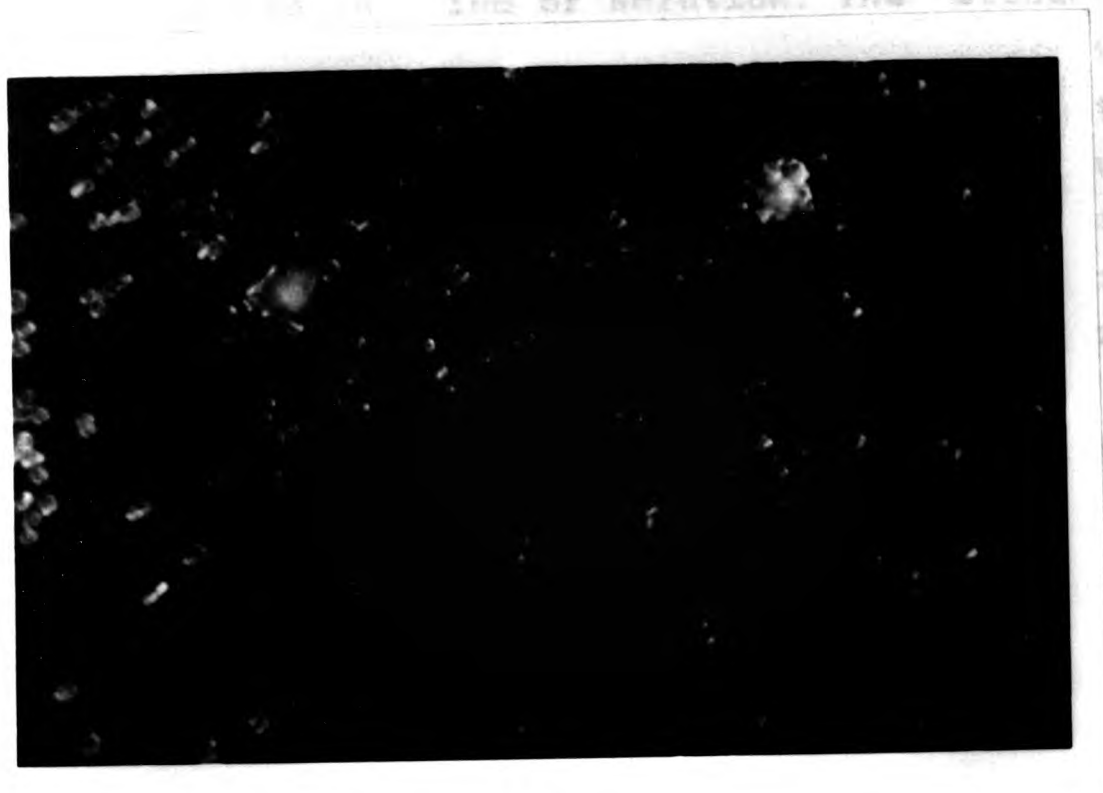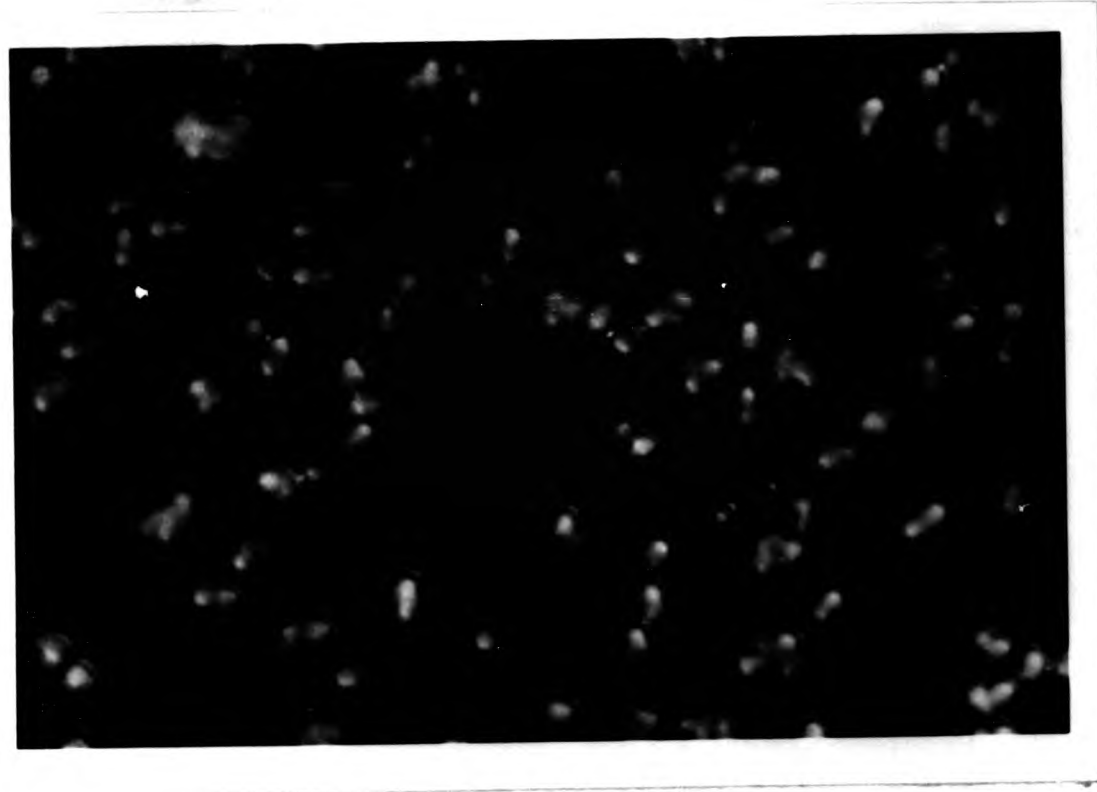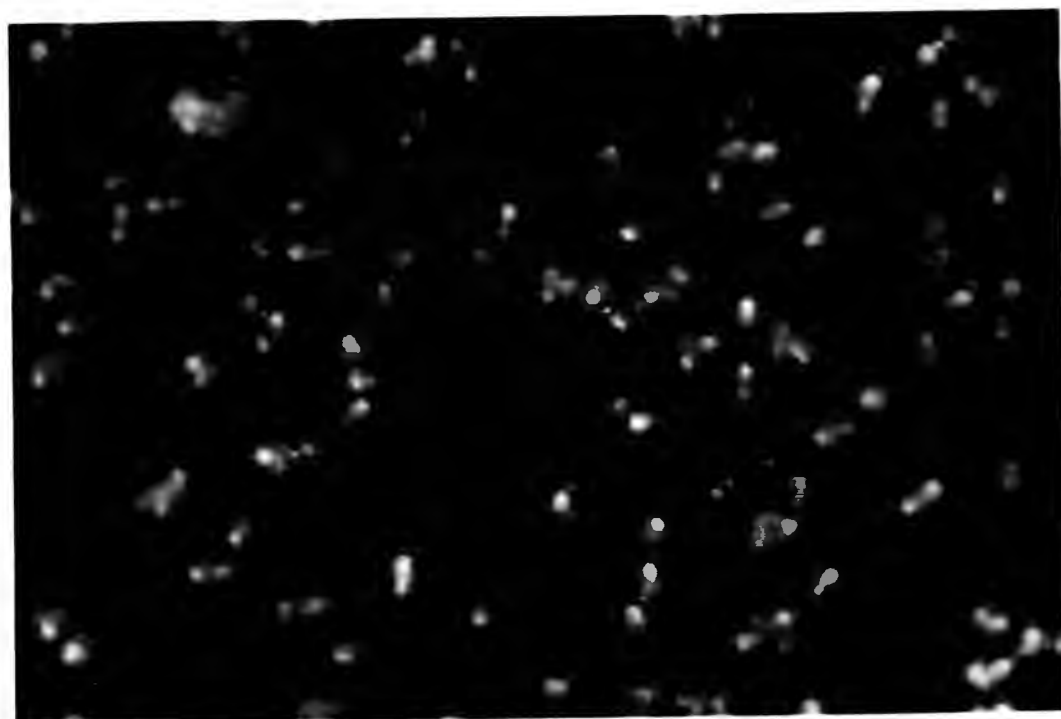
sample was submerged in ⁻ 1cm of solution. The etchant was manually agitated throughout the etching period. It was critical that the sample was never exposed to air at any stage during the etching to avoid sporadic etch features. Etching was stopped by flushing the etchant away with a large amount of DI H_2O. The etched sample was left in DI H_2O for about 20 minutes before drying in filtered N2 and examining under a Normarski microscope.

There are three major defects commonly observed in epitaxial Si, namely, (a) dislocations, (b) stacking faults, and (c) saucer pits (S-pits).

(a) Dislocations

After a defect etch, dislocations in the layer are revealed as round or elliptical etch pits on a (100) surface, and on a (111) surface, they have the appearance of triangular or shade shapes. Fig.2.29 is a micrograph showing dislocation etch pit features observed in a Si-MBE layer after a 2 min Secco etch.

We also found that in some layers the dislocation pits appeared in pairs. A microgragh of a layer after a 30s Wright etch showing the type of dislocations is given in Fig.2.30(a). Some of the features can be less than 1 um in size. Ota[9] has described them as dislocation loops generated at two microdefects. Dislocations generated as a result of plastic deformation of the substrate produced by thermal stresses are revealed as rows of etch pits along the slip lines. A micrograph of a 1 min Secco etched sample of a substrate which was heat-treated at ⁻950°C is shown in Fig.2.31. Dislocation etch pits along the slip lines are clearly visible in the micrograph.

The effect of increasing etch period on the appearance of the etch pits is significant. Fig.2.30(a),(b) and (c) are a series of micrographs showing the etched surfaces of the same layer after 30s, 1min and 2mins of Secco etch. In Fig.2.30(a) and (b), the dislocation pits are well-defined and separate, and the pairing feature can be easily recognized. In Fig.2.30(c), the etching has

Fig.2.31 Dislocations revealed by a 1min Secco etch along the slip lines generated in the Si substrate which had been heated above ~900°C.

Fig.2.32 Typical micrograph of a (100) Si-MBE layer after 30s Secco etch showing a uniform distribution of stacking faults.

Fig.2.31 Dislocations revealed by a 1min Secco etch along the slip lines generated in the Si substrate which had been heated above ~900°C.

Fig.2.32 Typical micrograph of a (100) Si-MBE layer after 30s Secco etch showing a uniform distribution of stacking faults.

enlarged the pits to the extent that each pair of pits becomes one elongated pit. The difference in the dislocation density amongst the micrographs is due the fact that they represented a variation in the dislocation density across the layer.

(b) Stacking Faults

Stacking faults (SF's) are generally visible on the as-grown epitaxial surface. When defect etched, they appear as either single lines or partial/ complete polygons. On (100) surfaces, the polygons are square and on (111) surface, they appear as equilateral triangles. Fig.2.32 is a typical micrograph of a (100) Si-MBE layer after a 30s Secco etch. Since the size of a SF is directly proportional to the depth of the nucleation point below the epitaxial surface, this offers a simple method of determining the thickness of the layer when the SF is nucleated at the substrate surface. The linear dimension L of the SF is related to the thickness t of the layer by the expression t = 0.707L or 0.816L for (100) and (111) surfaces respectively. In some layers, the SF's are not uniform in size indicating that they were generated during various stages of growth. For the purpose of defect density assessment, each partial or complete polygonal feature is defined as one stacking fault[92].

(c) Saucer pits (S-pits)

These are shallow etch features which are not related to the dislocation pits. They can be distinguished from the dislocation pits by their shallow and rounded bottom depressions. Fig.2.33 is a micrograph of a 7μm thick CVD epitaxial layer after a 30s Secco etch. Two types of S-pits have been classified according to their size[118]. The larger pits are known as the A-clusters and the smaller pits as the B-clusters.

S-pits have been found to be associated with the grown-in microdefects in the substrate (generally referred to as the "swirl defects"). For example, the "swirl" pattern has been observed to follow the dopant impurity

82

Fig.2.33 Saucer pits (S-pits) revealed in a 9μm thick (100) Si-CVD layer after 2 min Secco etch. Note that dislocation pits (D) are also revealed in the layer.

Fig.2.34 Replica TEM micrograph of the same etched sample shown in Fig.2.32 where corresponding features of stacking faults and dislocation pits can been identified between the two micrographs.

83
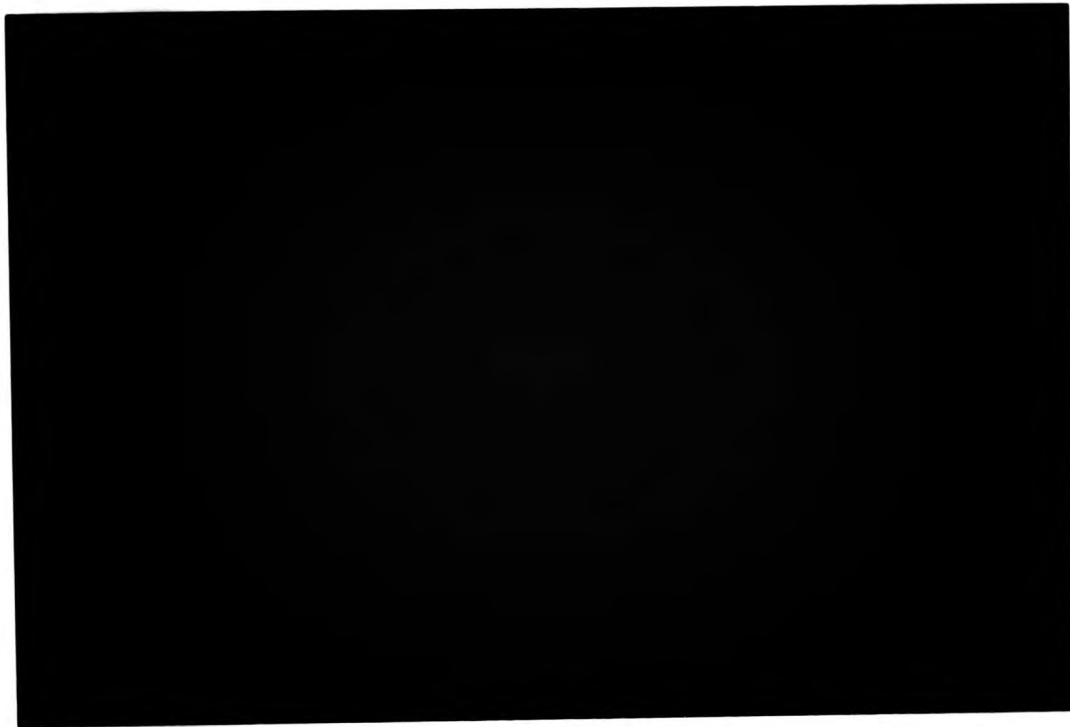
Fig.2.33 Saucer pits (S-pits) revealed in a 9µm thick (100) Si-CVD layer after 2 min Secco etch. Note that dislocation pits (D) are also revealed in the layer.

Fig.2.34 Replica TEM micrograph of the same etched sample shown in Fig.2.32 where corresponding features of stacking faults and dislocation pits can been identified between the two micrographs.

83

striation in the grown ingot. Correlation between metallic contamination such Fe, Cr and Cu and S-pits in epitaxial layers has been reported[119,120].

We have also examined some of the etch features using replica TEM. Fig.2.34 shows a TEM micrograph of a carbon replica of a 30s Wright etched sample as compared to its optical (Normarski) micrograph. Stacking faults can be easily identified in both micrographs, whereas the dislocation etch pits observed in the optical micrograph appear in the replica TEM micrograph as depressions each with a tail pointing in a crystallographically related direction. This observation supports our assessment that the etch pits seen under the Normarski microscope are associated with crystallographic defects.

Choice of etching times is important since it can affect the detailed appearance of the etch features. The micrographs shown in Figs.2.30 of a sample etched for different periods illustrate this effect. Though extended etching time gives deeper and larger etch pits, , it also degrades the amount of detailed etch features. For assessing stacking faults, a short etching time of ¯30s is adequate to produce well-defined features for accurate identification. In the case of dislocations, it is more difficult to be precise on the etching time. For layers thicker than $2\mu m$, a choice of 1 min is a good compromise which give reasonably deep dislocation pits aiding defect identification and yet retaining the detailed features. Generally, we found it helpful to monitor changes in the defect features with etching for periods of 30s , 1 min and 2 mins.

When practiced with care, preferential chemical etching provided us with a useful in-house method of assessing the crystallographic quality of our layers.

2.2.6 Thickness Measurement

The thickness of layers grown was routinely determined by means of a Talystep equipment (Rank Taylor Hobson Ltd., Leicester). The Talystep measures the thickness by transversing a stylus across a step produced by masking the deposition from part of the substrate. The vertical movement of the stylus is detected by a transducer and amplified electronically. The step height is then recorded as the difference between the surface levels of the layer and substrate. The step necessary for the thickness measurement was conveniently obtained in our layers where the substrate holder masked the substrate from deposition at the edges. Though the specified accuracy of the Talystep equipment was better than 2%, a poor step formation would prevent this accuracy to be achieved.

2.2.7 Secondary Ion Mass Spectrometry (SIMS)

In this technique, a primary beam of energetic Ar, O or Cs ions is used to bombard the surface of the sample such that the surface matrix is sputtered off as neutral and charged species (viz secondary ions). These secondary ions are energy-filtered and mass-analyzed by a quadropole mass spectrometer located close to the sample. The ions are detected by an electron multiplier and counted. In the SIMS profiling technique, a primary beam at an energy between 1-10 keV is used such that the significant rate of material removal is achieved. The secondary ions of the required element are monitored as a function of sputter time and by measuring the depth of the crater, a chemical concentration profile with depth can be obtained.

The SIMS equipment itself is highly complex. Details of the design and performance of modern SIMS instrumentation have been reviewed by Wittmaack in a recent review[121]. Our in-house SIMS facility (EVA 2000) was designed and built at CLP. Vast experience in profiling Si materials has been acquired by the SIMS group. In the SIMS

analysis of Si-MBE layers, a primary O^+ beam was used, the energy of the beam was carefully selected so as to minimize matrix mixing effects and maximize depth resolution consistent with the profiling requirements.

2.2.8 Auger Electron Spectroscopy (AES)

Auger electron spectroscopy[122] is a nominally non-destructive method for surface chemical analysis. The basis of AES is as follows. A primary electron beam with an energy between 1 -10keV is used to excite the surface atoms of the sample. The excited atom can return to its stable state via a number of processes which may involve emission of X-ray, UV radiation and secondary electrons. In the Auger process, secondary electrons are ejected with well-defined energies characteristic of the energy levels of the surface atoms. By measuring the energy spectrum $N(E)$ of the ejected Auger electrons, one can thus identify the surface atoms. Auger electrons are generally referred by the electron shells involved in the excited atom. For example, a $KL_1L_{2,3}$ Auger electron is one emitted from the $L_{2,3}$ shell when an electron from the L_1 shell falls into the vacancy created in the K shell by the primary electron beam.

In our Auger analysis, the sample was placed at about 5-10 mm from the Auger electron spectrometer (CMA Model 342/116, VG Scientific Ltd.,UK). A 3keV primary electron beam at $100\mu A$ (measured with the sample at +30V) was used. The primary beam was modulated at 20kHz witha modulation voltage of 4Vpp. The emitted Auger electrons were energy-filtered using a cylindrical mirror analyzer. The energy spectrum of the Auger electrons was measured at and presented in the form of its energy differential dN/dE vs E. Typically, the signal-to-noise ratio obtained at the 78 eV peak in the Auger spectrum of a clean Si surface was about 250-300.

86

Etchant	Formula	Epitaxy
Secco(114)	1 0.15M CrO_3: 2HF	<100>
Wright(113)	60ml HF 30ml HNO_3 30ml 5M CrO_3 2g $Cu(NO_3)_2 \cdot 3H_2O$ 60ml Acetic acid 60ml H_2O	<100> <111>
Schimmel(115)	1 0.75M CrO_3: 2HF	
dilute Schimmel(116)	1 0.75M CrO_3: 2HF: $1.5H_2O$	<100> <111>
Dash(117)	1 HF(48%): $3HNO_3$: 10 Acetic acid	<100> <111>
Stirl(155)	1 5M CrO_3: 1HF(48%)	<111>

Table 2.1 A list of commonly used preferential etchants used for assessing crystallographic defects in Si.

87

Chapter 3: Growth and Properties of Undoped Layers

3.1 Substrate Preparation

3.1.1 Ex-situ chemical cleaning

Our ex-situ chemical treatment of substrates is similar to that described by Ishizaka et al[36], and is commonly known as the "Shiraki" chemical treatment. The advantage of this method is twofold; it is a very effective means of preparing surfaces with low levels of C contaimination and relatively low in-situ heat treatment $(700 - 800^{\circ}C)$ is required to remove the protective oxide. The treatment procedure is as follows:

a) degrease: DI H_2O rinse (18Mohm ,0.2μm filtered)
             10 mins in boiling Propan-2ol
             DI H_2O water rinse

b) HNO_3 boil/oxide strip: 10 mins boil in $1HNO_3:1H_2O$
             DI H_2O rinse
             remove oxide in 2.5% HF
             DI H_2O rinse

c) repeat b) three times

d) HCl boil: 10 mins boil in $3HCl:1H_2O_2:1H_2O$
             DI H_2O rinse

e) drying: blow dry with filtered N_2 or spin dry

The chemical treatment was carried out in a Class 100 air flow in a clean air workstation. Pyrex glassware was used in our early experiments, but was later replaced with quartzware. PTFE and polypropylene containers were used for HF and DI H_2O. After the chemical treatment, some of the substrates were examined under a Normarski

microscope. The treated surfaces were optically smooth with only occasional small increase in particle count (<200 cm^{-2}) as compared to the as-received substrates.

The surface conditions of the chemically treated and untreated substrates were further examined by using Auger electron spectroscopy (AES) after loading into the MBE system. The pump-down cycle typically took less than 15 minutes to reach below $1x10^{-8}$ mBar. Typical AES spectrum of as-received and Shiraki chemical treated surfaces are illustrated in Fig.3.1. A small C peak at 270 eV was always observed on as-received substrates. The size of this peak and thus the surface coverage varied from batch to batch. The C peak on a Shiraki treated surface was generally smaller and often below the detection limit of our Auger equipment. Another small peak at 180eV was observed only on Shiraki treated surfaces. According to Handbook of AES there are two possible elements attributable to this peak, namely, B and Cl. Henderson[6] attributed a similar peak in his chemically treated surfaces to B rather than Cl because of the absence of the KLL Cl peak expected at 2200 -2400 eV region in the Auger spectrum. He suspected that the B contamination came from the pyrex glassware used in the chemical treatment. We also failed to detect the KLL Cl peak in the Auger spectrum of our chemically treated surface, though it is probable that a KLL Cl peak would have been below the detection limit of our AES equipment.

Despite the absence of the KLL Cl peak, there are a number of indications that this peak was due to surface coverage of Cl. Firstly this peak could be reduced by employing extended period of DI H_2O rinse after the chemical treatment or by using a reduced proportion of HCl in the final peroxide solution. Secondly this peak was readily removed by heat treatment of the surface at as low as $550^{\circ}C$. Similar results were reported by Ishizaka et al[36], who also considered the peak arose from Cl contamination. Thirdly, use of quartzware in the chemical treatment has not affected the appearance of the Cl peak.
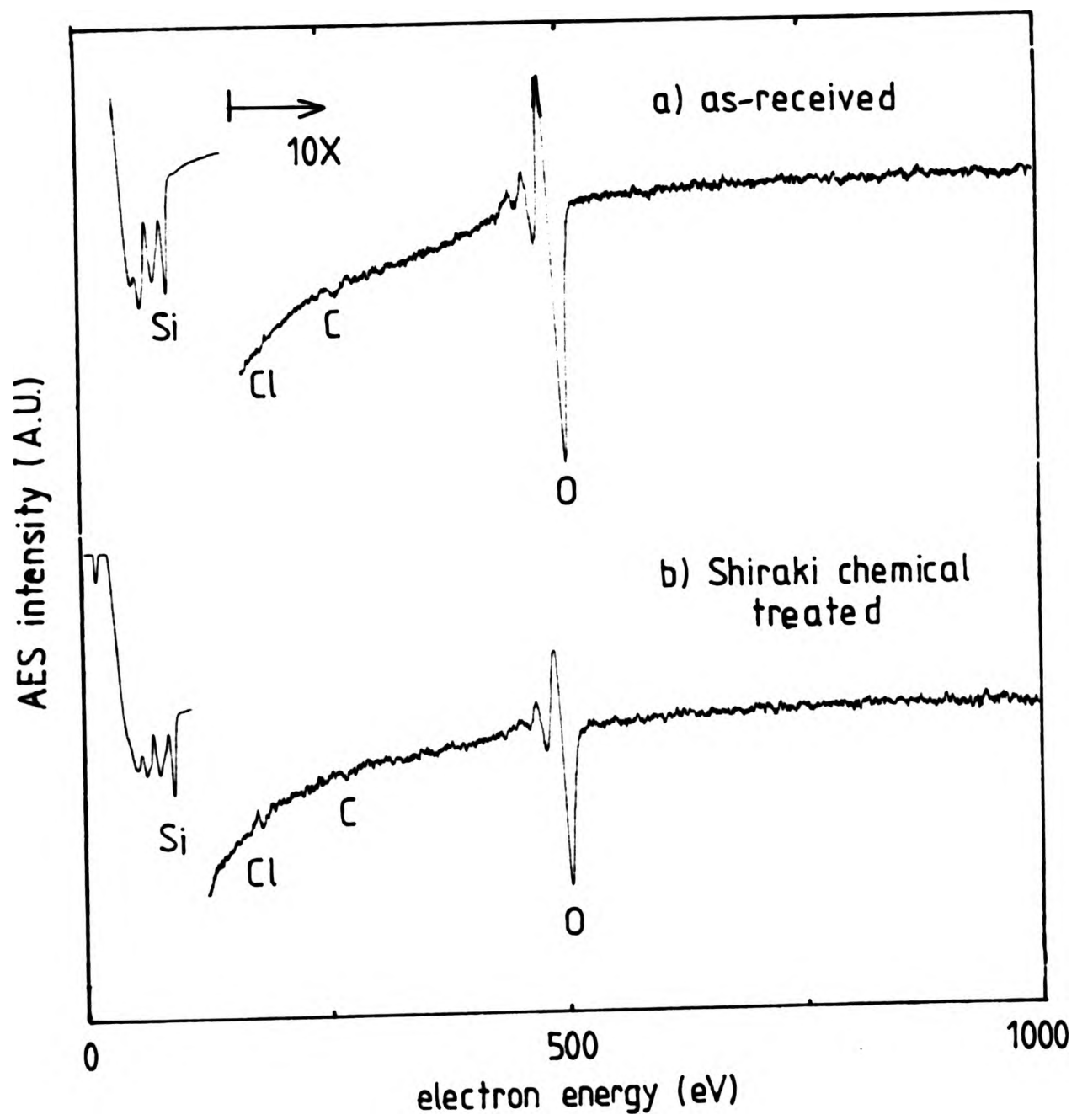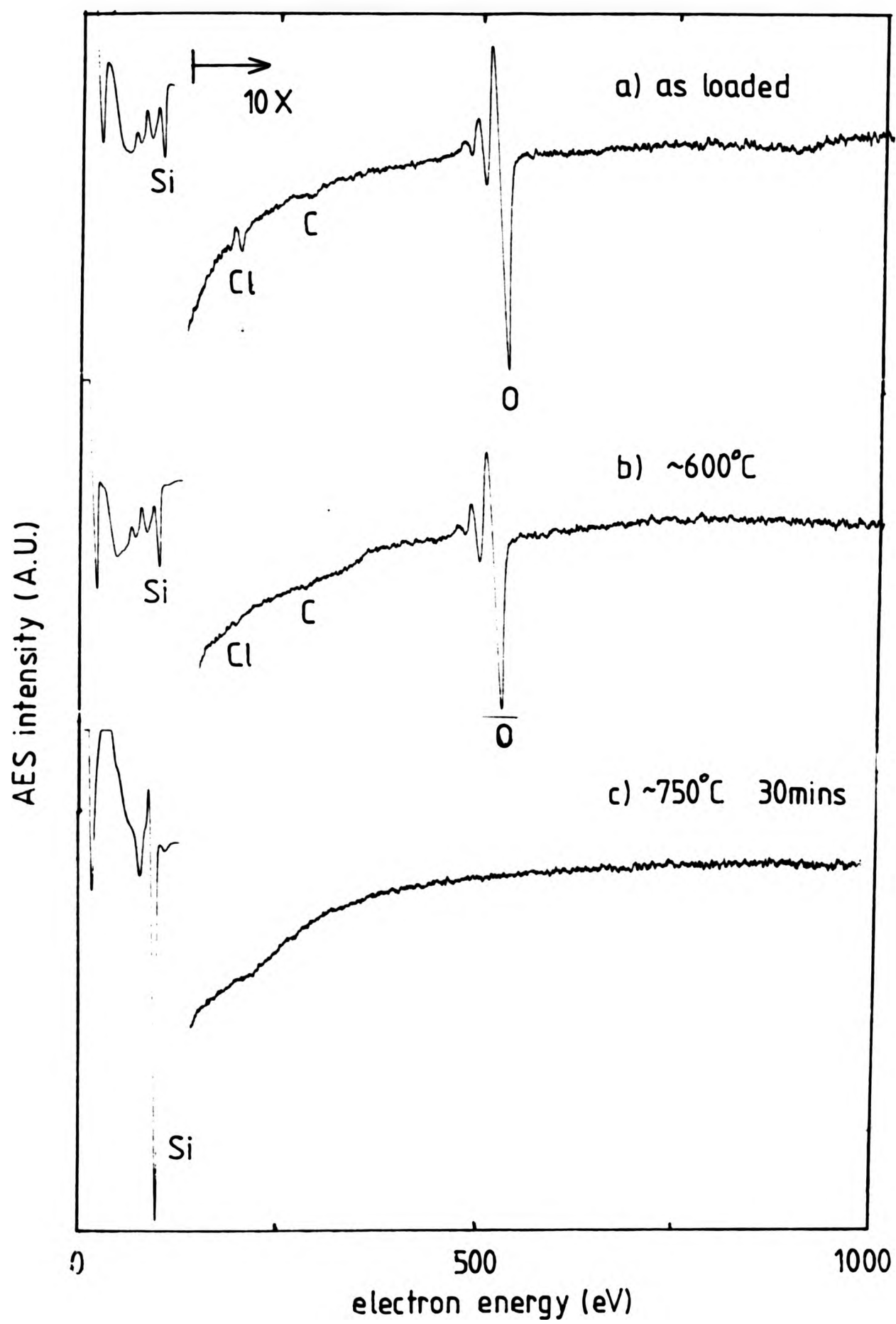
89

Fig.3.1 The surface conditions of (a) as-received and (b) Shiraki-chemical treated Si substrates as monitored by Auger electron surface analysis.

Fig.3.2 Removal of C and O from the surface of a Shiraki chemical treated Si substrate by heat treatment at different temperatures in UHV.

91

The Auger features around 510eV are attributed to O atoms indicating an oxide coverage on both types of surfaces. The peaks at 78 and 92 eV are attributed to Si bonded to O and elemental Si respectively[123]. The reduction of the Si=O peak at 78eV together with a strong Si peak as compared to as-received surface indicates a thinner oxide coverage.

When the Shiraki-treated surface was heat treated at ~600°C briefly, only the Cl peak was observed to disappear from the Auger spectrum (Fig.3.2(b)), and all other major peaks remained unaffected. When the temperature was raised to 750°C for 30 minutes, the O peak disappeared below the detection limit. The elemental Si peak increased dramatically and simultaneously with the disappearance of the Si=O peak. The C peak, when present initially, was unaffected by the heat treatment but on heating the surface further to above 850°C, the C peak was reduced to below detection limit (Fig.3.2(c)). The total surface C and O contamination after the heat treatment at 850°C for 30 minutes was probably less than 0.1% of a monolayer[123]. Our observations confirm the results reported by Ishizaka et al[36].

The C peak was found to increase gradually when exposing both types of surfaces to electron beam irradiation in UHV at room tempeature. We also also observed that both C and O peaks on a freshly grown epitaxial layer gradually increased with exposure under UHV at room temperature even in the absence of direct electron beam irradiation. To study this increase of surface contamination of C and O on clean Si surface, epitaxial layers were grown and their surfaces monitored using AES following exposure to the UHV environment (10^{-9}-10^{-10}mBar) at room temperature. Care was taken to ensure a new area of the epitaxial layer was examined each time and the duration of electron beam irradiation was minimized for each analysis. A plot of the C and O coverage with exposure time is given in Fig.3.3. It can be seen that the

C and O contamination on the surface increased rapidly for the few hours after growth and subsequently levelled off. No significant increase was detected even after 80 hours of further exposure.

Henderson[31] found that a clean Si surface generated by heat treatment at $1200^{\circ}C$ after exposure to a vacuum of $<5 \times 10^{-10}$ Torr for 7×10^7 sec at room temperature produced SiC on the surface when re-heated to $800^{\circ}C$. He concluded that adsorbed hydrocarbon species on the surface led to the carbide formation. The chemical composition of the gaseous adsorbate was not, however, identified. Studies by Joyce et al[4] showed that neither CO or CO_2 adsorbed on an atomically clean Si surface produced by heating at $1200^{\circ}C$ in UHV. Electron beam irradiation assisted adsorption on Si surfaces was studied by Coad et al[124] who found that both C and O accumulated on the surface at enhanced rates. The amount of C accumulated on an initially clean surface was observed to be much less than on a carbide contaminated surface. They reported that no O peak was found to accumulate on clean Si surfaces for as long as 22.5 hours which contradicts our own observations. They concluded that the gas involved in the assisted adsorption on Si was CO.

The C and O contamination accumulated on our freshly grown epitaxial layers with exposure to UHV were readily removed below the detection limit of AES by heating the surface to $850^{\circ}C$. However after the surface had been irradiated by the Auger or MEED electron beam, the absorbed C could not be totally removed by the same preheat treatment. Apparently the C adsorbed on the later surface was chemically bonded to the surface by the electron irradiation, presumably as the stable SiC precipitates which are well known to be very resistant to preheat treatment[31].

Chang[125] found that C would not accumulate on a clean GaAs surface even under Auger electron beam irradiation provided that the surface was kept above
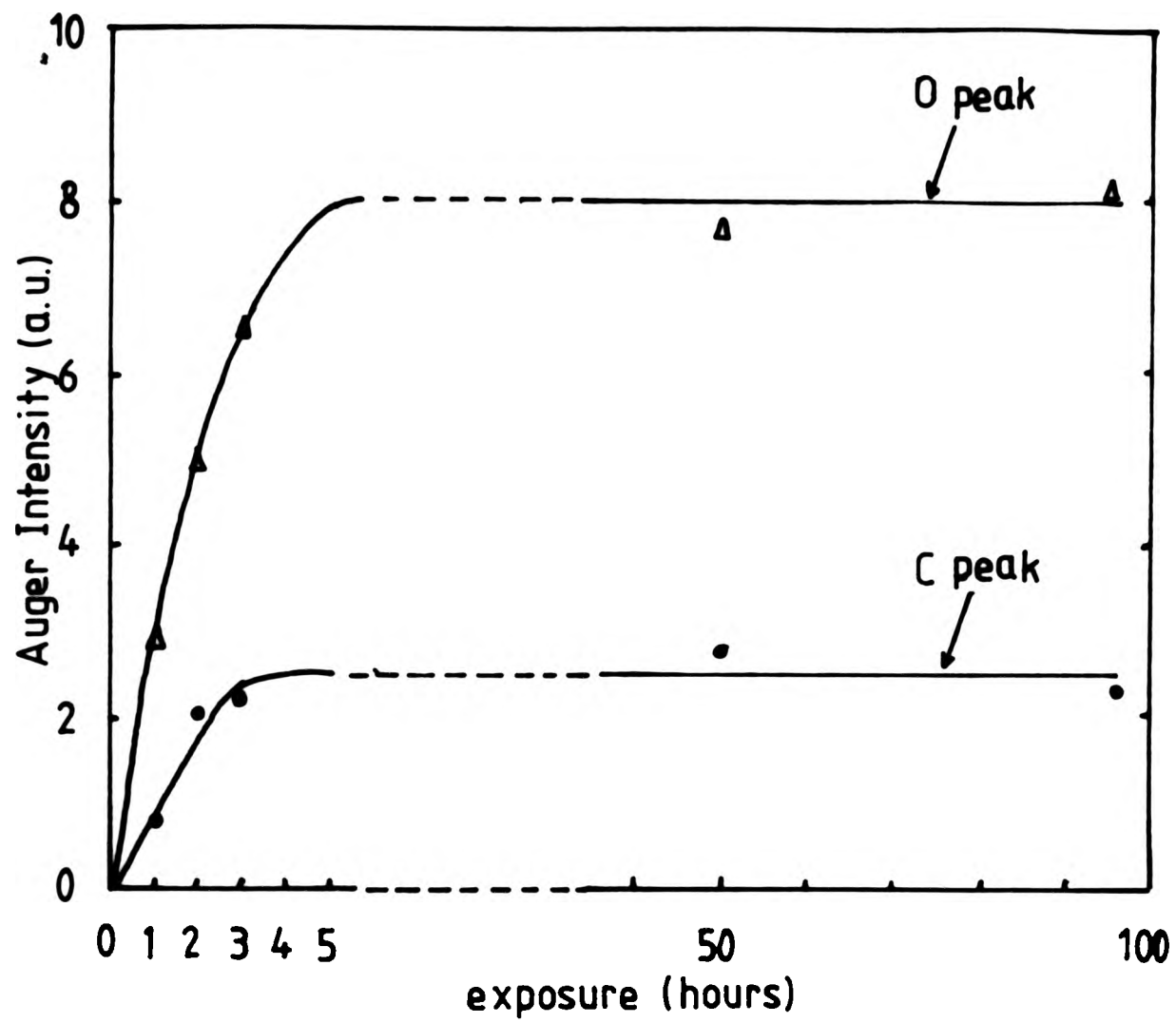
93

Fig.3.3 Accumulation of C and O on freshly grown Si
epitaxial surface at room temperature with time of exposure
in UHV as monitored by AES.

94

350°C after immediately the thermal treatment. It is clear from the above observation that once a clean surface has been prepared, it should not be exposed to electron beam irradiation at room temperature in order to avoid carbide formation on the surface.

3.1.2 Sputter Cleaning

Some preliminary studies were made using the sputter cleaning method. Our sputter cleaning facility consisted of a fast atom saddle field source (Model FAB94, Ion Tech (UK)) which produces near 100% neutral atom beam. The substrates were bombarded with Ar (99.99% purity) at energies of about 3KeV for a period of 10 to 15 minutes at room temperature. The substrates were rotated during the cleaning to achieve a more uniform removal of surface material. The substrates were transferred to the growth chamber before annealing at 850°C for 30 minutes prior to growth.

Though the preliminary cross-section TEM analysis of the epitaxial/substrate interface showed that no gross surface damage remained after the annealing process[126], defect etching assessment of layers grown revealed very high densities of stacking faults (Fig.3.4). It appears that these stacking faults were nucleated at the sites of minute particles on the surface. The etched surface became progressively worse towards the edge of the substrate indicating that sputtered products from the substrate holder were contaminating the adjacent area of the substrate. There were serious reservations[127] were expressed on the purity of the fast atom beam generated by the sputter gun as supplied by the manufacturer. It was suspected that gross products might be sputtered off from the front graphite cathode grid.

The energies of the bombarding species available from the as-supplied sputter gun were limited to >= 3 keV. This is a serious disadvantage since it has been

Fig.3.4 Short defect etch reveals that a layer grown on a Ar sputter cleaned substrate which was annealed at 850oC prior to epitaxy to be grossly defected indicating apparent re-contamination of the substrate surface by the sputter gun used.

Fig.3.4 Short defect etch reveals that a layer grown on a
Ar sputter cleaned substrate which was annealed at 850oC
prior to epitaxy to be grossly defected indicating apparent
re-contamination of the substrate surface by the sputter
gun used.

demonstrated that[38] lower energy ions are required to minimize surface damage to the substrate and to prevent trapping of bombarding species below the surface which cannot be adequately annealed out at 850°C.

3.2 Growth of Undoped Layers and Their Crystallographic Defects

3.2.1 Growth conditions

High resistivity (100) substrates as supplied by Wacker were used in this study. The resistivity was in the range of 17-33 ohm cm for boron doped substrates and 5-7 ohm cm for phosphorus doped substrates. The substrates were either chemically treated by the Shiraki method before loading into system or loaded as-received. The substrates were then heat-treated in vacuo at ~850°C for 10-30 minutes immediately prior to epitaxial growth. Surface conditions of the substrates after the heat treatment have been described in Section 3.2. Growth rates between 1 to 11μm hr^{-1} were used and the range of substrate temperatures used was 700 -900°C. However most of the layers were grown at 2 to 3 μm hr^{-1} and at a typical substrate temperature of 850°C. Layer thicknesses varied between 2 and 6 μm. Though for analytical purposes, layers as thin as 0.2 μm to as thick as 18 μm were also grown.

The residual pressure in the growth chamber at the beginning of a growth run was typically 5×10^{-8} mBar which gradually decreased to about 1×10^{-8} mBar towards the end. The residual gas analysis of the chamber during growth showed H and CO as the major constituents. On some occasions where the cryopump was saturated with He, the He peak became dominant and the total residual pressure could be as high as 5×10^{-7} mBar.

3.2.2 As-grown Epitaxial Surfaces

All as-grown epitaxial surfaces, regardless of the ex-situ substrate treatment, were visually smooth and indistinguishable from the substrates. When examined under strong illumination[128], a uniform distribution of minute light scattering points were apparent on the epitaxial surface. When the layers were further examined under a Normarski microscope, most of the layers were smooth indicating the occurence of 2D epitaxial growth. In some of the thick layers, a wavy surface texture was visible. The same type of surface texture was also observed by Ota[9], but only on (111) epitaxial surfaces. The minute light scattering points described above were identified under the microscope as regions of highly disrupted 3D growth. At the centre of each disrupted growth region was a particle which apparently has been incorporated into the epitaxial layer. SEM and replica TEM analysis of the as-grown surfaces were also occasionally used. Both techniques confirmed the occurence of smooth 2D epitaxial growth and the other growth features using the Normarski microscope.

3.2.3 Dislocations

The crystallographic defects in the layers were further revealed by means of preferential chemical etching as described in Section 2.2.4. Secco and Wright etches were used in our study and a etch period between 15s and 2 minutes were adopted according to the thickness and the defects to be revealed. The etched surfaces were then examined under a Normaski microscope. Etch features relating to different types of defects could be identified and counted.

Dislocation etch pits were the most commonly observed features in our layers. In the earlier growth series, the layers were found to have dislocation densities above $10^8 cm^{-2}$. Gradually, the dislocation density dropped to a level between 5×10^3 and 10^6 cm^{-2} as the

98

system became progressively cleaner. The dislocation etch pits were found to be non-uniformly distributed across the slice. In many cases, the density of etch pits was higher at the central region of the slice. However, the situation was reversed in a number of layers with no obvious reasons. Suspects were placed on the possibility of influence from the non-uniform substrate heating during growth. The non-uniform lateral distribution of substrate temperature was made apparent from the radial variation in the dopant concentration distribution across the slice (Section 2.1.4). We attempted to improve the substrate temperature uniformity by reducing the contact area between the ring support and substrate at the edge. Though a more uniform distribution of dislocation etch pits was observed in some layers, the result was not consistent.

It was so far proved difficult to pinpoint the factors governing the source of dislocations in our layers. However, we observed a number of growth conditions under which were more likely to give high dislocation densities. If the substrate holder and graphite ring support were not degassed adequately before use, the layer grown was considerably more defective at the edge region of the slice. The porous nature of graphite presumably caused it to act as a gaseous contaminant source following the air exposure during substrate loading. The outgassed products later re-contaminated the substrate surface during the preheat treatment. It was found neccessary to outgas the substrate holder and graphite ring support each time before use in the heating stage available in the preparation chamber at temperatures exceeding 1200°C. The need of regular outgassing of the substrate holder was inconvenient and undesirable. We later replaced the graphite ring support with a similar Ta support which was partially reduced the requirement of regular outgassing. Layers were also found to be more defective whenever a) there were interruption to the Si molecular beam flux during the growth, b) rapid heating and cooling of the

substrate and c) extensive exposure of electron beam irradiation (RHEED) of the surface of the substrate at low substrate temperature prior to growth.

It is considered that dislocations in the substrate can propagate into the growing epitaxial layer[29]. However, with the availability and use of dislocation-free substrates, we do not believe the substrate material itself contributed significantly to the dislocation content in our layers by the above mechanism.

Hall measurements were made on a number of undoped layers with their defect contents assessed by defect etching. Fig.3.5 is a plot of the Hall mobility μ_H at 300K against the defect content of the layers. It can be seen that the Hall mobility of the layers was not significantly influenced by their dislocation content up to as high as $10^8 cm^{-2}$. In one layer (denoted by letter D in Fig.3.5) which was grown under a number of interruption to the Si molecular flux and substrate heating, defect etching revealed the layer to be heavily dislocated, the Hall mobility in this layer dropped to ~50% of the expected bulk value. The p-n junction isolation of this layer was found to be very leaky indicating a poor substrate/epitaxial interface. A micrograph of this layer after 30s Secco etch is given Fig.3.6 showing small patches of relatively dislocation-free areas surrounded by highly dislocated areas. It is evident that the Hall mobility measurement does not provide a sensitive indication to the crystallographic quality of the layers.

The correlation between dislocations and C contamination on the substrate surface prior to epitaxial growth was demonstrated by McFee et al[28]. They showed that there was a direct relationship between the surface concentration of C at the substrate epitaxial interface and the dislocation content in the layer. However, they found no similar connection with the surface concentration of O at the interface. In Section 3.2.1, we described that after the heat treatment at $850^{\circ}C$, both O and C peaks in

100
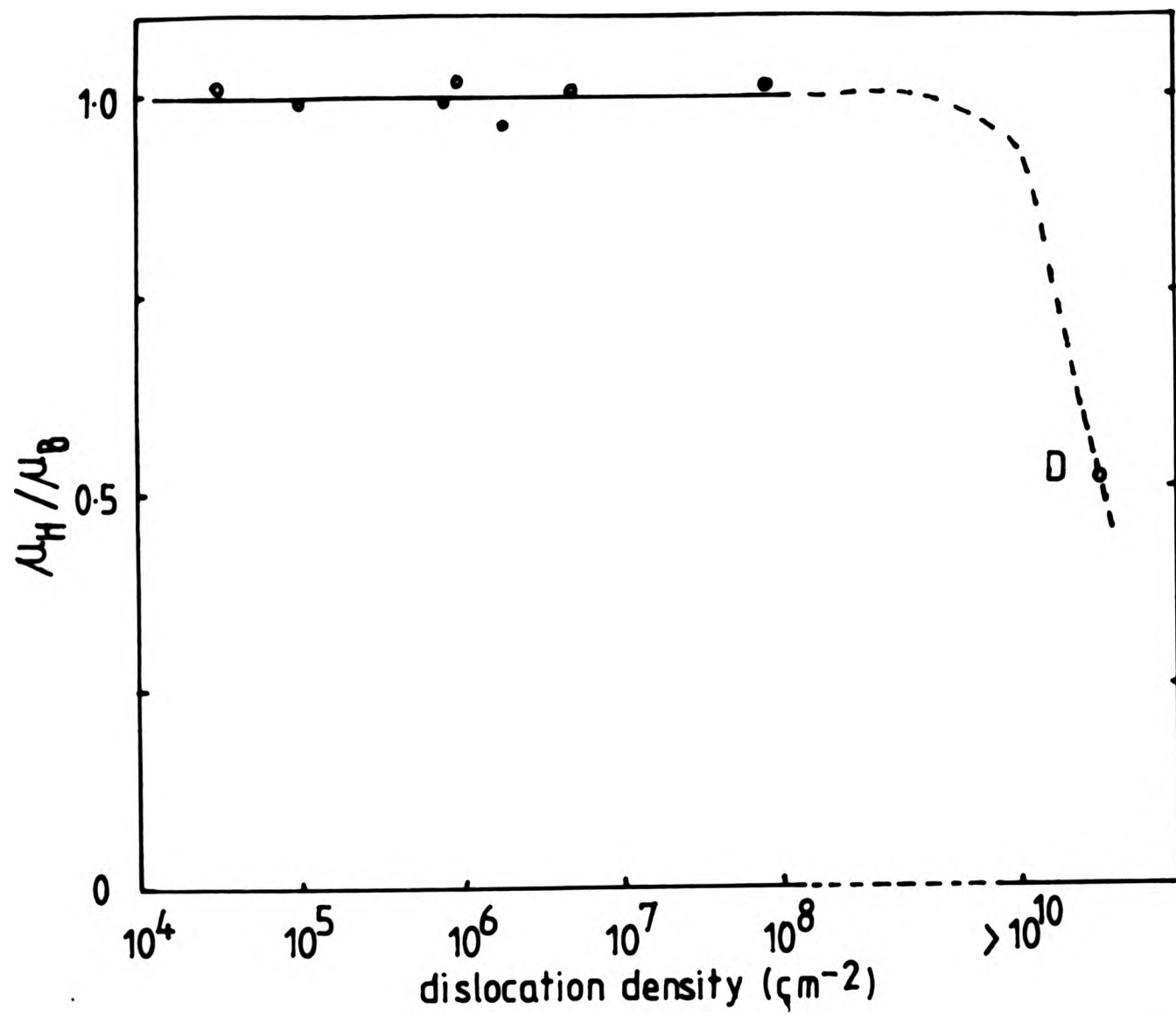
Fig.3.5 The effect of dislocation densities in undoped layers on their measured Hall mobolities μ_H (μ_B = bulk Hall mobility).

Fig.3.6 A micrograph of a defect etched Si-MBE layer, grown
under a number of interruptions to the Si molecular beam,
which is revealed by the 30s Secco etch to be highly
dislocated.

Fig.3.6 A micrograph of a defect etched Si-MBE layer, grown under a number of interruptions to the Si molecular beam, which is revealed by the 30s Secco etch to be highly dislocated.

the Auger spectrum of the substrate surface were generally below the detection limit of our equipment (⁻0.1% of a monolayer). The upper limit of the surface concentration of C and O were therefore below $10^{12}cm^{-2}$. If each impurity atom formed a nucleating site for dislocation then we would expect dislocation density of $=< 10^{12}$ cm^{-2}. This is substantially higher than what we observed in our layers. It is known that the surface C diffuses into the substrate when heat treated to above $1100^{o}C$ leaving behind a carbon-free "atomically clean" surface. To date, the best Si-MBE materials[87] with the lowest dislocation density (⁻ 100 cm^{-2}) was claimed on layers grown on substrates prepared by preheat treatment at $1100^{o}C$ for ⁻ 1 minute. Unfortunately, we were unable to reach such high temperatures with our substrate heater.

In Section 2.1.1, we indicated that our system after a bakeout at $170^{o}C$ for 24 hours showed a RGA sprctrum consisting mainly of H, He, CO^{+} and $C_2H_4^{+}$ (peaks at 2, 4 and 28amu respectively). Using the peak height at 43 amu as an guide to the level of hydrocarbons in the vacuum environment, it appeared that comparable amount of hydrocarbons were also observed in an ion-pumped V80 system. Though direct comparison of the cleanliness of systems is unreliable, there was no firm indication to suggest the UHV quality generated by the close-cycle He pumps was inferior compared to other similar systems using different primary pumps. Though it is generally accepted that C-containing gaseous species were harmful to the epitaxial growth in Si-MBE, we did not observe an increase in the dislocations or stacking faults in layers grown under a poor UHV environment (e.g. presence of an air leak in the system). Increasing the preheat treatment above $900^{o}C$ did, however, improve the quality of the layers in this respect.

Slip-lines were seldom seen in our layers provided that the substrates were loosely held during heating and not heat-treated above $900^{o}C$ at any stage. When the

substrate temperature was above 900°C, severe thermal slip occurred in the substrate, despite that it was supported loosely in the substrate holder. Dislocations generated along the slip line in the substrate to accommodate the thermal stress were propagated into the growing epitaxial layer[29]. The dislocations generated by thermal slip were distinguishable by the fact that they always appeared in a row along the slip line. Preliminary examinations using the X-ray topography of our layers confirm the assessment obtained by the chemical defect etching. It therefore appeared that whenever the substrate was heated above 900°C, the stresses induced by the temperature gradient *were* severe enough to cause plastic deformation. Similar observations have been reported by Ota[9]. This is not considered a severe limitation since low growth temperatures, preferably below 900°C, are generally used in Si-MBE to reduce the effect of autodoping and diffusion of dopant atoms in the epitaxial layers.

3.2.4 Stacking Faults

Stacking faults (SF's) were seldom seen in our layers. Layers grown on Shiraki-treated and as-received substrates were found to have SF densities of well below $1 \times 10^3 \text{cm}^{-2}$. The growth conditions under which high densities of stacking faults were obtained in our layers were when the substrate had been contaminated by the substrate holder which had not been sufficiently degassed at high temperature. Replacement of the graphite ring with a Ta ring proved effective in reducing the density of stacking faults, presumably as a consequence of a reduction of the amount of outgas products from the support ring.

When the substrate surface was deliberately contaminated with carbon by removing the protective oxide from the surface with HF prior to loading into the system, high densities of SF ($>10^5$ cm^{-2}) were obtained in the

grown layer. The stacking faults were uniform in size and evenly distributed over the entire wafer indicating that they were nucleated at the epitaxial substrate interface. The indication that C contamination would lead to nucleation of stacking faults in the layer was evident from the persistent C peak in the Auger spectrum of the substrate surface even after a heat treatment at 900°C for 30 minutes.

3.2.5 Saucer Pits

Another common etch features in some of the layers were the so-called saucer pits (S-pits)[119]. They are distinguishable in a defect etched surface from the dislocation pits by their shallower and round bottomed depressions[118]. A micrograph of a (100) layer which was Secco etched for 30 sec is given in Fig 3.7. The deeper dislocation pits appear as the bright features in the micrograph. Note the substantial density of S-pits ($>10^6$ cm^{-2}) as compared to the dislocation pits (5×10^4 cm^{-2}).

We do not know, at present, the cause of S-pits in our layers. Ota[129] indicated that he frequently observed S-pits in layers grown under (a) a poor vacuum and at low substrate temperature, (b) non-uniform substrate heating, (c) high thremal stress in the substrate, (d) high level of dopant flux, (e) unstable Si molecular flux, and (f) metallic contamination due to electron bombardment of walls by the e-gun evaporator. However no systematic data was present to support these observations.

Though the role of metallic contamination in the formation of S-pits has been demonstrated in CVD Si, to date, there are few systematic studies to elucidate the nature of the cause of S-pit formation in Si-MBE layers.

3.2.6 Particle-induced defects

105

Fig.3.7 Typical optical Normarski micrograph of a ~2.0μm thick Si-MBE layer after 30s Secco etch showing the S-pits S and dislocation pits D.

Fig.3.7 Typical optical Normarski micrograph of a ~2.0μm thick Si-MBE layer after 30s Secco etch showing the S-pits S and dislocation pits D.

106

In all the Si-MBE layers, isolated growth disturbances were observed. These features appeared as a particle surrounded by multiple stacking faults (these features will be referred to as Particle-induced Stacking Faults, PSF's, in the text). A typical micrograph of an as-grown layer with PSF features is shown in Fig.3.8. Note that the stacking faults associated with each particle are not uniform in size indicating that the particles are located at different depths from the epitaxial surface, though the size of the particles themselves could vary between 1μm and a few tens of μm. The "multiple stacking fault" features were revealed clearly when the layer was defect etched briefly. Fig.3.9 is a micrograph showing the etch feature of PSF after 30s Secco etch. With such short period of etching, the particles remained at their sites. Upon further etching of the layer ($>>$ 2 mins), however, a number of etch pits similar to the dislocation pits were revealed at the centre of each site.

The PSF's were found to be uniformly distributed across the slice, except in areas where surface contamination or damage have occurred during substrate handling. The PSF densities in layers with thicknesses more than 2 μm were between 5×10^3 cm^{-2} and 1×10^4 cm^{-2}. In layers less than 2um thick, the PSF density was generally found to be $< 1 \times 10^3$ cm^{-2}, and in submicron thick layers, few PSF features were observed or could be positively identified. In addition, areas where epitaxial growth was apparently inhibited were observed. It is suspected that these areas could be the original sites for the particles which would have nucleated the PSF features if the epitaxial layer was thick enough to retain the particles in the layer.

It was at first suspected that these particles accumulated either during the ex-situ substrate cleaning or from exposure to the laboratory environment. However there are a number of observations to suggest that neither cases were a major source of particle contamination

107

Fig.3.8 A micrograph of the as-grown epitaxial surface of a (100) Si-MBE layer showing a number of particle-induced defects (PSF's).
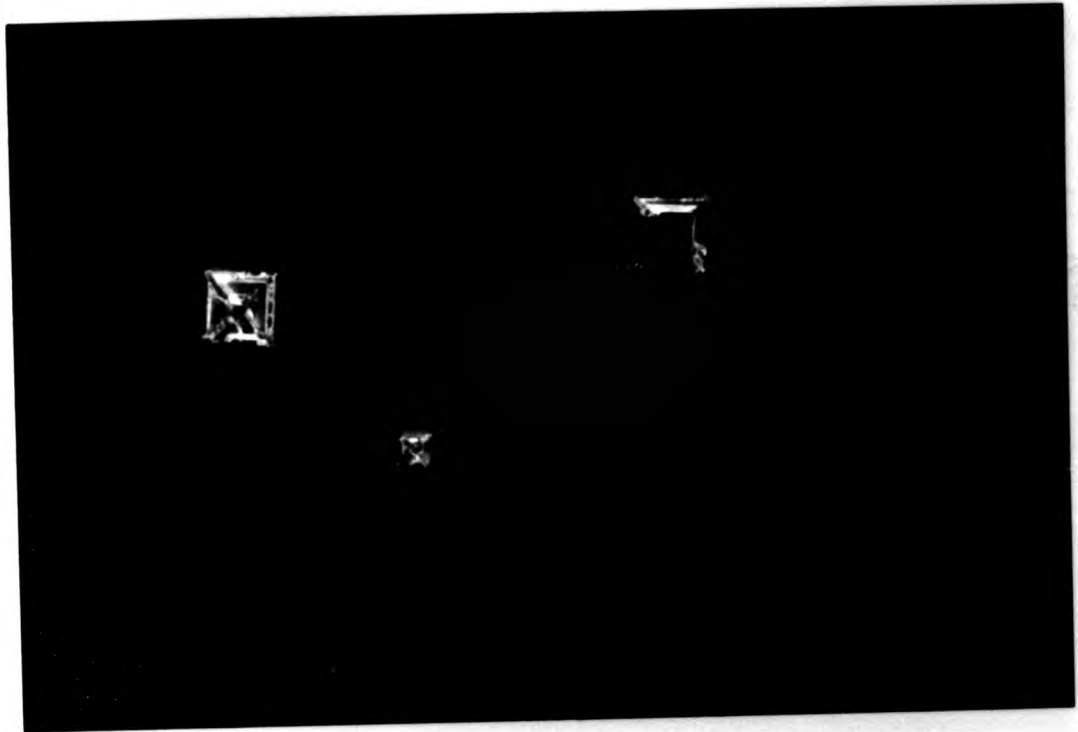

Fig.3.9 Typical etch features of the particle-induced defects revealed on the surface after a brief 30s Secco etch.

Fig.3.8 A micrograph of the as-grown epitaxial surface of a (100) Si-MBE layer showing a number of particle-induced defects (PSF's).
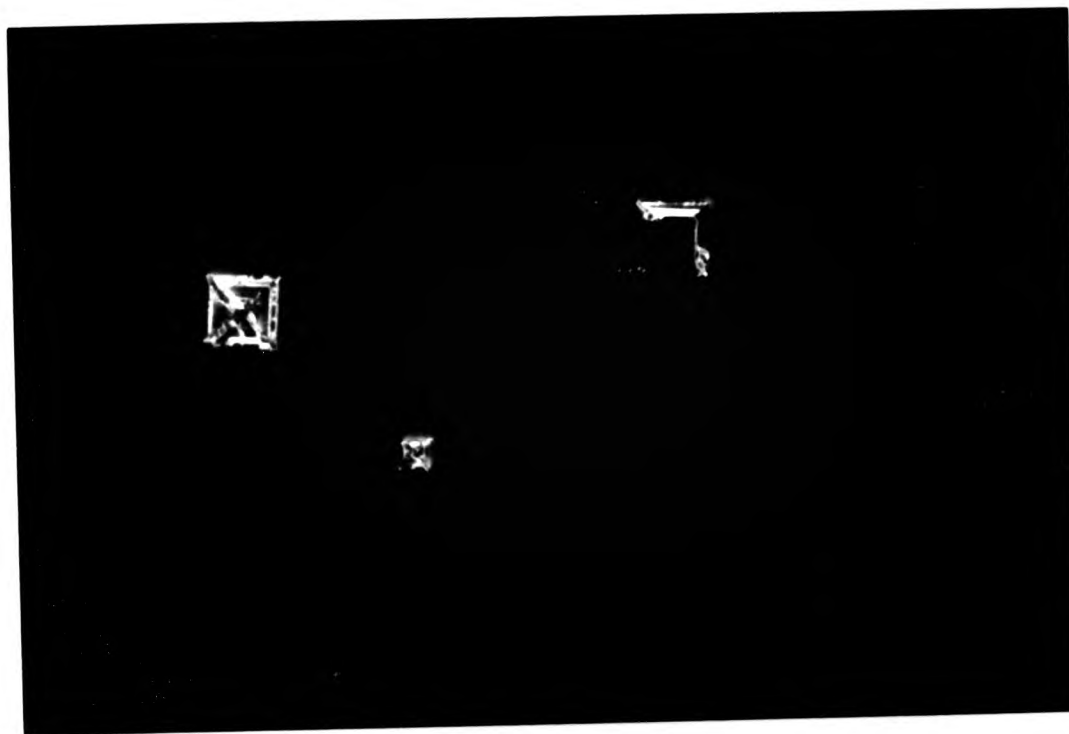

Fig.3.9 Typical etch features of the particle-induced defects revealed on the surface after a brief 30s Secco etch.

responsible for the PSF features seen in the layers,
namely,

(a) these particles have been identified as elemental Si
    by using EDAX

(b) the particle count after ex-situ substrate cleaning
    and before loading into system was well below
    200 cm^{-2}

(c) layers grown on as-received substrates with the
    minimium in-house treatment were found to be similarly
    affected by particles.

(d) the variation of size of the stacking faults
    associated with the PSF features indicates nucleation
    of the SF at different depths within the layer.

Fig.3.10 shows a micrograph of an as-grown epitaxial layer
on a substrate which was accidentally scratched during
transferring within the UHV system. Debris of Si were left
along the length of the scratch. A high density of
disrupted growth features similar to PSF's can be clearly
seen along and near the scratch mark on the substrate.

To clarify the nature of the problem of
particle-induced defects in the layers, a thick epitaxial
(100) layer was cleaved to reveal its [011] plane. The
cleave plane was examined under the Normarski microscope.
Fig.3.11 is a micrograph of the cleave plane showing the
cross section view of the epitaxial layer. Stacking faults
can be clearly seen emerging from particles at different
levels below the epitaxial surface. It is evident from the
above observations that PSF are indeed the consequence of
disruption to the epitaxial growth by Si particles adhering
to the growing surface during the period of growth.

Our initial attempts to overcome the problem with
particles involved the obvious steps of cleaning the growth
chamber of Si deposits as thoroughly as practicable at the
end of each growth series and ensuring a smooth flux
generation from the e-gun evaporator to minimize
spitting of the molten Si pool. Neither steps proved to
affect the PSF density in the layers grown in any

109

Fig.3.10 A micrograph of the as-grown surface of a layer
grown on a substrate with surface scratch prior to epitaxy.
Note the very high and localized density of PSF features
near/at the region of surface scratch of the substrate.

Fig.3.11 A micrograph of the [011] cleave plane of a ~18μm
thick (100) Si-MBE layer showing the cross-sectional view
of the PSF features. The PSF features can be seen to be
originated at different depths.

Fig.3.10 A micrograph of the as-grown surface of a layer grown on a substrate with surface scratch prior to epitaxy. Note the very high and localized density of PSF features near/at the region of surface scratch of the substrate.

Fig.3.11 A micrograph of the [011] cleave plane of a ˜18μm thick (100) Si-MBE layer showing the cross-sectional view of the PSF features. The PSF features can be seen to be originated at different depths.

systematic way.

It later became clear that the Si deposits on the cryopanel in the growth chamber were flaking off onto the base flange housing the two e-gun evaporators and the Knudsen dopant sources. The Si deposits found on the cryopanel were very powdery and could be easily removed. In contrast, deposits found on warm parts of the stainless steel wall were more resistant to flaking.

To avoid excessive Si flaking onto the base flange, we attempted to collimate the Si flux so as to avoid Si deposition on the cryopanel. A Ta shroud was constructed enclosing the e-gun evaporator with appropriate holes cut to allow the Si flux to reach the substrate and quartz crystal sensor head (See illustration in Fig.3.12). Another Si collector consisting a circular Ta plate was suspended a few cm below the substrate heater.

Several improvements to the general environment in the growth chamber were apparent after installing the Si collectors. The amount of Si deposits found on the base flange was substantially reduced indicating that the collectors were effective in preventing the stray Si flux from reaching the cryopanel and forming powdery deposit. The thick Si deposit on the inside surface of the Ta shroud was very resistant to flaking due to it being rather hot during the deposition. The usual glow of the RHEED screen during the operation of the e-gun evaporator was eliminated by the use of the Ta shroud indicating that stray electrons from the e-gun evaporator were prevented from bombarding the chamber walls.

The effectiveness of the use of the Ta shroud in influencing the particle accumulation is made apparent from the progress chart of the PSF density in the layers as shown in Fig.3.13. The growth series are divided into four groups A, B, C and D. The shroud was not installed on the e-gun evaporator during the groups of growth series A and C. The PSF densities in layers grown in groups A and C were between a factor of 2 to 100 higher than in layers
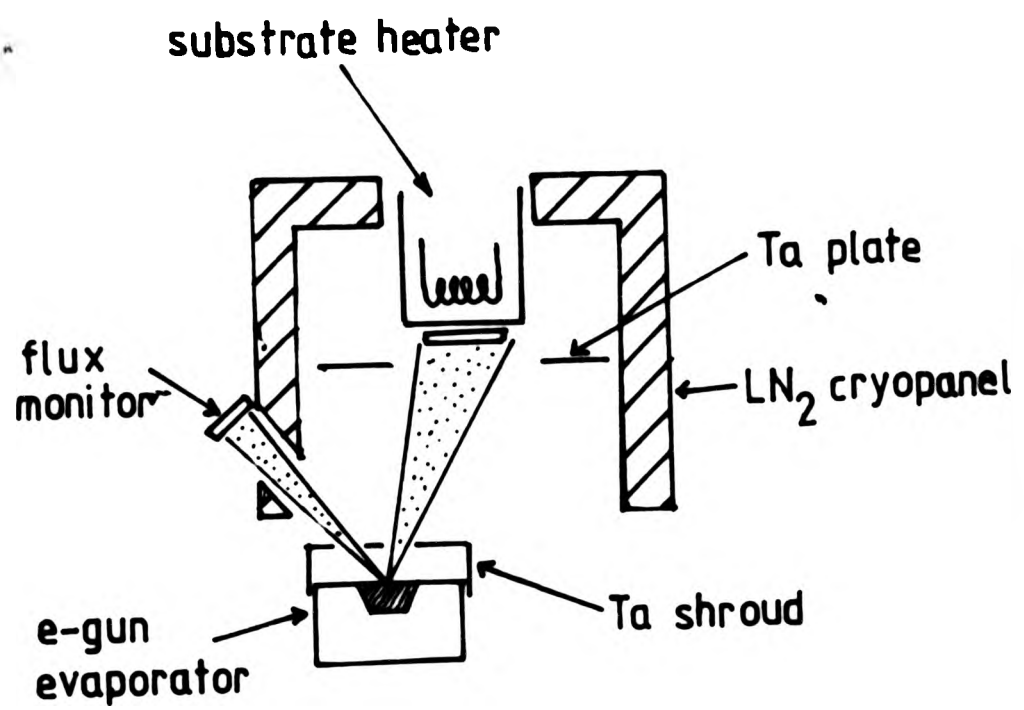
111

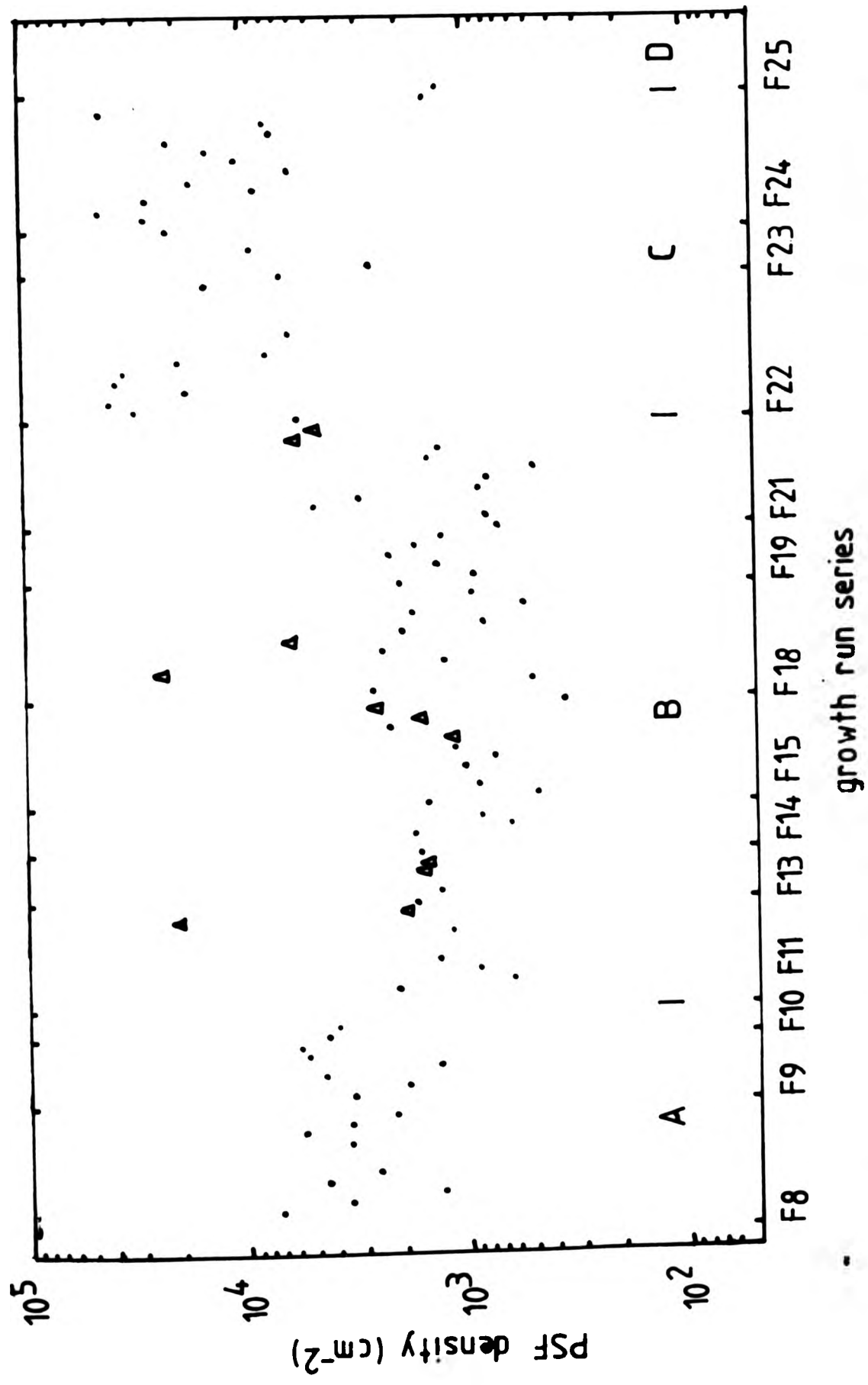Fig.3.12 Collimation of the Si flux generated in the e-gun evaporator using a Ta shroud.

Fig.3.12 Plot of the PSF densities measured in the layers grown under different conditions of e-gun evaporation of Si. Layers grown using e-gun evaporator 1 are shown as (·) and e-gun evaporator 2 as (▲).

grown in groups B and D. The PSF densities in group C is higher than in group A. This difference could be a consequence of the fact that the e-beam of the e-gun evaporator was swept magnetically in group C to increase the effective spot size and was accelerated to higher voltages. During the growth series group B, the second e-gun evaporator which did not have a Ta shroud installed was sometimes used for Si depostion, this generally produced higher PSF densities in the layers. It is evident therefore that the major cause of the particle accumulation was related to the operating conditions of the e-gun evaporators.

Ota[9] described some of the problems he experienced with Si deposits on cold metal surfaces flaking onto various components in his system. He stated that the flaking could be detrimental to the epitaxial growth if they happened to "disrupt" the electron beam path of the e-gun evaporator. He recommended that the Si deposits should be properly collected and later removed after each growth run in order to ensure a proper subsequent growth and further discussed the construction of Si collectors around his e-gun evaporator.

It is useful to examine the circumstances under which the Si particles could conceivably come to adhere to the substrate surface before and during growth. It seems unlikely that significant particle accumulation on the surface occurred in the load-lock during the pumpdown This was substantiated by the low particle count on the surface after putting the substrate through the pumpdown cycle. Substrates are generally batch-loaded and left in the preparation chamber for days before growth. Again it was not considered that significant particle accumulation occurred during this period because of low particle count and the lack of a plausible mechanism by which particles on the preparation chamber walls can be transferred to the substrate surface.

We believe that most of the particle accumulation

114

occurred in the growth chamber. Our results indicated that the particle accumulation was a direct result of the use of the e-gun evaporator. In the III-V MBE systems where e-gun evaporators are seldom used, such particle accumulation on the epitaxial surface is virtually unknown. One possible scenario is where the Si flakes falling in the vicinity of the electron beam of the e-gun evaporator acquire a negative charge and are then repelled by the space charge region produced by the e-beam towards the substrate. A crude calculation can be made to check whether this is kinetically feasible. Considering the case of a 2 μm particle with the e-gun evaporator operating at 7kV and 200mA. The particle at the e-gun evaporator must acquire a total kinetic energy sufficient to overcome the gravitational pull in order to reach the substrate, which is about 0.3m above the evaporator.

As the particle falls into the electron beam it is irradiated by the electron beam. Assuming a circular cross-section with radius R of 1cm for the electron beam, the rate of electrons impinging on the particle is about 1×10^{10} s^{-1}. The maximium amount of charge qN_{max} that a 2μm conducting sphere with radius r can receive from a 7keV electron beam is determined by the potential of the sphere ($V = Q/4\pi \epsilon r$) reaching 7kV which gives $N_{max} = 5 \times 10^6$ for r = 1μm. The time taken for the particle to fall through the electron beam under gravity is of the order of a few milliseconds. During this short period, the number of electrons irradiated on the particle is about 1×10^7.

To calculate the instantaneous electron density in the beam, we require the current density I/A and velocity v of the electron flow. The velocity v of the electrons with energy of E is given by (non-relativistic)

$$E = \frac{1}{2} m_e v^2 \qquad \text{------------- (3.1)}$$

where m_e= mass of electron, and the electron density N_b

115

is given by

$$N_b \, qv = I/A \qquad \text{------------- (3.2)}$$

In a radial symmetrical beam, the Poisson's equation can be expressed as

$$\frac{\partial}{\partial r}\left(\frac{1}{r}\frac{\partial V}{\partial r}\right) = -\rho/\epsilon \qquad \text{------------- (3.3)}$$

By solving the above equation using the boundary conditions of $V(r>R) \simeq 0$ and $E(r>R) \simeq 0$ where R is the beam radius, it can be shown that the potential at the centre of the beam is given by

$$V = -\frac{N_b q}{4\epsilon}R^2 \qquad \text{------------- (3.4)}$$

For a particle charged with n electrons at the centre of the beam, its potential energy is nqV. To overcome the gravitational pull and reach the substrate at a height of h, it must have

$$nqV > mgh \quad \text{or} \quad n > mgh/qV \qquad \text{-------- (3.5)}$$

where m = mass of particle, and g = gravitational acceleration. A value of $n \simeq 6 \times 10^3$ which is substantially less than N_{max} is obtained. This crude calculation shows that particles charged by the electron beam of the e-gun evaporator could conceivably receive sufficient energy from the interaction with the electron beam to reach the substrate.

In summary, the Ta shroud installed over the e-gun evaporator has proved effective in reducing particle accumulation on the substrate surface. We have also demonstrated that the particle accumulation was a direct consequence of the use of the e-gun evaporator. We believe our Ta shroud served two useful purposes. Firstly it prevented the stray Si particles from falling into the

116

e-gun evaporator. Secondly it collected a major part of the Si flux on the inner surface to form a more stable deposit. Further work is in progress to elucidate the nature of the mechanism of particle accumulation.

3.3 Residual Doping

Studies of our intentionally undoped layers show that there are two separate aspects to residual doping in the layers. Firstly the layer is continuously doped by the gaseous dopant species throughout the growth period. Secondly surface contamination of the substrate with B prior to layer growth leads to a narrow p-type region at the epitaxial/substrate interface. These two aspects will be dealt separately in the following sections.

3.3.1 Boron Contamination of Substrate

The B contamination was one of the more unexpected observations in our study of residual doping. The contamination was observed in virtually all the substrates used in our experiments regardless of the substrate conductivity type, except in the case where sputter cleaning of the substrate was employed. One example of the effect of the surface B contamination is illustrated in Fig.3.14 which shows the electrochemical CV profile of an nominally undoped layer grown on a p- substrate at 850°C. A high hole carrier concentration spike at a depth of 1μm coinciding with the epitaxial substrate interface is clearly evident. To confirm the chemical identity of the electrically active impurity reponsible for the p-type region, an undoped layer grown on a n- substrate was analyzed for elemental B using SIMS (Fig.3.15). The SIMS analysis shows a profile with a B spike at the expected epitaxial substrate interface. Estimate of the surface contamination, obtained by intergrating the carrier concentration profile or SIMS profile spike, varies between
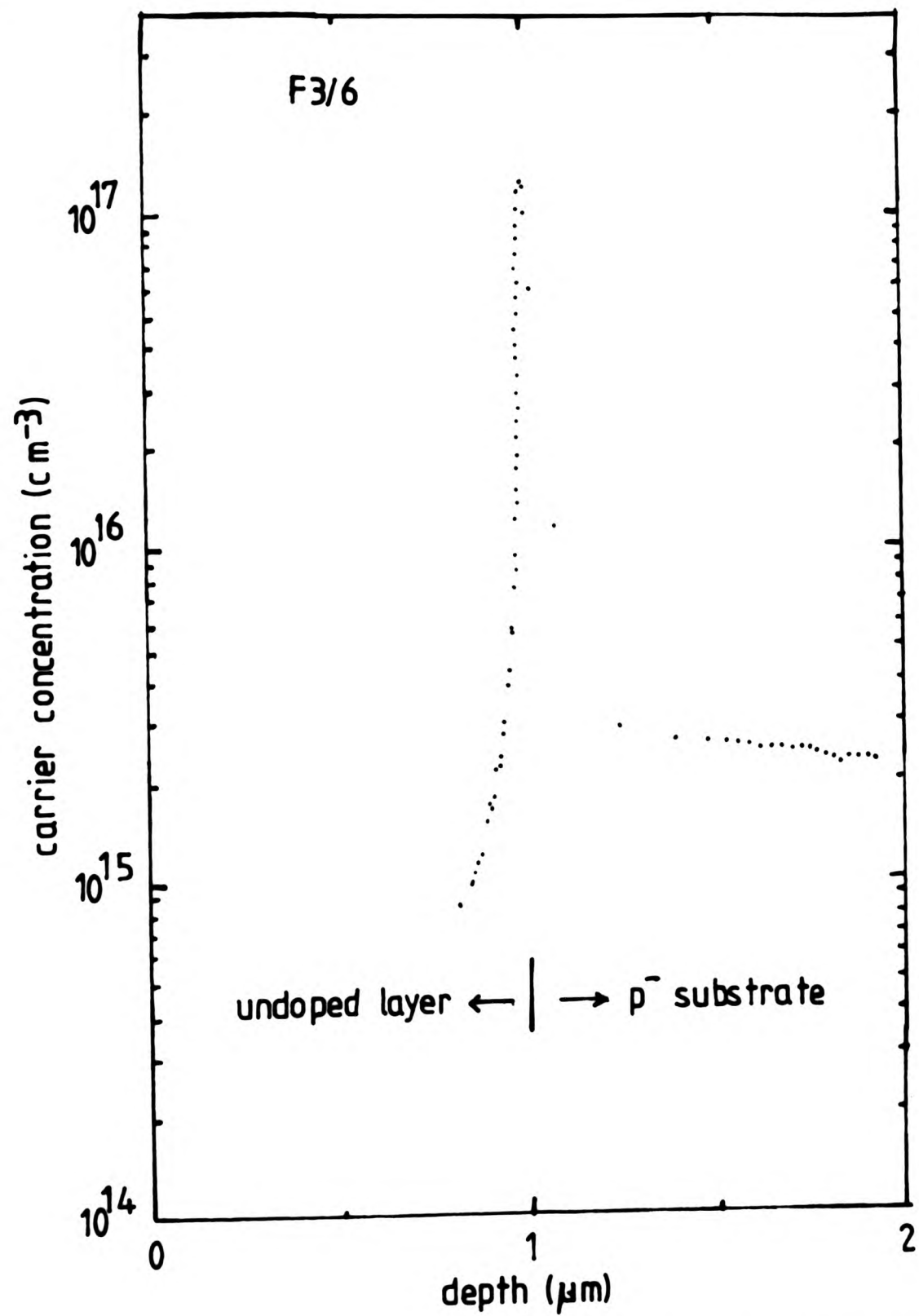
117

Fig.3.14 The electrochemical CV profile of an undoped layer
indicating a high p-type region at the substrate/epitaxial
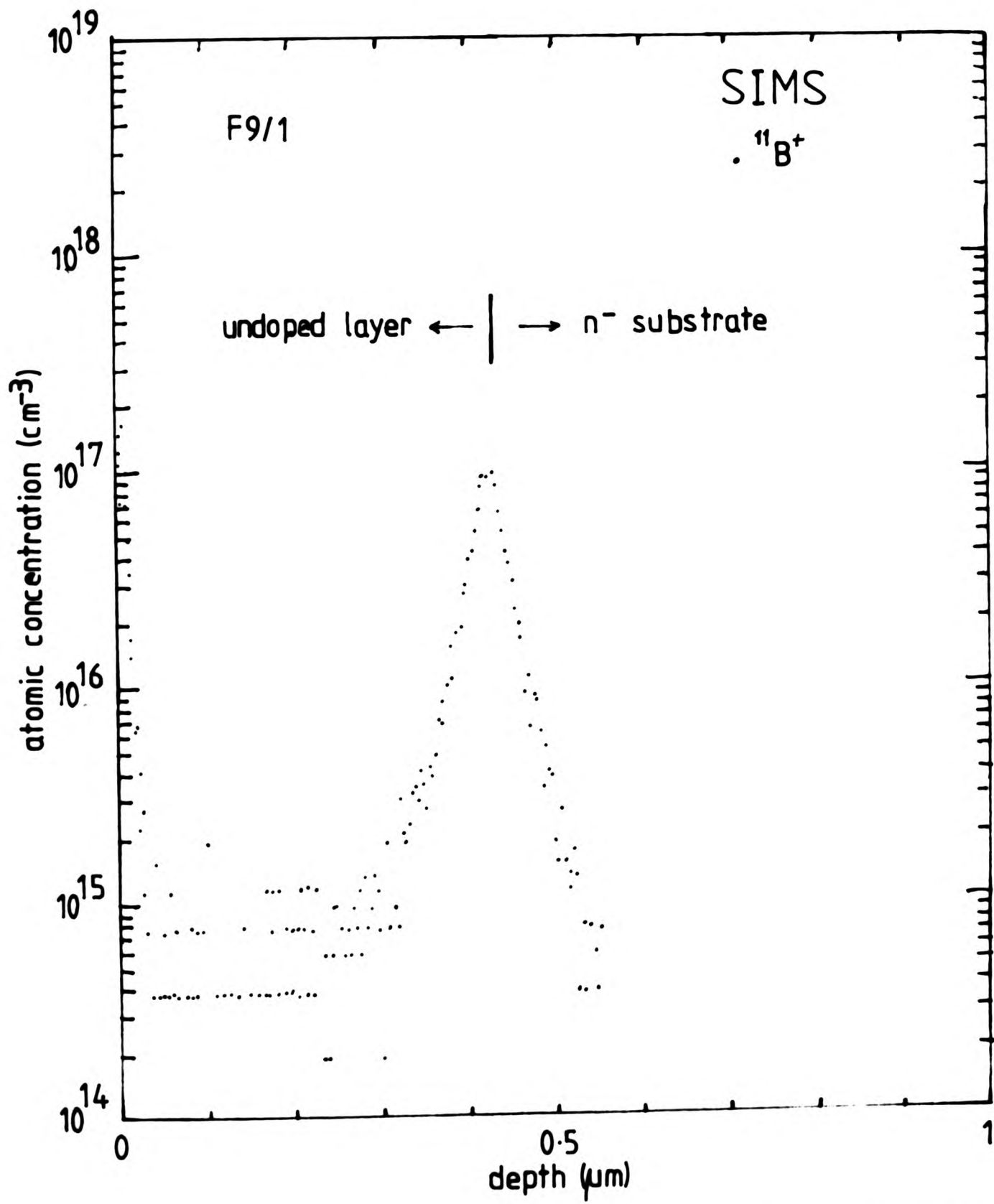interface.

118

Fig.3.15 The SIMS analysis of a 0.4 μm thick undoped layer: evidence of boron contamination at the substrate/epitaxial interface.

10^{12} and 10^{13} cm^{-2}.

The "disruptive" influence of the p-type region on the electrical measurement of the properties of the layers is considerably. Two examples showing its effect on the electrochemical CV measurement of n-type dopant profiles are illustrated in Figs.3.16 and 3.17. In both cases, difficulties were experienced by the Post Office Profiler as the depleted region approached the contaminated region near interface. The measurement near the interface , not surprisingly, was found to be unrealiable and misleadingly. The measured carrier concentration profile at this region was susceptible to any small changes to the bias potential used in the measurement. From the phase angle (dC/dV) measured at this region, one can infer that it was probably p-type.

The B contamination can also seriously affect the interpretation of Hall measurements on nominally low doped layers. Fig.3.18 shows a spreading resistance (SR) measurement of a 2.7 μm thick n-type doped layer on a p-substrate. The profile shows that a p-type region due the B contamination spreads deeply into the epitaxial layer reducing the effective thickness of the n-type layer by nearly a factor of 2. Hall measurements on the layer without taking the p-type region into account would underestimate the carrier concentration. It is therefore essential to determine the effective layer thickness by other independent profiling techniques such as CV and SR measurements. However, the B contamination can produce heavy compensation in very thin low n-type layers and the SR and CV measurements can give potentially misleading results.

On the basis of our own experience with the difficulty in getting reliable measurements on low doped and undoped layers, it is necessary that some reservations should be expressed on a number of reported very low residual doping levels achieved in very thin layers.

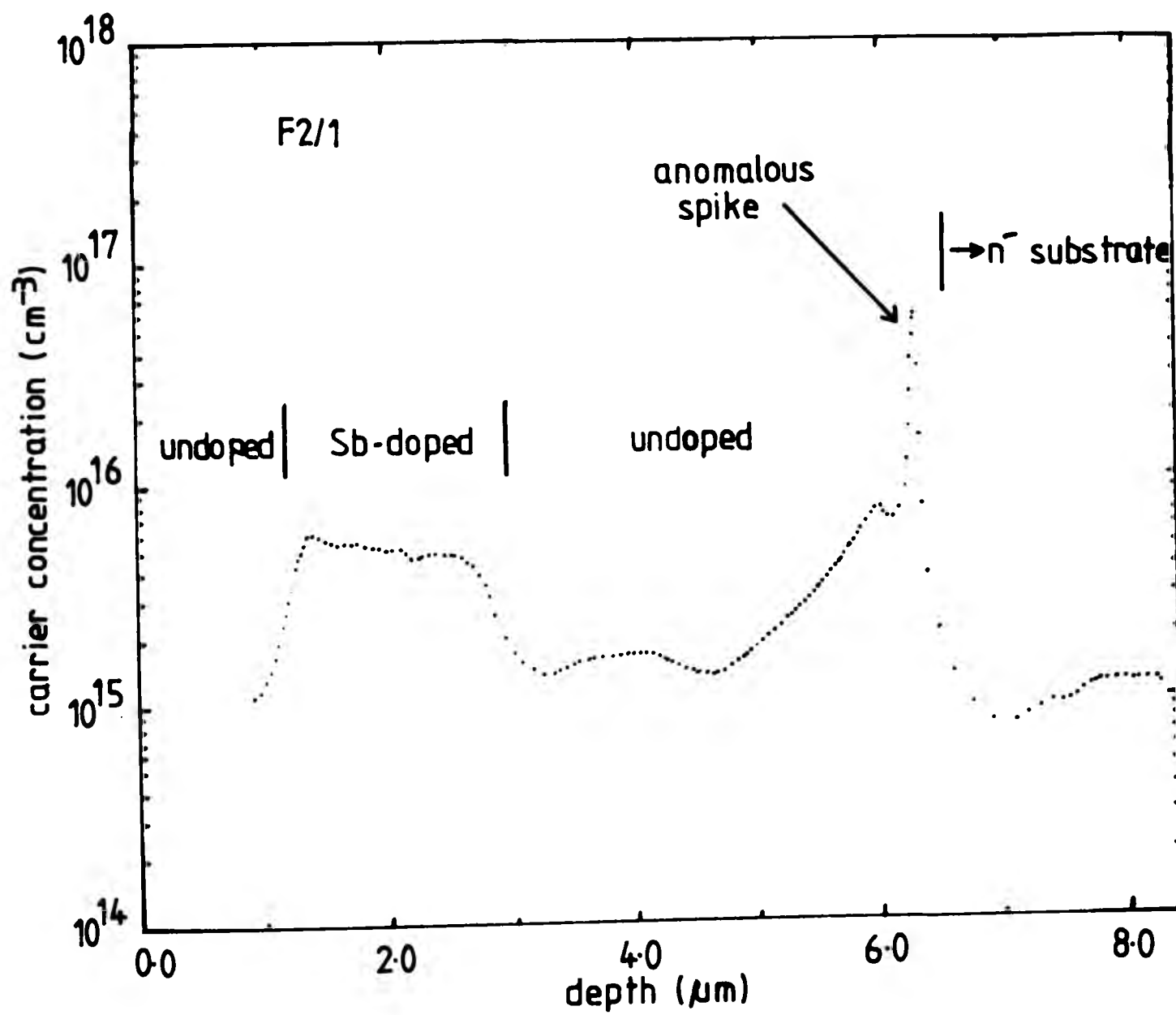Any boron-containing component in the growth chamber

120

Fig.3.16 Anomalous measurement at the epitaxial/substrate interface in the electrochemical CV profile of a Sb-doped layer grown on a n⁻ susbtrate due to boron contamination.
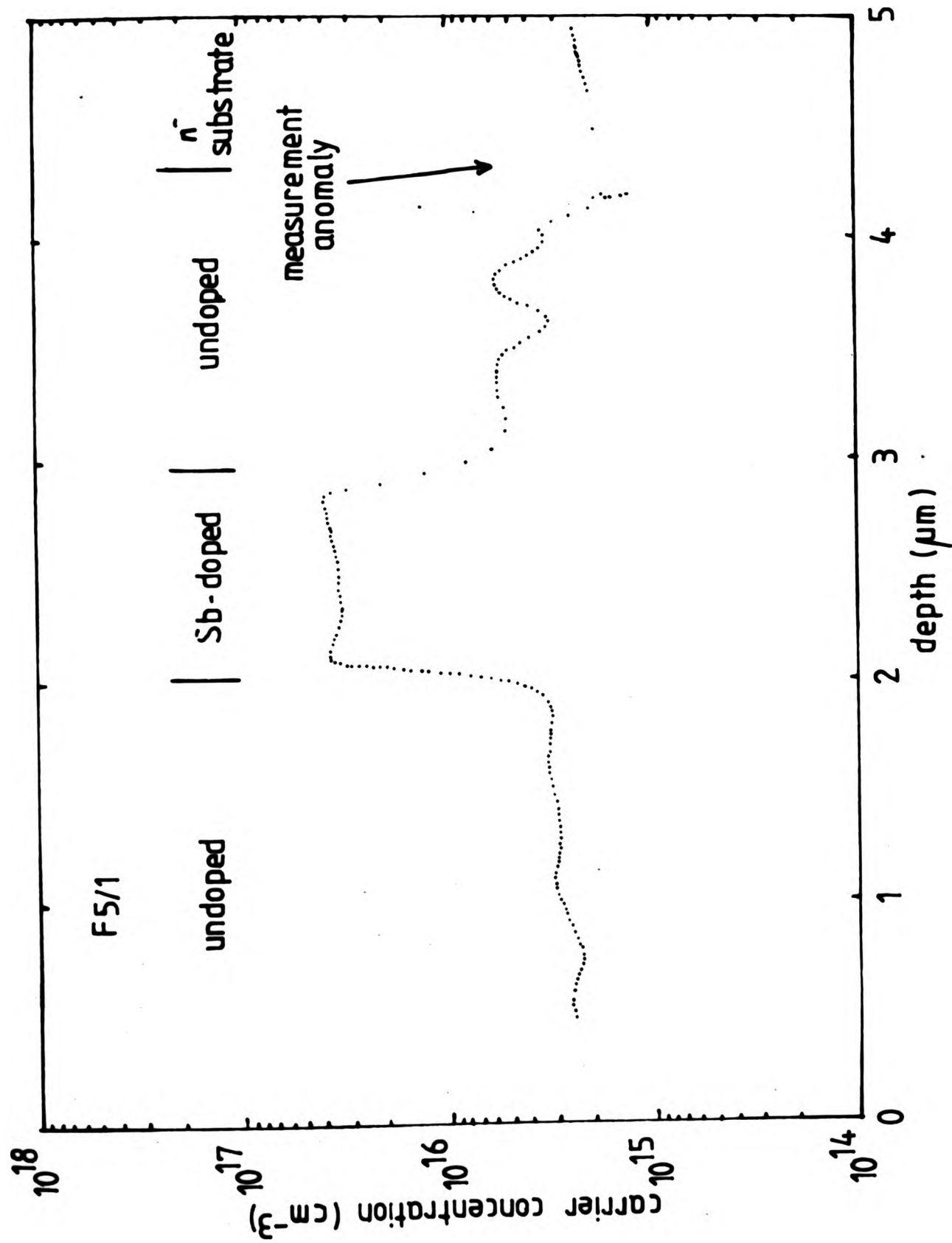
Fig.3.17 The "disruptive" effect of a p-type region at the interface in the electrochemical CV profile of a low Sb-doped Si-MBE layer grown on a n- substrate due to the boron contamination.
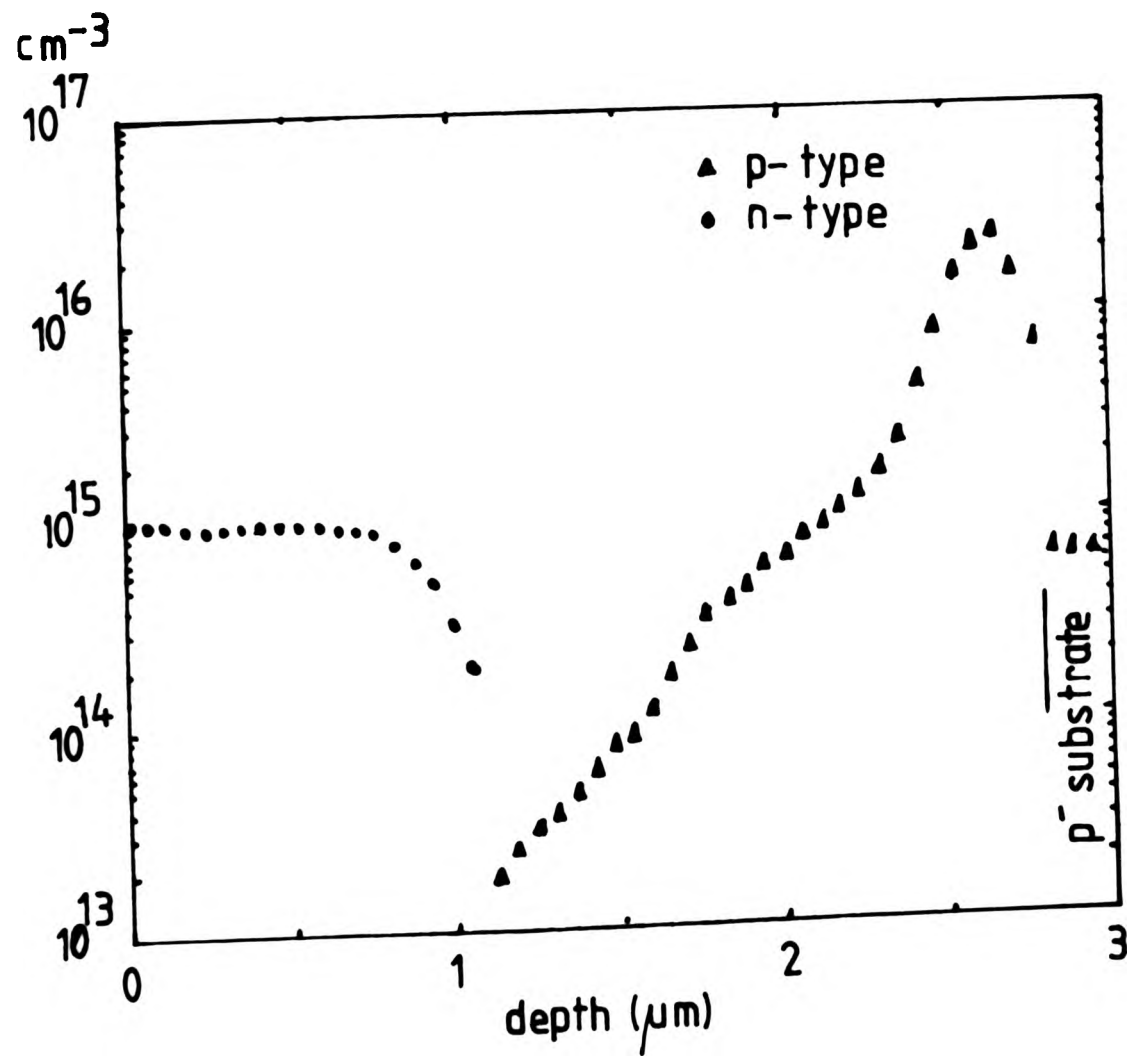
Fig.3.18 SR profile of a 2.7µm thick undoped layer grown on a p⁻ substrate. Note that the boron surface contamination at the interface has reduced the "effective" thickness of the n-type region in the layer significantly.

can be a potential source of such contamination. Two Knudsen dopant source cells were fitted with pBN linings and the typical operating temperature range was 250-600°C. We did not consider them likely as a major source of the contamination due the fact that the problem persisted regardless of the operating conditions of the source cells. Some pBN tubings were used in our substrate heater as supports for the heater filament tapes. These tubings were heated to above 1100°C during use. Though we suspected them as worrying features in the substrate heater design, a number of workers using different types of substrate design have also admitted experiencing a similar contamination problem on the substrate surface[130]. Insertion of a quartz plate between the heater and substrate did not apparently remove the boron contamination. While substituting the pBN tubings with non boron-containing material is desirable, there are unfortunately few suitable materials available for serious consideration.

Henderson[35] reported surface comtamination of his chemically treated substrates with B from the Pyrex glassware used in the chemical treatment. However we have rejected this possibility in the discussion in Section 3.3.1. When layers were grown on as-received substrates (Wacker) of both conductivity types and on a limited number of substrates from a number of sources (Monsanto, Wacker, Shinetsu), no major differences in the contamination level were seen. It was also clear to us that the Shiraki chemical treatment was not effective in reducing or preventing the Boron contamination.

The method of "flash" heating at 1200°C for generating "atomically" clean Si surfaces[31] was not used in our study. We can, however, infer from the appearance of a p-type region at the epitaxial substrate interface in the doping profile published by Metzger and Allen[131] that this was also ineffective at removing the B contamination. The only method we found successful

124

in reducing the B contamination was by ion-sputter cleaning. Incidentally, Bean[132] who routinely employs this method for substrate cleaning also claims no surface contamination of B in his layers. Fig.3.19 shows a SR profile of a 0.2 μm thick undoped layer grown on a n-substrate which received 10 minutes of 4KeV Ar sputter cleaning and followed by annealing at 850°C for 30 minutes prior to growth. No sign of a p-type region is evident at the interface from the profile.

To investigate the origin of the B contamination, we grew a series of multi-layered structures, and the new epitaxial surface of each layer in the structure was exposed to a different environment. For example, one newly grown surface was unloaded from the MBE system and left in the Class 100 workstation for a short period before loading back into the system, and a new layer was grown immediately. SIMS analysis of the elemental B content in these multi-layered structures are shown in Figs.3.20(a), (b) and (c). In (a), the newly grown epitaxial surface was exposed to air for 1 hour before reloading and growing the next layer. Boron contamination on the surface was clearly indicated by the SIMS analysis. In (b), the epitaxial growth was interrupted twice for 10 minutes, no boron contamination was found at the two corresponding interfaces. In (c), the newly grown surface was exposed to N_2, generated from evaporating liquid nitrogen, in the load-lock for about 5 minutes. It was probable that the liquid nitrogen contained some dissolved air. A significantly reduced amount of boron contamination was detected at the interface. These results appear to show that B contamination occurred only when the new Si surface had been exposed to a oxygen-rich atmosphere under which an oxide formation on the surface was likely. In the case of the N_2 exposure which was produced from evaporating liquid nitrogen, a smaller amount of oxygen was present as impurity, a reduced B peak was evident from the SIMS profile. The phenomenon of oxide enhanced accumulation of B
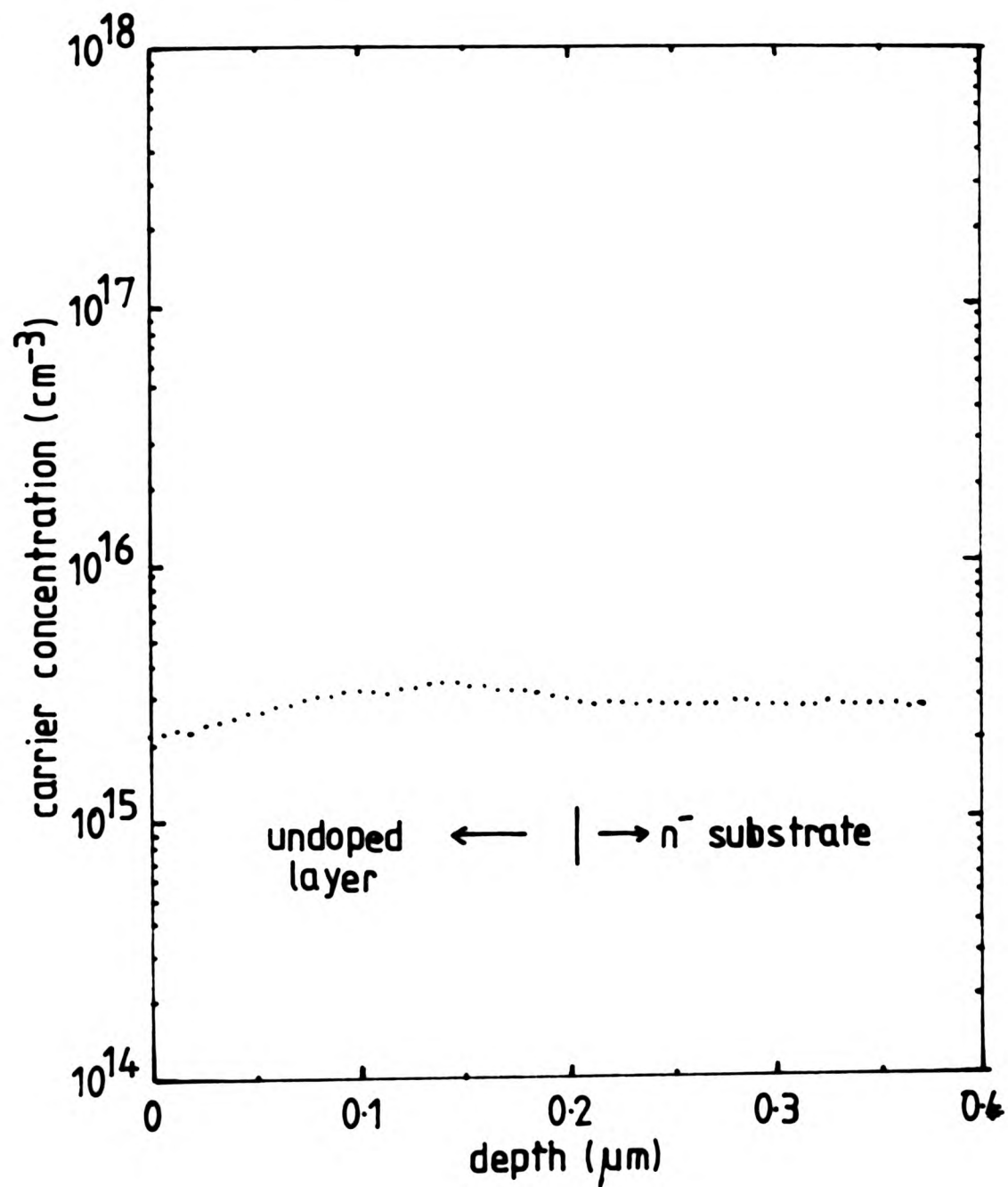
125

Fig.3.19 SR profile of a 0.2μm undoped layer grown on an Ar sputter cleaned substrate which was annealed at 850°C for 30 mins prior to the layer growth.
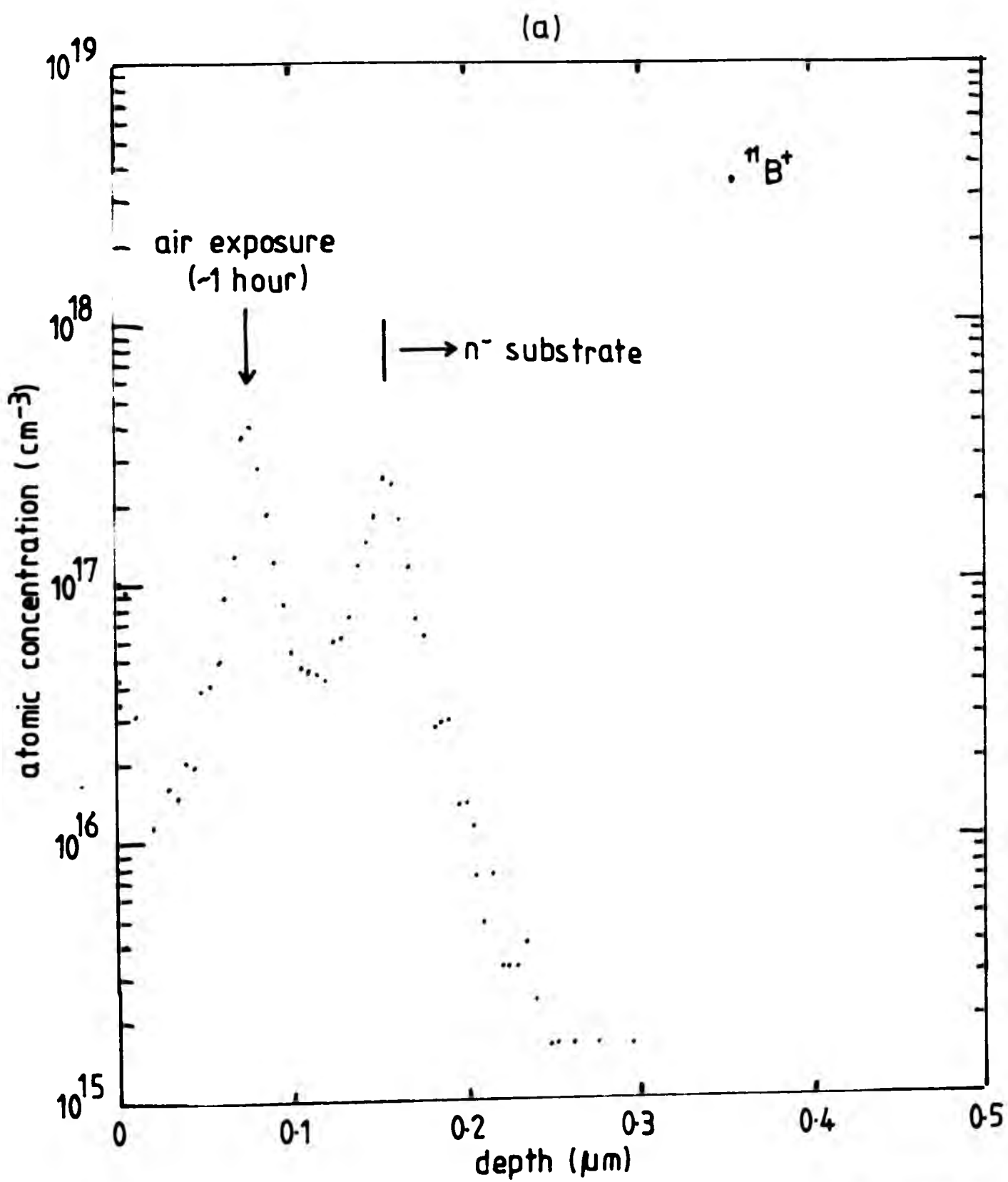
(a)

Fig.3.20(a),(b) &(c) SIMS profiles of undoped Si-MBE layers grown on Si surfaces after exposure to the different environments as indicated. The level of boron contamination detected at the interface is seen to vary according to the amount of O content in the exposure.
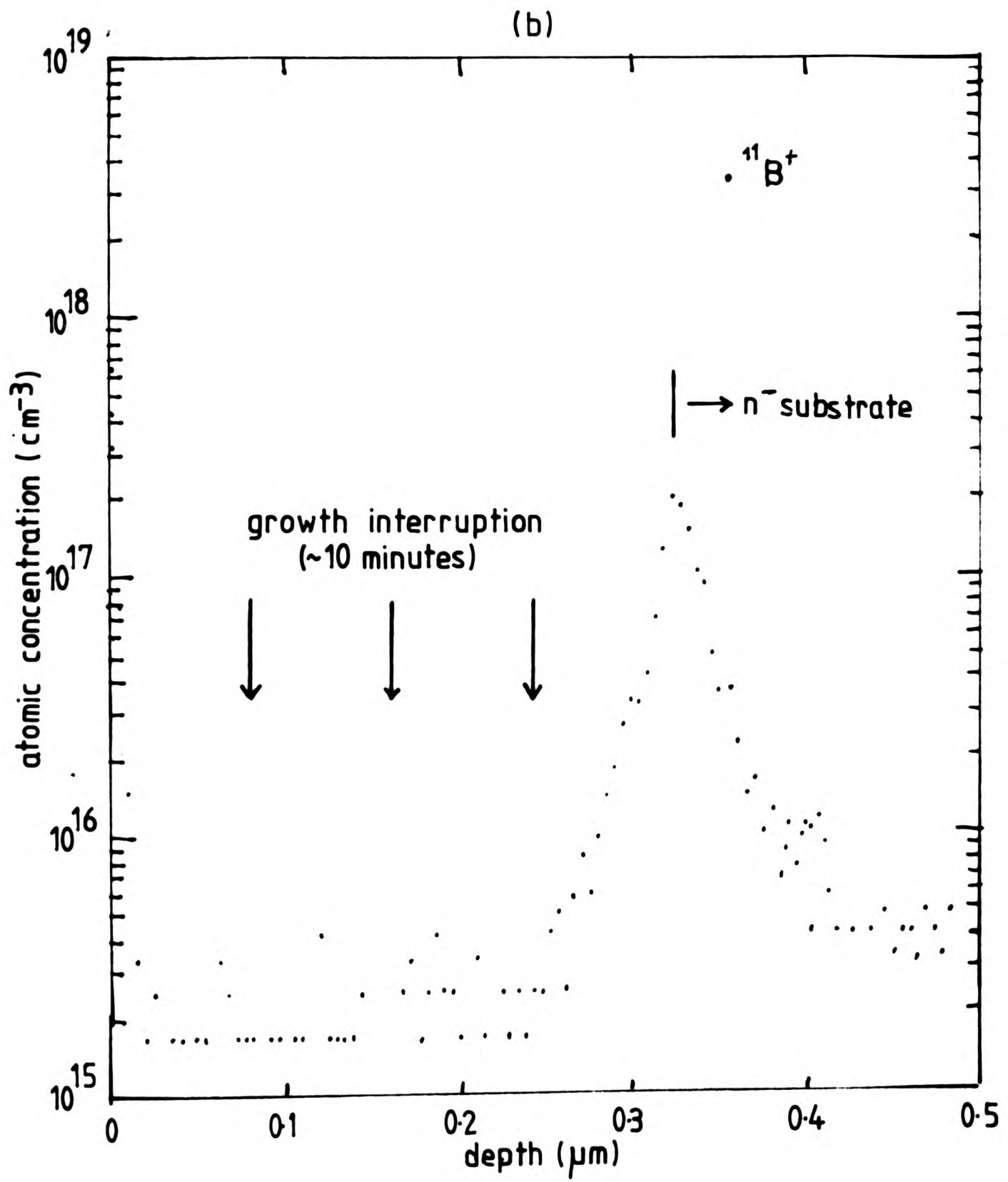
(b)

growth interruption
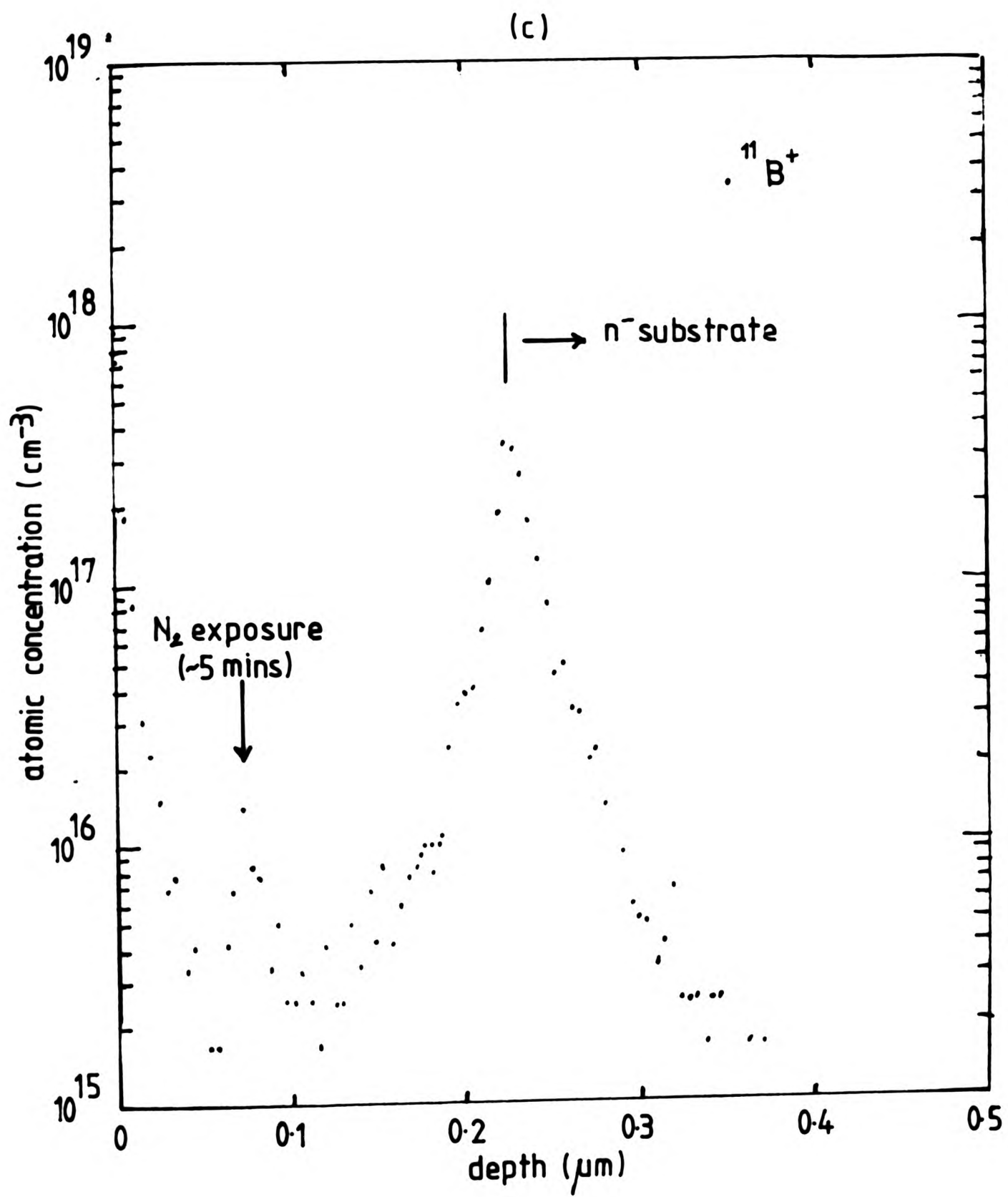(~10 minutes)

. $^{11}B^+$

→ n⁻substrate

Fig.3.20(b) Contd.

128

(c)

Fig.3.20(c) Contd.

129

in thermally grown oxide on substrates has been previously reported[133].

Tabe et al[134] reported an investigation on the effect of air exposure to the RHEED reconstruction on "atomically" clean <111> Si surfaces generated by preheat treatment at >1200°C. They found that the oxide growth after 5 hours of air exposure was about 10Å thick (as measured by ellipsometry). This amount of oxide did not disrupt the (7x7) superstructure on the surface whereas a small fraction of a monolayer of metallic contamination has been observed to disrupt the reconstruction completely[135].

We thus tentatively conclude that since the RHEED reconstruction is not disrupted by air exposure, B contamination does not occur through the air exposure. The B contamination in our substrate was probably therefore accumulated through gaseous transport of B-containing species to the surface whilst the substrate was thermally treated to remove the oxide in the MBE system. The question of the nature of the B-containing species, however, remains unanswered.

3.3.2 Continuous Residual Doping

As Si-MBE is a low temperature growth process, autodoping from the substrate into the epitaxial layer is expected to be insignificant. The other potential source of residual doping are therefore the Si source charge and the background gaseous species in the MBE system. With the availability of ultra-high purity FZ Si source charges (total dopant impurity level =< $1 \times 10^{13} cm^{-3}$). we consider the dopant impurity in the Si source is not relevant significant for residual doping levels are in the mid $10^{14} cm^{-3}$. It is known from Ota's work[9] that (a) the resistivities of resultant p-type layers grown using B-doped Si charges were a factor of 2 higher that the source charge, and (b) when a As- or P-doped source charge

130

was used. As and P diffused rapidly away from the melted zone leaving behind a B-rich melt, and the resultant layers grown were mostly p-type.

The background gaseous dopant species might come from the re-evaporation of dopant deposits on warmed surfaces. Extensive cryopanelling was employed in the growth chamber to minimize such effects. Background dopants could also be derived from materials used in some components of the system. We did not specifically attempt to achieve the ultimate minimum level of residual doping in our layers by restricting the scope of our work, for example, by not incorporating major changes to the growth chamber or carrying out heavy doping studies. Intentionally undoped layers were grown throughout the growth series in between some of our doped layers. Growth rates between 1 to $4\mu m\ hr^{-1}$ were used. Layers with thickness as thin as $0.2\mu m$ to as thick as $18\mu m$ were grown. Most of the undoped layers were at least $3.5\mu m$ to minimize the difficulties in interpreting the measurement of the properties of the layers (See Section 3.4.1).

A progress chart of the residual doping level as determined by electrochemical CV, Hall and SR measurements in the layers is given in Fig.3.21. In this chart, the range of the carrier concentration measured across the layer thickness is indicated by a vertical bar. Some of the layers showed a uniform carrier concentration profile. However, in many cases the profiles showed a dip or hump in the carrier concentration within the layer Figs.3.22(a), (b) and (c) show some typical examples of the SR profiles of undoped layers. Whilst some of these features could be attributed to known interruption to the operation of the e-gun evaporator (say, in Fig.3.22(b)), there was no systematic trend for the measured carrier concentration with depth. All the undoped layers grown so far were found to be n-type, with a few exceptions where the layers were either very thin (< $1\mu m$) or grown at a very slow rate (i.e. <$1\mu m\ hr^{-1}$). The progress chart shows that the first

131
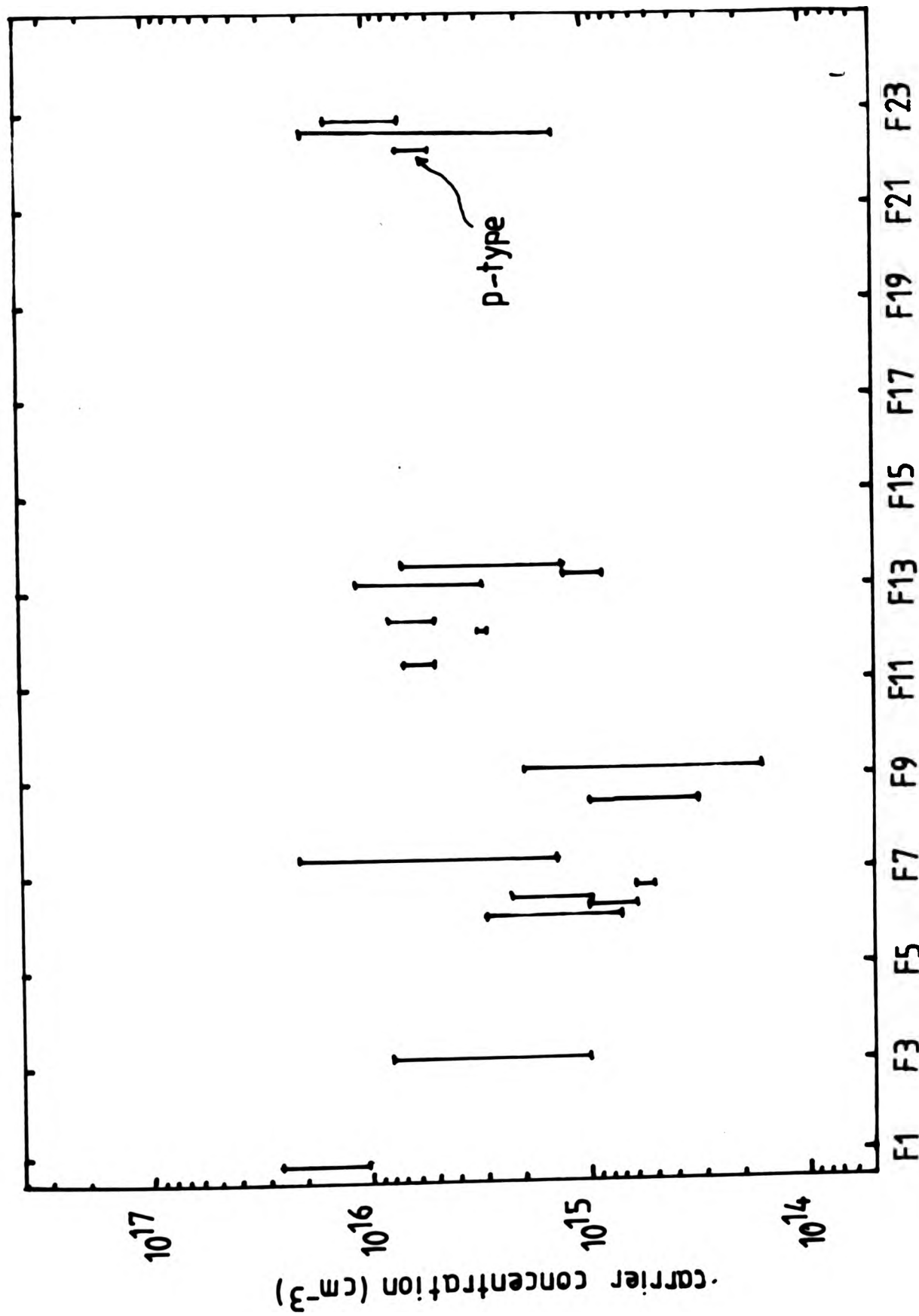
Fig.3.21 Plot of the carrier concentration levels measured in the undoped Si-MBE layers grown in our studies. The vertical bar in the plot represents the variation in the carrier concentration profile with depth as measured by electrochemical CV and/or SR measurements.
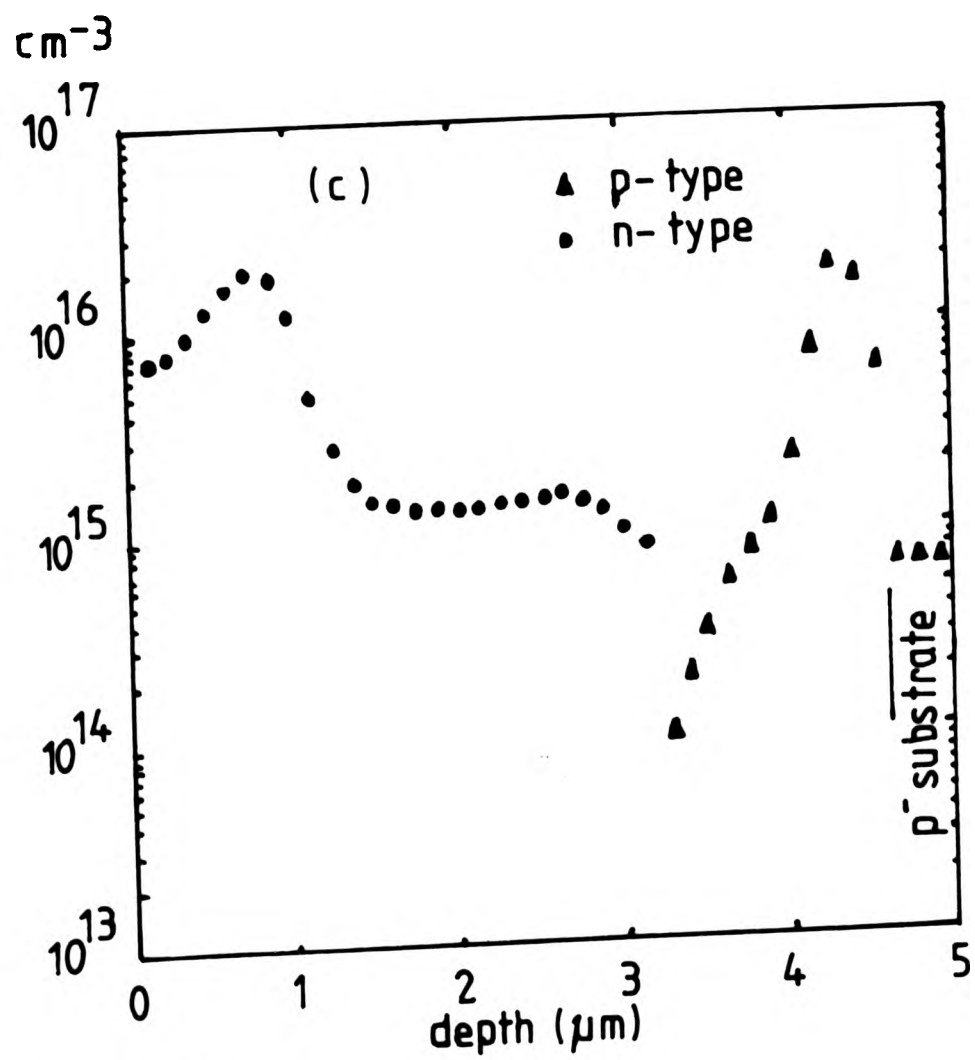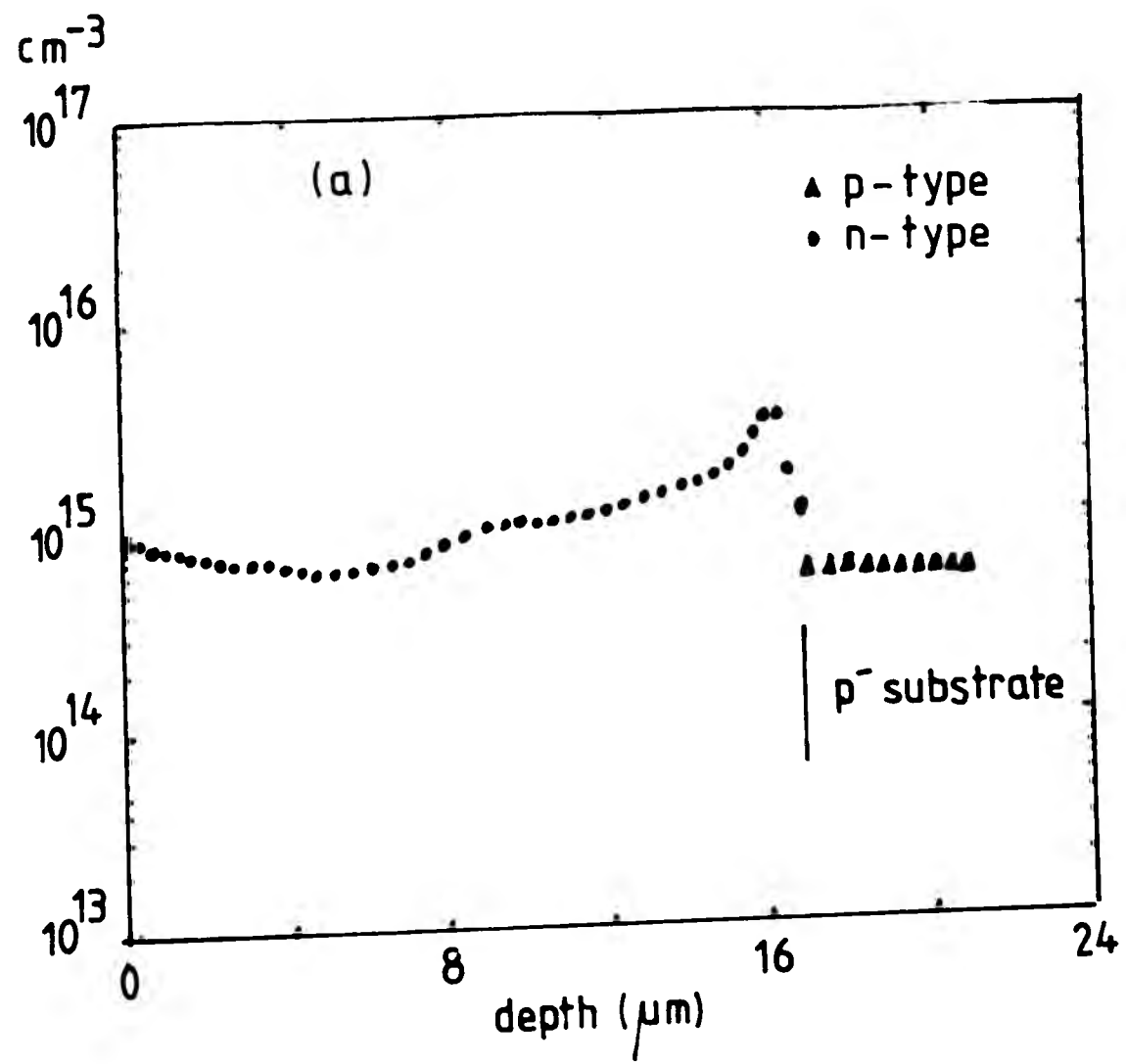
Fig.3.22(a)&(c) Contd.

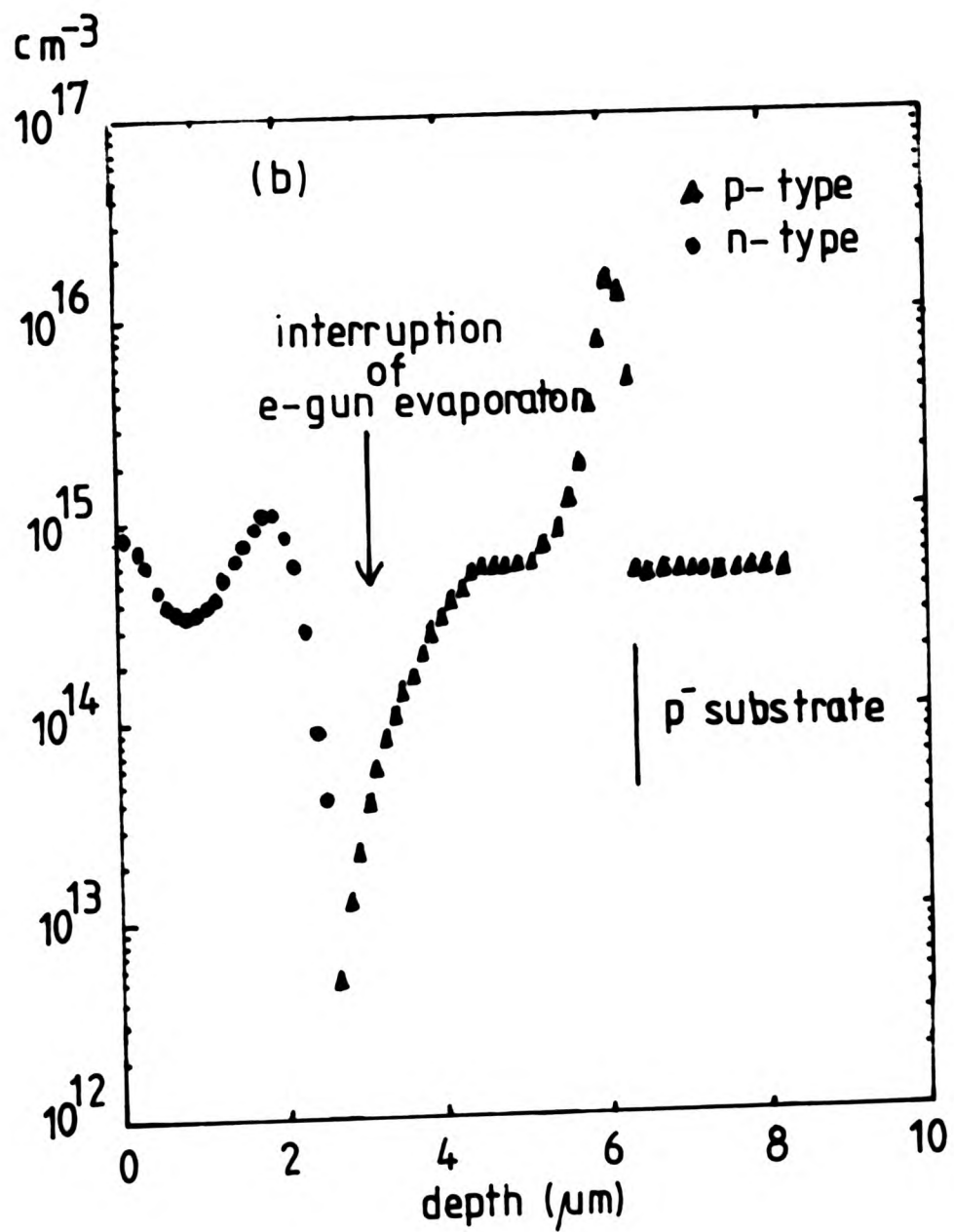Fig.3.22(a),(b)&(c)   Typical SR profiles of undoped Si-MBE
layers grown. Note the presence of a p-type region at the
epitaxial/substrate interface and variation in the carrier
concentration with depth in the n-type region of the
layers.

few undoped layers were relatively highly doped at about 1×10^{16}cm^{-3}. The measured carrier concentration gradually decreased with the growth series to a level between 5×10^{14} and 2×10^{15}cm^{-3}. In series F7, a number of major changes were made to the system. A new boron dopant source cell was installed for the first time. The e-gun evaporators and surrounding walls were shielded with high resistivity Si substrates in an attempt to reduce potential contamination caused by the electron bombardment. Though the subsequent series of layers F8 and F9 showed a drop in the carrier concentration, we suspect some compensation effects occured in some of these layers because of their comparatively low Hall mobilities. The Si source material (1000 ohm cm, Wacker polycrystal Si) was replaced with ultra high purity double pass FZ single crystal in series F12 and a high temperature bakeout of the system (~250°C for 24 hours) was carried out in series F13 representing attempts to further reduce background doping levels. The measured carrier concentrations of the layers grown in these series were in the region of mid to low 10^{15} cm^{-3}.

Our lowest residual doping level acheived during growth (mid 10^{14}cm^{-3}) is however still nearly an order of magnitude higher than the lowest reported levels of $1-3\times10^{13}$cm^{-3} by Ota[9]. In Section 3.4.2 we outlined some of the difficulties in obtaining reliable measurements of residual doping levels in very thin layers commonly grown by Si-MBE. It is our experience that the residual doping levels measured in most thick undoped layers which were grown in an environment where high doping work was also employed, were typically between high 10^{14} and mid 10^{15}cm^{-3}. No positive evidence for memory effects of dopants used in the system (Sb and B) was found at these levels.

We employed two analytical techniques to identify the residual dopant impurity species in our layers. The first technique[89] involved the study of the variation

of the carrier concentration, n, measured by Hall effect
with the absolute temperature of the sample T. Depending on
the degree of compensation in the layer, the slope of the
plot of log n vs 1/T over the limited temperature range
will be determined by the activation energy for ionization
of dopant atoms. The same technique also allows one to
estimate the level of compensation in the layer. Layers
grown in our early series were analyzed and a value of the
activation energy of 0.044eV was obtained indicative of
phosphorus doping[53]. The measurements also indicated
low degree of compensation effect and low $10^{13}cm^{-3}$ of
deep levels were present in our layers.

In the other technique, an Ar laser beam at 200mW
and 488 nm was used to optically excite the sample which
was held at 4.2K. The optical excitation of a
semiconducting material creates electron-hole pairs (
excitons) which then decay subsequently either radiatively
or non radiatively. The radiative decay was monitored by a
high resolution monochromator to give the photoluminescence
(PL) spectrum which is a plot of the detected radiation
intensity vs wavelength of radiation. The interpretation of
the spectrum involves the identification of associated
peaks at certain wavelengths which can be associated with the
presence of the impurity atoms in the crystal lattice. A
typical PL spectrum of our undoped layer grown at $850^{o}C$
is shown in Fig.3.23. The sharp and well-defined exciton
features in the PL spectra obtained in our layers indicated
excellent crystallographic quality of the layers. The
scarcity of peaks far away from the band edge indicated low
concentrations of deep levels confirming the low
temperature Hall measurement. The PL measurements on our
early series layers confirmed unambiguously that
phosphorous was the major residual dopant impurity. In
one layer grown in the later series, peaks which can be
associated to As were seen in the PL spectra. One
interesting result from the PL studies of our layers (and
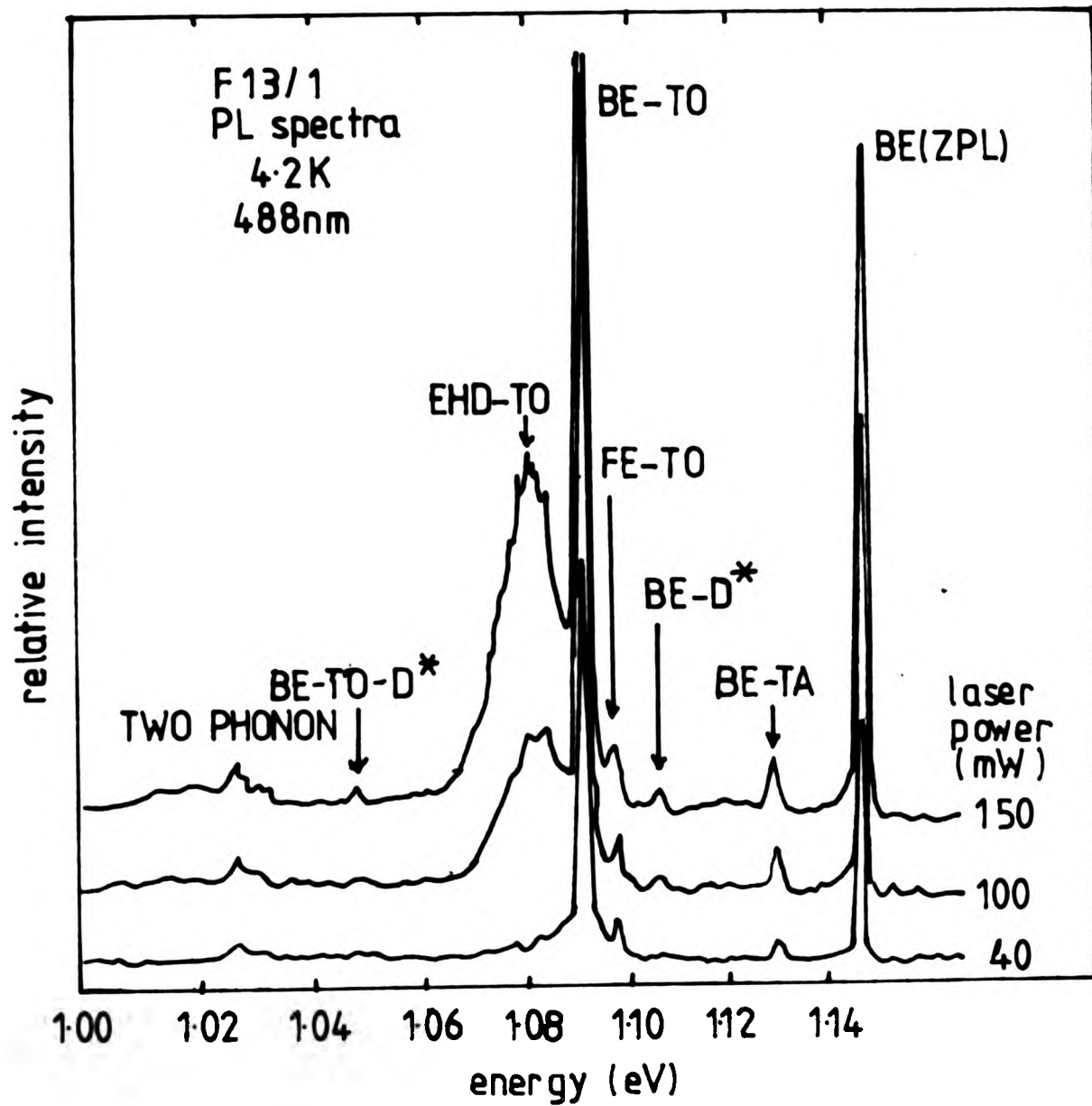subsequently other Si-MBE layers grown by other groups) was

136

Fig.3.23 Typical PL spectra of undoped Si-MBE layers grown at 850°C showing sharp and well-defined features indicative of their high crystallographic and electrical qualities.

the identification of the so-called G-transition in the spectra which has only previously *been* ∧ observed in C-rich Si materials which had been subjected to electron radiation[136]. In contrast, the same transition was not observed on epitaxial layers grown by CVD. Numerous studies of this transition implicated C as the active impurity, though the microscopic nature of the defect was not settled. This result suggests that C incorporation in the layers grown by Si-MBE *is* relatively high; probably due to the residual hydrocarbon background in the growth chamber.

A small peak at 31 amu was always present in the RGA spectra of the growth environment. Though phosphorous is expected at 31 amu, there are a number of hydrocarbons such as ethanol and methanol which can give cracking patterns with fractional peaks at the same mass[137]. On one occasion, we observed a large increase of the 31 amu peak immediately after operating the pneumatic gate-valve to the cryopump on the growth chamber. The gate-valve region was thus suspected as the source of phosphorus, and we later also discovered that the Viton O-ring seal used in the gate-valve had not been treated to the specification for UHV application by the manufacturers (VAT and VG Scientific). Subsequent operations of the gate-valve did not however produce a similar response in the RGA spectra. During the growth of one intentionally undoped layer, the gate-valve was operated repeatedly and used to isolate the cryopump from the growth chamber for a period of 15 minutes. The electrochemical CV profile of the layer is shown in Fig.3.24. No change in the measured carrier concentration was evident that could be associated with these operations, although there was a gradual fall in the level towards the epitaxial surface. We tentatively concluded that the cryopump and gate-valve were not the major source of phosphorous.

The high temperature bakeout and the additional shielding of stainless steel walls near the evaporator with high resistivity Si substrates did not produce any
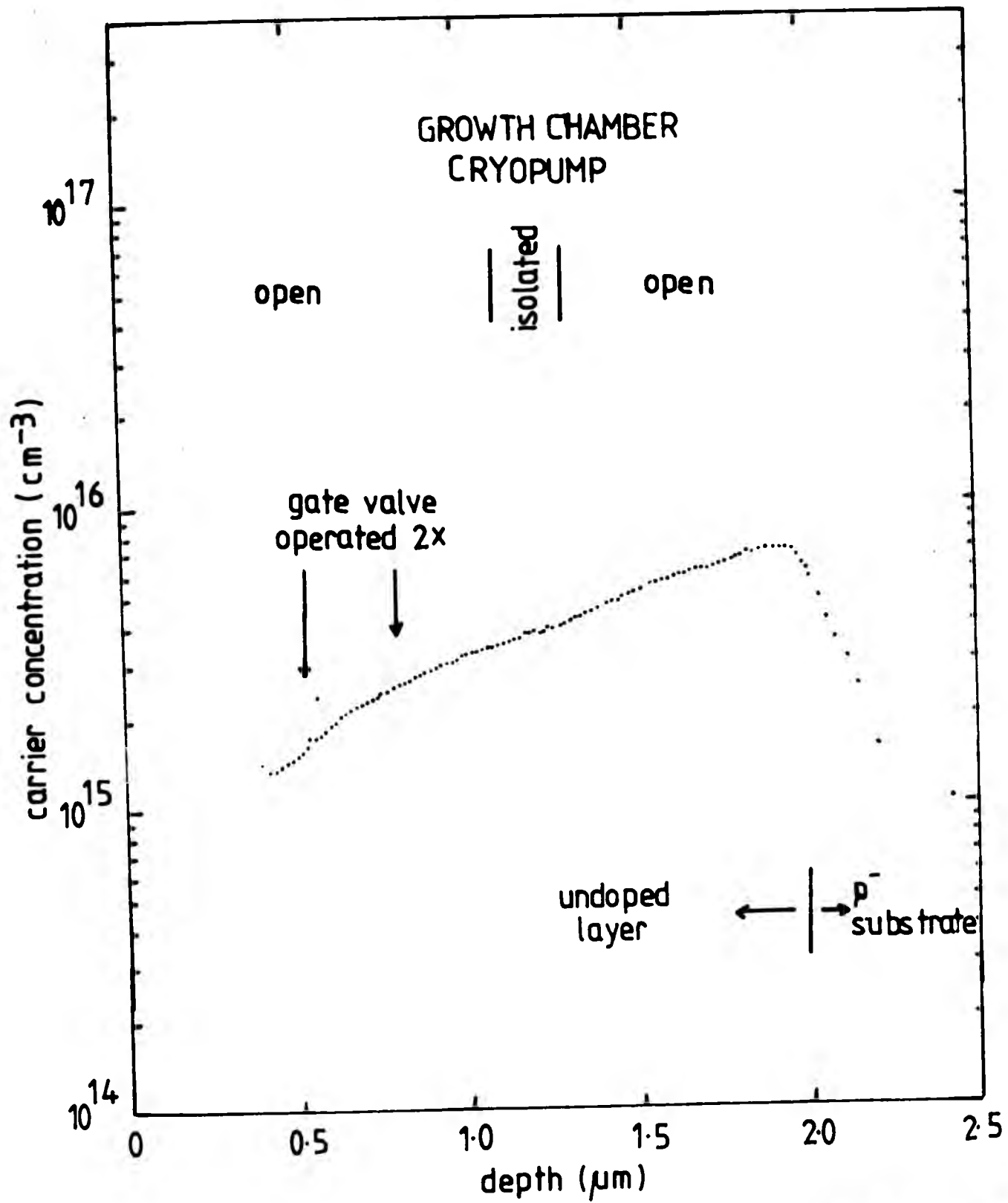
138

GROWTH CHAMBER CRYOPUMP

Fig.3.24 The electrochemical CV profile of an undoped layer grown with the cryopump isolated from the growth chamber and the gate valve operated as indicated. No induced change in the measured carrier concentration profile of the layer was apparent due to the above operations.

consistent reduction in the residual doping level. In the case of layers grown in later series (series F13 onwards), in addition to phosphorus, As impurity was also detected in the PL measurements, which we suspect was a consequence of cross contamination from a newly installed III-V MBE system nearby.

In Fig.3.25, the progress chart shown in Fig.3.21 is reproduced but with the accelerating voltage of the e-gun evaporator used to grow the layer indicated. Athough the data is limited, there seems to be some correlation between the measured carrier concentration of the layers and the accelerating voltage of the e-gun evaporator such that a lower voltage gave a lower residual doping level. We mentioned earlier that some of the dips and humps in the carrier concentration profiles could be attributed to interruption to the operation of the e-gun evaporator. Apparently the accelerating voltage and operation of the e-gun evaporator was influencing the desorption of gaseous dopant species in the system. However, it is difficult to understand why, despite our efforts at shielding the stainless steel walls against electron bombardment that the residual doping level was not consistently reduced. We observed further that when undoped layers were grown on substrates which were electrically isolated, their residual doping levels were a factor of 2 or more higher than normal. It is believed that the electric charge acquired by the isolated substrate and/or charged species from the e-gun evaporator might influence the residual dopant incorporation in the layer (see Section 4.2.1).

In summary, at this stage of our study, we are reasonably confident that we have positively identified phosphorus as the major residual dopant impurity in our layers grown in the early series. We believe the residual level of phosphorus in our layers was reduced well below $1 \times 10^{15} cm^{-3}$. However positive identification of the source remains uncertain. The B contamination on the substrate surface prior to growth was responsible for the
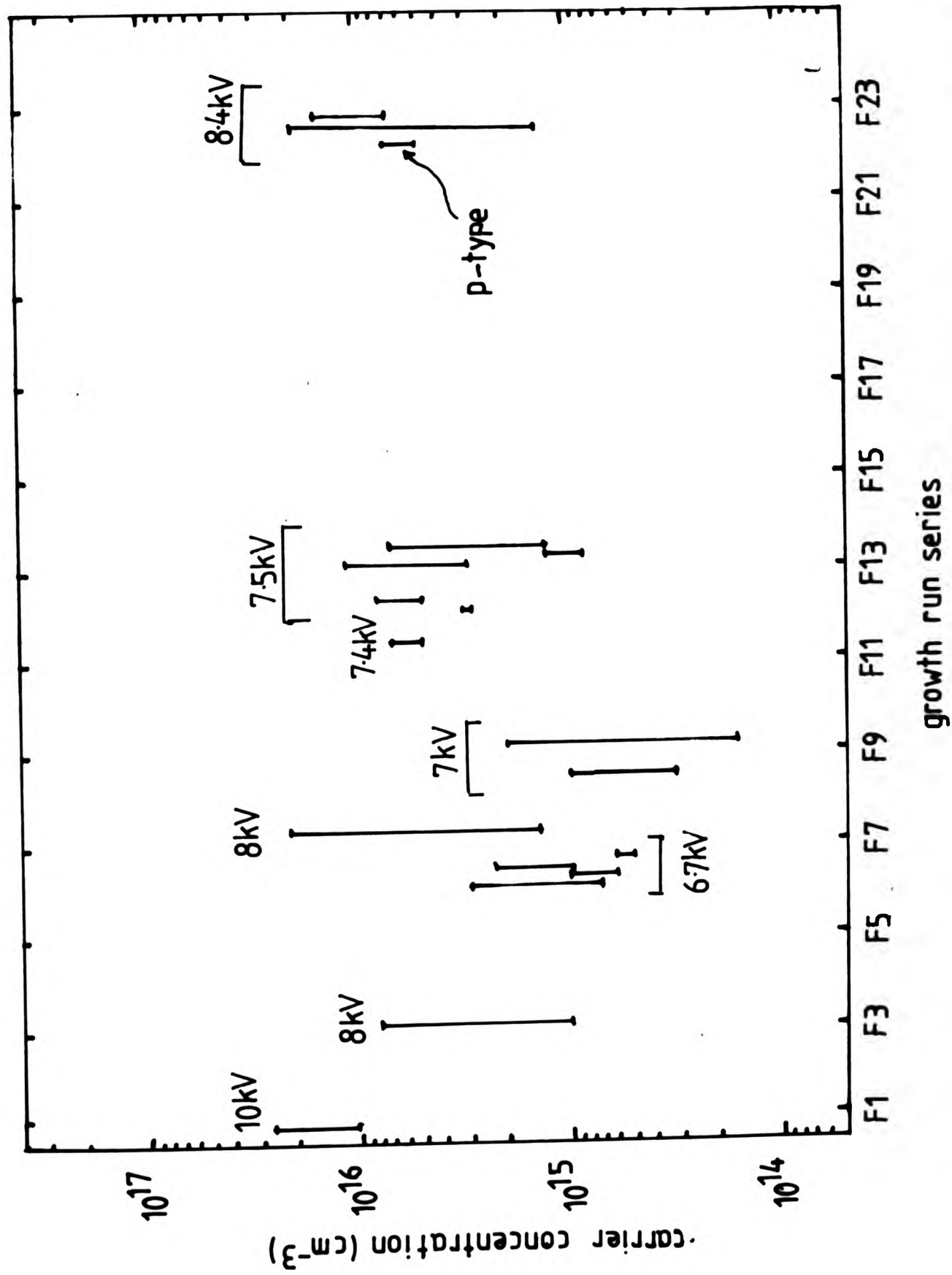
Fig.3.25 As in Fig.3.21, with the e-beam acceleration voltage used in the evaporator during layer growth indicated.

interfacial p-type region in our layers. We have not evaluated the memory effects extensively, the indications are that with Sb and B these effects are not significant for doping levels above mid 10^{14}cm^{-3}. The Hall measurements showed that bulk mobilities were obtained in our undoped layers. The sharp exciton features in the PL spectra indicated the high crystallographic quality of our layers and were comparable to or considered to be better than layers grown by CVD technique.

Chapter 4: n-type and p-type doping

4.1 Co-evaporative p-type Doping

The two p-type co-evaporated dopants studied in Si-MBE so far were Ga and Al[55]. In the case of Al, it was found that the dopant profile control was extremely poor even at high growth temperatures due to the severe surface accumulation effects. It was concluded that Al is unlikely be a useful dopant. Ga was, however, found to be promising when the growth temperature was above $600^{o}C$ where reasonable dopant profile control was achieved. Studies carried out by Iyer et al[64] on the technique of "building-up" and "flashing-off" the suface dopant layer with the epitaxial growth halted showed that very abrupt dopant concentration transitions can be obtained. However such interruptions to epitaxial growth and the rapid changes of substrate temperature required in the process are likely to introduce additional defects in the layer.

We investigated the potential use of boron as a new co-evaporated dopant in Si-MBE. It was suspected that due to its low vapour pressure characteristic and relatively small atomic size, boron might not accumulate on the surface like Ga and Al and thus facilitate very abrupt dopant profile control without resorting to the technique mentioned above. B is also a preferred dopant in the conventional Si technology where its physical behaviour has been well characterized.

4.1.1 Source Materials for Boron as Co-evaporated Dopant

Elemental boron which is readily available at purity of 5N's is an obvious choice. Solid boron is mechanically hard and brittle, and cannot be easily machined into useful shapes. High purity pBN is widely used in MBE as lining in Knudsen source cells and also as electrical insulators. It

143

is reported that pBN on heating to above 1700°C slowly dissociates into its constituent species[138]. Both B and pBN have the major disadvantage of requirement of very high temperatures (1200 -1800°C) to generate the dopant flux to achieve a useful range of dopant concentration.

Other boron compounds[139] such as B_2O_3, B_2S_3 and BP are unlikely to be a useful B source in MBE. Sublimation of B_2O_3 occurs in vacuum above 300°C whilst BP loses phosphorus at high temperatures to give lower phosphide $B_{12}P_2$. B_2O_3 vaporizes on heating and its decomposition would therefore have to occur at the epitaxial surface. In all cases, the decomposed species O, S and P from these compounds are likely to perturb the epitaxial growth.

On the criteria of flux purity, simplicity of use and UHV compatibility, it appears that there are only two suitable choices, B and pBN as a source of B, in spite of their high source temperature requirement.

4.1.2 Design of Boron Source Furnace

In order to achieve a useful range of dopant concentration in the layer(10^{14}-10^{20}cm^{-3}), we require source cell temperatures ranging between 1200 and 1800°C. Such high temperatures cannot be attained in the conventional Knudsen sources. We therefore constructed our own source furnace capable of reaching high temperatures at modest power inputs. A schematic diagram of our boron dopant source furnace is shown in Fig.4.1. The basic structure of the furnace was constructed exclusively of Ta material with the exception of the heater filament and source container. Extensive heat shielding of the furnace was employed.

In our first design, the heater element consisted of a conventional Ta boat containing 5N purity boron as the source. The boat was welded between the two electrical
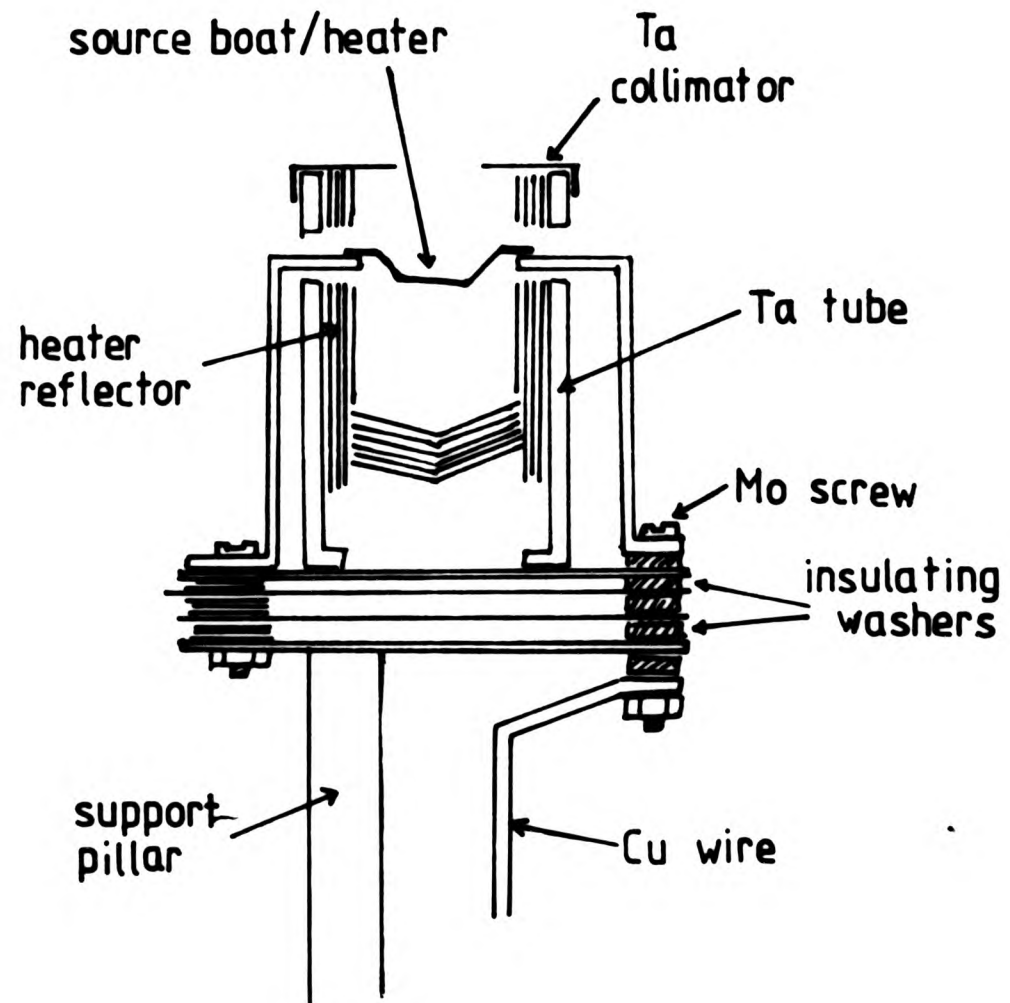
144

Fig.4.1 Construction of a Si-MBE boron dopant furnace.

feeds and resistively heated. Doping levels as high as $1 \times 10^{18} cm^{-3}$ were achieved using this source furnace. However the lifetime of the boat was short and apparently limited by the chemical reaction at high temperature between boron and tantalum. A number of other refractory metals such as molydenum and tungsten were also tried as the boat material, but with little or no improvement in the lifetime.

In the second design, the heater element was replaced with a strip of Ta foil/coil and pBN was used as the source. The pBN was either placed on top of the Ta strip or wrapped within the coil. Though the useful life of the heater element was considerably extended, the doping characteristics of pBN made it difficult to control and achieve uniform doping as shown by the electrochemical CV profile of a layer doped by a pBN source in Fig.4.2.

The next design consisted of a graphite cell (15mm length x 4mm diameter) heated within a tungsten coil. The open end of the graphite cell was mounted pointing towards the substrate. This design was proved very successful and doping levels above mid $10^{19} cm^{-3}$ were readily obtained. The exceptionally inert nature of graphite, even at elevated temperatures, was considered to be the major factor contributing to the long lifetime of the source element. One minor difficulty experienced was the erratic variation in the contact area between the tungsten coil and the conductive graphite cell during operation, which caused some variation in the power input to the furnace.

In our later design, a graphite tubing was used as both the heater element and container. The tubing (20mm length x 3mm diameter) was mounted vertically by clamping with Ta foils to the electrical feeds. The thin wall of the tubing (~1mm) was heated resistively. This design offered an improved control over the power input to the source furnace over other previous designs. Doping levels up to ~$1 \times 10^{20} cm^{-3}$ were reached.
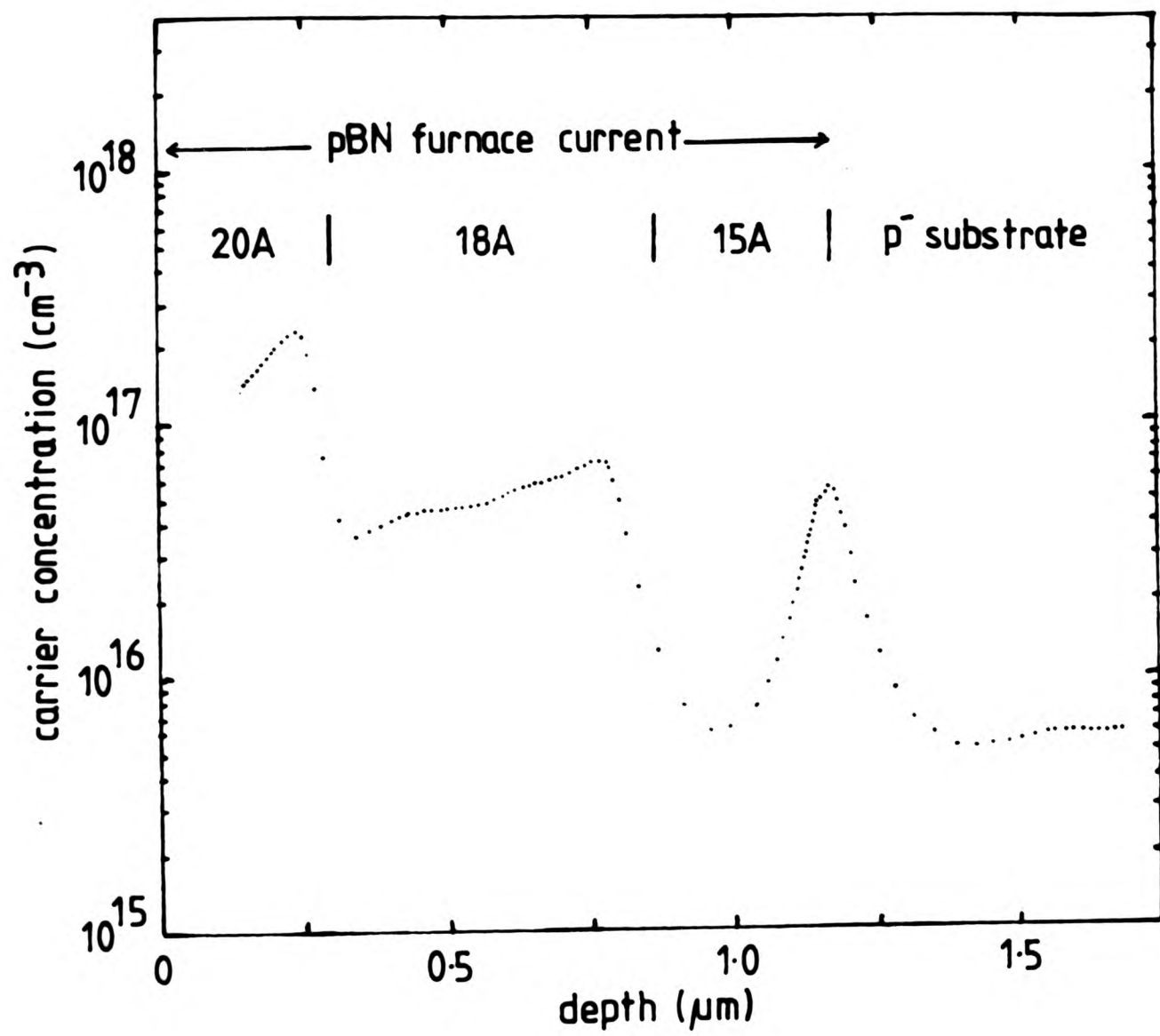
Fig.4.2 Electrochemical CV profile of a boron-doped layer
using the pBN source.

The dopant flux generated from the source was entirely controlled by the power input to the furnace. It suffered from the requirement for routine recalibration after replacement of the source/heater element. It is considered useful to incorporate a pyrometer to monitor the furnace temperature, and, using a feedback control system, to achieve a better control over the dopant flux.

4.1.3 Properties of Boron doped Layers[140]

Uniformly B-doped layers grown on n- substrates (1-10 ohm cm) with thickness varying between 2-6μm were used for Hall and electrochemical CV measurements. Typical growth temperatures were 700-900°C. The measured Hall mobility μ_H vs resistivity ρ of the layers are shown in Fig.4.3. Bulk data of Morin and Maita[141] for boron doped Si is indicated by the solid curve. It can be seen that the Hall mobilities of our layers are comparable to the bulk value over the range of 10^{16}-10^{20}cm^{-3}. The highest boron doping level reached was 1×10^{20}cm^{-3} (r=1), compared to an expected solid solubility limit of $~5\times10^{20}$cm^{-3} of B in Si at 850°C[53].

The relationship between the doping level and the power input to one typical boron source furnace is shown in Fig.4.4. It is evident that the doping level was independent of the substrate temperature within the experimental errors over the range of 700 - 900°C. The implication of the observed doping behaviour is the occurrence of unity sticking coefficient. This is in marked contrast to the all other coevaporated dopants such as Sb, Ga and Al. It is considered that due to the relatively small size of the boron atoms, they are incorporated into the Si lattice easily, and its low vapour pressure at the growth temperature precludes re-evaporation, that a high sticking coefficient is observed.
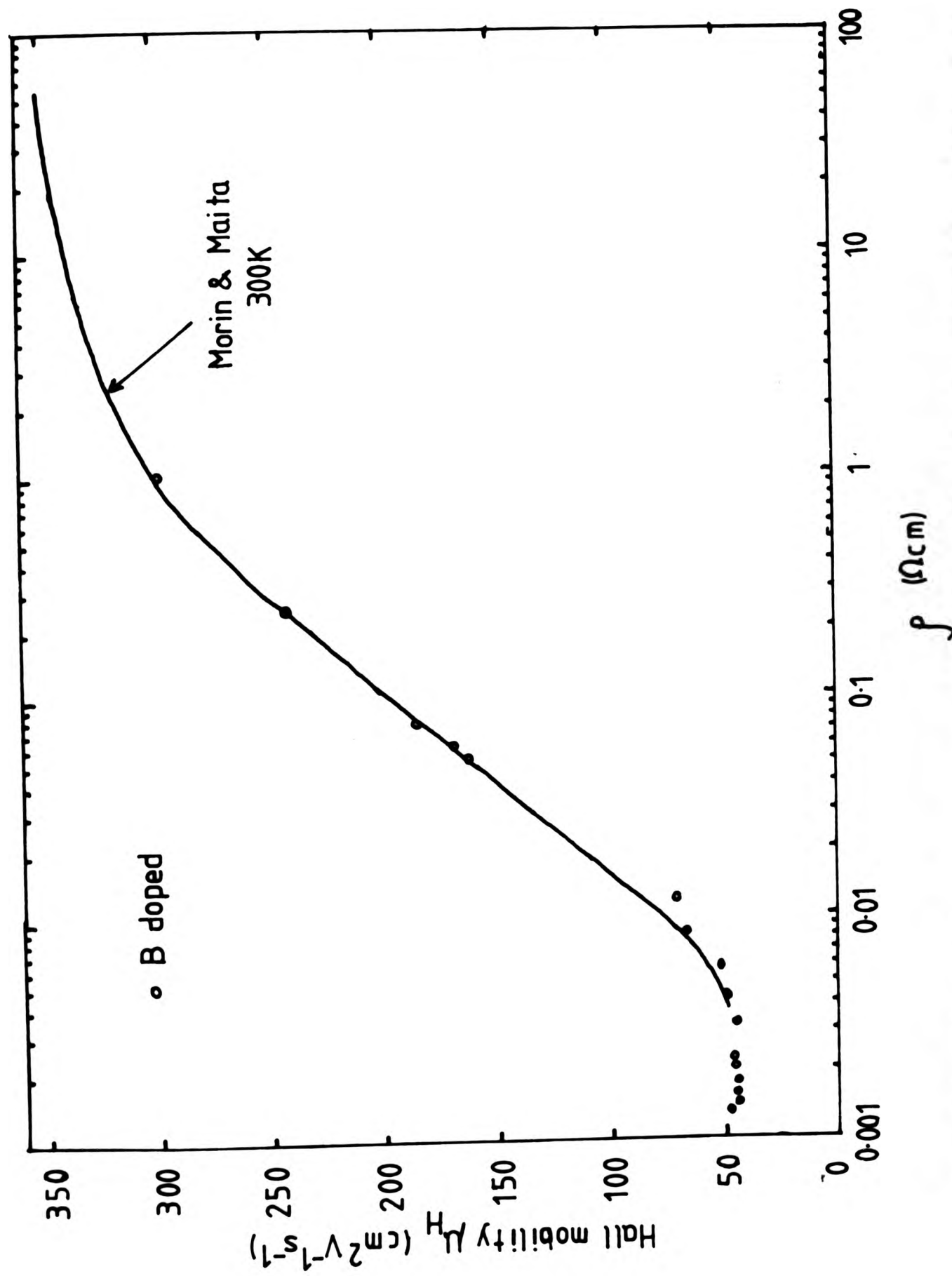
148

Fig.4.3 Plot of the measured Hall mobilities μ_H vs resistivities ρ in boron-doped layers at room temperature. The bulk Hall mobility data is represented by the solid curve in the plot.
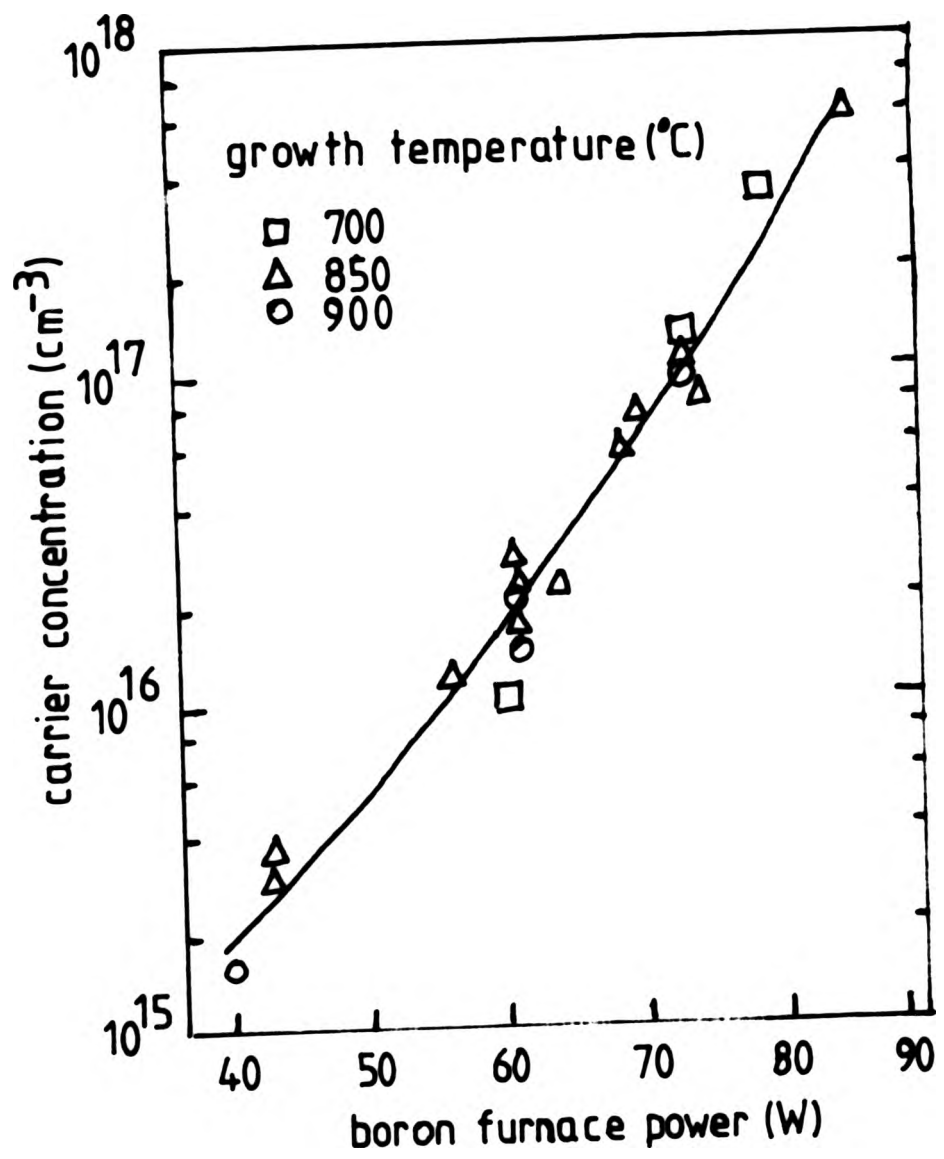
149

Fig. 4.4 The doping concentrations measured in layers grown at different temperatures vs the power inputs to the boron dopant furnace.

150

Defect assessment of the boron doped layers using preferential chemical etching indicated that no additional crystallographic defects were introduced through the use of boron doping. In cases of heavily doped layers (>$5 \times 10^{17} cm^{-3}$), it was found that the etched surfaces were stained by the Secco etch. However, staining did not occur when diluted etchants such as dilute Schimmel etch[116] were used showing that the staining was not associated with the defect content in the layers. Similar observations were also reported by Ota[129] on heavily doped materials.

It is suspected that some additional C incorporation in the boron doped layers may occur with the use of the graphite crucible in the boron furnace. The total vapour pressures of C at $1500^{o}C$ and $2000^{o}C$ compared to those of boron are lower by a factor of 5×10^{3} and 10^{2} respectively[142]. High C levels in Si substrates can have a detrimental effect on device performance during the processing stages[143]. We have not yet investigated the extent of C incorporation in the layers. Preliminary photoluminescence studies of undoped Si-MBE layers[136] indicated that C was incorporated in the layers during growth, although it is difficult to quantify to what extent. It was thought that the C originated from C-containing residual gas species such as CO and CH_4. We believe that any C incorporation derived from the graphite crucible could be avoided by employng a direct resistive rather than radiative heating of boron.

4.1.4 Boron Dopant Profiles in Layers

Layers with arbitrary dopant profiles were grown to assess the doping profile control obtainable using the boron source. The required doping levels were obtained by adjusting the power input to the boron furnace in accordance with a similar calibration curve as shown in

Fig.4.4. We estimated that the time constant of the temperature response of the furnace to be of the order of a few seconds and therefore well suited for rapid dopant flux changes. Fig.4.5(a) is a schematic diagram of the doping program used in growth of F15/4. Doping transitions were achieved either by operating the dopant shutter or ramping the power input. Fig.4.5(b) shows the SR and electrochemical CV profiles of F15/4. The concentration transitions at the dopant spikes can be seen to be as abrupt as 150 $\mathring{A}$/decade. However, there is a visible and gradual increase in the extent of smearing of the dopant spikes with their depths below the epitaxial surface.

This smearing of the profiles could be the result of a number of factors such as (a) measurement artifacts and (b) dopant diffusion in lattice. Since the smearing was observed when the dopant shutter was used instead of power input ramping, it is unlikely the thermal response of dopant source could not to be the cause of the smearing. Further work would be required in order to determine the contribution to profile smearing from (a) and (b). Rough estimate of the expected amount of boron diffusion at the growth temperature of $850^{\circ}C$ was made. For example, the deepest boron spike shown in Fig.4.5(b) was "annealed" at the growth temperature for about 40 minutes. At $850^{\circ}C$, the diffusion coefficient D of boron in $Si^{(53)}$ is about $3 \times 10^{-16} cm^2 s^{-1}$ giving a diffusion length $2\sqrt{(Dt)}$ of about $170\mathring{A}$. It appeared therefore that the smearing could be the result of dopant re-distribution due to solid diffusion in the layer.

This was confirmed by subsequent studies where two boron doped samples were heat-treated in a nitrogen atmosphere at $900^{\circ}C$ for a period of 30 and 60 minutes respectively. The dopant profiles of the sample after the heat treatment were re-measured using spreading resistance measurement as shown in Fig.4.6. It is evident from the profiles that boron diffused significantly at $900^{\circ}C$.
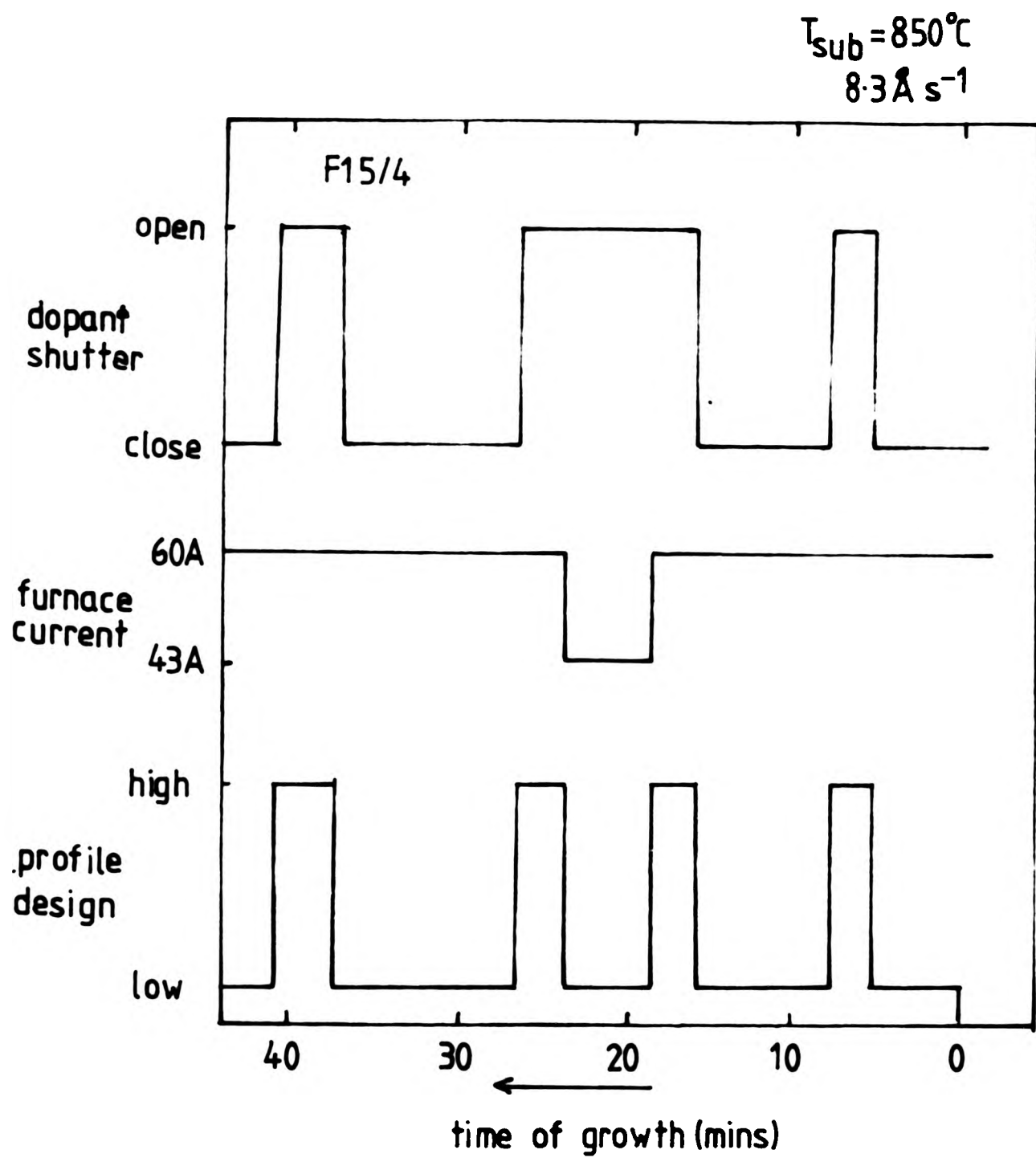
152
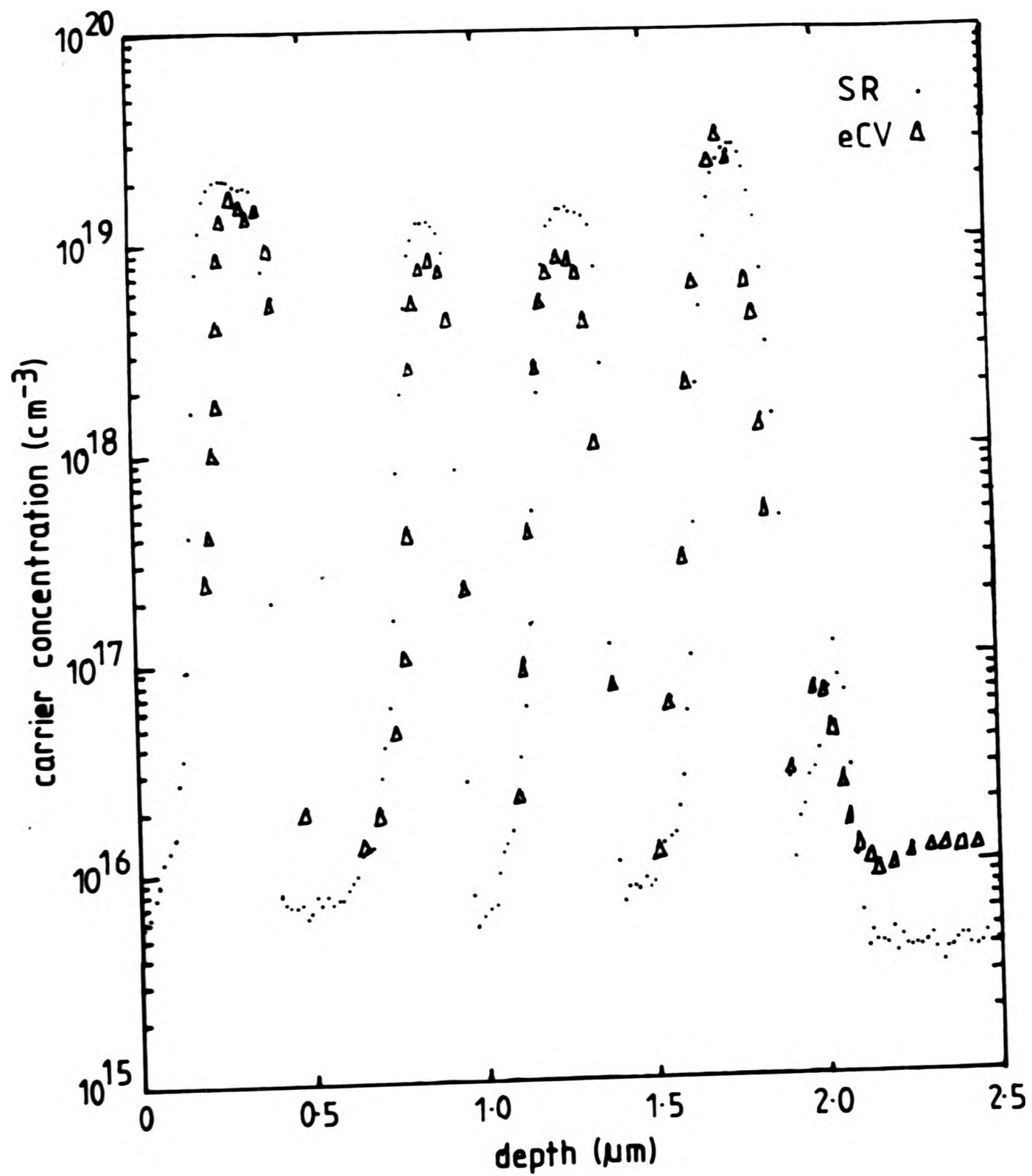
Fig.4.5 (a) Power input program of the boron dopant furnace used during the growth of a layer, and (b) the electrochemical CV profile of the layer.

153

Fig.4.5 (a) Power input program of the boron dopant furnace used during the growth of a layer, and (b) the electrochemical CV profile of the layer.

154

(a)

900°C 30mins

Fig. 4.6(a)&(b) SR profiles of the layer shown in Fig. 4.5 after further annealing at 900°C for periods of 30 and 60 minutes in an N_2 atmosphere indicating progressive boron diffusion in the layer.
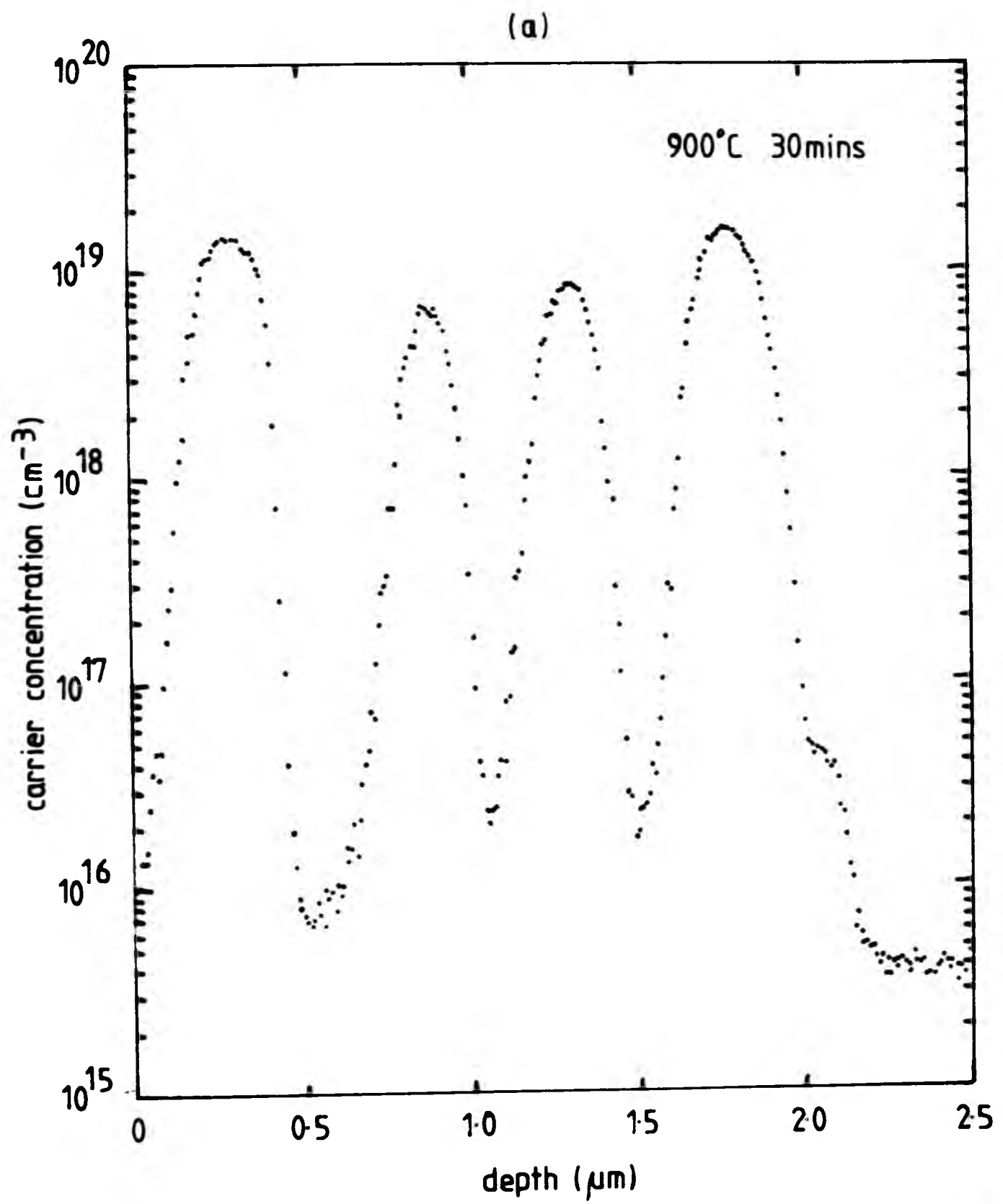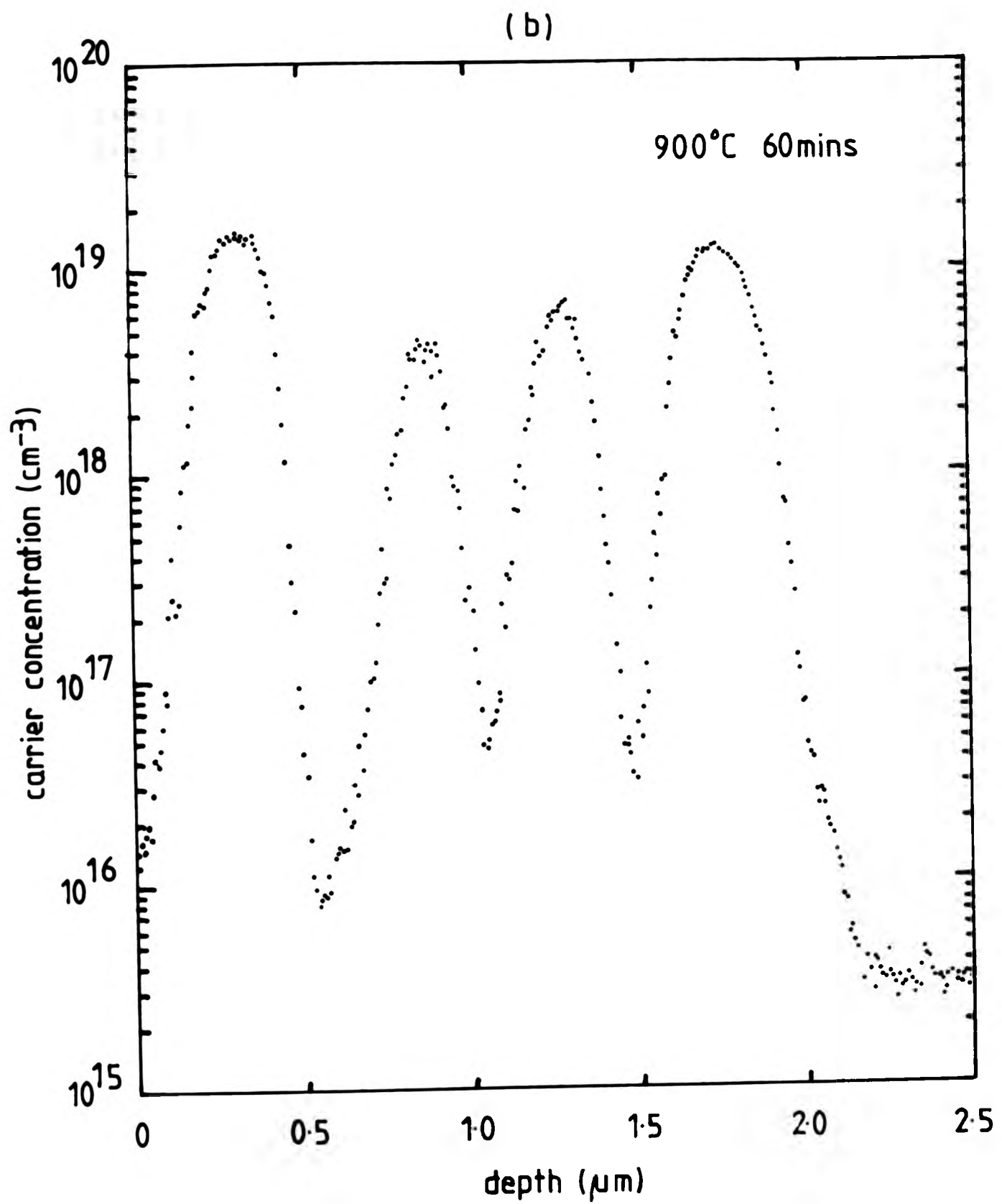
(b)

Fig.4.6(a)&(b) SR profiles of the layer shown in Fig.4.5 after further annealing at 900°C for periods of 30 and 60 minutes in an N_2 atmosphere indicating progressive boron diffusion in the layer.

Independent SIMS measurements of similarly heat-treated boron doped samples confirmed the boron diffusion at the growth temperature of 900°C. It is concluded that in order to avoid smearing of the boron dopant profile in the layer, a growth temperature below 800°C is essential.

4.2 Co-evaporative n-type Doping

The major problems associated with using Sb as a co-evaporated dopant in Si-MBE have been discussed in Section 1.4.1, namely, Sb has very low sticking coefficient at typical growth temperature of 850°C. As a result it is difficult to achieve doping levels much above 1×10^{18} cm^{-3}. The use of excessively high dopant flux or lowering of the growth temperature to < 650°C is neccessary to achieve doping levels above $1 \times 10^{18} cm^{-3}$. Sb also exhibits the undesirable effect of surface accumulation which hampers the introduction of abrupt dopant profiles without resorting to the "flash-off and build-up" technique[64].

In the course of this work we discovered a new co-evaporative doping method in which the sticking coefficient of the dopant is significantly enhanced by applying a potential to the substrate during growth. We later also show that this method offers a very simple and yet effective way of introducing dopant profiles and achieving very high doping levels in the epitaxial layers.

We have denoted this intriguing phenomenon of enhancement of sticking coefficient of dopants by applying an electrical potential to the substrate as Potential Enhanced Doping (PED).

4.2.1 Potential Enhanced Co-evaporative Doping Method

The effect of applying a substrate potential during layer growth on the incoporation of Sb in the layer is

illustrated in Fig.4.7, which shows a plot of the measured dopant concentration vs the applied substrate potential under typical growth conditions of $T_s = 800^{\circ}C$, $3\mu m\ hr^{-1}$ and $T_{Sb4} = 315^{\circ}C$.

It can be seen that the enhanced dopant concentration, n, is related to the substrate potential, V, by the expression:

$$n = N_o [\ V\ ]^p \qquad \ldots\ldots\ldots\ldots(4.1)$$

where N_o = dopant concentration at zero potential

V = negative substrate potential

p ~ 2   (Sb doping)

We found that the same expression also applied under other growth conditions of different dopant fluxes (namely different dopant source temperatures) and substrate temperatures over the range of $700-900^{\circ}C$. An enhancement of up to a factor of 1000 was seen. Changes in the growth parameters appeared to change only the value of N_o in Eq.(4.1). When a positive substrate potential was used, the enhancement effect was observed to be significantly weaker, i.e. a reduced value of p in Eq.(4.1). No substantial difference in the PED effect was observed between using Sb generated from InSb and from elemental Sb. It is known that the vapour generated from elemental Sb consists mainly of Sb_4 with a small fraction of Sb_2[144]. In accordance with the thermodynamic equilibrium of GaAs, it is believed that the vapour generated from InSb consists mainly of Sb_2. The ratio of In:Sb in the vapour is probably in the region of 1000:1.

Preliminary work on the PED effect using other dopants was initiated. Though the effect was also observed in As doping (generated from InAs and GaAs), it was significantly weaker regardless of the polarity of the substrate potential used (see Fig.4.7). In the case of boron, we found that the measured carrier concentration was
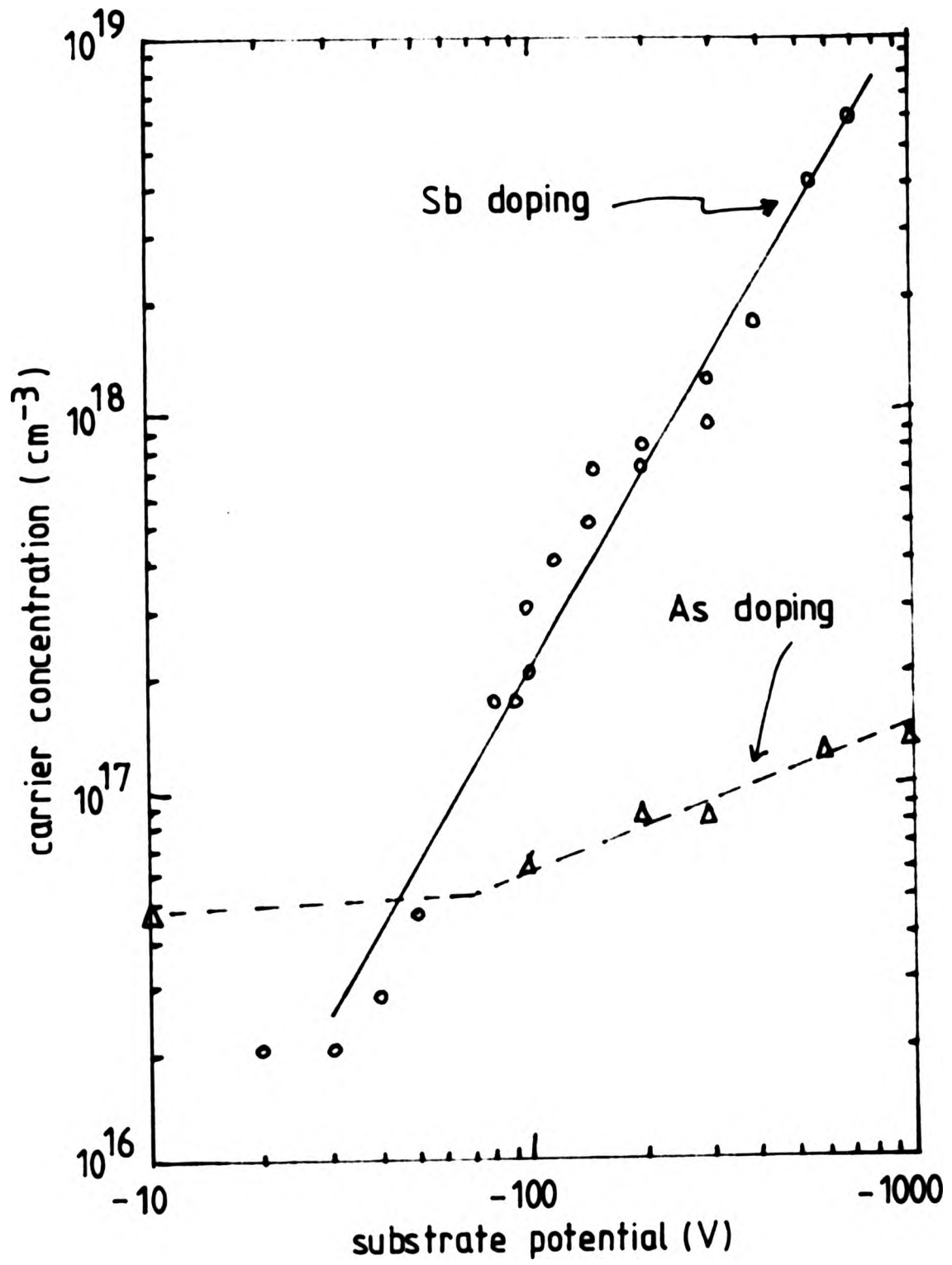
Fig.4.7 Enhanced co-evaporated Sb and As doping by the application of substrate potential during Si-MBE.

159

depressed by the use of substrate potential. Further assessment of these layers using Hall measurements indicated increased compensation in the layers which we suspect, was due to the enhanced incorporation of the n-type residual dopant species.

We observed that alteration to the source cell design and its positioning relative to the e-gun evaporator could alter the doping level vs substrate potential relationship as indicated by Eq.(4.1). Though we have not carried out a detailed study to elucidate the cause of the variation in the doping enhancement with the system geometry, it was considered that the proximity of the dopant flux to the e-gun evaporator could be crucial in the PED effect.

4.2.2 Properties of Enhanced Sb-doped Layers

A range of uniformly doped layers were grown by simply varying the substrate potential with the dopant flux kept constant. The Hall mobilities μ_H of these enhanced Sb-doped layers vs their resistivities ρ are shown in Fig.4.8. The bulk data of Morin and Maita[141] for phosphorus doped Si is represented by the solid curve. It can be seen that the use of PED effect did not degrade the Hall mobility in the layers.

No additional crystallographic defects were identified to be associated with the enhanced doping effect, even at doping levels as high as $^-2 \times 10^{19} cm^{-3}$. This is in marked contrast to most heavy Sb-doped layers as reported by other workers. Konig et al[62] found that at doping levels above $1 \times 10^{18} cm^{-3}$, clusters of stacking faults were frequently observed with densities of above $10^4 cm^{-2}$. They described these clusters as multiple and poly stacking faults. These poly stacking faults are not to be confused with the particle-induced stacking faults we described in Section 3.3.6 which are not affected by the
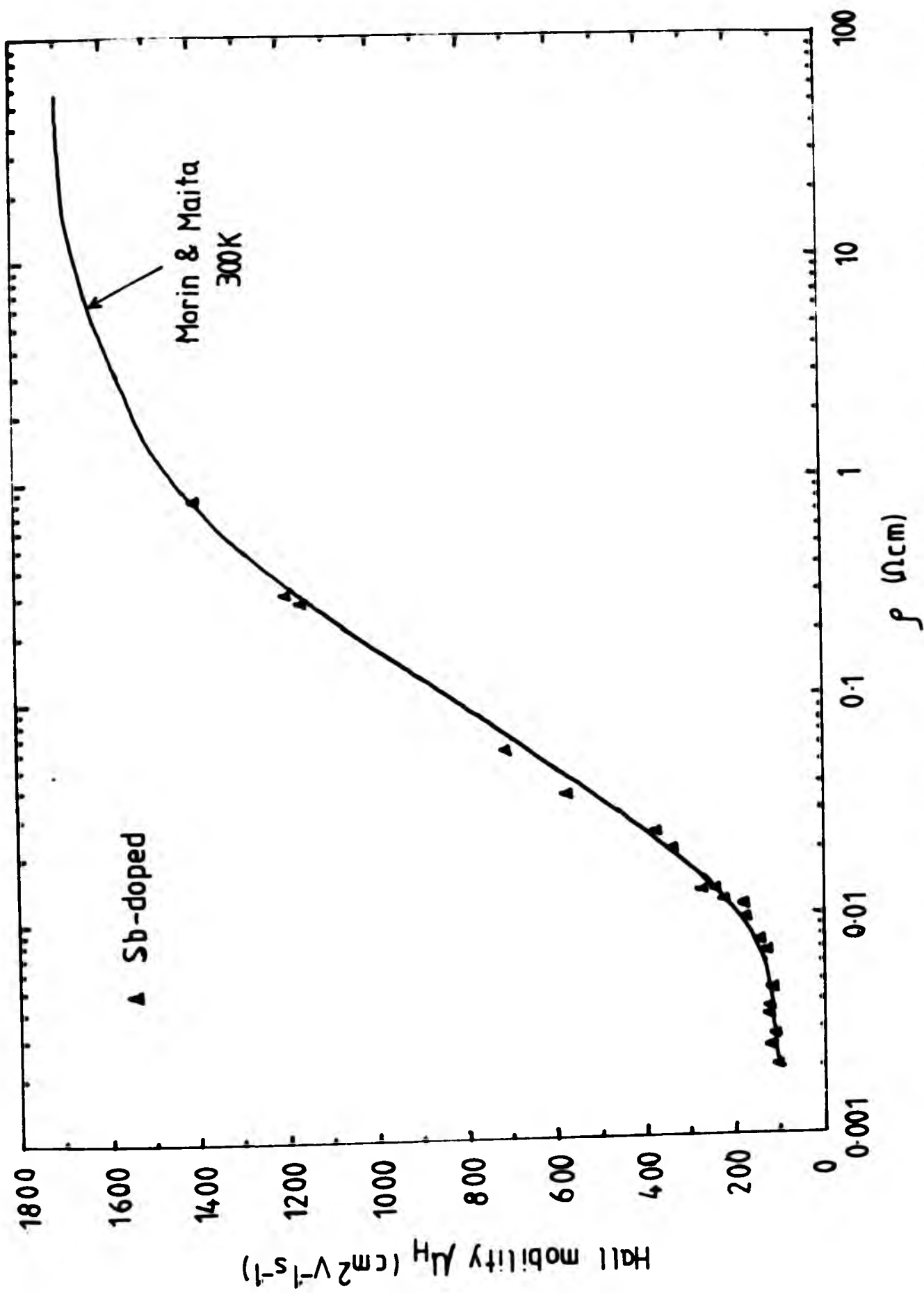
Fig.4.8 Plot of the measured Hall mobilities μ_H vs resistivities ρ in Sb-doped layers at room temperature. The bulk Hall mobility data is represented by the solid curve in the plot.

161

doping of the layers. They further showed that, at doping levels of $\sim 1 \times 10^{19} cm^{-3}$, poly stacking fault densities as high as $10^7 cm^{-2}$ were observed with an abrupt drop in the measured Hall mobilities. These defects were attributed to the high Sb fluxes required to obtain the high doping level. Shiraki et al[145] also reported the problem of excessively high Sb flux degrading the layer quality.

It is clear that use of the PED effect removed the need for high Sb flux and the lowering of the growth temperature in order to achieve heavy Sb-doped layers, and this led to the observed high quality of our n^+ materials.

4.2.3 Arbitrary Sb Dopant Profiles by PED Technique[146]

The simple expression relating the dopant concentration and substrate potential during growth suggests that, in principle, by applying a predetermined substrate potential profile, any dopant concentration profile can be obtained. Fig.4.9(a) is a typical example of a Sb dopant profile in a layer grown by this technique. With the substrate temperature at $850^{\circ}C$ and the Sb dopant source at $300^{\circ}C$, the substrate potential was ramped and the dopant source shutter was operated as indicated in Fig.4.9(b). Dopant concentration transitions of more than two orders of magnitude were obtained. This clearly illustrates the simplicity of the PED technique in introducing arbitrary dopant profiles with a wide dynamic range of doping levels.

Fig.4.10(a) is the profile of a low Sb-doped region of $\sim 0.2\ \mu m$ width embedded in an otherwise high Sb-doped layer on n- substrate. During the growth, the substrate was maintained at $-350V$, and the low doped region was obtained by closing the dopant source shutter for ~ 5 mins as shown in Fig.4.10(b).

162

Fig.4.9 (a) The electrochemical CV (Δ) and SR ($\cdot$) profiles of a typical Sb-doped layer grown using the PED technique. (b) shows the use of the dopant cell shutter and substrate potential during growth.
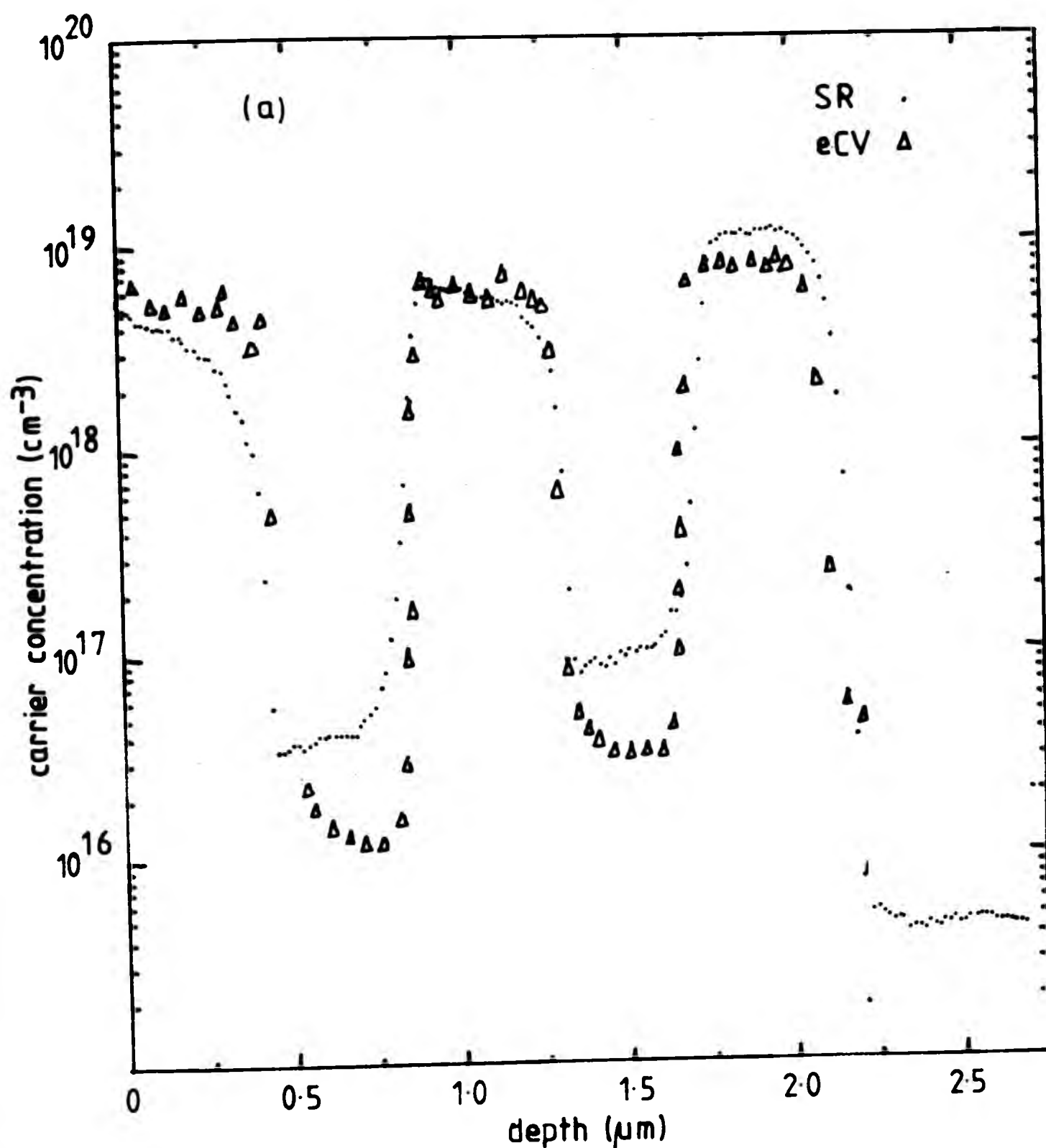
Fig.4.9 (a) The electrochemical CV (Δ) and SR (.) profiles of a typical Sb-doped layer grown using the PED technique. (b) shows the use of the dopant cell shutter and substrate potential during growth.

164
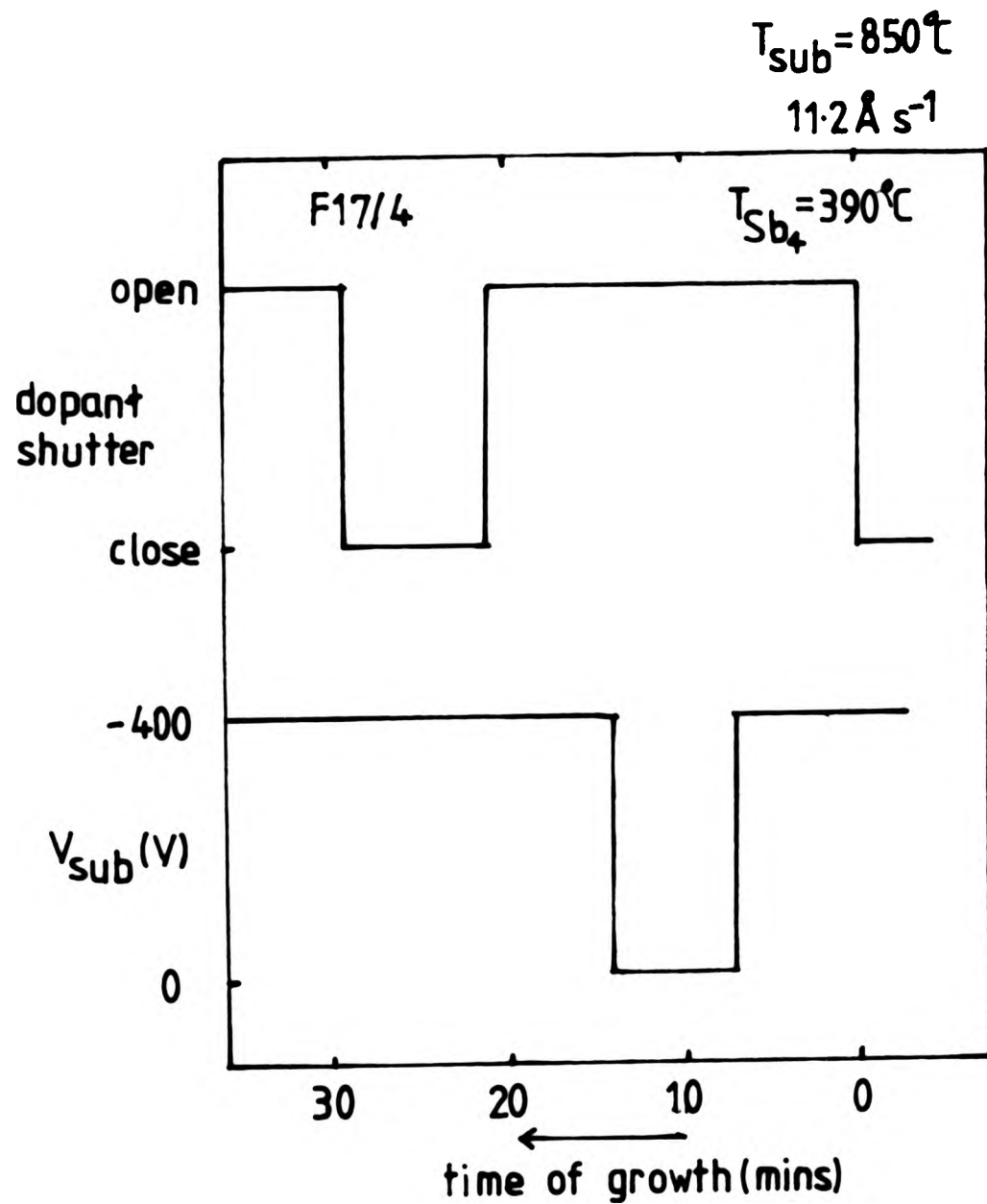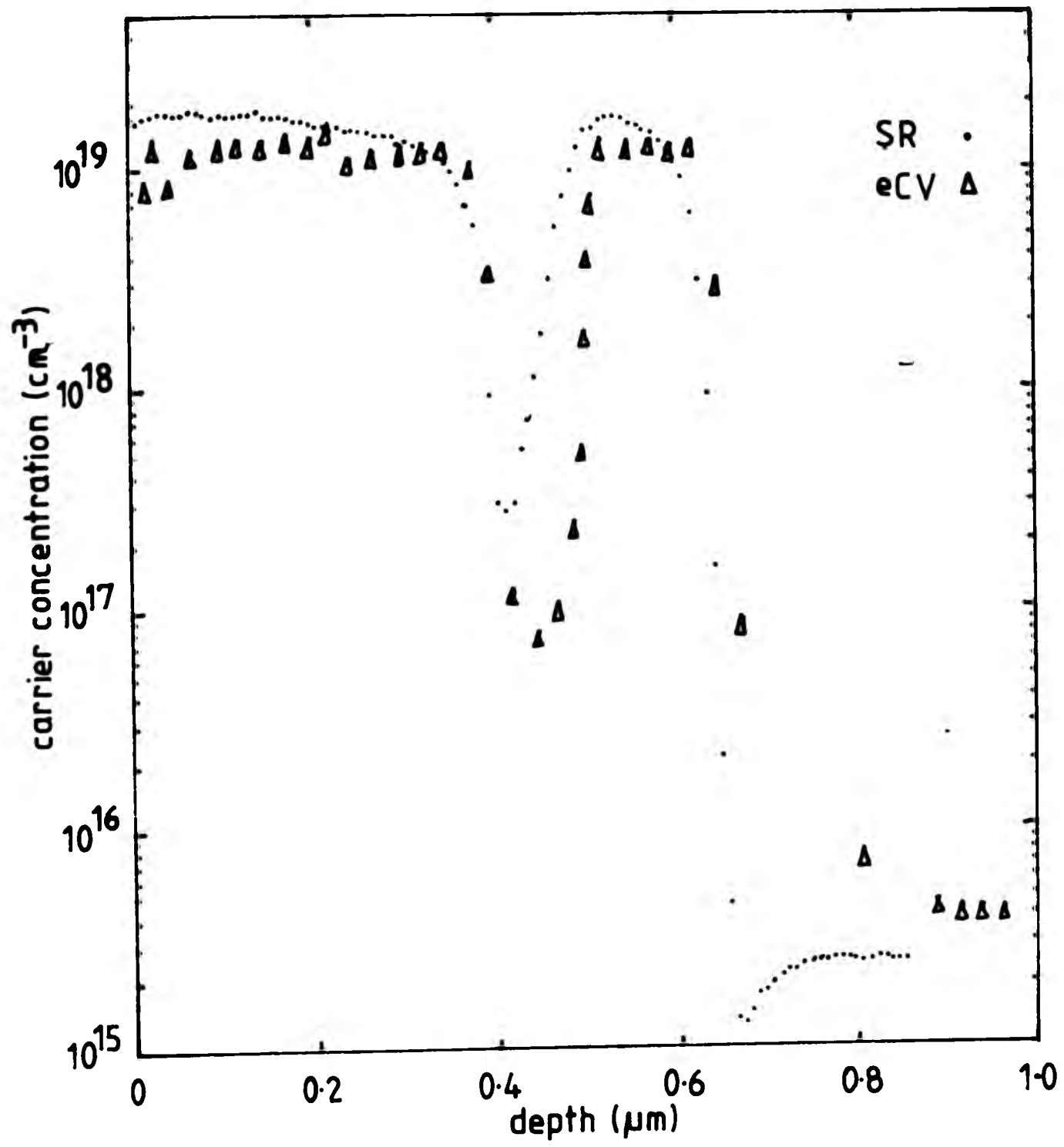
Fig.4.10(a)&(b) Growth of a low Sb-doped 0.2μm region embedded in an otherwise highly Sb-doped layer by closing the shutter of the dopant cell briefly whilst maintaining the substrate potential at -350V as indicated in (b).
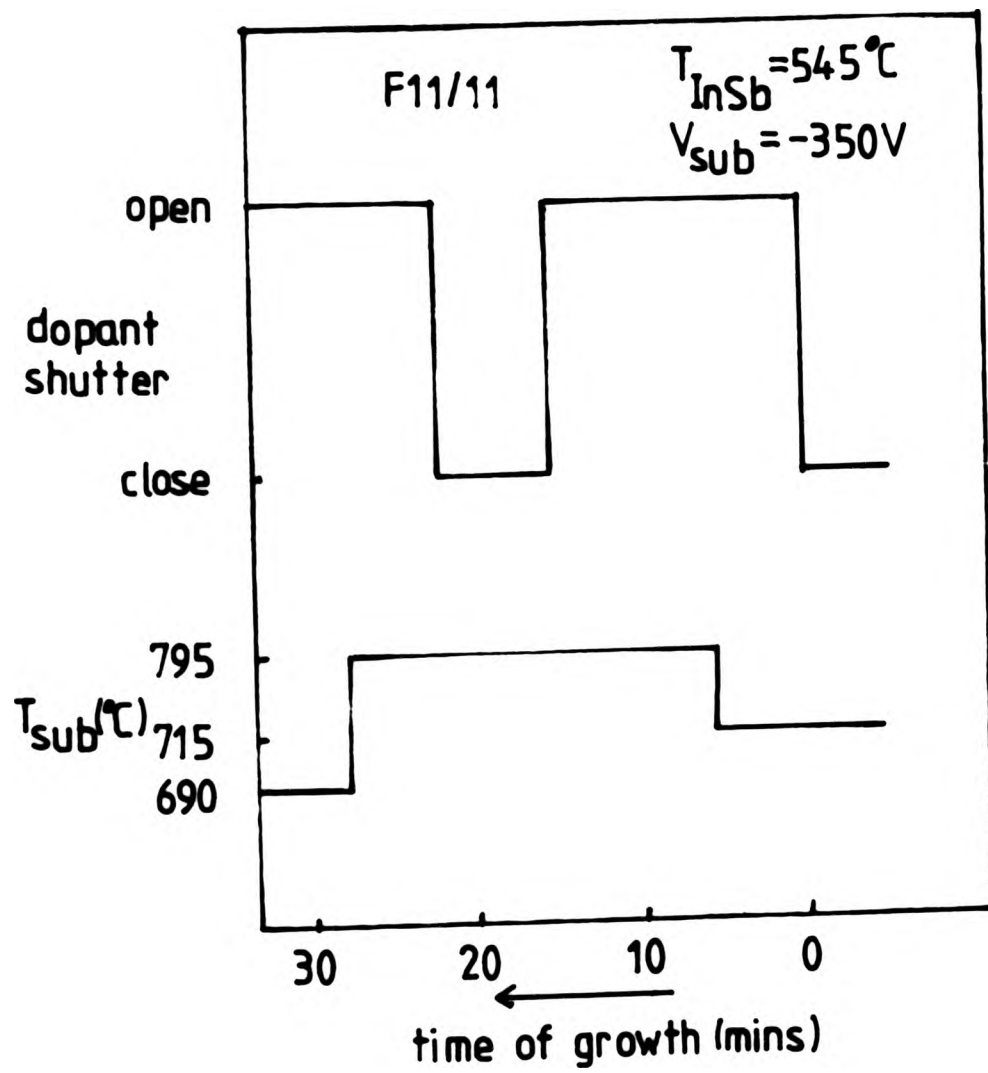
(b)

Fig.4.10(b) Contd.

166

Fig.4.13(a)&(b) The growth and electrochemical CV profile of a submicron Sb-doped structure with features of 250Å and 500Å wide.

Fig.4.13(a)&(b) The growth and electrochemical CV profile of a submicron Sb-doped structure with features of 250Å and 500Å wide.

Two layers grown on heavily As-doped substrates for single drift IMPATT device fabrication are shown in Figs.4.11 and 4.12 respectively. In Fig.4.11, the n^+ drift region was grown on the n^{++} substrate whereas in Fig.4.12, an n^{++} buffer layer was grown on the $n^{+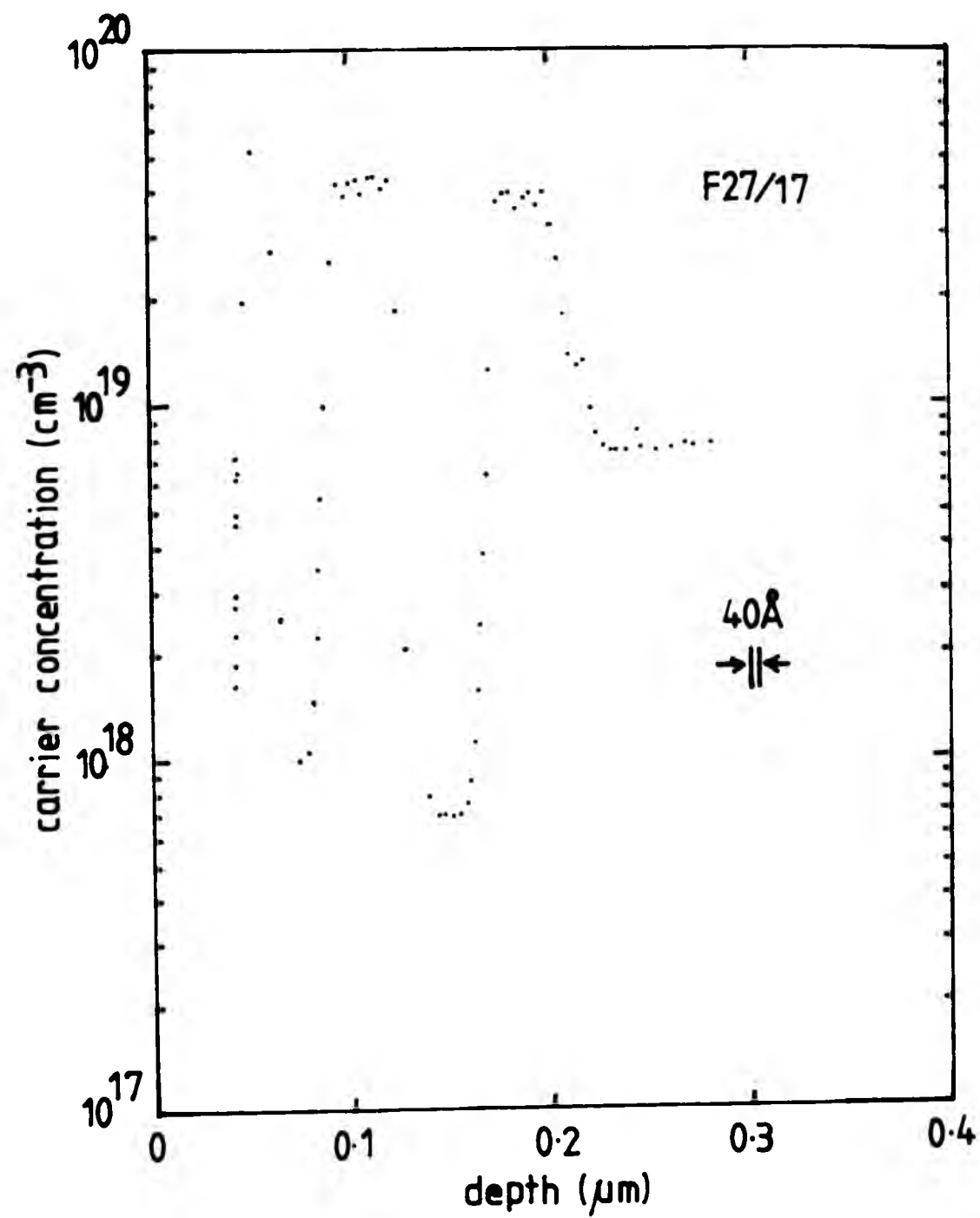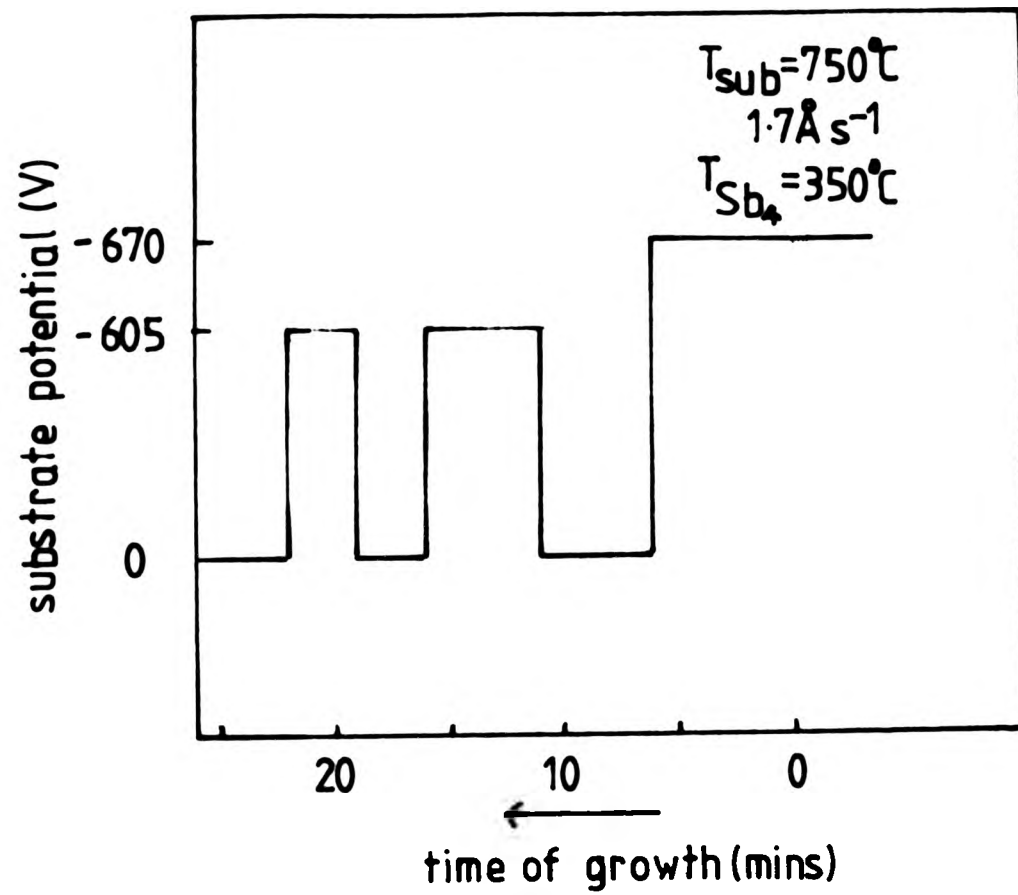+}$ substrate prior to the n^+ drift region. In both layers, abrupt dopant concentration transitions of <250 Å/decade were obtained indicating the absence of autodoping effect as a result of the low temperature growth in Si-MBE. The abruptness of the dopant concentration transition achieved was further confirmed by SIMS where transitions of ⁻100Å/decade in Sb-doped layers were measured.

The capability and ease of Si-MBE in conjunction with the PED technique to achieve dopant profiles of submicron dimensions is demonstrated in the electrochemical CV profile of a 0.2um layer shown in Fig.4.13(a) in which one 250Å wide and two 500Å wide Sb dopant spikes were introduced by simply ramping the substrate potential as indicated in Fig.4.13(b). The dopant spikes can be clearly identified in the electrochemical CV profile. The presence of these narrow Sb-doped regions in the layer was confirmed by a "bevelling and staining" technique[147].

4.2.4 Some Observations on Dopant Incorporation Behaviour

In the course of the work, we observed that the incorporation rate of dopants such as Ga, Sb and As in Si-MBE do not appear to be dependent on the growth rate as in GaAs:Si MBE. There was a recent report[148] which also pointed to a similar observation. To illustrate this behaviour, we have grown a number of layers in which the dopant flux was held constant whilst the growth rate was varied at intervals during growth. Figs.4.14 and 4.15 are the electrochemical CV profiles of two such layers doped with Sb and Ga respectively. Deposition rates ranging between $1.5 Å s^{-1}$ and $15 Å s^{-1}$ were used in the growth of

169
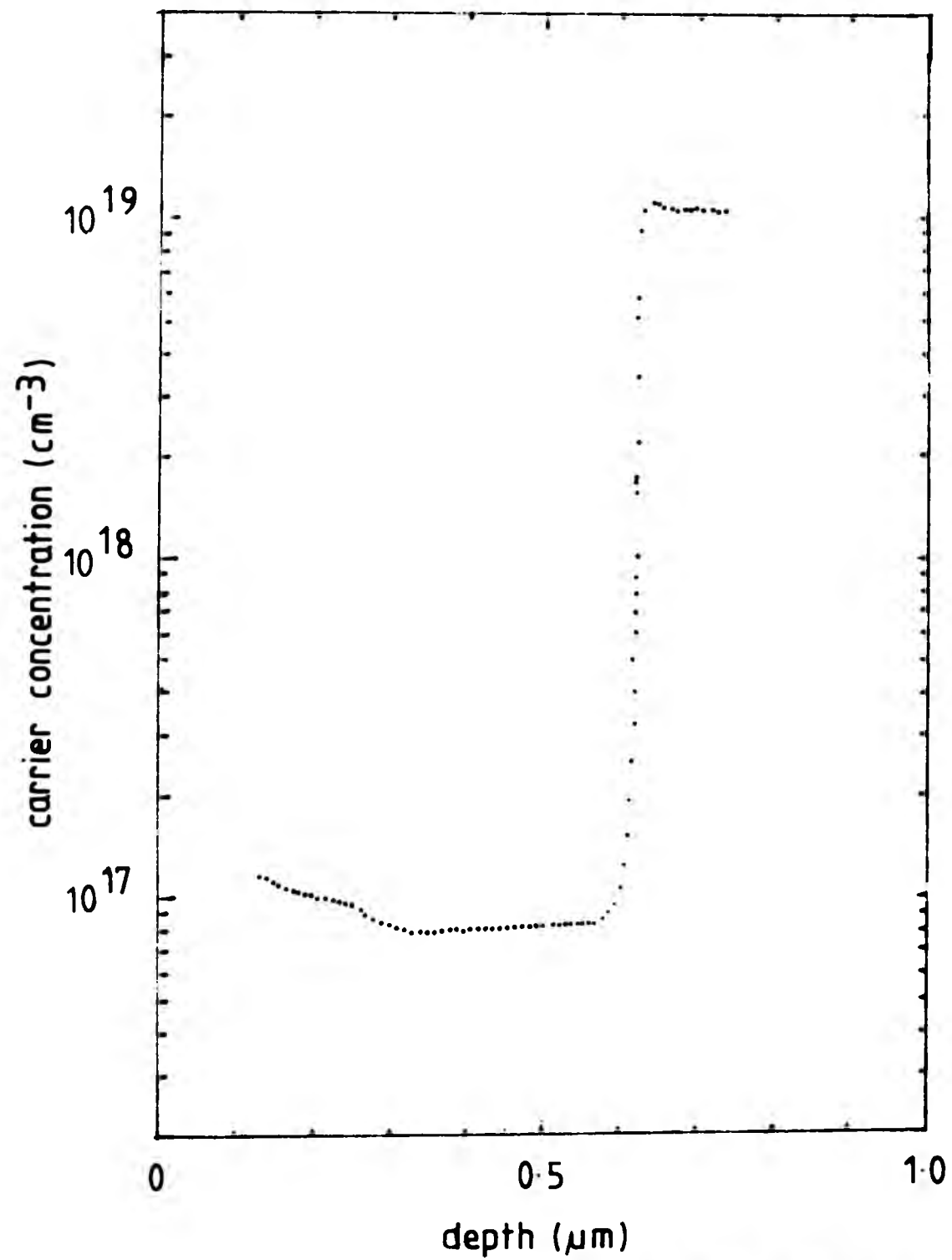
Fig.4.11 The electrochemical CV profile of a 0.6μm Sb-doped Si-MBE layer grown on a n++ substrate (As-doped). Note the abrupt dopant transition at the interface indicative of the absence of autodoping effect in the layer.

170
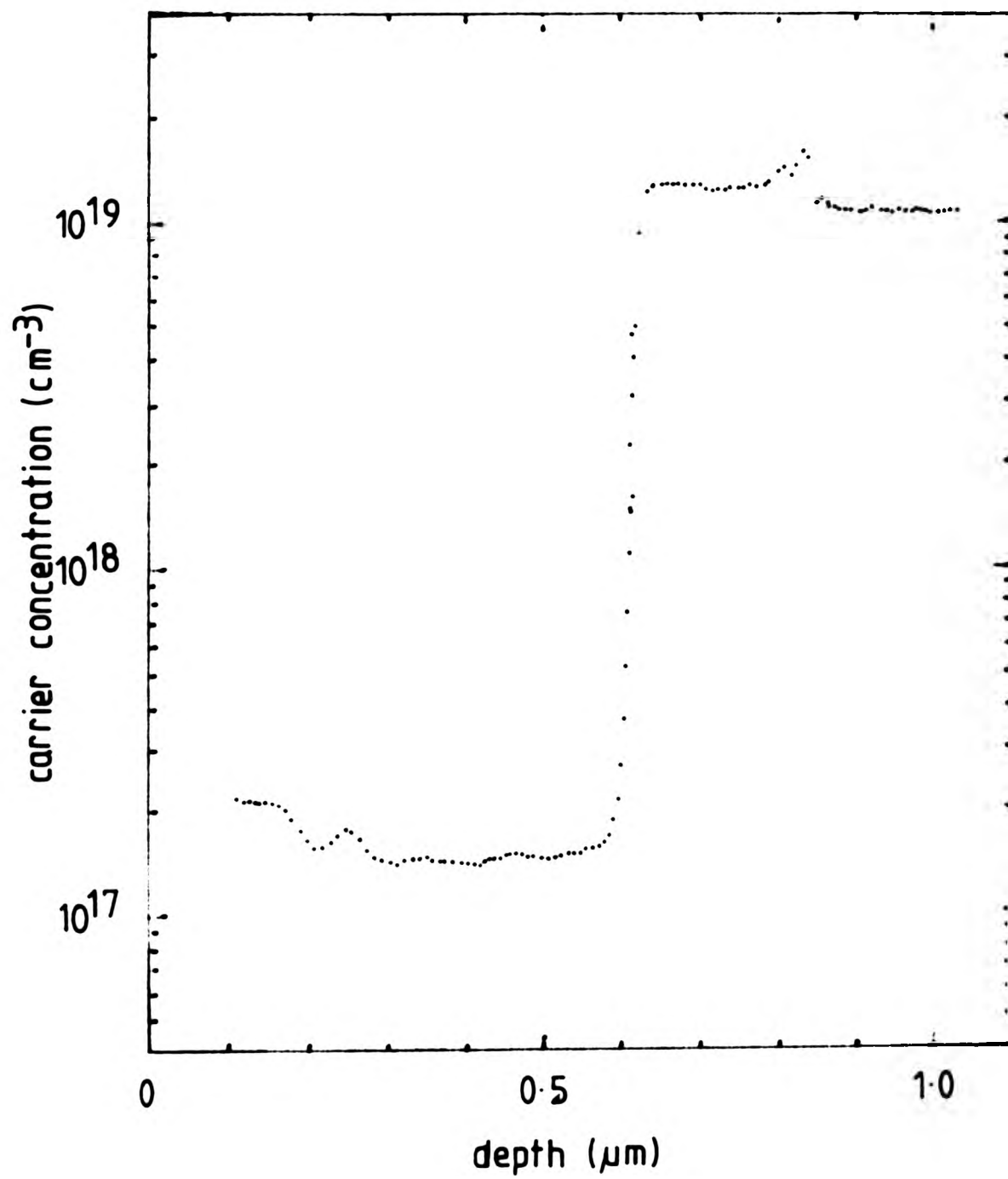
Fig.4.12 The electrochemical CV profile of a Sb-doped Si-MBE layer grown on a n^{++} substrate showing a 0.6µm low doped region on top of a 0.2µm heavily doped buffer region.
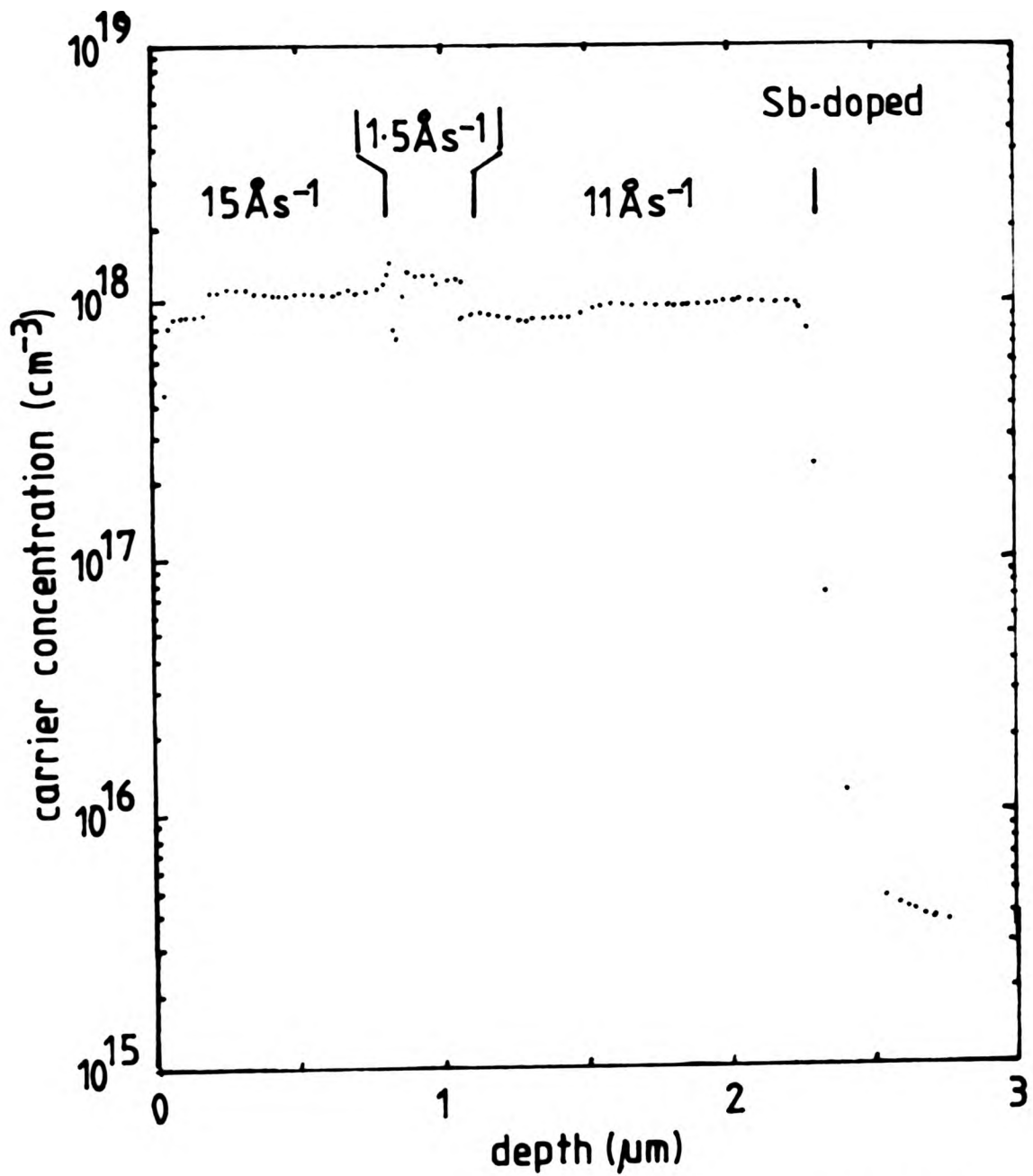
171

Fig.4.14 The electrochemical CV profile of a Sb-doped layer grown at 850°C under a constant Sb dopant flux. The deposition rate was varied during growth as indicated.
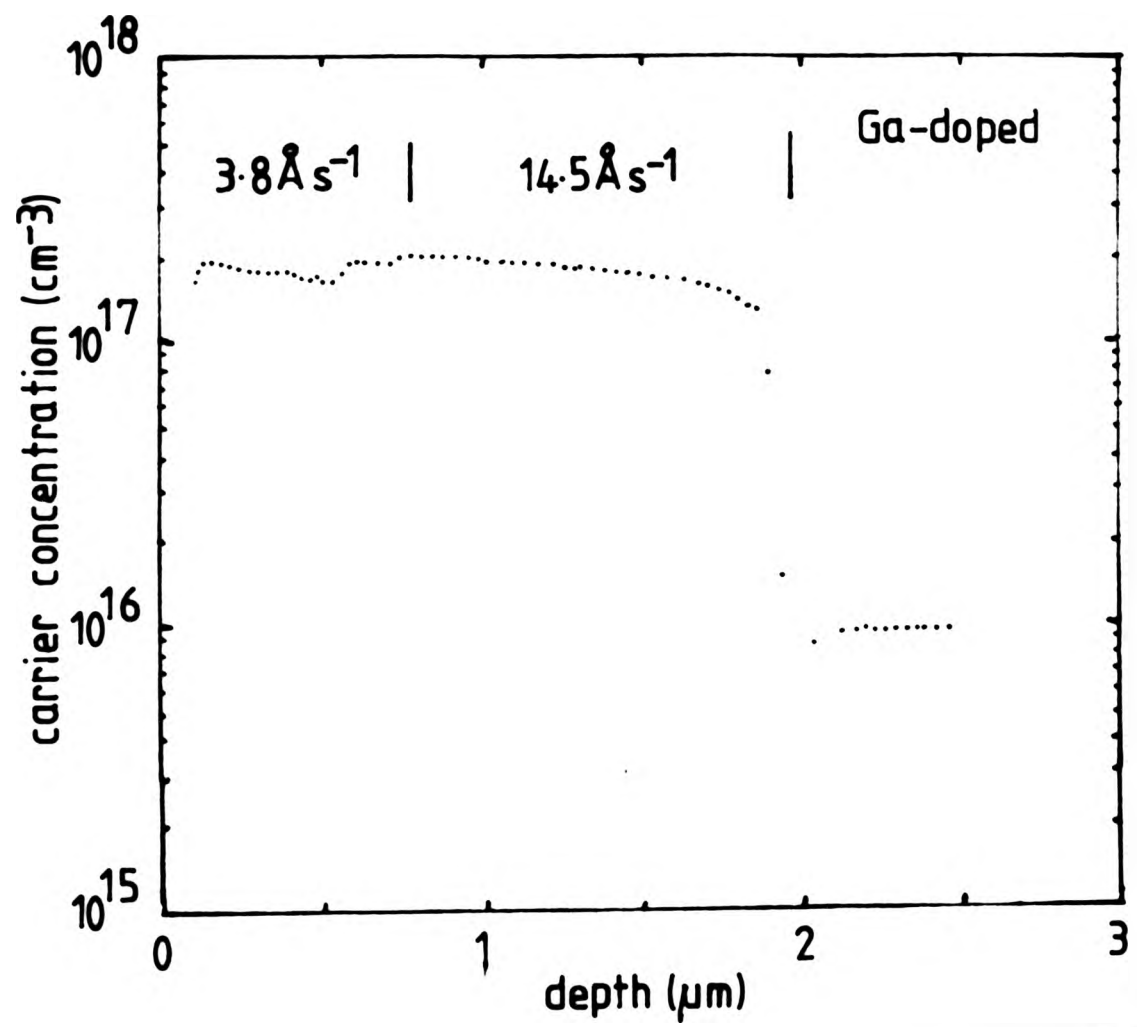
Fig.4.14 The electrochemical CV profile of a Ga-doped layer grown at 850°C under a constant Sb dopant flux. The deposition rate was varied during growth as indicated.

these layers. It can be seen that when the deposition rate was varied by a factor of as much as 10x, there was no corresponding change in the measured carrier concentration. Evidently, the incorporation of Ga and Sb was independent of the growth rate at the growth temperatures studied.

The implication of this behaviour is that the sticking coefficient S is a function of the growth rate, whereas it has generally been assumed that S was independent of growth rate in most doping studies in Si-MBE to date. The same incorporation behaviour was, however, not observed with boron. This difference may be accounted for by the fact that boron exhibits a unity sticking coefficient.

Tabe and Kajiyama suggested[148] that this independence of dopant incorporation of growth rate was a case for the existence of an equilibrium state between the surface and bulk dopant concentrations at the growing Si interface. Metzger and Allen[131] indicated that if the incorporation of dopant was determined by the lateral movement of the Si growth steps over the relatively immobile dopant clusters on the surface , S should be proportional to the growth rate and thereby the doping level would be independent of the growth rate as observed in our studies.

4.2.5 Kinetic Modelling of the Effect of PED

In this section, we utilize the kinetic model for the dopant incorporation mechanism, which was first introduced by Wood and Joyce[61] for III-V MBE and later modified by Metzger and Allen[131] for Si-MBE, and examine how the various parameters governing the transient behaviour of the dopant incorporation can be affected by the substrate potential, leading to abrupt profiles. It should be noted that the incorporation coefficient of dopant is generally assumed to be independent of growth

174

rate, which we have shown earlier, is not the case with Sb, Ga and As doping at growth temperatures above 700°C. However, it can be shown that under constant growth rate the above model describes the doping kinetics as intended.

In the model, a surface layer of adsorbed dopant atoms of density, N_{ds} (cm^{-2}) acts as a reservior from which the atoms are either incorporated into the growing layer or desorbed from the surface. The kinetics of the surface dopant density is governed by the equation:-

$$\frac{d N_{ds}}{dt} = F - K_d N_{ds}^{\,p} - K_i N_{ds}^{\,q} \qquad (4.2)$$

where F is the incident Sb flux, K_d and K_i are the desorption and incorporation coefficients and, p and q are the desorption and incorporation orders respectively. Metzger and Allen[131] have shown that under growth conditions typically used in our study (i.e. high growth temperature and low surface dopant coverage (below one monolayer)), $p=q=1$ applies. Using the boundary condition of $N_{ds}(0)$ at $t=0$ (i.e. initial dopant surface coverage at the beginning of growth or change of growth parameter), the solution to Eq.(4.2) is given by:_

$$N_{ds}(t) = \frac{F}{K}\left\{ 1 - \left[1 - \frac{K}{F} N_{ds}(0) \right] e^{-Kt} \right\} \qquad (4.3)$$

where $K = K_i + K_d$ and $N_{ds}(t)$ is the surface coverage of dopant at time t.

Since the bulk dopant concentration at time t, $N_{dB}(t)$, is given by

$$N_{dB}(t) = K_i\, N_{ds}(t)/v \qquad (4.4)$$

where $v =$ growth rate ($cm\ s^{-1}$), we obtain the expression for the bulk dopant concentration at time t, $N_{dB}(t)$, as:_

$$N_{dB}(t) = \frac{K_i \, F}{k \, v} \left\{ 1 - \left[1 - \frac{K}{F} N_{ds}(0) \right] e^{-Kt} \right\} \quad \text{---- (4.5)}$$

Using this expression, we can calculate the doping profile under different growth conditions.

Under the conditions of high growth temperature and low surface dopant coverage, the resultant bulk dopant concentration N_{dB} in the layer obtained under constant dopant flux was found to be unaffected by a change in the growth rate v. This implies that K_i must be a function of the growth rate such that K_i is proportional to v, i.e.,

$$K_i \propto v$$

In the examples to be discussed below where constant growth rates are involved, the growth rate dependent part in K_i and K in Eq.(4.5) remain constant and therefore will not affect the overall time dependence of $N_{dB}(t)$.

Consider a theoretical case where an epitaxial layer is grown at a deposition rate of 5Å s^{-1} and substrate temperature of $850^\circ C$ with a Sb flux of 1×10^{13} $\text{cm}^{-2}\text{s}^{-1}$. The incorporation and desorption coefficients are taken to be $1.1 \times 10^{-6} \text{s}^{-1}$ and $1.4 \times 10^{-2} \text{s}^{-1}$ respectively (coefficient data for Sb on (111) Si surfaces published by Metzger and Allen[131]). Two dopant concentration spikes are "introduced" in the layer by assuming an 10x increase in the sticking coefficient (S= K_i/K) through step-ramping the substrate potential as shown in Fig.4.16(a). Stepwise changes in K_i and K_d are assumed when the substrate potential is ramped. The dopant flux F is maintained constant through the growth.

There are three possible cases whereby an 10x enhancement in S can occur, namely, a) K_i increases by 10x while K_d remains constant, b) K_d decreases by 10x while K_i remains constant, and c) both K_i and K_d change such that S is increased by 10x. Their respective

176

transient dopant profiles as calculated are shown in Figs.4.16(a),(b) and (c). In cases a) and c), very abrupt profiles were obtained, whereas in case b), "smearing" of the profile steps was severe. Our experimental results are more closely represented by case a). This calculation implies that the substrate potential should affect the incorporation coefficient K_i more strongly than the desorption coefficient K_d in order to obtain a calculated profile closely matched to our experimental results.

We have also made a preliminary investigation to determine whether the surface coverage of dopant, N_{ds}, was affected by the use of substrate potential. A multilayer structure was grown at $850^{\circ}C$ under different substrate potentials, and at the end of each layer growth, the substrate was cooled rapidly below $<500^{\circ}C$ to minimize the re-evaporation of the adsorbed Sb layer on the surface[18] prior to the AES analysis. The presence of Sb on the surface was indicated by the peaks around 450 eV in the Auger spectra. When the substrate potential was changed from 0V to -600V, we found a small increase ($~10\%$) in the Sb peak height. When the layers were profiled, their respective carrier concentrations were found to be $1x10^{16} cm^{-3}$ and $1x10^{18} cm^{-3}$. Apparently, the substrate potential had not affected the surface coverage of Sb to a similar extent as the measured carrier/dopant concentration. This observation can be shown to be in accordance with assertion that K_i is the parameter principally affected by the substrate potential. From Eq.(4.3), at the steady state, $N_{ds}(t=\infty)=F/K$ where $K=K_i+K_d$. In the case where Ki increases 10x, the ratio of the surface coverages with and without the substrate potential is given by

$$K_i+K_d/(10K_i+K_d) =0.9993$$

,i.e. an insignificant decrease in the surface coverage with the substrate potential.

177

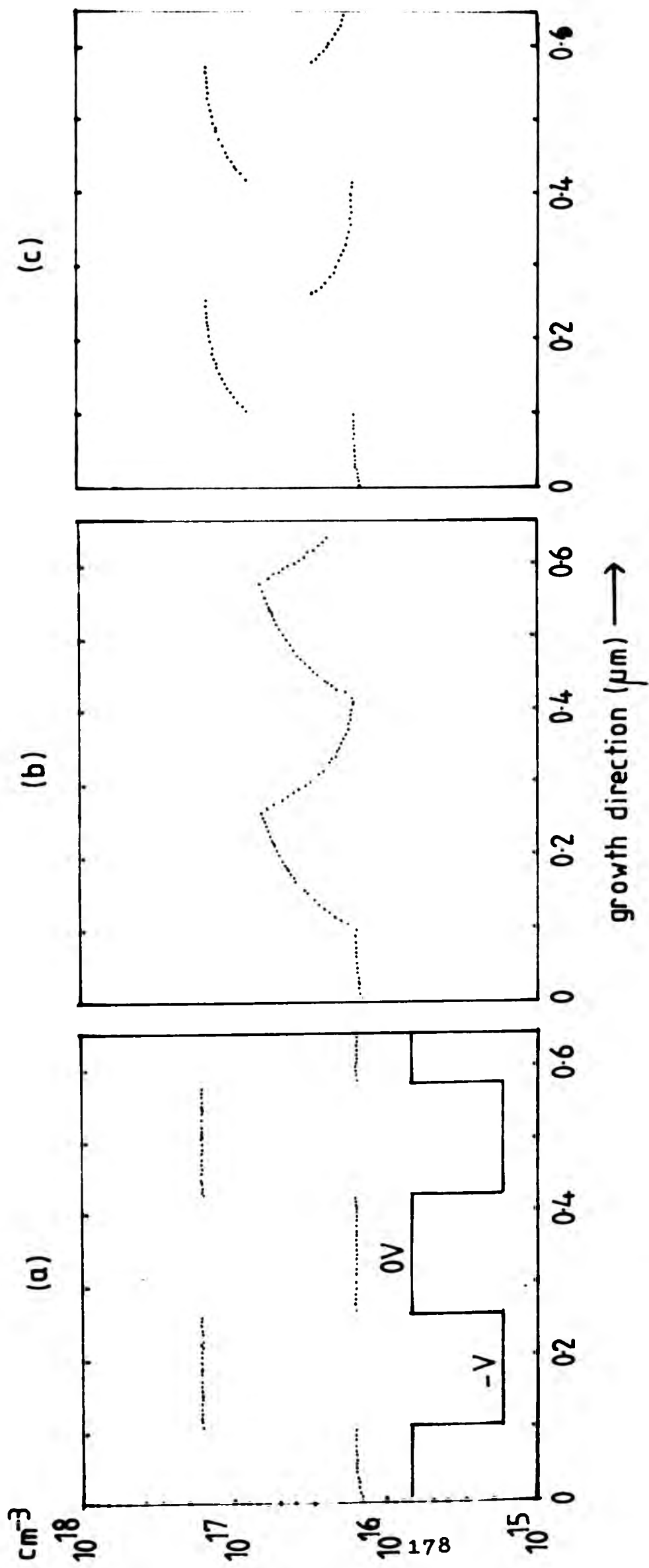Fig.4.16 The dopant profiles calculated using the Joyce-Wood kinetic model by assuming that the substrate potential used during Si-MBE growth alters the dopant incorporation and desorption coefficients, K_i and K_d, respectively. In the case of (a) K_i increased by 10x and K_d remained constant; (b) K_i remained constant and K_d decreased by 10x; and (c) K_i increased by 2x and K_d decreased by 2x.

178

4.2.6 Mechanism of Potential Enhanced Doping

Prior to our observation of the PED effect, there were reports of unexpected differences in the incorporation behaviour of co-evaporated Sb dopant in Si-MBE where different types of e-gun evaporators were employed[149]. Large discrepancies in the sticking coefficient data of co-evaporated Sb in Si-MBE as published by Ota[87], Bean[54] and Metgzer[131] have been noted and cannot be satisfactorily accounted for. Recently it was brought to our attention that similar doping enhancement effect under the application of a substrate potential during Si-MBE growth has also been observed independently at AEG-Telefunken[150]. It is now apparent that the strong influence that substrate potential has on the incorporation of co-evaporated dopants (particularly Sb) is linked to the use of the e-gun evaporators in Si-MBE.

We have considered two possible mechanisms to account for the doping enhancement we have observed in our potential enhanced doping studies. These mechanisms can be broadly described as:

(a) dopant implantation through bombardment of growing surface by charged species

(b) increased adsorption energy through polarization of dopant species produced by local electric field at irregularities on growing surface

(a) Bombardment by charged species

To investigate the possible role of bombarding charged species in the enhancement effect, we measured the current collected by the substrate with the e-gun evaporator and dopant source either on or off. No attempts were made to identify the chemical nature of the constituent species in the current. It is however expected

179

that charged Si and residual gas species and electrons are involved. Secondary electron emission arising from the bombarding species were neither suppressed nor accounted for in the measurement of the current.

With the e-gun evaporator off, a background/instrumental leakage current of about 2nA cm^{-2} was detected. When the e-gun evaporator was operated at 7kV corresponding to a growth rate of 5Å s^{-1}, the current density vs substrate potential relationship is given in Fig.4.17. It can be seen that the current collected at a negative substrate potential was a factor of 20x less than at a positive potential. It is considered that the difference can be attributed largely to the attraction of the secondary electrons from the e-gun evaporator under the applied electric field. When the shutter to the Sb dopant source at $330^{o}C$ was opened, the IV characteristic was unaffected indicating that the dopant source itself generated very few charged species. It can be seen that at a substrate potential of -500V, a current of ⁻1 μA cm^{-2} was measured. Assuming that the current was due entirely to Si^{+} ions, the proportion of Si^{+} ions reaching the substrate would be ⁻ 0.4% of the Si flux.

AEG-Telefunken[150] have suggested a mechanism in which Si ions accelerated by the field produced by the substrate potential implant some of the surface dopant atoms into the growing layer. Incorporation of the surface dopant atoms is considered to be affected by the probability of implantation of the dopant by the Si+ ions and the magnitude of the Si+ flux. With increased accelerating potential (i.e. more negative substrate potential), more Si+ ions will be attracted towards the substrate. By virtue of the higher Si+ flux, corresponding more dopant atoms will also be incorporated in the layer. The probability of implantation of dopant atom by Si+ ions may also be affected by the increased energy of the impinging Si+ ions and the morphology/structure of the
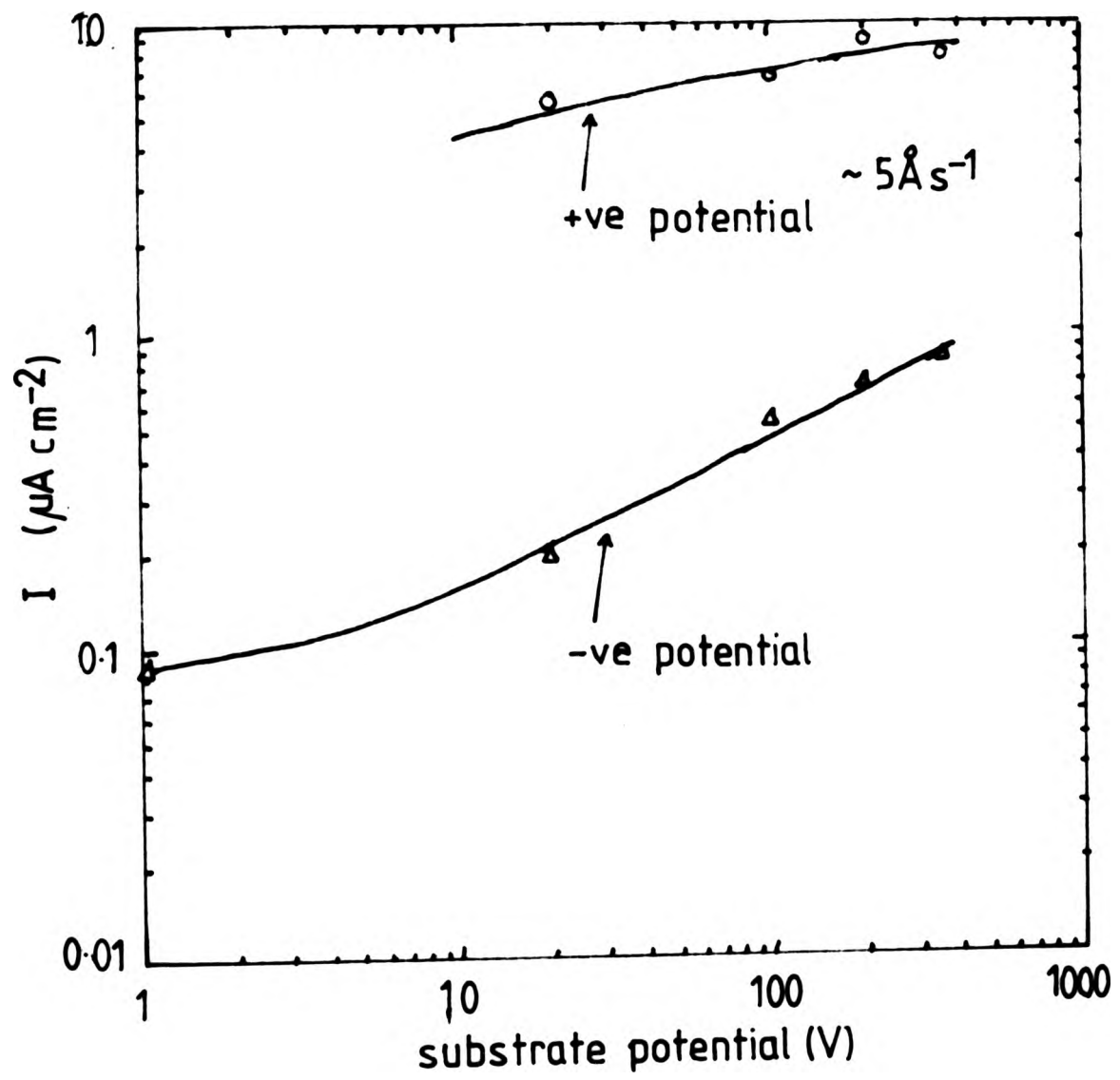
Fig.4.17 The measured current I at the substrate vs the substrate potential V with the e-gun evaporator depositing Si at a rate of ~5Å s⁻¹.

dopant adlayer. It has been suggested that Sb deposited on a clean Si surface at room temperature distributes to form a uniform adlayer whilst Ga forms island clusters on the surface[64,131]. It is considered that the difference in the morphological aspects of the dopant adlayer can at least partly account for the observed high enhancement of dopant incorporation of Sb compared to Ga in the PED effect.

Itoh et al[151] reported the effect of partially ionizing the Si flux during vacuum deposition with coevaporative Sb doping on the Si layer grown at $850^{\circ}C$ and maintained at a potential of -10kV. They observed that Sb incorporation was enhanced by a factor of 100 with a Si^+ ion current of $2\mu A\ cm^{-2}$ measured at the substrate corresponding to $^-0.6\%$ ionization of the Si flux. However when the Si^+ ion current was increased to $30\mu A\ cm^{-2}$ the Sb incoporation was not enhanced by the same factor. They speculated that a charge exchange between Si^+ and Sb occurred such that

$$Si^+ + Sb \rightarrow Si + Sb^+$$
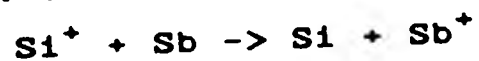
before arriving at the substrate with the Sb^+ ions being responsible for the observed enhanced doping efficiency.

Sakamoto and Komuro[154] studied the behaviour of Ga^+ ion doping in Si-MBE using a liquid metal ion source. They observed an increase in doping efficiency over co-evaporative doping by a factor of 50-100 using 0.5% ionized Ga dopant flux at a growth temperature of $700-800^{\circ}C$. With a 100% Ga^+ dopant flux, they observed a drop in the measured carrier concentration as the accelerating voltage was increased from 500V to 1000V. This result is difficult to understand since at a higher accelerating voltage a deeper implantation of the dopant ions should occur[27] and thus lead to a decrease in the possibility of re-evaporation of the Ga atoms from the surface.

182

(b) Polarization of dopant

Chopra[152] observed that large island formation of thermally evaporated Ag and Au was increased when an electric field was applied laterally across the substrate surface during the deposition. He suggested a mechanism involving polarization of the atoms which enhanced the island formation.

The assumption in context is that the dopant atoms on the surface are polarized by electric fields due to the applied substrate potential. The polarizability of an atom, α is determined by the strength with which the nuclear charge controls the electron distribution and prevents its distortion by an externally applied electric field. If the atom contains only a few electrons (i.e. low atomic number Z), the electron distribution is strongly controlled by the nuclear charge and α is low. For a large atom containing many electrons relatively distant from the nucleus, the degree of nuclear control over these electrons is weakened, and a higher value of is expected. The polarizability of an atom, α, can be related to its atomic structure by[153]:-

$$\alpha = Ze^2r^2/2\pi\epsilon I$$

where I = ionization energy of the outermost electron

r = radius of molecule

Z = atomic number

A plot of the atomic number Z vs α for a number of elements of interest in MBE is shown in Fig.4.18.

At a potential of 500V, we can expect a macroscopic electric field strength at the substrate surface to be of the order of 10^3v m^{-1}. It can be envisaged that at the growth steps the local field strength may be increased manyfold due to the abrupt changes in the surface topology. Dopant atoms near or approaching the growth steps would therefore be more strongly polarized. Since dopant incorporation is considered to occur at the growth steps,
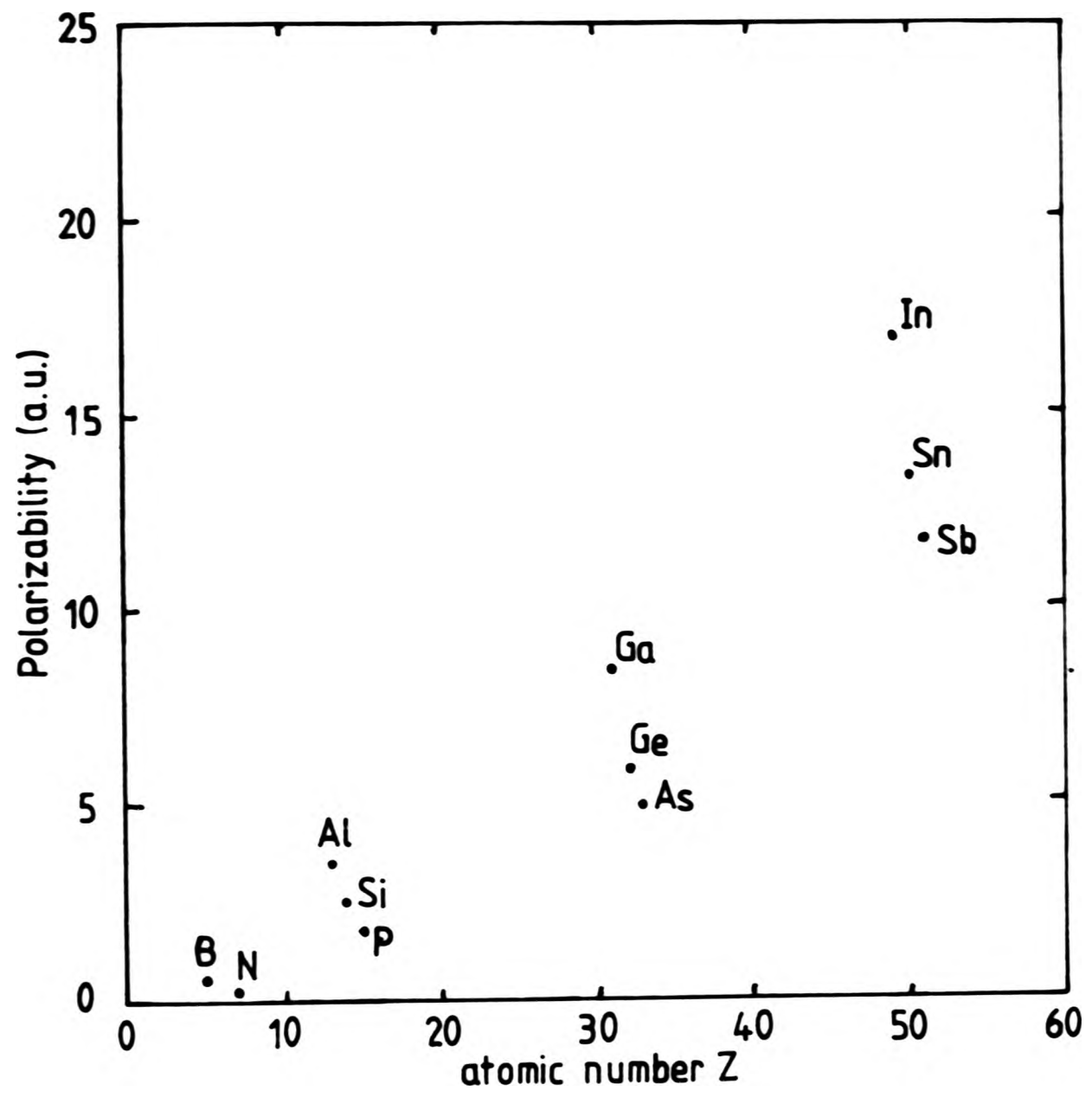
Fig.4.18 Plot of the polarizability of an atom α vs its atomic number Z.

184

it is believed that the incorporation energy could thus be strongly increased by the application of a substrate potential.

We noted a difference in the effectiveness of PED with dopant species. Three dopant species have been studied and we observed that the enhancement of dopant incorporation followed the order of Sb : As : Ga (with Sb being the most effective). With the exception of Ga, this is consistent with the relative magnitude of the polarizability of the dopant atoms as indicated in Fig.4.18.

The dopant polarization model suggests that enhancement of dopant incorporation should be equally effective at either polarity of the substrate potential. This is however contrary to our experimental observation where in the case of Sb the enhancement was substantially higher with a negative substrate potential.

It is clear that further studies are necessary to elucidate the PED mechanism with regard to its energy and species dependence. To date, it is considered that implantation of the adsorbed dopant atoms by the Si^+ ions generated in the e-gun evaporator is by far the more plausible mechanism. Further information on the nature of dopant adlayer and other possible physical interactions between Si^+ ions and dopant atoms (such as charge exchange and sputtering) and especially their energy dependence is required ~~to~~ for better clarification of the details of the PED mechanism.

4.3 Device Applications of Grown Si-MBE layers

Preliminary attempts were made using our layers for simple in-house device fabrication. In layers grown on substrates of opposite type conductivity, a p-n junction is produced at the epitaxial substrate interface. Mesa diodes

185

were made using these layers by masking and etching off the required region with the method described in Section 2.2.1.

An example of the IV characteristic of such diode consisting of a boron doped layer at $1 \times 10^{17} cm^{-3}$ on a n-substrate (~1 ohm cm) is given in Fig.4.19. A leakage current of ~85nA cm^{-2} was measured at -2V despite no passivation of the etched surface was used. This compares favourably with the reported leakage currents of ~2 and 9nA cm^2 (measured at -2V) in similar Si-MBE mesa diodes fabricated by Bean[10] and Ota[9] respectively. Junction breakdown of the mesa diode occurred at a reverse bias potential in excess of 135V.

Layers intended for single drift IMPATT devices were also grown. Their electrochemical CV profiles of some of these layers are depicted in Figs.4.11 and 4.12. In Fig.4.11, the abrupt dopant concentration step profile was formed between the epitaxial layer and the highly doped substrate, whereas in Fig.4.12, the abrupt step was grown within the epitaxial layer. The crucial feature of these layers is the abruptness of the dopant concentration steps which is estimated to be better than 250 Å/decade. No significant autodoping effect was evident in either layer. This is in marked contrast to similar layer structures grown by CVD. Results of the device fabrication and performance will be available shortly.
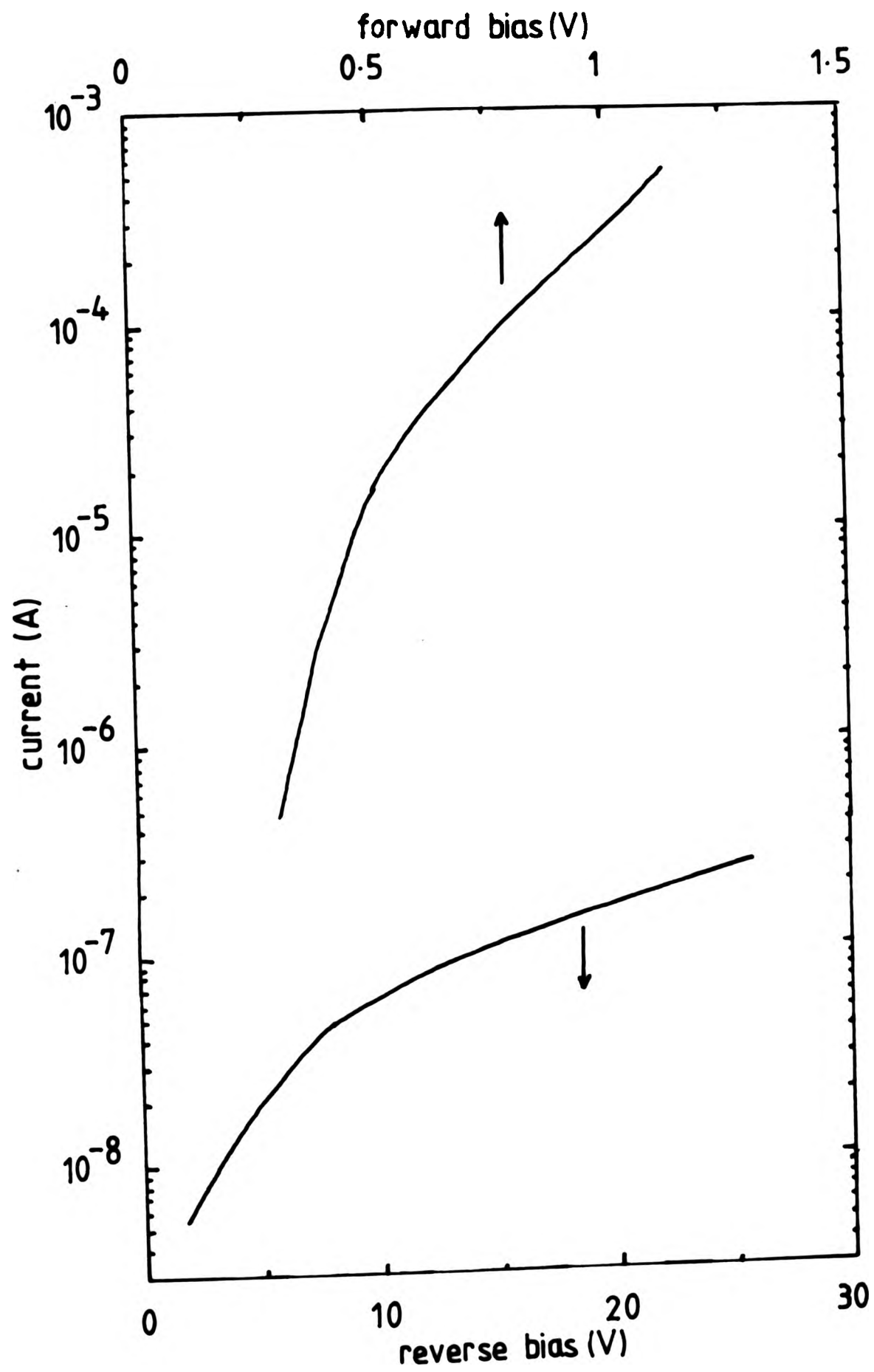
186

Fig.4.19 IV characteristic of a mesa diode fabricated using boron-doped Si-MBE material grown in our studies.

Chapter 5: Overview and Further Work

5.1 Overview of Si-MBE Work

We have examined a number of technological aspects of Si-MBE. One of the major difficulties with use of closed-cycle He pumping in UHV applications occurs during the system bakeout at elevated temperatures when high thermal radiation can overload the cryogenerator of the pump. We showed that this difficulty can be adequately overcome by incorporating a rotatable thermal baffle between the cryopump and baked region of the system. The introduction of the rotatable buffer facilitated an reduction of the thermal radiation reaching the cryogenic head of the cryopump during bakeout to acceptable levels whilst maintaining high pumping speeds during normal operation. The Si flux generation from e-gun evaporation has been observed to show short term fluctuation as the angular displacement from the vertical was large. . Good control of the Si deposition was achieved only when the angular placement of the flux monitor was reduced from an angle of 45° to 10°.

Small Si particles that were found embedded on the layers were thought to have originated from the flaking of deposits on cold surfaces due to stray Si flux from the e-gun evaporator. It was found that improved collimation of the Si flux at the e-gun evaporator was effective in reducing these defects. It is apparent that in MBE systems involving the use of e-gun evaporation more stringent considerations are required in controlling the stray deposits on cold surfaces.

The basic materials grown were generally of high quality with extended defect densities in the region of mid 10^3 and $10^4 cm^{-2}$. These materials are comparable to the materials grown in other laboratories that we have examined. It is clear that further improvements in the Si-MBE system technology and wafer handling/cleaning are

188

required before Si-MBE can be successfully adopted in the VLSI technology. Two electrically active contaminants, boron and phosphorus, have been positively identified in the grown materials. In the case of boron, we found that the contamination amounted to $^-10^{12}$ -$10^{13}cm^{-2}$ of boron atoms at the substrate/epitaxial interface in which the presence of an oxide layer on the substrate prior to the in-situ heat treatment and epitaxial growth apparently enhanced the accumulation of such contamination. Continuous residual phosphorus doping in the layers was at best in the region of low to mid $10^{14}cm^{-3}$. The sources of contamination were not as yet positively identified.

Two significant contributions to the use of co-evaparative doping in Si-MBE have been made. Firstly we reported the use of co-evaporated boron doping in Si-MBE, and we demonstrated it to be an excellent method of achieving accurately-controlled dopant profiles over a range of growth temperatures and with a wide dynamic range of doping levels. Some difficulties were encountered with the short lifetime of crucible for containing the boron source at the required high temperatures. Our experience showed high purity graphite to be a good crucible material although there remains fear of additional incorporation of C in the layer.

We have also reported a surprisingly simple way of enhancing the rate of incorporation of Sb in Si-MBE by applying a potential to the substrate during epitaxial growth and in which the dopant transition in the layer can be introduced by stepping the potential appropriately. The versatility in and ease of dopant profile control by this method rivals even the technically more difficult method of ion doping. We consider that both co-evaporated boron doping and PED technique will be serious contenders in the choice of doping method in the commercial application of Si-MBE.

5.2 Further Work

189

The technological problems related to Si flaking and the routine maintenance of clean growth environment will require close examination and have to be overcome in order for Si-MBE to be a potential commercial Si epitaxial growth technique. Knowledge of the effectiveness of the surface preparation on processed wafers is still lacking; work in this area is crucial in improving the yield obtained usng this epitaxial growth process.

Further investigations into co-evaporative doping including the PED effect are required to elucidate its mechanism and the role of the e-gun evaporator in the effect. Comparative studies in co-evaporative and ion doping are also essential to determine which doping technique is most suited to application in future production Si-MBE systems.

References

(1) B.A. Unvala, Vide, <u>104</u>, 109 (1963).

(2) H.C. Abbink, R.M. Broudy, and G.P. McCarthy, J. Appl. Phys., <u>39</u>, 4673 (1968).

(3) H. Widmer, Appl. Phys. Lett., <u>5</u>, 108 (1964).

(4) B.A. Joyce, J.H. Neave, and B.E. Watts, Surf. Sci., <u>15</u>, 1 (1969).

(5) B.A. Joyce, J.H. Neave, B.E. Watts, and G.R. Booker, Phil. Mag., <u>19</u>, 403 (1969).

(6) J.M. Charig and D.J. Skinner, Surf. Sci., <u>15</u>, 277 (1969).

(7) R.N. Thomas and M.H. Francombe, Appl. Phys. Lett., <u>13</u>, 270 (1968).

(8) see for example, A.Y. Cho and J.R. Arthur, Progress in Solid-State Chemistry, Chapter 10, Eds. G. Somerjai and J. McCaldin, Pergamon Press, New York, (1975).

(9) Y. Ota, Thin Solid Films, <u>106</u>, 1 (1983).

(10) J.C. Bean, Proc. Int. Electron Devices Meet. Washington, Dec 1981, IEEE, N.Y., p.6.

(11) Y. Shiraki, "The Technology and Physics of MBE", Ed. E.H.C. Parker, Chapter , Plenum, N.Y., 1985.

(12) J.C. Bean and S.R. McAfee, J. de Physique, <u>43</u>, C5-153 (1982).

(13) J.C. Bean, Appl. Phys. Lett., <u>36</u>, 741 (1980).

(14) Ishiwara, Nogaatomo, etc, Nucl. Instr. Methods, <u>149</u>, 417 (1979).

(15) K.C.R. Chiu, J.M. Poate, L.C. Feldman, and C.J. Doherty, Appl. Phys. Lett., <u>36</u>, 544 (1980).

(16) M. Matsui, Y. Shiraki, Y. Katayama, K.L.I. Kobayashi, A. Shintani, and E. Maruyama, Appl. Phys. Lett., <u>37</u>, 936 (1980).

(17) D. Streit, R.A. Metzger, and F.G. Allen, Appl. Phys. Lett., <u>44</u>, 234 (1984). J. Caber, H. Ishiwara, and S. Furukawa, Jpn. J. App. Phys., <u>21</u>, L712 (1982).

(18) J.C. Bean, L.C. Feldman, A.T. Fiory, S. Nakahara, and I.K. Robinson, J. Vac. Sci. Technol., <u>142</u>, 436 (1984).

(19) E. Kasper and W. Pebst, Thin Solid Films, <u>37</u>, L5 (1975).

(20) R. People, J.C. Bean, D.V. Lang, A.M. Sergent, H.L. Stormer, K.W. Wecht, R.T. Lynch, and K. Baldwin, Appl. Phys. Lett., <u>45</u>, 1231 (1984).

(21) R.N. Thomas and M.H. Francombe, Surf. Sci., <u>25</u>, 357 (1971).

(22) E. Kasper and H. Kibbel of AEG-Telefunken (W. Germany), private comm., (1984).

(23) A.R. Calawa, Appl. Phys. Lett., <u>33</u>, 1020 (1979).

(24) J.C. Bean and E.A. Sadowski, J. Vac. Sci. Technol., <u>20</u>, 137 (1982).

(25) E. Kasper, H.J. Herzog, and H. Kibbel, Appl. Phys., <u>8</u>, 199 (1975).

(26) C.T. Foxon and B.A. Joyce, "Current Topics in Materials Science", Ed. E. Kaldis, Vol. 7, Chapter 1,

North-Holland, (1981).

(27) F.W. Smith, B. Meyerson, and W. Miller, Appl. Phys. Lett., 31, 565 (1977).

(28) J.H. McFee, R.G. Swartz, V.D. Archer, S.N. Finegan, and L.C. Feldman, J. Electrochem. Soc., 150, 214 (1983).

(29) H.J. Quisser, J. Cryst. Growth, 17, 169 (1972).

(30) F.W. Smith, Surf. Sci., 80, 388 (1979).

(31) R.C. Henderson, R.B. Marcus, and W.J. Polito, J. Appl. Phys., 42, 1208 (1971).

(32) H. Suguira and M. Yamaguchi, Jpn. J. Appl. Phys., 18, 583 (1980).

(33) H. Suguira and M. Yamaguchi, Jpn. J. Appl. Phys., 19, 151 (1981).

(34) W. Kern, RCA Rev., 31, 234 (1970).

(35) R.C. Henderson, J. Electrochem. Soc., 119, 772 (1972).

(36) A. Ishizaka, K. Nakagawa, and Y. Shiraki, 2nd Int. Symp. in MBE and Related Clean Surface Techniques, Tokyo, (1982).

(37) A. Many, Y. Goldsteins, and N.B. Grover, "Semiconductor Surfaces", American Elsevier, N.Y., p.95, (1965).

(38) J.C. Bean, G.E. Becker, P.M. Petroff, and T.E. Seidel, J. Appl. Phys., 48, 907 (1977).

(39) I. Yamada, D. Martin, and F.W. Saris, Appl. Phys. Lett., 37, 563 (1980).

(40) P. Robinzohn, G. Gautherin, B. Agius, and C. Cohen, J. Electrochem. Soc., 131, 905 (1984).

(41) S. Wright and H. Kroemer, Appl. Phys. Lett., 36, 210 (1980).

(42) S.S. Iyer, R.A. Metzger, and F.G. Allen, J. Appl. Phys., 52, 5608 (1981).

(43) B.A. Joyce and Bradley, Phil. Mag., 15, 1167 (1967).

(44) A. Tabe, Jpn. J. Appl. Phys., 21, 534 (1982).

(45) J.A. McClintok, R.A. Wilson, and N.E. Byer, J. Vac. Sci. Technol., 20, 241 (1982).

(46) A. Tabe, Appl. Phys. Lett., 45, 1073 (1984).

(47) D.M. Zehner, C.W. White, and G.W. Ownby, Appl. Phys. Lett., 36, 561 (1980).

(48) L. Smit, T. de Jong, D. Hoonhout, and F.W. Saris, Appl. Phys. Lett., 40, 64 (1982).

(49) T.E. Seidel, "VLSI Technology", Ed. S.M. Sze, Chapter 6, Mc Graw-Hill, p.250, (1983).

(50) see for example, "Laser and Electron Beam Processing of Materials", Ed. C.W. White and P.S. Percy, Academic Press, (1980).

(51) E. Kasper and K. Worner, Proc. 2nd Int. Symp. VLSI Sci. & Technol., (1984).

(52) J.C. Bean, "Impurity Doping Processes in Si", Ed. F.F.Y. Wang, North Holland, (1981).

(53) S.M. Sze, "Phsics of Semiconductor Devices", Wiley, New York, (1981).

(54) J.C. Bean, Appl. Phys. Lett., 33, 654 (1978).

(55) G.E. Becker and J.C. Bean, J. Appl. Phys., 48, 3395

(1977).

(56) F. Alexandre, C. Raisin, M.I. Abdalla, A. Brenac, and J.M. Masson, J. Appl. Phys., 51, 4296 (1980).

(57) Y. Ota, J. Electochem. Soc., 126, 1761 (1979).

(58) J. Knall, J.E. Sundgren, and J.E. Greene, Appl. Phys. Lett., 45, 689 (1984).

(59) A.Y. Cho, J. Appl. Phys., 46, 1733 (1975).

(60) K. Ploog and A. Fischer, J. Vac. Sci. Technol., 15, 255 (1978).

(61) C.E.C. Wood and B.A. Joyce, J. Appl. Phys., 49, 4854 (1978).

(62) U. Konig, E. Kasper, and H.J. Herzog, J. Cryst. Growth, 52, 151 (1981).

(63) C.E.C. Wood and B.A. Joyce, J. Appl.Phys., 49, 4854 (1978).

(64) S.S. Iyer, R.A. Metzger, and F.G. Allen, J. Appl. Phys., 52, 5608 (1981).

(65) Y. Ota, J. Appl. Phys., 51, 1102 (1980).

(66) Coultron Corp., P.O. Box 1288, Boulder, CO80302.

(67) R.A. Swartz, J.H. McFee, A.M. Voshchenkov, and S.N. Finegan, Appl. Phys. Lett., 40, 239 (1982).

(68) H. Suguira, Jpn. J. Appl. Phys., 19, 641 (1980).

(69) H. Suguira, Rev. Sci. Instrum., 50, 841 (1979).

(70) H. Suguira, J. Appl. Phys., 51, 2630 (1980).

(71) M. Komuro, H. Hiroshima, and T. Sakamoto, Proc. Int'l Ion Engineering Congress -ISIAT'83 & IPAT'83, Kyoto, (1983).

(72) L. Swarlter of Bell Labs (US), private comm., (1984).

(73) C.A. Goodwin and Y. Ota, IEEE Trans. Electron Devices, ED-26, 1796 (1979).

(74) Y. Katayama, Y. Shiraki, K.L.I. Kobayashi, K.F. Komatsubara, and N. Hashimota, Appl. Phys. Lett., 34, 740 (1979).

(75) R.G. Swartz, J.H. McFee, P. Grabbe, and S.N. Finegan, IEEE Electron Device Lett., 2, 293 (1981).

(76) W.C. Ballamy and Y. Ota, Appl. Phys. Lett., 39, 629 (1981).

(77) R.G. Swartz, G.M. Chin, A.M. Voshchenkov, P. Ko, B.A. Wooley, S.N. Finegan, and R.H. Boseworth, IEEE Electron Device Lett., EDL-5, 29 (1984).

(78) R.A.A. Kubiak of CLP, private comm., (1984).

(79) K. Ploog and A. Fischer, Appl. Phys., 13, 111 (1977).

(80) G.J. Davies and D.A. Andrews, Vacuum, 34, 543 (1984).

(81) G.E. Becker, J. Vac. Sci. Technol., 14, 640 (1977).

(82) R.A.A. Kubiak, W.Y. Leong, R.M. King, and E.H.C. Parker, J. Vac. Sci. Technol., A1, 1972 (1983).

(83) VG Publication No.03-117, Vacuum Generators Ltd.,UK.

(84) R.J. Hill, "Physical Vapor Deposition", Airco Temescal, (1976).

(85) see for example, C.E.C. Wood, "Physics of thin Films", Ed. C. Hoff and M. Francombe, Vol.11, p35, Academic Press, N.Y., (1980).

(86) Talystep Instrument is manufactured by Rank-Taylor Hobson Ltd., Leicester, UK.

(87) Y. Ota, J. Electrochem. Soc., 124, 1795 (1977).

(88) L.J. Van der Pauw, Philips Res. Rep., 13, 1 (1958). L.J. Van der Pauw, Philips Tech. Rev., 20, 220 (1958).

(89) P. Blood and J.W. Orton, Rep. Prog. Phys., 41, 11 (1978).

(90) J.M. David and M.G. Buchler, Solid-St. Electron., 20, 530 (1977).

(91) R. Hill, D. Richardson, and S. Wilson, J. Phys. D: Appl. Phys., 5, 185 (1972).

(92) Annual Book of ASTM Standards, Part 43 (Electronics), F84, (1982).

(93) W.J. Patrick, Solid-St. Electron., 9, 203 (1966).

(94) P. Kramer and I.L. Van Ruyven, Solid-St. Electron., 20, 1011 (1972).

(95) P. Severin, Solid St. Electron., 14, 247 (1971).

(96) J.R. Ehrstein, "Non-destructive Evaluation of Semiconductor Materials and Devices", Ed. J.N. Zemel, Chapter 1, Plenum Press, N.Y., (1973).

(97) P. Blood and J.W. Orton, Rep. Prog. Phys., 41, 11 (1978).

(98) C.L. Miller, IEEE Trans. Electron. Devices, ED19, 1103 (1972).

(99) P.J. Baxandall, D.J. Colliver, and A.F. Fray, J. Phys. E.: Sci. Instrum., 4, 213 (1971).

(100) C.D. Sharpe and P. Lilley, J. Electrochem. Soc., 127, 1918 (1980).

(101) T. Ambridge, C.R. Elliot, and M.M. Faktor, J. Appl. Electrochem., 3, 1 (1973).

(102) T. Ambridge and M.M. Faktor, J. Appl. Electrochem., 4, 135 (1974).

(103) T. Ambridge and M.M. Faktor, J. Appl. Electrochem., 5, 319 (1975).

(104) T. Ambridge, C.R. Elliott, and M.M. Faktor, J. Appl. Electrochem., 3, 2 (1973).

(105) T. Ambridge and D.J. Ashen, Electronics Lett., 15, 647 (1979).

(106) C.D. Sharpe, P. Lilley, C.R. Elliott, and T. Ambridge, Electronics Lett., 15, 622 (1979).

(107) Post Office Profile Plotter is manufactured by Bio-Rad Semiconductor Measurement Systems (Polaron Ltd.), Watford Busines Park, Watford, Hertfordshire WD1 8XG.

(108) J. Wilde formerly of Polaron Ltd.(UK), private comm., (1983).

(109) A. Uhlir, Bell System Tech. J., 35, 333 (1956).

(110) D.R. Turner, J. Electrochem. Soc., 105, 402 (1958).

(111) C.D. Sharpe and B.S. Achar, paper presented at seminar organized by Polaron Ltd.,UK, (1984).

(112) P. Kramer, C. de Vriess, and L.J. Van Ruyven, J. Electrochem. Soc., 122, 314 (1975).

(113) M.W. Jenkins, J. Electrochem. Soc., 124, 757 (1977).

(114) F. Secco d'Aragona, J. Electrochem. Soc., 119, 948 (1972).

(115) D.G. Schimmel, J. Electrochem. Soc., 126, 479 (1979).

(116) V.D. Archer, J. Electrochem. Soc., 129, 2075 (1982).

(117) W.C. Dash, J. Appl. Phys., 27, 1193 (1956).

(118) S.M. Hu, J. Vac. Sci. Technol., 14, 17 (1977).

(119) C.W. Pearce, R.G. McMahon, J. Vac. Sci. Technol., 14, 40 (1977).

(120) C.J. Werkhoven C.W.T. Bulle-Lieuwma, B.J.H. Leunissen, and M.P.A. Viegers, J. Electrochem. Soc., 131, 1388 (1984).

(121) K. Wittmaack, Vacuum, 32, 65 (1982).

(122) C.C. Chang, "Characterization of Solid Surfaces", Ed. P.F. Kane and G.B. Larrabee, Chapter 20, Plenum Press, N.Y., (1974).

(123) C.C. Chang, Surf. Sci., 23, 283 (1970).

(124) J.P. Coad, H.E. Bishop, and J.C. Riviere, Surf. Sci., 21, 253 (1970).

(125) Chin-An Chang, J. Vac. Sci. Technol., 21, 663 (1982).

(126) N. Chew of RSRE(UK), private comm., (1984).

(127) L. Swarlter of General Electric(US), private comm., (1984).

(128) Annual Book of ASTM Standards, Part 43, F154, 1982.

(129) Y. Ota, J. Cryst. Growth, 61, 439 (1983).

(130) D. Robbins of RSRE(UK), L. Schwalter of General Electric(US), E. Kasper of AEG-Telefunken(W. Germany), private comm., (1983-1984).

(131) R.A. Metzger and F.G. Allen, J. Appl. Phys., 55, 931 (1984).

(132) J.C. Bean of Bell Labs.(US), private comm., (1984).

(133) A.S. Grove, "Physics and Technology of Semiconductor Devices", John Wiley & Sons, Inc., p.69, (1969).

(134) M. Tabe, K. Arai, and H. Nakamura, Surf. Sci., 99, L403 (1980).

(135) Shah et al, Phys. Rev. Lett., 37, 1622 (1976).

(136) D. Robbins, R.A.A. Kubiak, and E.H.C. Parker, paper presented at 3rd Int. Conf. on MBE August 1984, San Francisco, USA; to be published in J. Vac. Sci. Technol., March 1985.

(137) A. Cornu and R. Massot, "Compilation of Mass Spectra Data", Heyden & Son Ltd., London.

(138) R. Thompson, "Borides: Their Chemistry and Applications", Lecture Series 1965 No.5, Royal Institute of Chemistry, UK.

(139) N.N. Greenwood, "Comprehensive Inorganic Chemistry", Ed. J.C. Bailar et al, Vol. 1, Chapter 11, Pergamon Press, p.665-991 (1973).

(140) R.A.A. Kubiak, W.Y. Leong and E.H.C. Parker, J. Appl. Phys. Lett., 44, 878 (1984).

(141) F.J. Morin and J.P. Maita, Phys. Rev., 96, 28 (1954).

(142) R.E. Honig and D.A. Kramer, RCA Rev., 30, 285 (1969).

(143) B.O. Kolbesen and A. Mahlbauer, Solid St. Electron.,

195

$\underline{25}$, 759 (1982).

(144) C.T. Foxon and B.A. Joyce, "Current Topics in Materials Science", Ed. E. Kaldis, Vol. 7, Chapter 1, North-Holland, (1981).

(145) Y. Shiraki, Y. Katayama, K.L.I. Kobayashi, and K.F. Komatsubara, J. Cryst. Growth, $\underline{45}$, 287 (1978).

(146) R.A.A. Kubiak, W.Y. Leong, and E.H.C. Parker, paper presented at 3rd Int. Conf. on MBE August 1984, San Francisco, USA; to be published in J. Vac. Sci. Technol., March 1985.

(147) M. Pawlik of GEC Hirst RC(UK), private comm., (1984).

(148) M. Tabe and K. Kajiyama, Collected Papers of MBE-CST-2, Tokyo, (1982).

(149) Y. Shiraki of Hitachi (Japan), private comm., (1983).

(150) E. Kasper of AEG-Telefunken(W. Germany), private comm., (1984).

(151) T. Itoh, T. Nakamura, M. Muromachi, and T. Sugiyama, Jpn. Appl. Phys., $\underline{15}$, 1145 (1976).

(152) K.L. Chopra, J. Appl. Phys., $\underline{37}$, 2249 (1966).

(153) P.W. Atkins, "Physical Chemistry", p.775, 2nd edition, Oxford University Press, (1983).

(154) T. Sakamoto and M. Komuro, Jpn. J. Appl. Phys., $\underline{22}$, L760 (1983).

(155) E. Stirl and A. Adler, Z. Metallkd., $\underline{52}$, 529 (1961).

Acknowledgments

I would like to thank the Department of Physics for providing the ILEA funding and research facilities necessary for my Ph.D. work at the City of London Polytechnic. I am indebted to Drs. E.H.C. Parker, R.A.A. Kubiak and R.M. King for their supervisions, criticisms and encouragements (and occasional arguments) over the three years of the research work. I would also like to thank Dr. J.D. Grange (formerly of GEC Hirst RC) as my external supervisor.

Acknowledgments are due to Drs. M.G. Dowsett and D. McPhail of CLP (SIMS analysis), Drs. M. Pawlik and R. Groves of GEC Hirst RC (SR measurement), Drs. D. Robbins, R. Series and N. Chew of RSRE (PL, SR and TEM analysis), Dr. B. Hamilton and A. Sandhu of UMIST (PL and DLTS measurements), P. Cook of CLP (replica TEM), and R. Houghton of CLP for their contributions in the analysis of our Si-MBE materials; Dr. A. Hing of GEC Hirst RC for his support of the Si-MBE work and IMPATT device fabrication; and D. Gasson and Dr. R. Hardeman of RSRE for their collaborative work.

The support and advice from our technical staff of G.J.C. Burton, A. Albridge, K. Booke, P. Driscoll, W. Hugglestone, V. Manning and J. Hill have been invaluable and are gratefully acknowledged.

My sincere thanks are due to Dr. C. Sharpe of BTRL for his invaluable guidance on the use of the electrochemical CV profile plotter; and Dr. W. Bardsley (formerly of RSRE) for arranging my stay at RSRE (G. Malvern) during July-August 1982.

The Si-MBE research work at the City of London Polytechnic was carried out in collaboration with GEC Hirst Research Centre (Wembley, UK), British Telecom Research Laboratories (Martlesham Heath, UK) and VG Semicon Ltd. (East Grinstead, UK).

197

D56341 '85

END